

# Fatigue of Forged AZ80 Magnesium Alloy

by

Andrew Gryguć

A thesis

presented to the University of Waterloo

in fulfillment of

the thesis requirement for the degree of

Doctor of Philosophy

in

Mechanical and Mechatronics Engineering

Waterloo, Ontario, Canada, 2019

© Andrew Gryguć 2019

## Examining Committee Membership

The following served on the Examining Committee for this thesis. The decision of the Examining Committee is by majority vote

External Examiner	FILIPPO BERTO, Ph.D. Professor, Norwegian University of Science and Technology
Supervisor	HAMID JAHED, Ph.D. Professor, University of Waterloo
Supervisor	MARY WELLS, Ph.D. Professor, University of Waterloo
Internal Member	GREGORZ GLINKA, Ph.D. Professor, University of Waterloo
Internal Member	ADRIAN GERLICH Ph.D. Professor, University of Waterloo
Internal-External Member	SUSAN L. TIGHE, Ph.D. Professor, University of Waterloo

## Authors Declaration

This thesis consists of material all of which I authored or co-authored: see Statement of Contributions included in this thesis.

This is a true copy of the thesis, including any required final revisions, as accepted by my examiners.

I understand that my thesis may be made electronically available to the public.

## Statement of Contributions

The research detailed in this thesis was supported by Natural Sciences and Engineering Research Council of Canada (NSERC) through the Automotive Partnership Canada (APC) with contributions from Multimatic Technical Centre, Ford Motor Company, and Centerline Windsor. Furthermore, the content presented in Chapters 3 to 5 have been taken from manuscripts which have been published. The candidate is the primary author of all manuscripts, and was responsible for directly collecting data or co-ordinating the collection of data, and for conducting the synthesis and analysis of the results. As a result, a number of co-authors have contributed to the current work. The individual contributions from all of the co-authors are as follows:

Prof. Hamid Jahed and Prof. Mary Wells: supervised and mentored all work which was completed in this thesis. They also provided both technical and editorial feedback in the preparation of the individual manuscripts in Chapters 4-6 as well as this document.

Dr. Seyed Behzad Behravesh: acted to provide both technical and editorial feedback in the preparation of the individual manuscripts in Chapters 4-6.

Dr. Sugrib Kumar Shaha: performed X-Ray Diffraction tests on a variety of samples and provided pole figure data. This data was utilized to infer the local texture of the material and was a vital part of the conclusions drawn in the work presented in Chapter 4.

Dr. Bruce Williams: acted as the liaison between CanmetMATERIALS and the University of Waterloo to facilitate successful forging of a variety of different AZ80 Mg forging configurations. Both the simple upset open-die radial forgings (chapter 4) and the closed-die I-beam forgings (chapters 5 and 6) were instrumental in characterizing forged AZ80 material.

Dr. Xuming Su: facilitated collaboration between research labs and provided load frames/equipment at Ford's Research and Innovation Center in Dearborn, MI for doing fatigue testing. He also acted to provide technical feedback and advice throughout this work. The data which were resulting from this collaboration is reported in chapters 4 and 5 of this report.

## Abstract

The majority of research surrounding the fatigue of Mg alloys generally exhibits a rigid dichotomy between theoretical and applied contributions. This research work addresses both of these domains of the field from a more holistic sense, yet still remains highly detail oriented. Automotive suspension components generally have complex geometries and undergo highly multiaxial loading. This is partly due to the packaging constraints imposed by the many dynamic systems within a vehicle, and the impetuous towards lightweighting to improve efficiency and reduce greenhouse gas emissions. As such, the current optimal solution for such a component typically a complex shape made from a material with high specific strength. Both forging and casting lend themselves to facilitating large scale production of such components using industrially compatible processes. Forging however produces a product with attributes which are more optimally suited for advanced vehicle lightweighting applications.

Of the commercially available Mg alloys, the AZ80 alloy is a Mg alloy with good forgeability, a high aluminium content, and superior strength. However the fatigue properties of this alloy are largely unknown, especially in complex multiaxial loading paths such as which automotive suspension components undergo. This thesis acts to fill this gap in knowledge, by providing the foundation for the understanding of the complex cyclic behavior of forged AZ80 Mg, as well as predicting its fatigue life to ensure the satisfaction and safety of the end consumer. Various small scale forging methods were investigated and characterized in such a way that it one can connect them to the larger scale component in the engineering application. Two varieties of base material were selected to be forged into these small scale forgings, cast and extruded. Furthermore, an understanding was developed on the influence of material texture on the cyclic deformation mechanism and resulting fatigue life. The implications of multiaxial loading on the fatigue behaviour was also characterized as well as the effect of non-proportional loading. A variety of different models were utilized to reliably predict the fatigue life of forged AZ80 Mg in both simple uniaxial and complex non-proportional bi-axial loading paths. The culmination of all of these research objectives enabled effective utilization of forged AZ80 Mg as a lightweight material for a variety of different fatigue critical engineering applications.

It was concluded that the thermomechanical history imparted to the material via forging resulted in a texture intensification and a rotation of the crystallographic cells to align with the loading direction during forging. Secondly, following forging, both the cast-forged and extruded-forged material exhibited an significant increase in fatigue life. It was also discovered that the style of closed-die forging being investigated had spatially varying properties with texture orientations which varied based on the local forging directions and intensities which were dependent on the starting texture as well as the

thermomechanical history. Furthermore, following characterization of the materials behaviour over a variety of different loading paths, the biaxial fatigue response is somewhat dominated by the axial component and the non-proportional effect to be detrimental to the fatigue life. Finally, it was concluded that the optimal forging condition tends towards the coldest temperature and fastest strain rate which are pragmatically possible (within the context of warm forging) that produce a forging free of defects and of high quality. This optimal condition corresponded to extruded AZ80 Mg forged at a temperature of 250°C and 20 mm/sec.

## Acknowledgements

I fully acknowledge that from the beginning of my graduate studies I was very fortunate to be a part of a great research group with many knowledgeable and passionate colleagues. It would be naive of me to believe that this journey could have been completed in isolation. Thus, I would like to take this opportunity to thank those key people who have contributed to the completion of this thesis and my degree.

To my supervisors, Hamid Jahed and Mary Wells, I am deeply privileged to have had the opportunity to interact with both of you on various facets of my academic and professional careers. From fostering my research development in its infancy to the support you both gave me to pursue new ideas and embracing my inquisitive nature. This has provided me with the opportunity to not only grow as a prolific researcher, but also mature as a human being. I am also grateful for the several reference letters which you both happily provided me along the way which not only reinforced the fact that you had confidence in my abilities, but that you recognized the potential which I possess to make valuable contributions to the scientific community.

To my remaining committee members, Gregorz Glinka, Adrian Gerlich, Susan L. Tighe, and Filippo Berto, I give you my sincerest thanks in your guidance in completing this work. Your feedback and contributions have helped improve both the quality of the work contained within this thesis but its prolificacy in the larger scientific community. Gregorz Glinka, your mentorship as a former professor as well as a committee member is greatly appreciated. Much of my foundational knowledge in fatigue has come from your teachings, intriguing questions and remarkable feedback. Adrian Gerlich, it was your graduate course which I took early on in my studies which sparked my appetite for materials engineering and fueled my passion for experimental research. Susan L. Tighe, your feedback during my comprehensive exam brought much of the direction of my latter research into focus. Your attention to detail, and insightful questions are much appreciated. Finally, Filippo Berto, your scientific contributions in the topics of fatigue and fracture of additively manufactured material are particularly interesting to me, as that is the direction which I intend to take with my future research. Your feedback was invaluable, and truly allowed me to enhance my dissertation to make the largest scientific contribution possible.

To my research colleagues, both within the University of Waterloo and beyond. Collaboration and dissemination of my research has been a valuable skill that was highly reinforced via our interactions. Academia is truly a global community, and understanding the nuances of how research is conducted worldwide offers a unique perspective which has enhanced both my research efficacy and its impact. Specifically, Mr. Dwayne Toscano whom designed the updated biaxial tubular specimen geometry to fit

within the I-beam forging spatial constraints. This facilitated extraction of several samples from one forging and seamless testing and strain measurement using our Instron Bi-Axial load frame. The data which were resulting from this specimen design is reported in chapter 5 of this report. Although not a co-author on any of the work presented here, as an academic colleague his contribution was significant.

Furthermore, I would like to acknowledge the support of Natural Sciences and Engineering Research Council of Canada (NSERC) through the Automotive Partnership Canada (APC) under APCPJ 459269-13 grant throughout this work. Further support from NSERC via an Industrial Post Graduate Scholarship (IPS1) and Ontario Graduate Scholarship (OGS) were also instrumental in supporting this research work.

Finally, I would like to acknowledge the support of my family, for without them I would not have had the opportunity to grow into an inquisitive minded individual with a passion for learning and a thirst for knowledge.

## Table of Contents

Examining Committee Membership .....	ii
Authors Declaration .....	iii
Statement of Contributions .....	iv
Abstract .....	v
Acknowledgements .....	vii
List of Figures .....	xii
List of Tables .....	xviii
List of Abbreviations .....	xix
1. Introduction .....	1
1.1. Background .....	1
1.2. Objectives .....	2
1.3. Thesis Structure .....	3
2. Literature Review .....	6
2.1. AZ80 Magnesium Alloy .....	6
2.1.1. Microstructure .....	7
2.1.2. Physical and Mechanical Properties .....	7
2.1.3. Fatigue Properties .....	9
2.1.4. Forging and other thermomechanical processing of AZ80 Mg Alloys .....	10
2.2. Elasto-Plastic Modelling .....	13
2.3. Fatigue Life Modelling .....	14
3. Methodology .....	15
3.1. Introduction .....	15
3.2. Material Processing & Forging .....	15
3.3. Experimental Methodology .....	17
3.3.1. Specimen Preparation and Characteristics .....	17
3.3.2. Microstructure and Texture .....	19
3.3.3. Superficial Hardness .....	20
3.3.4. Strain Measurement .....	21

3.3.5.	Quasi-Static (Monotonic) Tests.....	22
3.3.6.	Stress Controlled Fatigue Tests.....	22
3.3.7.	Strain Controlled Fatigue Tests.....	23
3.3.8.	Multiaxial Fatigue Tests .....	24
3.3.9.	Fractography .....	25
3.4.	Fatigue & Life Modelling Methodology .....	27
3.5.	Overview of Research Methodology.....	27
4.	Monotonic and cyclic behaviour of cast and cast-forged AZ80 Mg.....	29
4.1.	Introduction .....	31
4.2.	Experimental .....	33
4.3.	Results & Discussion .....	35
4.3.1.	Microstructure and Texture.....	35
4.3.2.	Monotonic and Cyclic.....	38
4.3.3.	Fatigue Life.....	46
4.3.4.	Fracture Mechanisms.....	47
4.3.5.	Fatigue Life Modelling.....	49
4.4.	Conclusions .....	54
5.	Low-cycle fatigue characterization and texture induced ratcheting behaviour of forged AZ80 Mg alloys .....	56
5.1.	Introduction .....	58
5.2.	Experimental .....	59
5.3.	Results & Discussion .....	61
5.3.1.	Microstructure and Texture.....	61
5.3.2.	Monotonic and Cyclic.....	64
5.3.3.	Fatigue Life.....	68
5.3.4.	Fracture Mechanisms.....	69
5.3.5.	Fatigue Life Modelling.....	71

5.4.	Conclusions .....	76
6.	Multiaxial cyclic behaviour of extruded and forged AZ80 Mg alloy .....	77
6.1.	Introduction .....	79
6.2.	Experimental .....	80
6.3.	Results & Discussion .....	82
6.3.1.	Monotonic and Cyclic.....	86
6.3.2.	Uniaxial Fatigue Life (Paths A and B).....	90
6.3.3.	Biaxial Fatigue Life (Paths C, D and E) .....	95
6.3.4.	Fracture Mechanisms.....	101
6.4.	Conclusions .....	103
7.	Discussion .....	105
7.1.	Advanced Vehicle Lightweighting using Forged AZ80 Mg Alloy .....	105
7.2.	Forging Process Optimization .....	105
7.3.	Conclusions .....	112
8.	Summary, Conclusions and Future Work .....	114
8.1.	Summary .....	114
8.2.	Conclusions .....	114
8.3.	Recommendations and Future Work.....	117
	Letter of Copyright Permission.....	118
	References.....	122
9.	Appendix A – Experimental Data .....	131

## List of Figures

Figure 1 - Multi Material Lightweight Vehicle (MMLV) Body in White Material Distribution (64% Aluminum & 36% Steel) [3] (Copyright © 2015 SAE International. All rights reserved).....	2
Figure 2 - Key findings and contributions of the conducted research to fundamental knowledge and engineering applications. ....	4
Figure 3 - Typical tensile strength and elongation for most common commercial wrought Mg alloys (© Reproduced via full text provided by author) [5] .....	6
Figure 4 - S-N curve obtained from (a) stress-controlled LCF test and (b) $\epsilon$ -N curve obtained from total strain control LCF test for various AZ31, AZ61 and AZ80 Mg Alloys (Reproduced with permission from Elsevier) [16] .....	9
Figure 5 - Mechanical Properties of die-casting and wrought Mg alloys (Reproduced via full access from Wiley ©) [35].....	10
Figure 6 - Automotive forgings made from AZ80 Mg (a) connecting rod* (b) wheel (c) shock absorber head (d) differential case (e) suspension control arm [*Shown is ZC71/SiC/12P part, however an AZ80 forged part was also forged]. [28] Reproduced with permission from Taylor and Francis, [29][32] reproduced with permission from Elsevier, [31] reproduced with permission from Sage Publishing, [30][22] Reproduced via full text provided by author, [8] reproduced via full access provided by Wiley.	11
Figure 7 - Critical Resolved Shear Stress (CRSS) as a function of temperature for a variety of different deformation mechanisms for Mg Alloy [42]. ....	13
Figure 8 - Interlaken 500T Hydraulic Press. Forgings were produced on this press located at CanmetMATERIALS in Hamilton, Ontario, Canada. ....	15
Figure 9 - Various stages of processing for two styles of forging (open die and closed die) .....	16
Figure 10 - Schematic representation of temperature history for various stages of the processing during forging. Different line weights show approximate effect of convective cooling on the slower rate forgings. ....	16
Figure 11 - Orientation of samples from within a (a) cylindrical billet (b) I-Beam forging.....	17
Figure 12 - Surface roughness within the gauge section of various sample geometries of the flat "dogbone" sample used for uniaxial monotonic and fatigue tests along the (a) the flat surface (b) the side curved surface and then (c) the outer surface of the hollow tubular samples used for the pure shear and biaxial tests.....	18
Figure 13 - Axial "dogbone" specimen geometry .....	19
Figure 14 - Hollow tubular specimen geometry .....	19
Figure 15 - United True Blue II Rockwell Hardness Tester .....	20
Figure 16 - Bruker D8-Discover equipped with a VANTEC-500 area detector.....	20

Figure 17 - GOM Aramis 3D 5MP DIC System with detailed view of specimen surface .....	21
Figure 18 - Epsilon 3550 Biaxial extensometer, shown without adhesive coating applied.....	22
Figure 19 - Example setup of uni-axial stress controlled fatigue test. ....	23
Figure 20 - Example setup of a uni-axial strain controlled fatigue test. ....	24
Figure 21 - Loading paths used for the fatigue experiments (a) pure-axial, (b) pure shear, (c) proportional (d) 45° out of phase and (e) 90° out of phase.....	25
Figure 22 - Fracture surface EDX analysis example .....	26
Figure 23 - Quantitative analysis of fracture surface using Light Optical Microscopy .....	26
Figure 24 – Definitions of elastic (grey) and plastic (yellow) strain energy densities (SED) for a schematic cyclic hysteresis loop. [55] .....	27
Figure 25 - Graphical Illustration of Research Methodology .....	28
Figure 26 - A. Gryguć et al., “Monotonic and cyclic behaviour of cast and cast-forged AZ80 Mg,” Int. J. Fatigue, vol. 104, pp. 136–149, 2017.....	29
Figure 27 - Schematic image showing tensile/fatigue and compression sample extraction from (a) the as-cast billet, (b) the sample forged at 39 mm min <sup>-1</sup> and 350°C.....	34
Figure 28 - Typical LOM microstructure and XRD pole figures for As-Cast ((a) and (c)), forged condition S1 ((b) and (d)), forged condition S2 ((e) and (g)), and forged condition S3 ((f) and (h)) .....	37
Figure 29 - Relationship between basal pole figure max intensity and average grain size for as-cast and forged conditions (S1, S2, and S3) .....	38
Figure 30 – Tensile (a) monotonic and (b) cyclic stress-strain curves for as-cast (black) and forged Mg (red).....	40
Figure 31 – Compressive (a) monotonic and (b) stabilized cyclic stress-strain curves for as-cast (black) and forged Mg (red).....	40
Figure 32 - Summary of (a) monotonic yield strengths and (b) change in yield strengths following cyclic testing for both the as-cast (black) and forged (red) material in tension and compression.....	41
Figure 33 - Axial cyclic behaviour of AZ80 at a strain amplitude of 0.5% in (a) as-cast and (b) forged samples.....	43
Figure 34 - Axial cyclic behaviour of AZ80 at a strain amplitude of 1.0% (a) as-cast and (b) forged samples.....	43
Figure 35 – Plastic strain response during strain-controlled cyclic testing showing variations in peak tensile and compressive plastic strain vs. number of cycles for both as-cast (black) and forged material (red), at 1.0% and 0.5% strain amplitudes .....	45
Figure 36 - Stress response during strain-controlled cyclic testing showing variations in mean stress vs. number of cycles at various strain amplitudes (results for 0.3% are only shown up to 10,000 cycles).....	45

Figure 37 - Stabilized cyclic axial behaviour of (a) as-cast and (b) forged AZ80 Mg alloy .....	46
Figure 38 – $\epsilon$ -N curves for as-cast (black) and forged (red) AZ80 Mg alloy obtained at strain amplitudes between 0.1 and 1.4% .....	47
Figure 39 - Fracture surfaces of the as-cast ((a) and (b)) and forged conditions ((c) and (d)) for samples tested at a strain amplitude of +/- 0.3%. As-cast sample fractured at 15, 644 cycles and forged sample at 66, 171 cycles. FCI denotes the fatigue crack initiation location and arrows denote the approximate propagation direction. Images (b) and (d) show a detailed view of the surface morphology in the final fracture (FF) zone. ....	48
Figure 40 - Strain-life data used for extracting Coffin-Manson constants in (a) as-cast and (b) forged AZ80 Mg; (c) SWT damage parameter evolution with number of cycles to failure for both as-cast and forged AZ80 Mg; and (d) the correlation between SWT-predicted fatigue life and experimental life for both as-cast and forged AZ80 Mg.....	51
Figure 41 – Strain energy-life data used for extracting energy-based constants in (a) as-cast and (b) forged AZ80 Mg; (c) Jahed-Varvani damage parameter evolution with number of cycles to failure for both as-cast and forged AZ80 Mg; and (d) the correlation between the Jahed-Varvani predicted fatigue life and experimental life for both as-cast and forged AZ80 Mg.....	53
Figure 42 - A. Gryguć et al., “Low-cycle fatigue characterization and texture induced ratcheting behaviour of forged AZ80 Mg alloys,” Int. J. Fatigue, vol. 116, pp. 429–438, 2018.....	56
Figure 43 – (a) schematic of AZ80 Mg closed die forgings with asymmetric I-beam cross section conducted at (b) 375°C and 20 mm/sec ram speed prior to trimming off the flash extruded then forged. .	60
<i>Figure 44 – Microstructural characterization of Cast AZ80 forged at 375°C and 20 mm/sec. Basal and prismatic pole figures are presented in locations 7 (a), location 15 (b), and location 8 (f) of the forging. Figure (c) and (e) show LOM images of locations 1 and 8, respectively within the forging (view in the longitudinal direction). Figure (d) denotes the spatial variation of superficial hardness (30T) in the direction normal to the cross-section of the forging. FD denotes forging direction, TD: transverse direction, and LD: longitudinal direction. ....</i>	63
Figure 45 - Microstructural characterization of AZ80 extrusion forged at 375°C and 20 mm/sec. Basal and prismatic pole figures are presented in locations 7 (a), location 15 (b) and location 8 (f) of the forging. Figure (c) and (e) show LOM images of locations 1 and 8, respectively within the forging (view in the longitudinal direction). Figure (d) denotes the spatial variation of superficial hardness (30T) in the direction normal to the cross-section of the forging. FD denotes forging direction, TD: transverse direction, and LD: longitudinal direction.....	64

Figure 46 - Tensile monotonic engineering stress-strain curves for as-received materials as well as cast-forged and extruded forged conditions in two different locations within the forging. The tall-flange corresponds with location 1 and the web corresponds to location 8.....	65
Figure 47 - The axial cyclic behaviour of as-cast and cast-forged AZ80 at a fully reversed stress amplitude of 190 MPa. Forged samples were taken from location 3 in tall-rib.....	66
Figure 48 – The axial cyclic behaviour of as-extruded and extruded-forged AZ80 at a fully reversed stress amplitude of 180 MPa. Forged samples were taken from location 10 in the web. ....	67
Figure 49 – Mean engineering strain response during stress-controlled cyclic testing for both as-received material as well as cast-forged and extruded-forged. Cast-forged response is shown for location 3 and extruded-forged for location number 10 within the web. ....	68
Figure 50 - S-N curves for as-cast and cast-forged (black) as well as as-extruded and extruded-forged (red) AZ80 Mg. Samples were taken from a variety of different locations throughout forging, location within forged billet denoted next to datapoint. ....	69
Figure 51 – Final fracture surfaces of the (a) cast-forged (b) and extruded-forged conditions for samples tested under stress control at 190 MPa. (a)(c)(e) are a cast-forged sample (b)(d)(f) are an extruded forged sample. FCI denotes fatigue crack location. ....	70
Figure 52- (a) JV damage parameter evolution with a number of cycles to failure for both as-received and forged AZ80 Mg; and (b) the correlation between two parameter predicted fatigue life and experimental life for both as-received and forged AZ80 Mg. (c) the correlation between prediction of two parameter and JV energy based model predictions for the as-received material. Locations within the billet for each forging are denoted beside each datapoint. The dashed lines in (b) and (c) denote bounds of $\pm 2.5$ .....	75
Figure 53 - A. Gryguć et al., “Multiaxial cyclic behaviour of extruded and forged AZ80 Mg alloy,” Int. J. Fatigue, vol. 127, pp. 324–337, 2019.....	77
Figure 54 - a) Closed die forging schematic with top/bottom dies shown (grey) and extruded billet (yellow) prior to forging. (b) Axial (Red), shear (white) and microstructural/texture (green) sample orientation within forged billet. FD denotes forging direction, LD: Longitudinal Direction and TD: Transverse Direction. ....	82
Figure 55 - Specimens’ geometries and sizes: (a) flat specimen for axial tests, (c) tubular specimen for torsion tests. All dimensions in mm. ....	82
Figure 56 - Loading paths used for the fatigue experiments (a) pure-axial, (b) pure shear, (c) proportional (d) 45° out of phase and (e) 90° out of phase.....	84
Figure 57 - Microstructural characterization of AZ80 extrusion forged at 250°C and 20 mm/sec. Basal and prismatic pole figures are presented in locations 1 (a), location 15 (b) and location 8 (f) of the forging. Figure (c) and (e) show LOM images of locations 1 and 8, respectively within the forging (view in the	

longitudinal direction). Figure (d) denotes the spatial variation of superficial hardness (30T) in the direction normal to the cross-section of the forging. FD denotes forging direction, TD: transverse direction, and LD: longitudinal direction..... 86

Figure 58 - Axial stress strain response for as-extruded and extruded forged AZ80 Mg. Solid lines indicate monotonic response and dotted symbols indicate the stabilized cyclic response..... 87

Figure 59 - Shear stress strain response for extruded forged AZ80 Mg. Solid lines indicate monotonic response and symbols indicate the stabilized cyclic response. .... 88

Figure 60- Evolution of (a) peak axial stress and (b) mean axial stress with number of cycles for various Path A (pure axial) strain amplitudes..... 89

Figure 61 - Evolution of shear (a) stress amplitude and (b) mean shear stress with number of cycles for various Path B (pure shear) strain amplitudes. .... 90

Figure 62 -  $\epsilon$ -N curves for loading path A (pure axial) for as-extruded (black) and forged (red) AZ80 Mg alloy obtained at strain amplitudes between 0.2 and 2.0%. For reference, triangular symbols are included showing a previous study done on cast and forged AZ80 Mg by Gryguc et al. [95]. (For interpretation of the references to colour in this figure legend, the reader is referred to the web version of this article.) .... 94

Figure 63 - Relationship between SWT damage parameter (a) and Total Energy (Jahed-Varvani) (b) vs. number of reversals to failure for loading path A (pure axial) for all three material conditions (ED, RD, forged)..... 94

Figure 64 - Correlation between experimental life and predicted life for loading path A (pure axial) for all three material conditions (ED, RD, forged). Circular symbols denote life predictions using SWT model, and the triangular symbols denote life predictions using the Jahed-Varvani Model. The dashed lines denote bounds of  $\pm 2.0$ ..... 95

Figure 65 -  $\epsilon$ -N curves for loading paths A,B,C,D and E for the forged material ..... 97

Figure 66 - Stabilized cyclic hysteresis loops for (a) axial and (b) shear for various strain paths. For biaxial paths (C, D and E) the corresponding strain of the other axis is shown following the phase angle. .... 98

Figure 67 – Relationship between Total Energy (Jahed-Varvani) vs. number of reversals to failure for the forged material for loading paths A,B,C,D and E..... 100

Figure 68 - Correlation between experimental life and predicted life for the loading paths A,B,C,D, and E for the forged material. The dashed lines denote bounds of  $\pm 2.0$ ..... 100

Figure 69 – Macroscopic crack path of forged specimens: (a) monotonic axial (b) monotonic shear, (c) path A  $\Delta\epsilon/2 = 0.4\%$  and  $N_f = 9220$  cycles, (d) path B  $\Delta\epsilon/2 = 0.7\%$  and  $N_f = 15\ 296$  cycles, (e) Path C,  $N_f = 1201$  cycles, (f) Path D,  $N_f = 3798$  cycles, (g) Path E,  $N_f = 1492$  cycles. Scale bars shown for reference. .... 102

Figure 70 – Fracture surface of (a) path A $\Delta\varepsilon/2 = 0.4\%$ and $N_f = 9220$ cycles and (b) Path E, $\Delta\varepsilon/2 = 0.4\%$ , $\Delta\gamma/2 = 0.5\%$ , $N_f = 1492$ cycles. Fatigue crack initiation site is denoted by ‘FCI’. Scale bars shown for reference.....	103
Figure 71 - Definition of components of static behaviour contribution to the objective function.....	107
Figure 72 - Definition of components of fatigue behaviour contribution to the objective function .....	107
Figure 73 - Superficial hardness maps from forgings done at 300°C. (a) Cast-Forged AZ80, (b) Extruded-Forged AZ80, (30T scale).....	108
Figure 74 - Optimization surfaces for (a) as-cast then forged and (b) as-extruded then forged material for AZ80 Mg. Areas in red indicate the processing temperature and strain rate which results in the optimum performance of the forged material.....	109
Figure 75 - Peak flow stress for (a) as-cast then forged and (b) as-extruded then forged material AZ80 Mg alloy. Areas in red indicate the processing temperature and strain rate which results in the highest flow stress during isothermal open die simple upset forging of cylindrical billets. Data shown for extruded material was taken as the maximum from either the radial or transverse directions. ....	110
Figure 76 – $\varepsilon$ -N curves for all of the investigated AZ80 Mg material conditions .....	111
Figure 77 - Energy Life curves for all of the investigated AZ80 Mg material conditions.....	112

## List of Tables

Table 1 - Summary monotonic properties found in literature for various forms of AZ80 Mg .....	8
Table 2 - Summary fatigue properties found in literature for various forms of AZ80 Mg .....	8
Table 3- The relationship between microstructural, monotonic, and cyclic properties of as-cast and forged AZ80-F Mg alloy. Tensile properties are presented first, followed by compressive properties in parenthesis.....	38
Table 4 - Coffin-Manson parameters for SWT model for cast and forged AZ80 Mg .....	50
Table 5 - Energy-based parameters for the Jahed-Varvani model for cast and forged AZ80 Mg .....	52
Table 6- The relationship between microstructural, superficial hardness, and monotonic properties of as-cast, as-extruded and cast-forged (CF) and extruded-forged (EF) AZ80 Mg alloy. Tensile properties are presented first, followed by compressive properties in parenthesis, where available.....	62
Table 7 - Energy-based parameters for the JV and two parameter models for the as-cast, as-extruded, as well as closed die cast-forged and closed die extruded forged at 375 deg C and 20 mm/sec.....	73
Table 8 - The relationship between monotonic axial and shear properties of as-extruded and extruded-forged at 250°C and 20 mm/sec AZ80 Mg. Note: Values in parenthesis show delta to cyclic yield strength (i.e. increase in yield strength due to cyclic hardening).....	83
Table 9 - Description of the investigated strain amplitudes for fatigue experiments for each loading path. ....	84
Table 10 - Coffin-Manson parameters for SWT model and Energy based parameters for Jahed-Varvani model for as-extruded and forged AZ80 Mg for Path A (pure axial) .....	92
Table 11 - Coffin-Manson parameters for SWT model and Energy based parameters for Jahed-Varvani model forged AZ80 Mg for Path B (pure shear).....	93
Table 12 - Summary of the axial loading path strain life ( $\epsilon$ -N) and energy life parameters for all the investigated material conditions.....	111
Table 13 – List of abbreviations for all AZ80 Mg material conditions presented in appendix experimental data.....	131
Table 14 - Cyclic Axial Test Summary (Path A - Uni-Axial) .....	131
Table 15 - Cyclic Shear Test Summary (Path B Uni-Axial). *Note all samples are from the Longitudinal Direction (LD) of forged condition E (Ext-Forged Closed-Die (250°C @20.0 mm/min).....	135
Table 16 – Cyclic Bi-Axial Test Summary (Path C,D,E). *Note all samples are from the Longitudinal Direction (LD) of forged condition E (Ext-Forged Closed-Die (250°C @20.0 mm/min).....	135

## List of Abbreviations

BCC – Body Centered Cubic

CF – Cast-Forged

CRSS – Critical Resolved Shear Stress

ED – Extrusion Direction

EF – Extruded-Forged

-F – As Fabricated

FCC – Face Centered Cubic

FCI – Fatigue Crack Initiation

FCP – Fatigue Crack Propagation

FD – Forging Direction

FF – Final Fracture

FS – Fatemi-Socie

HCF – High Cycle Fatigue

HCP – Hexagonal Closed Packed

HR30T – Hardness Rockwell 30 Ton

IST – Incremental Step Test

JV – Jahed-Varvani

LCF – Low Cycle Fatigue

LD – Longitudinal Direction

LOM – Light Optical Microscopy

Mg – Magnesium

ND – Normal Direction

RD – Radial Direction

SED – Strain Energy Density

SEM – Scanning Electron Microscopy

SWT – Smith-Watson-Topper

TD – Transverse Direction

UTS – Ultimate Tensile Strength

XRD – X-Ray Diffraction

YS – Yield Strength

# 1. Introduction

## 1.1. Background

Responsible energy consumption has been at the forefront of the media attention and public engagement for the past few decades. The public as a whole is more aware of their carbon footprint and environmental impact with both the products we buy, and the way we use them. Each and every day we make conscious choices to minimize our energy consumption in an effort to live more sustainable lifestyles. Often as a by-product of consuming energy, the emissions of undesirable pollutants into our atmosphere is somewhat inevitable. Often the scape-goat in the greenhouse gas conversation is the auto industry, in particular, fossil fuel burning automobiles. The demand for increasing automotive efficiency is on the rise, currently the United States Department of Transportation stipulates that every car sold to the public must be 30% more fuel efficient than those sold five years ago. Fast forward to the year 2025 and corporate average fuel economy requirements mandate that number jumps to 95% better than where we are today[1]. Although some might say it is an optimistic goal, automakers are currently developing advanced technologies on many different fronts to solve the energy consumption dilemma. Many of these consist of increasing efficiencies in the vehicles, engine, powertrain, and aerodynamics, but by far the most effective near term solution for reducing fuel consumption is decreasing the vehicles mass. A lighter vehicle requires less energy to move (be it accelerate, decelerate or turn).

A new emerging philosophy is that of a multi material lightweight vehicle or MMLV (Figure 1), where not only is a conventional material substituted for a lightweight one, but the lightweight material is used in a location where its performance is optimal. For example, the b-pillar structure in a vehicle is very active in a side impact event where low intrusion into the occupant compartment is important. For this, steel is the optimal material as it provides the high strength and stiffness required to meet these unique requirements in this part of the vehicle. However, in a frontal or rearward crash, where the vehicles crumple zones are engaged, aluminum performs well as it has good ductility and energy absorption abilities. Intelligently utilizing high strength conventional materials such as steel and aluminum can yield significant weight savings on its own, however incorporation of other advanced materials into vehicle light weighting shows promising untapped potential. For components which are driven by cyclic loading or fatigue, such as a suspension control arm, there is a unique opportunity to utilize magnesium as it offers superior performance to all other structural metals in this service environment [2]. Magnesium offers similar strength and fatigue properties to aluminum, but at two thirds of the mass [2]. The weight savings compared to steel is even more dramatic at over 77%. Exploiting the benefits of this material to its full potential would have a profound impact, for a typical passenger car, a 70kg weight savings is attainable. This equates to a 4% reduction in overall vehicle mass and a 2% reduction in fuel consumption.

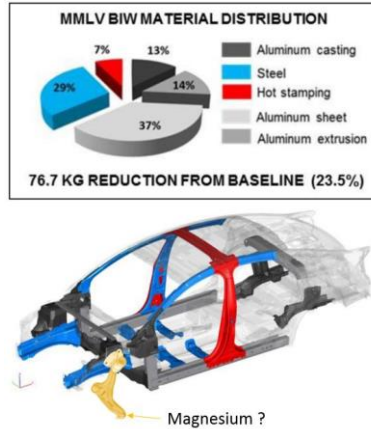


Figure 1 - Multi Material Lightweight Vehicle (MMLV) Body in White Material Distribution (64% Aluminum & 36% Steel) [3] (Copyright © 2015 SAE International. All rights reserved)

However, the inferior cast properties, and poor formability of magnesium (Mg) alloys at room temperature resulting from strong crystallographic texture, and consequential anisotropic mechanical properties commonly formed during processing, limits the application of Mg alloys for manufacturing of complex geometry parts such as a control arm. Forging is a near net-shape manufacturing technique that has been widely accepted in the past to offer a great benefit as a material processing technique to produce a heavily refined wrought microstructure, lower internal defect density and recrystallized grain structure resulting in superior strength, improved ductility and longer fatigue life [4]. The focus of this research is to examine the effect of hot and warm forging, on the mechanical properties of the Mg parts and their feasibility to be manufactured in this way into complex, load bearing Mg parts such as an automotive suspension control arm. The domain of this research within the framework of the integrated computational materials engineering (ICME) method towards designing products lies within the scope of the structure-properties-performance relationship. The interaction between these domains as it applied to forged Mg is of particular relevance and can be considered to be the general focus of this research work. Successful development and implementation of this lightweight material technology will not only play a significant role in solving the global energy problem, but it will enable society as a whole to live more sustainable and responsible lifestyles.

## 1.2. Objectives

The research detailed in this thesis was conducted as part of Natural Sciences and Engineering Research Council of Canada (NSERC) through the Automotive Partnership Canada (APC) under APCPJ 459269-13 grant with contributions from Multimatic Technical Centre, Ford Motor Company, and Centerline Windsor are acknowledged. The authors would also like to acknowledge J. McKinley from CanmetMATERIALS, Hamilton for forging trials. The APC project expands on the results of prior research in the field of fatigue of Mg alloys with the overall goal of developing discovery-level base

knowledge of the thermomechanical behaviour, durability performance and life enhancement, corrosion protection strategies and performance, metallic smart structures, and computer aided engineering design of forged magnesium alloys. Through this research, enabling technology necessary for the optimum design of magnesium fatigue-critical components, and robust strategies for die forging and part design will be developed. The project itself is composed of seven major tasks (i) Optimization of the magnesium forging process, including development of the microstructure and the manufacturing process of the magnesium forged parts (ii) Lightweighting design optimization (iii) Residual stress and life enhancement through cold spray coating and shot peening and optimization of the processes through parameter testing (iv) Optical-based in situ measurement of residual stress using novel embedded (FBG) sensors (v) Fatigue and fracture characterization, constitutive modeling, quantification of plasticity induced anisotropy, and full-scale testing (vi) Corrosion performance characterization, modeling, and validation (vii) Corrosion performance characterization, modeling, and validation

The objective of the research detailed in this thesis was to address tasks (i) and (v), i.e. the development and optimization of the magnesium forging process and the fatigue and fracture characterization. Although addressing these tasks were the primary focus of this work presented here, these efforts were not done in isolation, each task is very much connected and effective knowledge transfer and frequent collaboration was necessary to fulfill the task objectives and meet the overall project goals.

To this end, the objectives of this research are:

1. To characterize the effect of forging on the mechanical properties of both cast and extruded AZ80 Mg.
2. To develop an understanding of the influence of texture on the cyclic deformation mechanism and fatigue life.
3. To characterize the cyclic response and fatigue behaviour of forged AZ80 Mg in a variety of different loading paths.
4. To predict the fatigue life of forged AZ80 Mg in a variety of different loading paths.
5. To enable the effective utilization of forged AZ80 Mg as a lightweight material in structural applications which are fatigue critical for a variety of engineering applications.

### 1.3. Thesis Structure

The remaining contents of this thesis are organized as a manuscript based thesis. Chapter 2 provides a review of the key topics and literature which is relevant to the current research. Chapter 3 outlines a detailed overview of the research methodology for this work. It describes in detail the background and

context of the material processing and forging, as well as the experimental and modelling methodologies which were utilized in the subsequent chapters of this work. Chapters 4 to 6 are manuscripts which have been published in the International Journal of Fatigue which report on key research findings. The candidate is the primary author of all manuscripts, and was responsible for directly collecting data or co-ordinating the collection of data, and for conducting the synthesis and analysis of the results. A full description of the contributions from all co-authors was provided in the Statement of Contributions. The only modifications made to each article were in the form of harmonizing references, table and figure numbers to integrate into this larger thesis document. Introductory paragraphs have been included prior to each manuscripts in order to provide overall context for the publication, and better connect its key contributions. References for the necessary copyright permissions are provided in each individual acknowledgements section of the article. As noted in the preceding section, the research contained within this thesis makes original and important contributions to both fundamental discovery level knowledge and engineering applications in materials characterization and fatigue of lightweight materials. A schematic diagram showing the structure of the thesis and the relevant contributions is shown in Figure 2.

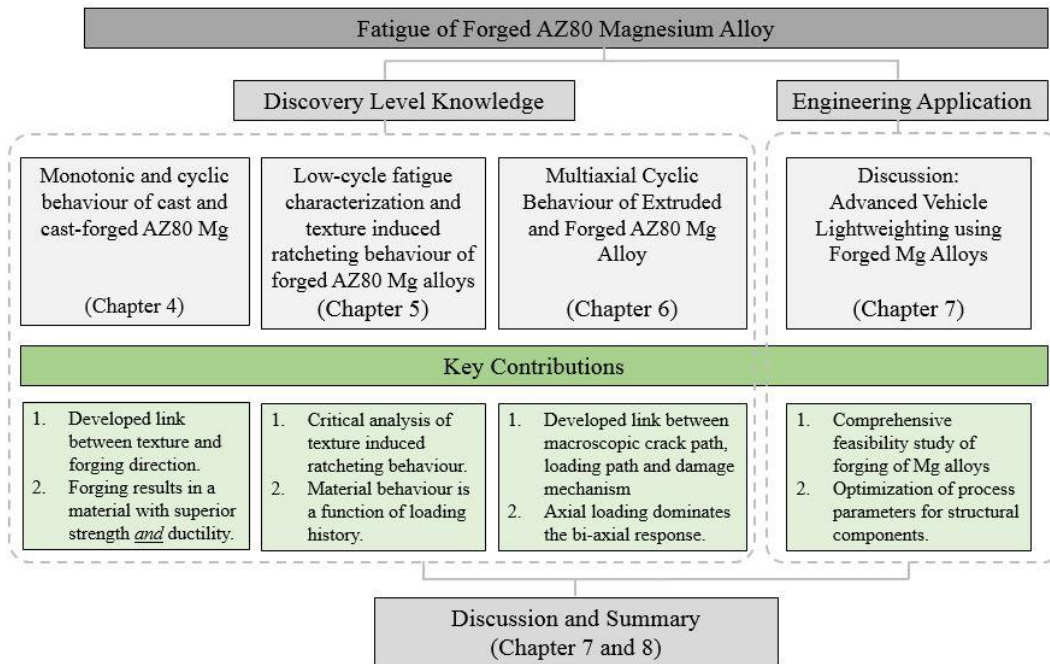


Figure 2 - Key findings and contributions of the conducted research to fundamental knowledge and engineering applications.

Chapter 4 discusses a detailed characterization and experimental work surrounding the monotonic and cyclic behaviour of cast and cast-forged AZ80 Mg. This article really had no precedent in the literature as little to no research had been done on cyclic characterization of *forged* AZ80 Mg. The key contributions of this article were the development of a link between texture and forging direction. Furthermore, the

promising conclusion was made that forging of AZ80 Mg leads to a material with superior strength and ductility to that of the parent material (properties which are generally considered to be mutually exclusive), this was very encouraging in that it confirmed the attractiveness and suitability of forged Mg for structural components. Chapter 5 builds upon the previous chapter, in such a way as to investigate the nuances of forged AZ80 Mg's material behaviour in a different loading history. It discusses the low-cycle fatigue (LCF) characterization and texture induced ratcheting behaviour of forged AZ80 Mg alloys. The key contributions of this article are a critical analysis of the cause-effect relationship of texture induced ratcheting behaviour, and secondly, the conclusion that the material behaviour is a function of the loading history. Chapter 6 once again builds upon the contributions of the previous chapters, now extending the discussion to the final discovery level knowledge work as it explores the multiaxial cyclic behaviour of extruded and forged AZ80 Mg alloy. The key contributions here are the development of a link between the macroscopic crack path, loading path and damage mechanism and how they all interface to predict the material behaviour. Secondly, the important and novel conclusion was drawn that the axial loading dominates the bi-axial response of forged AZ80 Mg alloy. In parallel to the experimental, analysis and numerical work that was done in these three discovery level knowledge chapters as well as dissemination of this research, application of this research to solve engineering problems was also done in connection with task (i) of the larger research project. A more comprehensive high level overview of Advanced Vehicle Lightweighting using Forged Mg Alloys is detailed in chapter 7 of this thesis. It contains lessons learned from the engineering application of the discovery level research, and a comprehensive feasibility study of forging of Mg alloys. Secondly, it details a very practical contribution of an optimization function which incorporates the properties of the forged material for use in selection of the process parameters for forged Mg structural components to be utilized by industry. This chapter is loosely based upon relevant content from a journal article which is still in its infancy as it is an ongoing work throughout the duration of the larger project. For the purposes of this thesis, chapter 7 should be treated as a discussion of the application of the discovery level knowledge to solve real-world engineering problems such as those which are related to advanced vehicle lightweighting. Chapter 8 outlines the summary, conclusions and future works and acts to integrate all of the key research contributions into the research field surrounding this work. Finally, this is followed by sections containing letter of copyright permissions as well as a list of references presented in this work.

## 2. Literature Review

This section reviews prior research relevant to AZ80 Mg alloy, its mechanical behaviour (static and cyclic), the effect of thermomechanical processing, as well as elasto-plastic and fatigue models for wrought material. The section begins with an introduction on the state-of-the-art research that has been done on characterizing AZ80 Mg alloy, in particular its microstructure, physical and mechanical properties. Research done on fatigue properties are then reviewed followed by a detailed review on the effects of thermomechanical processing on AZ80 Mg alloy as well as an overview of the near net shape forgings which have been previously done for automotive applications. Finally, the most common elasto-plastic and fatigue models which have been developed for life estimation of wrought AZ80 Mg alloy are reviewed with special focus on those suitable for asymmetric and anisotropic material behaviour.

### 2.1. AZ80 Magnesium Alloy

Among the commercially available magnesium, the wrought form of the AZ family of alloys are those which possess a good compromise of strength and ductility which is suitable for automotive structural applications. Figure 3 illustrates the relationship between tensile strength and failure elongation for several commercially available wrought Mg alloys as well as a number of experimental alloys.

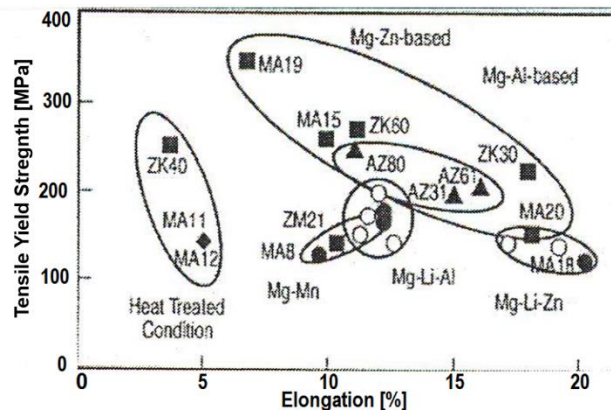


Figure 3 - Typical tensile strength and elongation for most common commercial wrought Mg alloys (© Reproduced via full text provided by author) [5]

Among these alloys AZ80 is one of the Mg alloys with good forgeability (combination of flow stress, die filling and degree of deformation), high aluminium content and superior strength. The majority of the published literature on AZ80 mechanical properties is focused on the static and fatigue properties of extrusions [5]–[16] casting [17]–[19][12] and plates [20]. Several researchers have investigated the fatigue behaviour of as-cast and wrought (extruded, rolled plate/sheet) AZ80 Mg in stress-controlled [5], [6], [9], [12]–[16], [21]–[24], strain-controlled [7], [16], [20], [25] and fatigue crack growth rate [9], [13], [26], [27] testing, some of which are subsequently discussed.

### 2.1.1. Microstructure

Zhou et al. [18] investigated the hot workability characteristics of as-cast AZ80 Mg and found that at temperatures lower than 300°C and strain rates of  $10^{-2} \text{ s}^{-1}$  flow localization bands limits the materials ductility making it difficult to deform. They also studied the Dynamic Recrystallization (DRX) behaviour and found that it occurred in a range of temperatures from 425°C to 500°C. Quan et al. [19] investigated the hot deformation characteristics of cast-homogenized AZ80 at 350°C and found a reduction in average grain size with increasing strain rate. The observed average grain size of the cast material was 240µm whereas once deformed (total height reduction of 60%) at 350°C the grain size was refined to 120, 110, 94, 50µm under strain rates of 0.01, 0.1, 1,  $10 \text{ s}^{-1}$  respectively. Typically the effect of hot deformation (open die upset) is not as pronounced as closed die forging as the strain history and flow behaviour are entirely different. Consequently reported works by the above researchers generally only show evidence of moderate levels of recrystallization and grain refinement.

### 2.1.2. Physical and Mechanical Properties

Table 1 summarizes the available literature which has presented monotonic properties for various forms of AZ80 Mg alloy. The majority of literature focuses on the tensile behaviour of as-extruded AZ80 with properties being investigated typically in the extrusion direction [ED]. Other forms (as-cast, plate and forged) materials are also available but much less numerous. In general, the forged studies that were done can be classified in two categories, open-die and closed die. Several researchers [10], [24], [28]-[32] have investigated the mechanical properties of near net shape forged AZ80 Mg for various automotive applications such as connecting rods [28], wheels [29][30][24], shock absorber heads [10], differential cases [32] and suspension control arms [31]. The processing conditions for the various forms of AZ80 presented in Table 1 are not explicitly differentiated, however they quite obviously contribute to the variability in mechanical properties exhibited in the published results. The results presented in Table 1 and Table 2 show the calculated average property (based on various researchers published value) as well as a standard deviation (where applicable), values shown in bold represent the most desirable form for AZ80 Mg of those investigated. It can be observed that with the exception of ductility, forged AZ80 Mg demonstrates superior monotonic strength in both tension and compression compared to other forms.

Table 1 - Summary monotonic properties found in literature for various forms of AZ80 Mg

ID	Temp	Grain size	$\sigma_{YS,T}$	$\sigma_{YS,C}$	$\sigma_{UTS,T}$	$\sigma_{UTS,C}$	$\epsilon_{FAIL,T}$	$\epsilon_{FAIL,C}$
	[°C]	[ $\mu\text{m}$ ]	[MPa]				[%]	
As-Cast		80-140 [12]	104±4.2 [12][33]		127±4.2 [12][33]		3.9±2.7 [12][33]	
As-Extruded [ED]		13.7±3.7 [12][16][32]	220±13.7 [12][16] [25][31]	162±13.2 [16][13][31]	332±21.4 [12][16] [25][31]	341 [25]	15.3±3.6 [12][16][25][31] [32]	
Plate [RD]		50.0 [20]	187±22.6 [20][34]	109±35.4 [20][34]	341±15.6 [20][34]	350±31.1 [20][34]	11.7±2.7 [20][34]	<b>19.3±1.7</b> [20][34]
Forged	180		<b>308</b> [10] (LD) 268[10] (TD)		<b>389</b> [10] (LD) 346[10] (TD)		8.1[10] (LD) 1.6[10] (TD)	
	240		276[10] (LD) 221[10] (TD)		348[10] (LD) 306[10] (TD)		7.5[10] (LD) 5.2[10] (TD)	
	250	<b>7.6</b> [31]	248[31]	<b>190</b> [31]	361[31]		15[31]	
	300	12[32]	274[32]274[28]	182.5[32]	<b>389</b> [32] <b>389</b> [28]	402[32]	8.0[32]8.0[28]	<b>11.0</b> [31]
	340		235[10] (LD) 126[10] (TD)		324[10] (LD) 229[10] (TD)		13.6[10] (LD) 6.4[10] (TD)	
	350	16.1[31]	207[31]	175[31]	349[31]	<b>418</b> [31]	<b>16</b> [31]	<b>11.0</b> [31]
	375				320-330[29]		10-12[29]	
	Unknown		250[30]110- 183[24]		345[30]		5.0[30]5.3- 10[24]	

Table 2 summarizes the available literature which has presented fatigue properties for various forms of AZ80 Mg alloy, which is much less numerous than work which has been done on the monotonic characterization. In particular, the material parameters required for  $\epsilon$ -N fatigue modelling (which is the generally accepted method for automotive applications) are non-existent, especially for forged material. It can be observed that the fatigue endurance strength of forged AZ80 Mg is very similar to that of extruded AZ80 in the ED. Other than the work of this current research there is no literature which currently exists regarding the multiaxial fatigue of AZ80 Mg alloys.

Table 2 - Summary fatigue properties found in literature for various forms of AZ80 Mg

ID	Temp	Characterization	Modelling			
		Stress-Life	$\sigma$ -N		$\epsilon$ -N	Energy
	$\sigma_{END} @ 10^7$	$\sigma_f$	b			
	[°C]	[MPa]	[MPa]			
As-Cast						
As-Extruded [ED]		135.9±26 [23][14][12][13]	844.4[13]	-0.138[13]	[16][25]	
Plate					[20]	
Forged	Unknown	98[22]142[5]	378.3[5]	-0.061[5]		

### 2.1.3. Fatigue Properties

Fatigue characterization of the as-received material has been investigated in detail albeit only on the as-extruded form of AZ80 (no fatigue properties are available for as-cast AZ80 Mg). Nový et al. [12] investigated both the static and very high cycle fatigue (VHCF) properties using ultrasonic push-pull stress controlled testing. They observed in as-extruded AZ80 a yield and ultimate strength of 205 and 303 MPa respectively, a failure elongation of 20% and prominent intermetallic particles with sizes ranging from 5-9  $\mu\text{m}$ . They made the observation that only surface induced cracks occurred in AZ80 under cyclic loading with no observed endurance limit. They also discussed the fact that primary fatigue crack initiation sites are governed by microscopic defects such as pores, inclusions or intermetallics in the low cycle fatigue (LCF) to high cycle fatigue (HCF). In contrast, they revealed that in the VHCF, fatigue crack initiation is mostly controlled by the properties of the matrix and the role of microscopic defects is only minimal. Shiozawa et al. [13] investigated the effect of artificial aging (T5) heat treatment on as-extruded AZ80 Mg alloy and discovered that despite superior monotonic properties of the T5 treated alloy, the fatigue resistance was inferior to that of the as-extruded condition, especially in the VHCF regime. They also concluded that fatigue crack initiation is controlled by twinning irreversibility in LCF, whereas cyclic slip controls the mechanism in the VHCF regime. More recent work by Shiozawa et al. [16] showcases fully reversed LCF testing in both stress strain-controlled tension-compression techniques on extruded Mg alloys AZ31, AZ61, AZ80. They found AZ80 to have superior fatigue properties of the three investigated as shown below in Figure 4. Furthermore, Shiozawa made the observation that in under stress control, compressive mean strains resulted in the stabilized response, whereas under strain control, tensile mean stress developed [16]. They attributed these responses to the yield asymmetry between tension and compression of the wrought material in the extrusion direction.

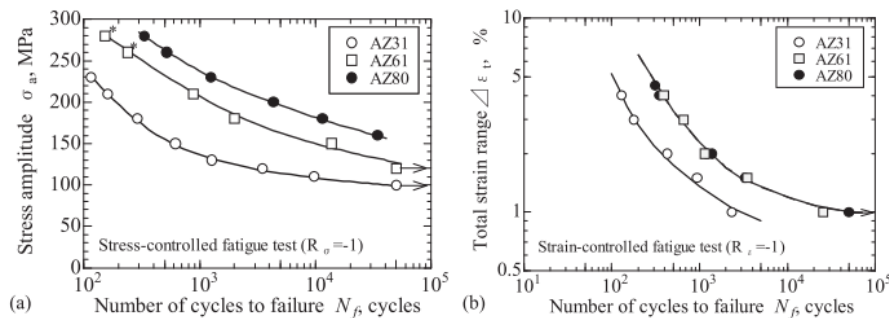


Figure 4 - S-N curve obtained from (a) stress-controlled LCF test and (b)  $\epsilon$ -N curve obtained from total strain control LCF test for various AZ31, AZ61 and AZ80 Mg Alloys (Reproduced with permission from Elsevier) [16]

Fatigue data on forged AZ80 Mg is very sparse in the literature, the majority of which was done on externally produced AZ80 prototype forgings with unknown processing parameters (temperature, rate, pre/post treatments etc.). Furthermore, the data presented in these studies is very preliminary in nature,

and rudimentarily characterizes the forged material behaviour in load control testing over a very narrow window of stress amplitudes. Rivers et al. [22] characterized the endurance limit using rotating bending testing of a closed die forged AZ80 Mg prototype wheel done by Timminco. They observed an endurance limit of 98 MPa in fully reversed loading. Moldovan et al. [5] conducted servo electric push-pull testing on extruded and forged AZ80 alloy once again produced by Timminco. They observed an endurance limit of 142 MPa at  $10^7$  cycles. They also found under SEM investigation, many intermetallic phases with high manganese content (MgMnAl phases) which contributed to accelerated failure in many samples due to a shorter crack initiations and propagation regimes. Since these preliminary works on forged AZ80 fatigue characterization do not present sufficient information to accurately predict the fatigue life, there is great opportunity to benefit the academic community in this emerging area of research.

#### 2.1.4. Forging and other thermomechanical processing of AZ80 Mg Alloys

Among those currently utilizing Mg alloys for industrial applications, the family of wrought Mg alloys typically is revered as superior in terms of mechanical properties to that of traditional die-cast alloys. Although in general, the strength of die-cast alloys can be almost equivalent to that of the wrought variety, their ductility is comparatively much lower [35]. This is due to gas porosities, shrinkage pores, blowholes and other defects which result in the material following solidification during the casting process. These defects are virtually non-existent in those alloys which are subjected to thermomechanical processing such as extrusion, rolling or forging (colloquially known as “wrought” alloys). Figure 5 illustrates the relationship between strength and failure strain for various die-cast and wrought Mg alloys. It can be observed that thermomechanical processing leads to improved strength and considerably increased ductility, which makes these forms of alloys desirable for automotive structural applications. Among the wrought alloys, extruding and rolling produces “semi-finished” products which would need to be subsequently processed to produce an automotive suspension arm. Contrasting to this, die forging can produce near net shape products (such as a suspension Front Lower Control Arm (FLCA)), with properties exhibiting the superior strength and ductility wrought Mg alloys typically possess. Thus to produce a complex geometry such as an automotive suspension FLCA with wrought material properties, die-forging has been selected as the production method of choice.

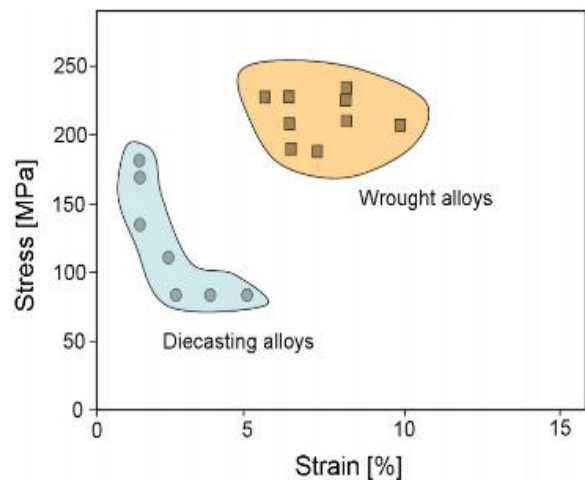


Figure 5 - Mechanical Properties of die-casting and wrought Mg alloys (Reproduced via full access from Wiley ©) [35]

Figure 6 showcases visual references of near net shape forgings made from AZ80 Mg for automotive applications which are currently available in literature. The applications are all structural (load bearing) components which are typically considered to be fatigue critical, not ones particularly important for crashworthiness (requiring high ductility and energy absorption). The researchers who published work regarding these forgings generally focused on the sensitivity of the properties and performance to forging process parameters, and characterization of microstructure and tensile monotonic properties of the as-forged part.

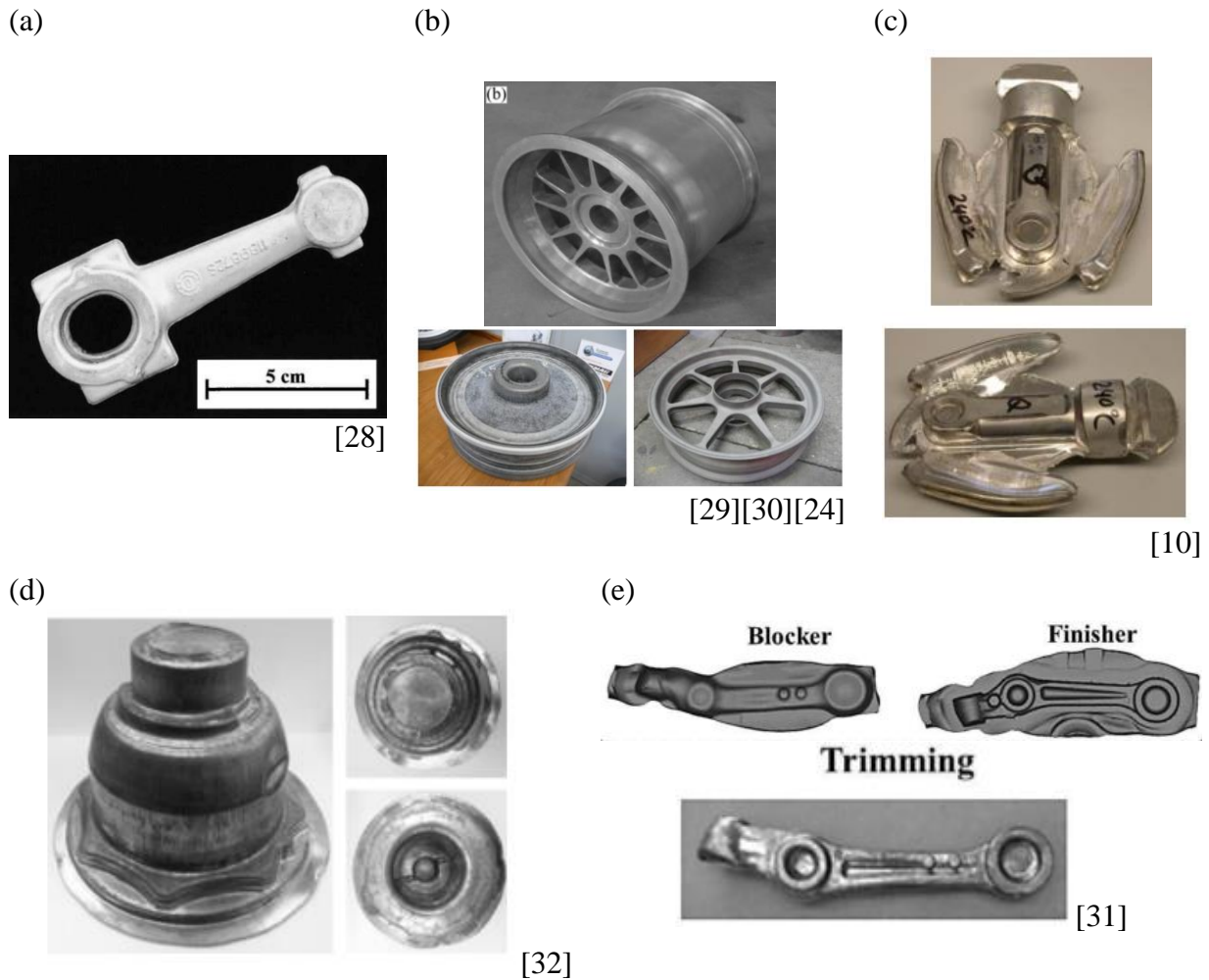


Figure 6 - Automotive forgings made from AZ80 Mg (a) connecting rod\* (b) wheel (c) shock absorber head (d) differential case (e) suspension control arm [\*Shown is ZC71/SiC/12P part, however an AZ80 forged part was also forged]. [28] Reproduced with permission from Taylor and Francis, [29][32] reproduced with permission from Elsevier, [31] reproduced with permission from Sage Publishing, [30][22] Reproduced via full text provided by author, [8] reproduced via full access provided by Wiley.

Detailed investigation of both characterizing and modelling the forging process to near net shape products is an emerging area of research with very little precedent for forged AZ80 Mg. As a result of this many researchers [5], [10], [11], [17]–[19], [22], [24], [28], [29], [31], [32], [36]–[41] have focused on the high temperature deformation behaviour of forged AZ80 in a very simple “open-die” configuration where

subsequent processing is required to achieve the final product shape. Despite this, studies that discuss the effect of thermomechanical history (resulting from the forging process) on the tensile/compressive and fatigue properties of AZ80 after forging are fairly limited. Kobold et al. [36] performed both axial and radial open die forging of extruded AZ80-T5 at rates between 5-20 mm/sec, and observed no significant difference on the anisotropy of the material flow regardless of the forging direction. Furthermore they concluded that optimal isothermal forging temperature to be 350°C, and also recommending that this optimum condition tends toward lower temperatures with increasing strain rate. Kurz et al. [10] observed in die-forged AZ80-F that increasing the forging temperature decreases the mechanical strength due to a grain growth but enhances ductility due to a more homogeneous microstructure. He also concluded that at higher deformation rates (300-400 mm/sec) lower forging temperatures are desirable (240°C) due to the added heat of deformation at higher rates. Rivers et al. [22] investigated the stress-controlled fatigue characteristics of samples machined from a forged AZ80 automotive wheel and observed an endurance limit of approx. 98 MPa. The effect of the forging process on strength, ductility and the strain controlled fatigue behaviour of AZ80 has yet to be investigated in detail and is one of the great academic opportunities being exploited by this research work.

The hexagonal closed packed or HCP crystal structure of Mg alloys results in a difficult in processing the material at low temperatures. Figure 7 illustrates the critical resolved shear stress vs. temperature for a variety of different deformation modes. At room temperature, basal slip has by far the lowest CRSS in the range of 2-4 MPa, if the grain orientation is not favourable for basal slip the next mode that will be activated is extension twinning which has a CRSS in the range of 7-10 MPa, this is followed by prismatic, pyramidal, and contraction twinning. Von Mises criterion states that for arbitrary plastic deformation at least 5 independent slip systems need to be able to be activated. At room temperature this is very difficult with magnesium, as basal slip typically dominates, however, at elevated temperatures in the range of 225-425°C the CRSS for other modes decreases dramatically improving the ability to plastically deform and thus its formability. What this means is that to successfully process magnesium and achieve large strain via forging, it must be done at elevated temperatures. This introduction of temperature into the processing equation complicates controlling the resulting microstructure quite a bit as now the process is highly thermomechanical.

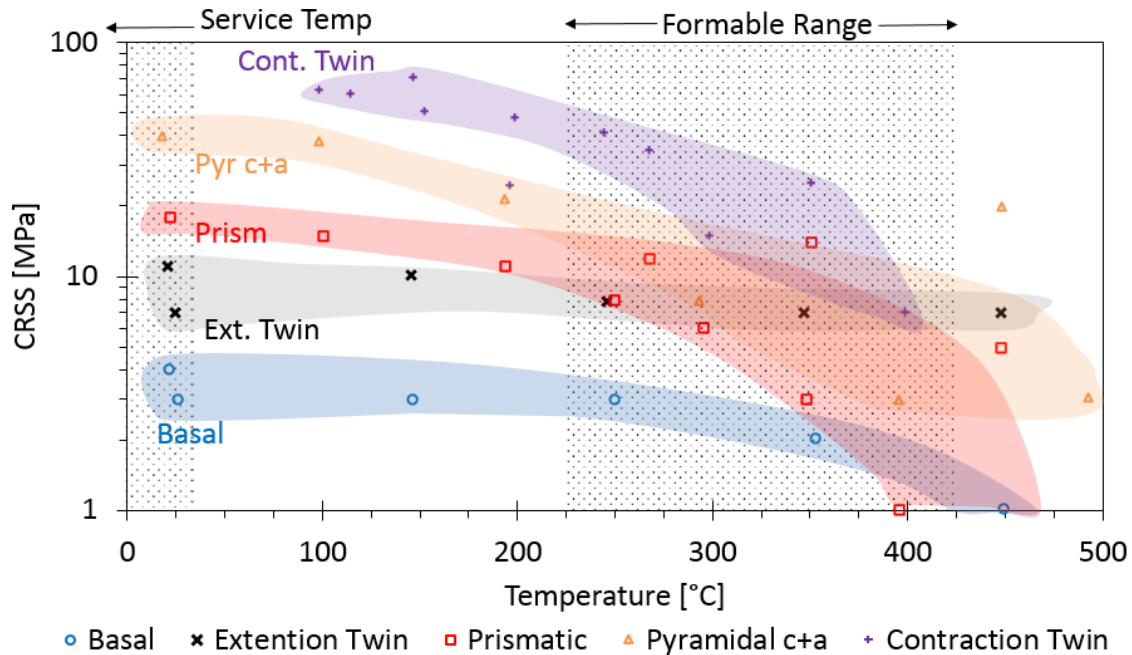


Figure 7 - Critical Resolved Shear Stress (CRSS) as a function of temperature for a variety of different deformation mechanisms for Mg Alloy [42].

## 2.2. Elasto-Plastic Modelling

Previously, modelling of wrought Mg alloys was uncommon as its complex HCP crystal structure causes an asymmetry in the yield locus between tension and compression [43]. Furthermore, the anisotropic nature of wrought Mg alloys requires a criterion for description that can accommodate this directional dependence of material behaviour. Cazacu and Barlat [44] initially modeled the asymmetry and anisotropy in yielding of pressure insensitive metals using a simple formulation with a relatively simple two material parameter model requiring the tensile and compressive yields stresses. This model can be seen as an evolution of the well know von Mises (VM) criterion as the model reduces to the well-established yield function when the stresses in tension and compression are equal. Progressing from this, Cazacu, Plunkett and Barlat (CPB) [45] developed an orthotropic yield criterion suitable for HCP materials, more commonly known as the Cazacu-Barlat (2006) criterion. This model is more complex than their previous one as it requires four additional material parameters which describe the tensile yield stress at  $45^\circ$  and  $90^\circ$  as well as the tension-tension biaxial yield stress. This model has been used extensively by many researchers [43][46][47] to model the elasto-plastic behaviour of sheet Mg alloy under plane stress. Andar et al. [43] investigated the validity of the Cazacu-Barlat (2006) or CPB2006 yield function using experimental data from uniaxial specimens (tension/compression) and cruciform specimens (biaxial tension) for AZ31 sheet. They found that the yield criterion was able to provide an accurate failure description of the anisotropy and asymmetry of the plastic work contours. Plunkett et al. [46] also demonstrated that not only was the CPB2006 model suitable for sheet AZ31 Mg, but other

textured metals as well such as aluminum, steel and titanium alloys. Yoon et al. [47] more recently utilized the model to simulate the axial crushing of a tube made of AZ31 Mg sheet. They noted that the model accurately captures the significantly different hardening rates in tension and compression which led to a higher fidelity crush response prediction. Very recently, Khayamian et al. [48] investigated a simpler asymmetric and isotropic Cazacu-Barlat yield criterion [44] based on the axisymmetric model of Jahed et. al [49] to model the behaviour of cast AZ80 tubular specimens under internal pressure and axial tension/compression [50]–[54]. Despite the previous work done surrounding elasto-plastic modeling of sheet Mg alloys under plane stress, to the knowledge of the author, nothing is available in literature regarding modelling bulk material behaviour of AZ80 Mg alloy under a three dimensional stress state.

### 2.3. Fatigue Life Modelling

In order to quantitatively compare the life during cyclic loading in wrought Mg, numerous fatigue damage parameters have been proposed in the literature. [53], [55]–[57] Researchers have formulated these parameters in such a way that they can be categorized into models which relate the experimental fatigue life to the stress, strain or energy associated with a single loading cycle. As exhibited in Figure 30, some forms of AZ80 may display perfectly plastic cyclic behaviour post cyclic yield or even cyclic softening, since within an arbitrary range of applied strain amplitudes, the stress may remain constant, or even decrease, however we know the life to be less with increasing values of strain. As a result of this, stress-based fatigue models are not ideal as they cannot accurately capture fatigue damage inflicted under these ranges of deformation conditions. This however does not mean that stress-based models for fatigue life prediction are not suitable for all Mg alloys, Lin et.al [58] successfully predicted the fatigue life of hot-rolled AZ31B Mg alloy under cyclic stress-controlled loading by proposing a stress-based damage parameter. Shiozawa et al. [16] modelled the fatigue life of AZ80 extrusion using a total strain energy density-based model, first developed for rolled AZ31 by Park et al. [59] and similarly Albinmoussa et. al [60] as a modification to the well-known Morrow model, to reliably predict the fatigue life of extruded AZ80 Mg alloy. More recently, Wang et al. [25] utilized this modified Morrow model to successfully predict the LCF life of extruded AZ80 using a total strain energy density based approach. The following statements will summarize the gaps in knowledge in the state-of-the-art literature, as these will be the focus of the novel contribution to this research work. Firstly, characterization of the effect of the forging process on strength, ductility and the strain controlled fatigue behaviour of AZ80 Mg. Secondly, elasto-plastic modelling of the *bulk* material behaviour of AZ80 Mg alloy (forged or otherwise) under a three dimensional stress state. Finally, fatigue life modelling of forged AZ80 Mg for not only simple uniaxial loading, but for more complex multiaxial, non-proportional, and out-of-phase loading environments.

### 3. Methodology

#### 3.1. Introduction

The methodology section of this work focuses on both the experimental and modelling methodology. Although not the direct focus of this work, contextual background is given regarding the details of the physical forging process (i.e. how the base material was thermomechanically processed into a different shape via compressive forces). Several different types of forging geometries were selected with the intention of capturing the nuances of material flow and thermomechanical history that is typical in an industrially relevant forging process. These include simple upset open-die forging as well as a closed die forging with a more complex geometry and material flow. This chapter also describes the rationale and details behind the specimen design and selection for the experimental campaign as well as the measurement techniques used to acquire the data necessary to fulfill the characterization and modelling objectives. Furthermore the details surrounding each experimental technique which was employed are discussed and relevant parameters for recreation of the experiment are given. Specific reasoning regarding why certain methods were employed are also discussed within the context of the objectives and constraints of this experimental campaign. By and large, the monotonic and fatigue tests were conducted with servo-hydraulic machinery with a number of different methods of both controlling and measuring various parameters throughout the test.

#### 3.2. Material Processing & Forging

Very generally, to produce the forged product, The AZ80 “base material” was taken in the form of a cylindrical billet and heated in a furnace to a prescribed elevated temperature (ranging from 250°C – 450°C) for a prescribed duration to ensure temperature uniformity. Following heating, the billet would be placed into isothermal temperature dies which then would apply compressive forces via a hydraulic press to cause bulk material flow and form the sample into the desired shape. Two forms of forging are investigated, open-die forging which has unrestricted flow in both the radial and longitudinal directions, and closed die which restricts material flow in both of these directions. Both forgings were performed on an Interlaken 500 Ton press, with heated tooling capable of going to 450°C and a maximum platen speed of 400 mm/min (see Figure 8). A schematic of these two types of forging which were conducted on this press and resulting geometries can be seen in Figure 9. More recently, full-scale



*Figure 8 - Interlaken 500T Hydraulic Press. Forgings were produced on this press located at CanmetMATERIALS in Hamilton, Ontario, Canada.*

component forging has been conducted on a Macrodyne 1200T press, with bolsters containing cartridge heaters and a maximum speed of 750 mm/min.

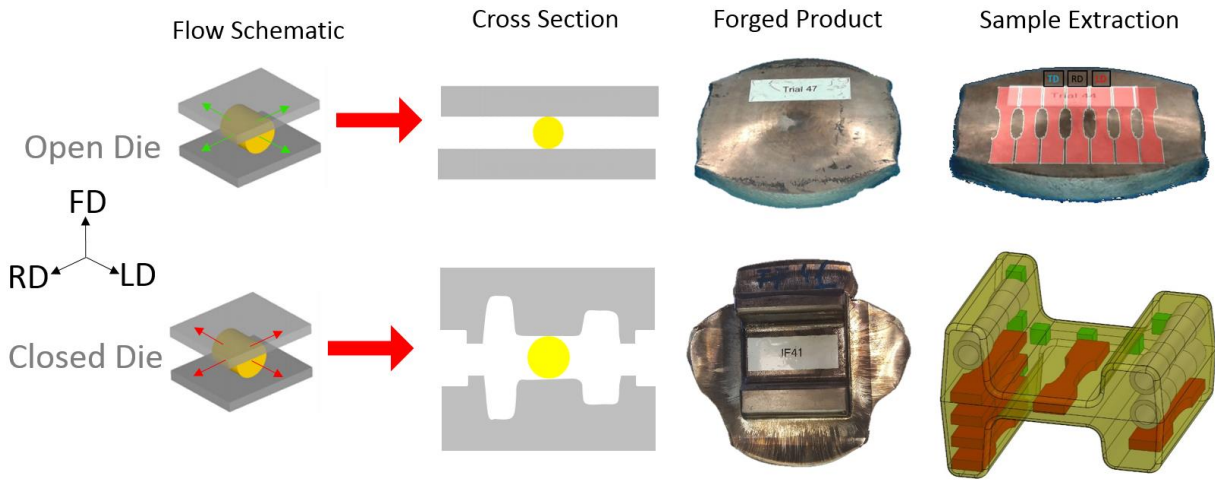


Figure 9 - Various stages of processing for two styles of forging (open die and closed die)

The forging process is controlled in such a way as to ensure a constant forging rate, and die temperature, however there are some effects of internal heating due to deformation as well as convective cooling to the environment which affect the desired isothermal nature of the process. The actual temperature history is a function of the base material condition, location within the billet, forging rate, and target temperature among other factors. Figure 10 illustrates a schematic temperature profile of a typical forging process. Following the forging step the sample is removed from the die and allowed to air cool in ambient room temperature environment.

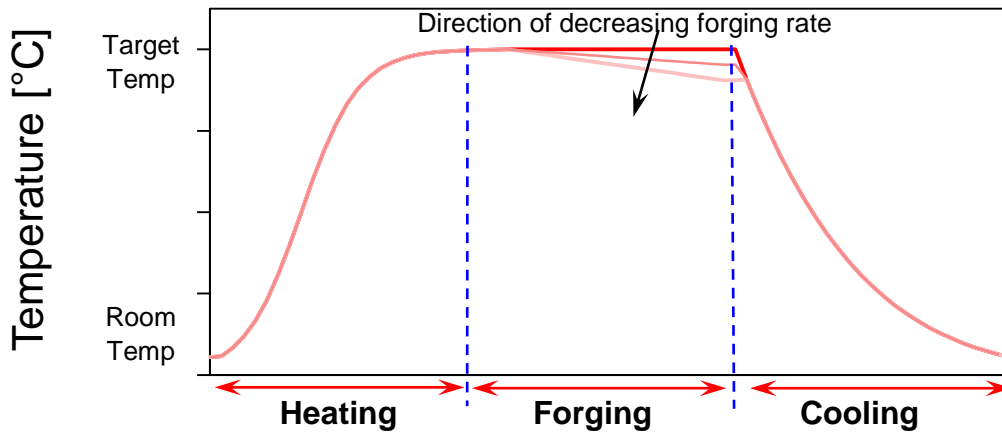


Figure 10 - Schematic representation of temperature history for various stages of the processing during forging. Different line weights show approximate effect of convective cooling on the slower rate forgings.

### 3.3. Experimental Methodology

#### 3.3.1. Specimen Preparation and Characteristics

Since a variety of different forms of AZ80 Mg were investigated, the location of sample extraction, the samples geometry, as well as the sample preparation techniques all play an important factor in the accuracy of the experimental data presented here. In general, “base material” and “forged material” are the categories from which all these samples originate. Of the base material, samples can be further divided into cast and extruded varieties. The data presented here for the base material is for the “as-fabricated” condition (-F), and the samples for both cast and extruded were extracted from larger cylindrical billets. These billets have different diameters and lengths depending on the specific variety of base material, however they always are cylindrical in shape. Thus the orientation of samples within these cylindrical billets can be broken down into LD (Longitudinal Direction), TD, (Transverse Direction) or RD (Radial Direction), see Figure 11. Important to note is the fact that for the extruded base material the ED (Extrusion Direction) is the same direction as the longitudinal direction and sometimes the terms are used interchangeably but refer to the same material orientation.

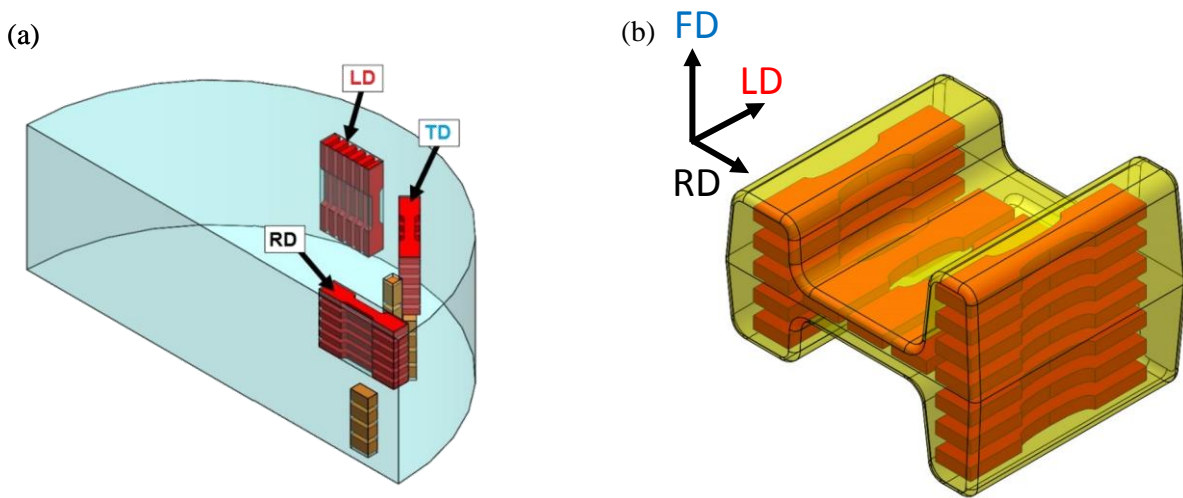


Figure 11 - Orientation of samples from within (a) cylindrical billet (b) I-Beam forging

In general, for the forged material, the locations and orientations of where samples were extracted is largely governed by spatial constraints due to the forging geometry. Thus an effort was made to orient the samples in an efficient way to optimize material utilization and extract as many samples as possible from each forging to provide a statistically relevant “bulk material” property. Despite this, the author recognizes inevitable spatial variation in material properties and makes a conscious effort to quantify this in the way the data is presented as well as the analysis and discussion of results. This characterization of the spatial variation is the focus of discussion throughout several chapters of this work and can be seen as a contribution towards the larger scientific community.

Efforts were taken to prepare the surfaces of all test samples according to their ASTM standard (if applicable) and reduce the risk of surface roughness induced premature failures. Following machining of the surface, if necessary additional polishing was conducted to ensure both an acceptable and consistent surface finish. Axial test samples had a nominal surface finish of  $Ra \leq 0.2 \mu\text{m}$ , however in practice the actual roughness was substantially less, around  $0.05 \mu\text{m}$ . Torsional (hollow tubular) test samples that were used for shear testing had a surface finish of  $Ra \approx 0.2 \mu\text{m}$ . A summary of the roughness profile within the gauge section of various samples which were utilized are illustrated in Figure 12, the measurements shown represent the worst (i.e. roughest) of all samples tested.

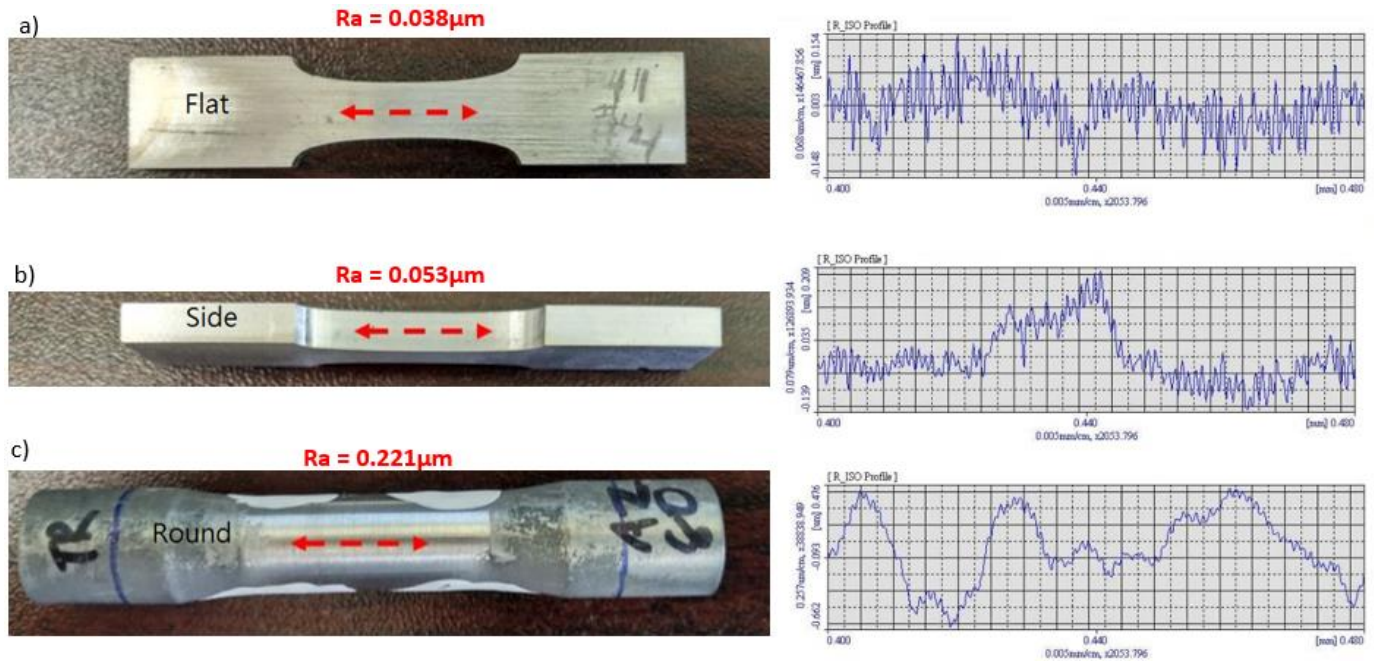


Figure 12 - Surface roughness within the gauge section of various sample geometries of the flat "dogbone" sample used for uniaxial monotonic and fatigue tests along the (a) the flat surface (b) the side curved surface and then (c) the outer surface of the hollow tubular samples used for the pure shear and biaxial tests

The sample geometries selected here are of three different types, cuboid (i.e. a cube with 7.6mm side lengths utilized for compressive monotonic tests), flat "dogbone" shaped, for axial monotonic and fatigue tests and then hollow tubular for pure shear and bi-axial tests. Details of the geometries for the dogbone and tubular specimens can be found below in Figure 13 and Figure 14 respectively.

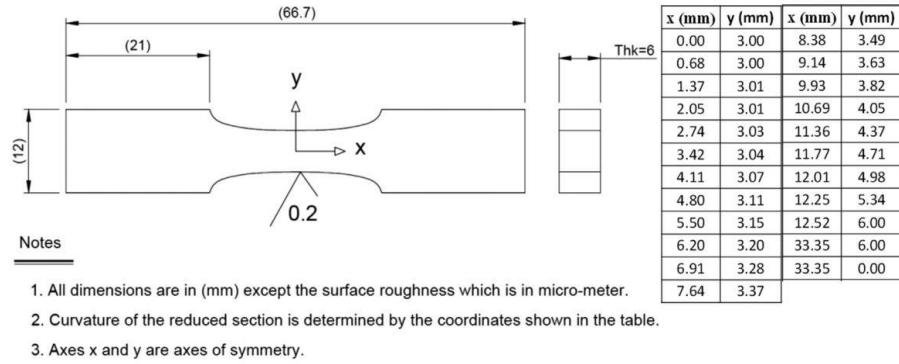


Figure 13 - Axial "dogbone" specimen geometry

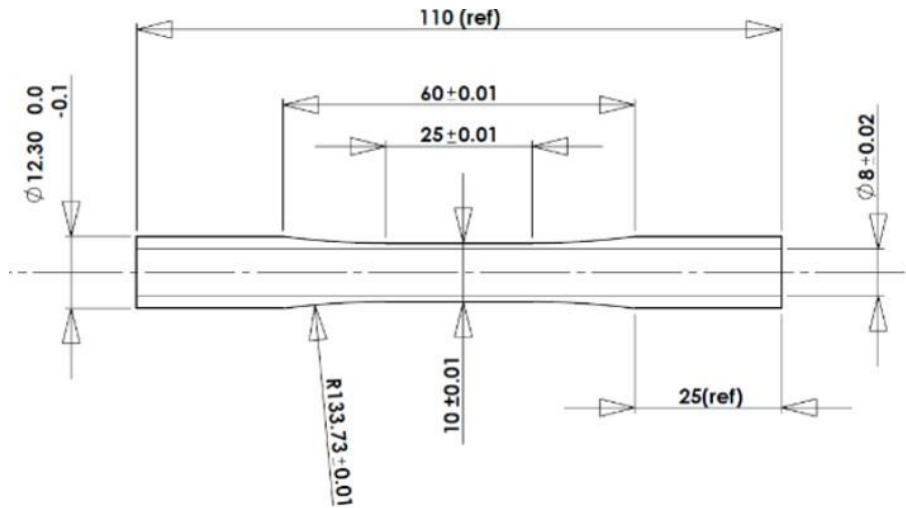


Figure 14 - Hollow tubular specimen geometry

### 3.3.2. Microstructure and Texture

The metallographic samples were prepared following the metallographic techniques outlined in ASTM E3-11 with acetic-picral etchant similar to that used by Roostaei et al. [61]. The microstructure was observed using a light optical microscope (LOM) and a scanning electron microscope (SEM), coupled with energy-dispersive X-ray spectroscopy (EDS). The average grain intercept method is used to quantify the grain size. The texture measurements were performed on polished samples using a Bruker D8-Discover equipped with a VANTEC-500 area detector, with a radius of 135 mm and using Cu-K $\alpha$  radiation at 40kV and 40 mA (see Figure 16). During the measurement, the incident beam and the detector were placed at a fixed  $2\theta$  angle of  $40^\circ$ . The collimator size was 1.0 mm. The sample was mounted on the motorized stage, which was oscillated at an amplitude of 1.5 and 2.5 mm, and a speed of  $3.5 \text{ mm s}^{-1}$  and  $5.5 \text{ mm s}^{-1}$  for the



X and Y axis, respectively. The samples were tilted between 0 and 75°, with a step of 15° considered as the  $\Psi$ -scan, while the sample rotation, known as  $\Phi$ -scan, was between 0 and 360°, with a step size of 5°. The sample was scanned for 20 s at each orientation. The Debye–Scherrer diffraction rings were collected using the area detector in a 2-D diffraction image. Then, the incomplete pole figures for the {0002}, {10 $\bar{1}$ 0}, {10 $\bar{1}$ 1}, and {1 $\bar{1}$ 02} planes were extracted from the diffraction rings. The complete pole figures were then calculated using the DIFFRAC.Suite: Texture software

Figure 16 - Bruker D8-Discover equipped with a VANTEC-500 area detector

### 3.3.3. Superficial Hardness

As a preliminary “screening” test, superficial hardness (indentation measurements) were conducted on the surface of the base and forged materials. This was to primarily investigate the presence of any spatial variation in properties which can be inferred by differences in superficial hardness. Especially in the closed die forgings, the material flow is multi-dimensional, and the thermomechanical history is spatially varying throughout the cross section of the forging, approximately 35 measurements were taken across the surface using a Rockwell 30T scale and a 1/16” ball indenter. Sufficient separation between indentations was ensure to eliminate any interaction between measurement points and plastic deformation zones. A United True Blue II closed-loop Rockwell hardness testing machine (Figure 15) was utilized to perform the measurements. Following data collection, contour plots were then generated to highlight the spatial distribution of the results and exaggerate any non-uniformities throughout the billet/forging cross section. Coupling these observations of apparent spatial variation in hardness with any variations which were observed in the monotonic/cyclic behaviour acted as further support to any conclusions that were drawn about the material strength, ductility and hardening behaviour and its link to the local thermomechanical history and final texture of the forged material.



Figure 15 - United True Blue II Rockwell Hardness Tester

### 3.3.4. Strain Measurement

For the monotonic tests (both axial and shear) strain measurement was accomplished using a GOM ARAMIS 3D 5MP DIC system which passively functioned to measure the strain. This non-invasive technique is used due to the large shock loading that can occur within the sample upon final fracture/failure which can damage conventional clip-on extensometers. The average strain rate within the gauge section of measurement was  $1.4E-3 \text{ sec}^{-1}$  for the axial tests and  $6.7E-4 \text{ sec}^{-1}$  for the shear tests. Within the gauge section, the sample surface was painted with a specific random speckle pattern to facilitate accurate calculation of strains using the digital image correlation (DIC) algorithm. The Digital Image Correlation algorithm has a typical displacement sensitivity of 1/100th of a pixel in plane, 1/30th pixel out of plane. This translates into about 5 to 15 microns per meter of field of view for 4-6 Megapixels stereo camera system. The strain sensitivity is highly dependent on the test conditions and will typically be between 50 and 100 microstrain. Filtering and optimization of the test conditions will result in better sensitivity results, however no extra (or additional) filtering was performed on the data presented in this study. Uncertainty is quantified by measuring the standard deviation of the displacement or strain distribution measured on a static object. 3 standard deviations is typically used to define the noise floor. The average noise floor in these particular tests (as defined by the aforementioned method) was well below three orders of magnitude less than the maximum strain during the test. I.e.  $< 0.01\%$ .



Figure 17 - GOM Aramis 3D 5MP DIC System with detailed view of specimen surface

For the purely axial fatigue tests, the strain was measured throughout the first 10,000 cycles using an MTS 632.26 extensometer with an 8-mm gauge and travel of  $\pm 1.2$ -mm until stabilization of the cyclic hysteresis loop was achieved. For the pure shear and biaxial fatigue tests, the strain was measured for using an Epsilon biaxial extensometer (model 3550, see Figure 18) with axial and shear ranges of  $\pm 5\%$  and  $\pm 3^\circ$  mounted on the specimen's gauge length. During strain control, the max strain rate averaged over the gauge section of measurement was  $\sim 1.5E-2 \text{ sec}^{-1}$  for the pure axial and pure torsional tests.

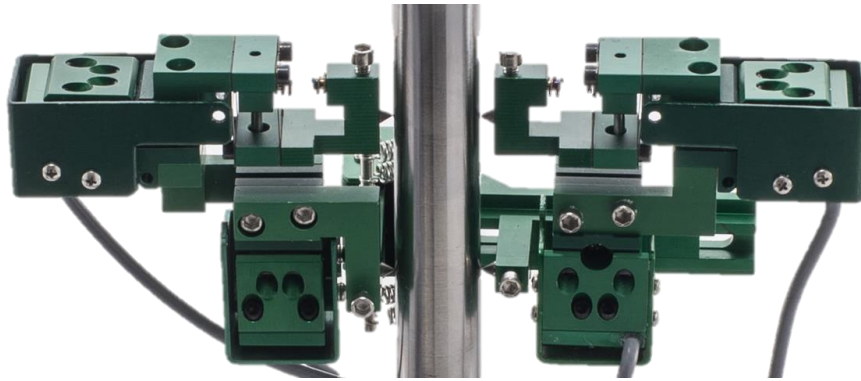


Figure 18 - Epsilon 3550 Biaxial extensometer, shown without adhesive coating applied.

In general, precautions were taken to ensure that slippage of the extensometer relative to the surface of the sample did not occur (as it would induce error into the measurement commonly manifesting itself as extensometer “drift”). The uni-axial extensometer was affixed to the sample surfaces using steel springs as well as Loctite 404 instant adhesive and Loctite 7452 accelerant. The bi-axial tubular specimens were coated with an adhesive coating which allowed the extensometer knives to achieve adequate tractive force to prevent slipping, without causing a defect on the sample surface which could potentially induce a premature failure. Both internal springs within the extensometer and an externally applied spring mechanism act to “preload” the contact patches against the surface and induce tractive force for the biaxial extensometer. Finally, in general, when controlling the strain (or simply measuring the strain) throughout the test the frequency of the loading is reduced to allow for good measurement resolution as well as stable and accurate control of the servo-hydraulic machine.

### 3.3.5. Quasi-Static (Monotonic) Tests

The quasi-static tensile tests were performed according to ASTM standard E8/E8M-15a using an MTS 810 Servo-Hydraulic test machine operating in displacement control mode with a displacement rate of 1 mm/min. The quasi-static shear tests were performed under rotation control mode at a rate of 12 deg/min. DIC was used to measure the strain within the gauge section, the reported strain values are the average quantities over this prescribed gauge area ignoring the fringe data which comes from the edges of the surface. The failure criteria for the tests were considered to be whichever of the two following conditions occur first a) final rupture of the specimen gauge section or b) a >50% decrease in the measured load/torque.

### 3.3.6. Stress Controlled Fatigue Tests

The stress controlled fatigue tests were performed as per ASTM E466-15 in an ambient environment using an MTS 810 Servo-Hydraulic test machine operating in stress control mode at a frequency range of 0.1 Hz to 30 Hz depending on the stress amplitude to maintain an approximately

consistent loading rate between all tests. In certain cases, the strain was measured throughout the first 10,000 cycles using an MTS 632.26 extensometer until stabilization of the cyclic hysteresis loop was achieved. The tests were conducted at a zero mean stress (i.e.,  $R_L = -1$ , sinusoidal fully reversed stress cycle) and stress amplitudes of between 140 MPa and 190 MPa. The failure criteria for the tests were considered to be final rupture of the specimen gauge section.



Figure 19 - Example setup of uni-axial stress controlled fatigue test.

### 3.3.7. Strain Controlled Fatigue Tests

The axial fatigue tests were performed as per ASTM E606 in an ambient environment using an MTS 810 Servo-Hydraulic test machine and shear/biaxial using an Instron 8874 test machine operating in strain control mode at a frequency ranges of 0.05 Hz to 2 Hz (LCF mode), and 1 to 30 Hz in force control mode (HCF mode) depending on the strain amplitude to maintain an approximately consistent loading rate between all tests. The tests were conducted at a zero mean strain (i.e.,  $R_L = -1$ , sinusoidal fully reversed strain cycle) and strain amplitudes ranging from 0.2% to 2.0%. The control parameters of the load frame controller were calibrated in such as to ensure accurate peak and valley values and stable operation over the wide range of frequencies tested. The controller was operated in closed loop mode to compensate for any variations in specimen stiffness throughout the test duration as the material cyclically hardened/softened or cracks developed. Data acquisition was sufficiently high frequency as to achieve a minimum of 50 data points per cycle to ensure accurate and high fidelity hysteresis loops and modelling parameters. The failure criteria for the fatigue tests was considered to be a 50% reduction in the peak tensile axial stress or a 50% reduction in peak or valley shear stress. For higher cycle fatigue (HCF) tests (i.e. greater than ~ 20 000 cycles), the cyclic response will stabilize and the hysteresis loop will remain

virtually constant. In these scenarios, the extensometer is then removed and the test is switched over to force control mode using the peak and valley stresses from the stabilized cyclic response as maxima and minima. This facilitates much higher frequency operation of the test where any transient hardening behaviour of the material has decayed and the cyclic response is now virtually constant until failure. The failure criteria in force control mode is the approached in a similar fashion to that outlined in section 3.3.6 of this thesis.



Figure 20 - Example setup of a uni-axial strain controlled fatigue test.

### 3.3.8. Multiaxial Fatigue Tests

The multiaxial tests were conducted in a similar fashion to those discussed in section 3.3.7 of this thesis, with the most significant difference being the presence of a combined loading (two simultaneous loading axis). During the strain control portion of the biaxial tests, the max strain rate averaged over the gauge section of measurement  $\sim 3.2 \text{ E-3 sec}^{-1}$ . Schematic diagrams of all of the loading paths investigated in this work are investigated in Figure 21 (c, d and e illustrate the biaxial loading paths). It is important to note is the loading waveform is controlled to be a sinusoidal variation between each loading axis maximum and minimum strain value. For proportional loading (where each loading axis strain magnitudes vary in a fixed proportion) this produces a maximum equivalent strain which occurs at a location which is coincident with both peaks of individual loading axis. However under non-proportional loading there is some phase shift between loading waveforms which varies between  $0-90^\circ$ , under this condition the angle at which the maximum equivalent strain occurs is more complex.

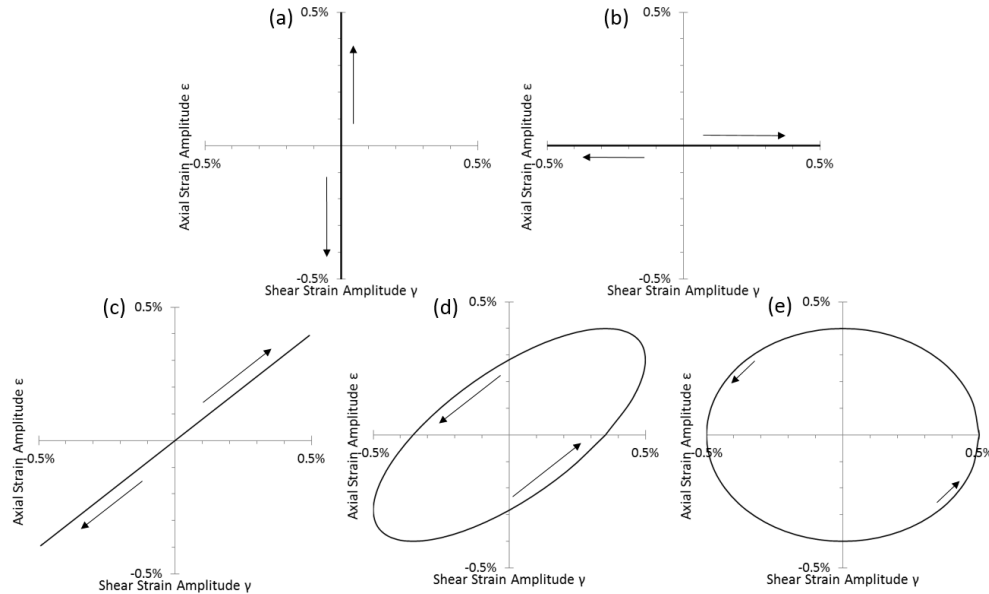


Figure 21 - Loading paths used for the fatigue experiments (a) pure-axial, (b) pure shear, (c) proportional (d) 45° out of phase and (e) 90° out of phase.

Once again similar to section 3.3.7 of this thesis, the failure criteria for the biaxial fatigue tests were considered to be a 50% reduction in the peak tensile axial stress or a 50% reduction in peak or valley shear stress (whichever occurred first). For tests in the HCF regime, a switch to force/moment control mode was once again adopted to facilitate higher frequency operation for higher duration tests. Data acquisition of forces, moments, and axial/shear strains were recorded simultaneously at a sufficiently high frequency to ensure a minimum of 50 data points per cycle. Typically in these tests visible cracks would form on the surface of the sample prior to reaching one of the failure criteria. The initiation location and propagation direction of these cracks was observed and recorded for further subsequent analysis.

### 3.3.9. Fractography

The fracture surfaces after tensile and fatigue tests were examined using SEM techniques (FEI Quanta FEG 250 ESEM with EDX). Both quantitative and qualitative analyses were performed to characterize the nature and morphology of the surface, as well as the topography from both a macroscopic and microscopic perspective (see Figure 22). Furthermore the macroscopic crack path was investigated and orientation determined via optical image analysis techniques. For a small proportion of the axial tests, the failure criteria would be achieved prior to final rupture of the specimen, thus in order to fully rupture the sample, an overload tensile force would be applied to cause catastrophic rupture. This process facilitated visual fractographic investigation of the surface. Careful precautions were taken as to ensure no significant compressive loading was introduced into the sample following failure as to preserve the features of the fracture surface and not induce any additional damage. The samples were then stored in a

desiccator with a controlled environment (nitrogen air chamber) to prevent oxidation of the surface prior to imaging via SEM.

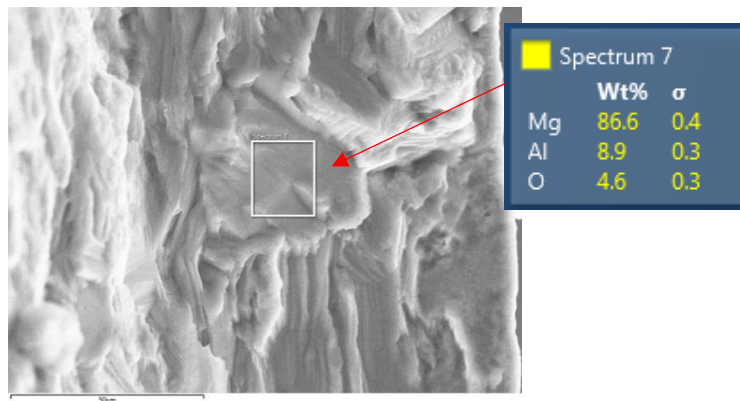


Figure 22 - Fracture surface EDX analysis example

Figure 23 illustrates the surface profile (and the roughness profile incorporating curvature correction) within a region of the fatigue propagation zone for a uniaxial fatigue specimen. The average surface roughness can be observed to be  $R_a = 2.24\mu\text{m}$ , distinct facets can be observed via the “stepped” elevation profile. Quantitative analysis techniques such as those obtained via a Keyence 6000 series Light Optical Microscope were used to further characterize fracture surface.

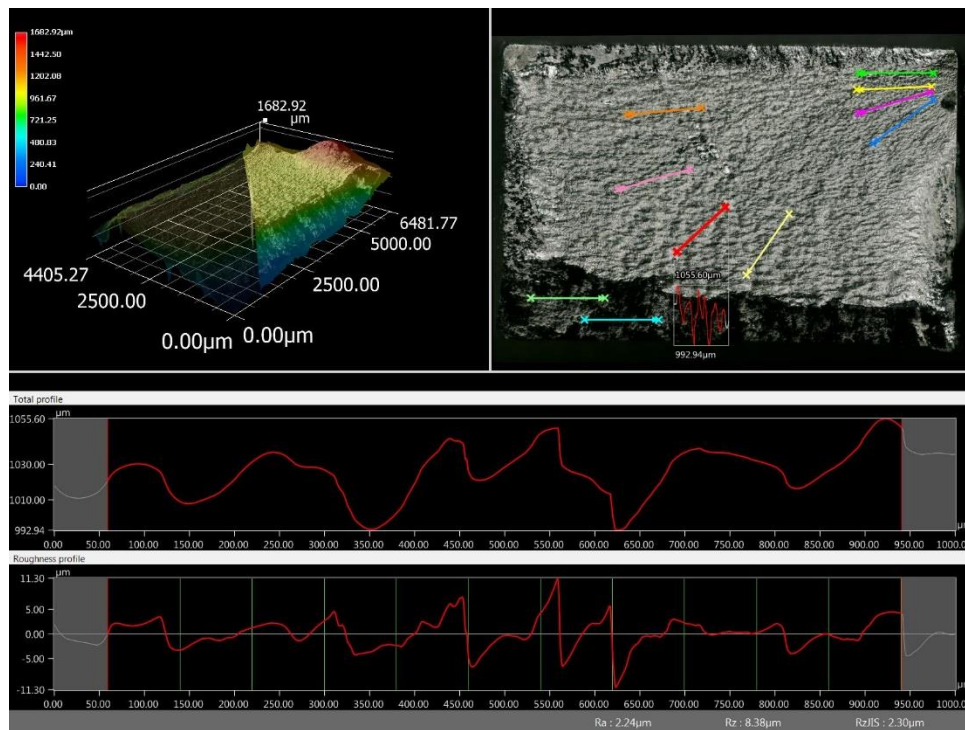


Figure 23 - Quantitative analysis of fracture surface using Light Optical Microscopy

### 3.4. Fatigue & Life Modelling Methodology

The basis of the methodology is to characterize the material in such a way that one is able to accurately predict the fatigue life of forged AZ80 Mg alloy given a loading history in the range of lifetimes which are typical automotive structural components. Several approaches have been implemented to quantify the damage associated with one fatigue cycle, being stress based approaches (S-N, Basquin), strain based approaches ( $\epsilon$ -N, Coffin-Manson) and energy based approaches (Jahed-Varvani, Fatemi-Socie etc.). The details of each of these techniques are discussed in subsequent chapters of this document. For energy based

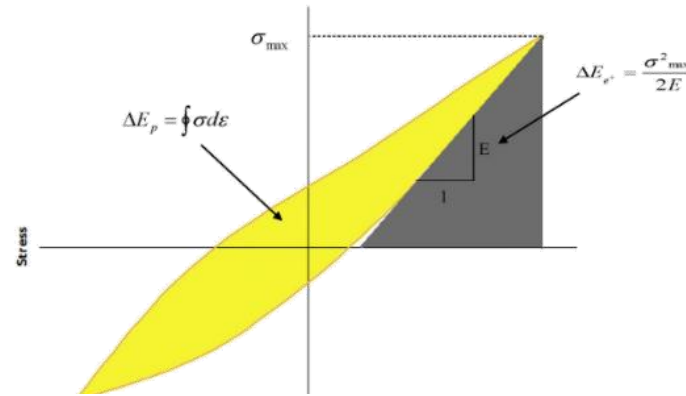


Figure 24 – Definitions of elastic (grey) and plastic (yellow) strain energy densities (SED) for a schematic cyclic hysteresis loop. [55]

approaches, Figure 24 describes the decomposition of elastic and plastic strain energy densities [62]. In general, decomposition of elastic and plastic components of both total strains and strain energy densities (SED's) is required for strain or energy based approaches (the focus of what is presented in this thesis). As such, the elastic modulus (or Young's modulus, denoted by 'E') is an important parameter which can have a dramatic effect upon the results of the modelling. For the purposes of this thesis, the average Young's modulus from multiple monotonic tests were utilized where applicable. This monotonic elastic modulus in most cases is virtually identical to the cyclic unloading modulus in the compressive reversal (as denoted in Figure 24). These values vary slightly, depending on material condition (base material, or various forged conditions) as well as the material direction (RD, TD, LD etc.), however in total these values ranged from 42.2 GPa to 46.8 GPa. Conventional wisdom might dictate that the elastic modulus is isotropic and not sensitive to processing conditions, however utilizing the correct elastic modulus for the specific material condition is vitally important in ensuring the accuracy of the predicted life especially when the elastic strains are a significant proportion of the total strain (i.e. high cycle fatigue). This technique was adopted here to further enhance the accuracy of both the characterization data (material constants) and the resulting life predictions.

### 3.5. Overview of Research Methodology

Despite the fact that the majority of scientific contribution of this work is in the realm of discovery level knowledge, the research methodology was both a very systematic and pragmatic approach (as to fulfill the objectives of the work, as well as the task objectives of the larger project). A graphical representation of the research methodology can be seen below in Figure 25.

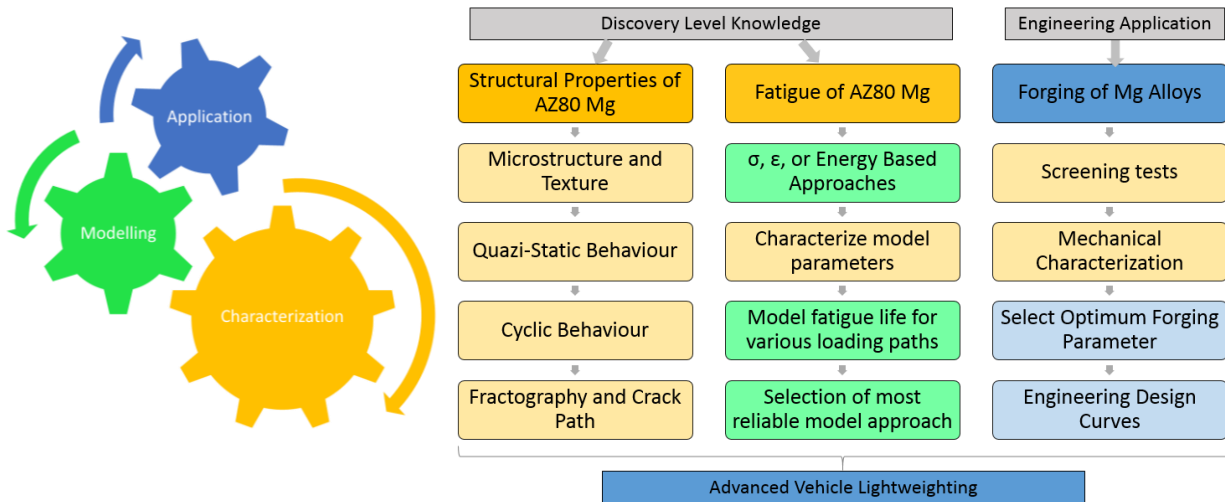


Figure 25 - Graphical Illustration of Research Methodology

## 4. Monotonic and cyclic behaviour of cast and cast-forged AZ80 Mg

This opening chapter of the thesis acts to form the foundational characterization knowledge for forged AZ80 Mg. The key focus of this chapter is two-fold, firstly characterization of the forged AZ80 Mg material, and secondly, understanding its cyclic behaviour. Firstly, research surrounding the characterization of forged AZ80 Mg thus far is extremely limited, and is very application based, with little discovery level work which has been done. Of the works that have been conducted, they can be separated into characterization of material which was forged as an intermediate processing technique (for subsequent processing) and near net-shape forging of a component which resembles the final part geometry.

The research which can be categorized as forging as an intermediate processing technique is mostly focused on characterizing the hot workability of the material and not the room temperature properties of the final product. Su et al. forged an aerospace cover plate [38] and indicated the optimum processing temperature for AZ80 Mg alloy is 283-310°C and strain rates of 0.001-0.0017 s<sup>-1</sup> to facilitate full dynamic recrystallization. The basis for this conclusion was on the hot workability and obtaining desirable microstructure. Kobold et al. [36] performed simple radial upset forging (similar in nature to the style of forging presented here in chapter 4) of extruded AZ80 Mg. They concluded that the optimum forging temperature was 350°C albeit at a much higher strain rate of 0.57-2.3 s<sup>-1</sup>; once again the conclusion drawn from the basis of hot workability and favourable material flow.

The research which can be categorized as characterization of near net shape forging is focused on microstructural investigations and monotonic properties assessment. Kevorkijan et al. [28] forged extruded AZ80 Mg into an automotive connecting rod at 415°C and a strain rate of 0.11 s<sup>-1</sup> and observed only slightly better structural properties compared with the base material. They also postulated that the mechanical properties developed in magnesium forgings depend on the strain hardening induced during forging. AZ80 in particular is subject to rapid grain growth at elevated forging temperatures so strain hardening is achieved by keeping the forging temperature as low as is practical as to not induce cracking.



### Monotonic and cyclic behaviour of cast and cast-forged AZ80 Mg

A. Gryguć<sup>a,\*</sup>, S.K. Shaha<sup>b</sup>, S.B. Behravesh<sup>a</sup>, H. Jahed<sup>a</sup>, M. Wells<sup>c</sup>, B. Williams<sup>b</sup>, X. Su<sup>c</sup>

<sup>a</sup>Department of Mechanical & Mechatronics Engineering, University of Waterloo, 200 University Avenue West, Waterloo, ON N2L 3G1, Canada  
<sup>b</sup>Centre for Materials, Natural Resources Canada, 183 Longwood Road South, Hamilton, ON L9P 0A1, Canada  
<sup>c</sup>Ford Research and Innovation Center, 2103 Village Street, Dearborn, MI 48124, USA

#### ARTICLE INFO

Article history:  
Received 1 December 2016  
Received in revised form 21 June 2017  
Accepted 28 June 2017  
Available online 9 July 2017

Keywords:  
AZ80  
Forging  
Texture  
Fatigue characterization  
Fracture  
Fatigue modeling

#### ABSTRACT

Tensile and strain-controlled fatigue tests were performed to investigate the influence of forging on the performance of cast AZ80 magnesium alloy. The obtained microstructural analysis showed that the as-cast AZ80 magnesium alloy has dendritic  $\alpha$ -Mg phase with eutectic Mg<sub>2</sub>Si morphology and a random texture. In contrast, the forged samples showed refined grains and a strong basal texture. During tensile testing, a maximum yield and ultimate tensile strength of 182 MPa and 312 MPa were obtained for the forged samples, representing increases of 121% and 33%, respectively, from the as-cast condition. At the same time, a significant improvement (73%) in ductility was obtained in forged samples. It was also observed that the forged samples achieved comparatively longer fatigue life under strain-controlled cyclic loading. Analysis of the fracture surfaces showed that a cleavage-type morphology was typical for the as-cast samples, while the occurrence of dimples and other evidence of plastic deformation were identified in the fracture surfaces of the forged specimens, indicating a more ductile response. Voiding caused grain refinement and texture modification, both of which enhance alloy performance by improving strength and ductility, and leading to longer fatigue life. Strain and energy-based models were investigated for their suitability to predict the life of the forged material. Both the Smith-Watson Topper and the Jahed-Yarvan energy-based models gave reliable life prediction.

© Crown Copyright © 2017 published by Elsevier Ltd. All rights reserved.

#### 1. Introduction

There has been a growing strong impetus to increase fuel efficiency and decrease emissions in the automotive industry over the past several decades. Implementation of lightweight materials in structural applications are at the forefront of this effort, as this strategy can improve vehicle efficiency, longevity, and performance. The multi-material lightweight vehicle (MMLV) is an emerging philosophy, and includes extensive use of lightweight materials for structural components. Importantly, this philosophy dictates that their location in the vehicle be determined directly by the location of their optimal performance. Magnesium (Mg) and its alloys have significant promise in this area, with widespread applicability in fatigue-critical components, such as suspension control arms, since they are the lightest commercially available structural metal and their cyclic properties are similar to those of the heavier, more conventional materials used in industry [1]. However, the inferior cast properties and poor formability of Mg alloys at room temperature, resulting from strong crystallo-

graphic texture and consequential anisotropic mechanical properties commonly formed during processing, limits the application of Mg alloys for manufacturing of complex parts such as a control arm. Forging is a near net-shape manufacturing technique that offers significant benefits as a material processing technique to produce a heavily refined wrought microstructure, lower internal defect density, and recrystallized grain structure, resulting in superior strength, improved ductility, and longer fatigue life [2]. The focus of the present study is to examine the effect of forging, as an alternative for manufacturing complex Mg parts, on the monotonic and fatigue behaviour of Mg.

The AZ80 alloy is a Mg alloy with good forgeability, a high aluminium content, and superior strength. The majority of published literature on AZ80 mechanical properties has focused on the static and fatigue properties of extrusion [3-14], cast [15-17,8], and plate [18] AZ80 Mg. Several researchers have investigated the fatigue behaviour of as-cast and wrought (extrusion, rolled plate/sheet) AZ80 Mg in stress-controlled [3,5,9,12,19-23], strain-controlled [12,13,18,23], and fatigue crack growth rate [5,9,24,25] testing. Zhou et al. [16] investigated the hot workability characteristics of as-cast AZ80 Mg and found that at temperatures below 300 °C and strain rates of 10<sup>-3</sup> s<sup>-1</sup>, flow localization bands limit the mate-

\* Corresponding author.  
E-mail address: agryguc@uwaterloo.ca (A. Gryguć).

https://doi.org/10.1016/j.ijfatigue.2017.06.010

Figure 26 - A. Gryguć et al., "Monotonic and cyclic behaviour of cast and cast-forged AZ80 Mg," *Int. J. Fatigue*, vol. 104, pp. 136-149, 2017.

Both types of characterization work that has been done is very limited in its breadth of discovery level knowledge, and only deals with one facet of the characterization which is required to successfully understand, model and predict the behaviour of forged AZ80 Mg. This knowledge gap illuminates a valuable opportunity for the work of this thesis to make meaningful scientific contributions, in particular to develop the structure-properties relationship for forged AZ80 Mg alloy. The work presented here in chapter 4 illustrates that forging of AZ80 Mg can result in mechanical properties which are very desirable for structural applications, and significant increase in strength and ductility when compare to the base material (attributes which typically are mutually exclusive).

The second key focus of this chapter encompasses research surrounding the fatigue characterization of AZ80 Mg is quite limited, led by only a few cornerstone works. By in large the knowledge base on understanding how AZ80 Mg behaves under cyclic loading is very much a topic which is under development. Chapter 2 detailed a compressive literature review on the state-of-the-art of fatigue of AZ80 Mg, however pertaining to this chapter of the thesis, the work that has been done in the domain of  $\epsilon$ -N fatigue of AZ80 Mg alloy is [25][63][64][16][20]. Of these, the work by Xiong and Jiang [20] can be considered to be the most comprehensive, as it investigates the effect of material orientation on the cyclic deformation and fatigue behaviour of AZ80 rolled plate. Their key conclusions are as follows; the rolled plate has a preferential texture orientation, which affects the level of asymmetry exhibited at higher strain amplitudes in the cyclic response depending on the orientation of the loading axis. Secondly, twinning-detwinning dominates the cyclic plastic deformation at higher strain amplitudes and dislocation slip prevails at lower amplitudes ( $<0.35\%$ ). Finally, trans-granular cracking is characterized by lamellar-like features occurs during fatigue crack propagation (FCP), and intergranular fracture characterized by dimple-like features in the final fracture (FF) region. These works have laid the foundation for developing the link between texture, forging direction and cyclic response, however addition of the thermomechanical effects which forging introduces into the material is something lacking in these works and is a great opportunity for scientific contribution.

When looking more specifically at the literature surrounding fatigue characterization of forged AZ80 Mg alloys it becomes much more limited, Moldovan et. al [5] conducted very rudimentary work on the stress controlled fatigue of AZ80 Mg alloy of unknown processing conditions and forging configuration. They indicated that many inclusions with manganese content could lead to rapid failure of the material, and thus recommended it was desirable to have minimal inclusions, porosities or coarse intermetallic particles. Rivers et al. [22] conducted stress controlled fatigue tests on the spokes of a forged AZ80 Mg automotive wheel and observed that a distinct endurance limit of 98 MPa exists. Furthermore, they indicated the presence of a preferred texture orientation, however they did not give substantial detail as to

its causation or its implications. This vast knowledge gap illustrates the most valuable contribution of this particular work, the fatigue characterization of forged AZ80 Mg alloy. These key contributions align very well to satisfy the research objectives 1 thru 4 for uniaxial strain controlled loading paths. This knowledge will enable researchers and industry to understand the structure-properties relationship and apply it to model the static and cyclic responses of forged AZ80 Mg as well as reliably predict its fatigue life.

The following journal article published in the International Journal of Fatigue (July 8, 2017) has been presented exactly as published, with the exception of modifications made for harmonizing references, table and figure numbers to integrate into this larger thesis document. A version of this work was also presented at the Fatigue and Damage of Structural Materials (FDSM XI) conference in Hyannis, USA in September of 2016.

#### 4.1. Introduction

There has been a growing strong impetus to increase fuel efficiency and decrease emissions in the automotive industry over the past several decades. Implementation of lightweight materials in structural applications are at the forefront of this effort, as this strategy can improve vehicle efficiency, longevity, and performance. The multi material lightweight vehicle (MMLV) is an emerging philosophy, and includes extensive use of lightweight materials for structural components. Importantly, this philosophy dictates that their location in the vehicle be determined directly by the location of their optimal performance. Magnesium (Mg) and its alloys have significant promise in this area, with widespread applicability in fatigue-critical components, such as suspension control arms, since they are the lightest commercially available structural metal and their cyclic properties are similar to those of the heavier, more conventional materials used in industry [65]. However, the inferior cast properties and poor formability of Mg alloys at room temperature, resulting from strong crystallographic texture, and consequential anisotropic mechanical properties commonly formed during processing, limits the application of Mg alloys for manufacturing of complex parts such as a control arm. Forging is a near net-shape manufacturing technique that offers significant benefits as a material processing technique to produce a heavily refined wrought microstructure, lower internal defect density, and recrystallized grain structure, resulting in superior strength, improved ductility, and longer fatigue life [4]. The focus of the present study is to examine the effect of forging, as an alternative for manufacturing complex Mg parts, on the monotonic and fatigue behavior of Mg.

The AZ80 alloy is an Mg alloy with good forgeability, a high aluminium content, and superior strength. The majority of published literature on AZ80 mechanical properties has focused on the static and fatigue properties of extrusion [5]–[16] cast [17]–[19][12] and plate [20] AZ80 Mg. Several researchers have investigated the fatigue behaviour of as-cast and wrought (extrusion, rolled plate/sheet) AZ80 Mg in stress-controlled [5], [6], [9], [12]–[16], [21]–[24], strain-controlled [7], [16], [20], [25], and fatigue crack growth

rate [9], [13], [26], [27] testing. Zhou et al. [18] investigated the hot workability characteristics of as-cast AZ80 Mg and found that at temperatures below 300°C and strain rates of  $10^{-2} \text{ s}^{-1}$ , flow localization bands limit the materials ductility, making it difficult to deform. They also studied the dynamic recrystallization (DRX) behaviour and found that it occurred over a temperature range of 425°C–500°C. Quan et al. [19] investigated the hot deformation characteristics of cast-homogenized AZ80 at 350°C and found a decrease in average grain size with an increase in strain rate. The observed average grain size of the cast material was 240  $\mu\text{m}$ . Following deformation, (total height reduction of 60%) at 350°C, the grain size was refined to 120, 110, 94, and 50  $\mu\text{m}$  under strain rates of 0.01, 0.1, 1, 10  $\text{s}^{-1}$ , respectively. Nový et al. [12] investigated both the static and very high-cycle fatigue (VHCF) properties using ultrasonic push-pull stress-controlled testing. In as-cast AZ80, they observed a yield and ultimate strength of 107 and 130 MPa, respectively. They found ductility to be very limited with a failure elongation of only 2%, and prominent intermetallic content with sizes ranging from 5–20  $\mu\text{m}$ . They also observed that only surface-induced cracks occurred in AZ80 under cyclic loading, with no observed endurance limit. They also discussed the finding that primary fatigue crack initiation sites are governed by microscopic defects such as pores, inclusions, or intermetallics in the low-cycle fatigue (LCF) to high-cycle fatigue (HCF). In contrast, they observed that in the VHCF, fatigue crack initiation is mostly controlled by the properties of the matrix, while the role of microscopic defects is minimal. Shiozawa et al. [16] performed LCF strain-controlled tension-compression fatigue tests on Mg extrusion AZ31, AZ61, AZ80, in which AZ80 had superior fatigue properties relative to the other alloys [66]. They also observed that in strain-controlled fatigue testing, a tensile mean stress was developed, caused by the tension/compression yield asymmetry typical of textured Mg alloys and the resulting twinning-detwinning cyclic deformation mechanism. They utilized a total strain energy density-based model, first developed for rolled AZ31 by Park et al. [59] as a modification to the well-known Morrow model, to reliably predict the fatigue life of extruded AZ80 Mg alloy. More recently, Wang et al. [25] utilized this modified Morrow model to successfully predict the LCF life of extruded AZ80 using a total strain energy density-based approach.

Many researchers have focused on the high temperature deformation behaviour of forged AZ80 [5], [10], [11], [17]–[19], [22], [24], [28], [29], [31], [32], [36]–[41]. However, studies that discuss the effect of thermomechanical history resulting from the forging process on the tensile/compressive and fatigue properties of AZ80 after forging are limited. Kobold et al. [36] performed both axial and radial open die forging of extruded AZ80-T5 at rates of 5–20  $\text{mm s}^{-1}$ , and observed no significant differences in the anisotropy of the material flow regardless of the forging direction. Furthermore, they concluded that the optimal isothermal forging temperature was 350°C, and that the optimum condition tends toward lower temperatures and higher strain rates. Kurz et al. [10] observed in die-forged AZ80-F that increasing the forging temperature decreases the mechanical strength, but enhances ductility as a result of an increase in

grain size and more homogeneous microstructure. They also concluded that at higher deformation rates (300–400 mm s<sup>-1</sup>), lower forging temperatures (240°C) are desirable. Rivers et al. [22] investigated the stress-controlled fatigue of samples machined from a forged AZ80 automotive wheel and observed an fatigue strength of approximately 98 MPa. The effect of the forging process on the strength, ductility, and strain-controlled fatigue behaviour of AZ80 has yet to be investigated in detail.

In this study, the effect of forging parameters on the tensile/compressive and forging on fatigue behavior of AZ80 was examined in detail and compared with the as-cast condition. A texture and microstructural link between the mechanical behavior of as-cast and forged AZ80 was established. The effect of material orientation on the tensile and compressive behavior of AZ80 is also discussed. Results from a complete fully reversed fatigue test results spanning from LCF to HCF are presented. Coffin-Manson and energy-based fatigue properties of as-cast and forged AZ80 were obtained, and the suitability of energy-based fatigue parameter in predicting the life of AZ80 was examined.

## 4.2. Experimental

The material used in this investigation was commercially-available AZ80 Mg alloy (8.0 ±0.2% Al content, with other elements composition as per ASTM B91-12 standard). The material was received from Magnesium Elektron North America Inc. in the form of an as-cast billet with a diameter of 300 mm and a length of 500 mm in the as-fabricated condition. The forging of the material was conducted at CanmetMATERIALS (Hamilton, Canada) using billets (∅ 63.5 mm, 65-mm long), which were machined from the 300-mm diameter AZ80 casting at a position of 70% of the radius. All forging trails were carried out on a 500-ton hydraulic press with an upper and lower platen (die), which were both flat. Two forging temperatures (350 and 450°C) were examined. The billet and tooling were heated separately to the same temperature. The orientation of the billet to the press was such that the radial direction was along the direction of the press stroke (i.e. direction of forging was coincident to the radial direction of the billet). Forging was carried out at two different displacement rates (39 and 390 mm/min), which fall within the slower regime of die forgings presented by Kevorkijan et al. [28]; however the approximate average strain rates presented in this study lie between those presented by Kevorkijan et al. [28] and Kurz [10]. For the quasi-static study, three forging conditions investigated in this study will subsequently be referred to as S1 (350°C and 39 mm min<sup>-1</sup>), S2 (450°C and 39 mm min<sup>-1</sup>), and S3 (450°C and 390 mm min<sup>-1</sup>). The cast and machined billets were forged to a height of 13 mm, then air cooled. Graphite lubricant was used to coat the surface of every billet prior to forging. Although the die temperature remained almost constant throughout the test, heat loss to the surrounding air during forging was expected for the billet, particularly for the slower forging rate condition. Figure 1(a) and (b) show the orientation for which the metallographic, tensile, and fatigue-tested specimens were extracted from both the cast and forged billets. LD, RD, TD, and FD



side lengths of 7.6 mm were extracted as shown in Figure 27 (a) and (b). The quasi-static compressive tests were performed using a MTS 810 Servo-Hydraulic test machine operating in displacement control mode. For both compressive and tensile monotonic tests, the displacement rate of the crosshead was 1 mm min<sup>-1</sup>. Strain measurement was accomplished using a GOM ARAMIS 3D 5MP DIC system. The average strain rate within the gauge section of measurement for both tests were 1.4E-3 sec<sup>-1</sup>.

The fatigue tests were performed as per ASTM E606 in an ambient environment using a MTS 810 Servo-Hydraulic test machine operating in strain control mode at a frequency range of 0.25–2 Hz. Strain was measured and controlled using a MTS 632.26 extensometer with a 6-mm gauge and travel of ± 1.2-mm, until stabilization of the cyclic hysteresis loop was achieved; for HCF tests with elastic response, the test was switched to force control mode, and the frequency was increased to 30 Hz. The tests were conducted at a zero mean strain (i.e.,  $R_L = -1$ , fully reversed strain cycle) and strain amplitudes of between 0.1% and 1.4%. Failure criteria for the test was considered to be a 50% drop in peak load during strain control mode or final rupture of the specimen gauge section in force-control mode. The fracture surfaces after tensile and fatigue tests were examined using SEM techniques (JEOL JSM-6610LV SEM equipped with AZ-TEC EDS).

### 4.3. Results & Discussion

#### 4.3.1. Microstructure and Texture

As depicted in Figure 28(a) and (c), the as-cast sample was found to consist of primarily  $\alpha$ -phase, in which aluminium-rich  $\beta$ -phase ( $Mg_{17}Al_{12}$ ) is precipitated along the grain boundaries. This agrees with the microstructure of as-cast AZ80 observed by Nový et al. [12], the grain morphology of which was similar to that observed here, while the average grain size (80–140  $\mu m$ ) was slightly more refined than that observed in this study. The forged conditions S1, S2, and S3 (Figure 28(b), (d), (e)–(h)) all exhibit a recrystallized microstructure with fairly homogeneous grain morphology, albeit “pancake”-like in nature. For all forged conditions, the precipitate morphology observed at higher magnifications have a discontinuous intergranular structure, which is similar to that observed by Lai et al. [67] in extruded AZ80 that was aged at 300°C for 1 hr, which is comparable to the thermal history experienced in the forged samples presented in this study. The average grain size for the forged conditions ranged from 14.1–34.4  $\mu m$ , with condition S1 (Figure 28(b)) having the most refined microstructure. As the forging temperature and rate increase, the observed average grain size also increases (Figure 29).

Figure 2 illustrates the as-cast and forged conditions S1 ((b), (d)), S2 ((e), (g)), and S3 ((f), (h)). The as-cast condition (Figure 28 (c)) exhibits randomized basal (0002) and prismatic (10 $\bar{1}$ 0) texture. All forged conditions (Figure 28 (d), (g) and (h)) exhibit strong basal texture. Based on the basal pole figures, it is clear that the c-axis orientation of the forged material is coincident with the forging direction; similar

reorientation of the c-axis due to forging has been reported by several researchers [68]–[55]. Previous work by Gryguc et al. [69] on axially and radially forged AZ31B extruded billets show an analogous c-axis reorientation in extruded AZ31 following forging. The effect of forging on the initial random texture is a local reorientation of newly recrystallized grains, causing their crystal axis to align with the forging axis as the deformation progresses. This causes the basal texture strengthening to be planar in nature for all forged conditions. Wang et al. [70] found that in both extruded and sheet AZ31 Mg, following significant plastic strain, most c-axis orientations, which are favourable for twinning, will re-orient themselves to the direction of forging; this directly supports the findings presented here. The texture intensity in the forged material is inversely correlated to temperature, with very weak sensitivity to forging rate. The changes in grain size and basal pole figure intensity as a function of forging condition are depicted in Figure 29. The highest basal intensity and lowest grain size were achieved at the lower temperature (350°C) and forging rate (39 mm min<sup>-1</sup>). An increase in temperature had the effect of decreasing texture intensity and increasing average grain size. This observation agrees with earlier findings of several other researchers [31][40][71].

Many researchers have investigated the effects of processing parameters on the mechanical properties of AZ80 using simple compressive upset testing using Gleeble thermomechanical testing equipment. Quan et al. [19] investigated the effect that strain rate had on cast AZ80 at 350°C. They found that with a total height reduction of 60% (lower than the 80% height reduction considered in this study), grain refinement is more pronounced at higher strain rates as a result of more vigorous DRX behaviour. Liu et al. [72] presented similar findings for cast AZ91 Mg at various temperatures (250–450°C); they revealed that the effect of increasing strain rate was an increase in grain refinement, while an increase in temperature caused grain growth and improved microstructure homogeneity. Lou et al. [66] presented analogous results when investigating the effects of strain rate on extruded AZ80 at temperatures ranging from 250–450°C, both of which support the finding of this study that lower temperature forging conditions results in more refined microstructure (Figure 28). However, other researchers have observed that an increase in strain rate resulted in more vigorous grain refinement on their temperature-controlled Gleeble specimens, which were water quenched following testing [19][66][72]. These results differ from those presented here (Table 6, Figure 28) as condition S3 (390 mm min<sup>-1</sup>) has an average grain size that is ~13 μm larger than condition S2 (39 mm min<sup>-1</sup>). This can be attributed to the fact that during forging, only the die temperature and initial billet temperature were controlled, unlike the conditions of the Gleeble tests, in which the billet temperature is controlled throughout deformation. Since the heat of deformation is greater for the higher rate forging, the temperature rise due to deformation in condition S3 would be larger than that in S2, potentially causing the observed grain growth. Additionally, following deformation, the forgings were left to air-cool, unlike the water quenching following the Gleeble tests. Finally, this difference can be attributed to the difference between the style of forging during a Gleeble test (axial upset of small cylindrical sample) and this study

(radially upset bulk forging). The lower temperature forging condition S1 is considered to produce the best microstructure of all three samples, based on the more refined and recrystallized morphology it possesses. At higher forging temperatures (450°C) forgings (S2 and S3), microstructure homogeneity further improved, and was coupled with grain growth and apparent refinement in  $\beta$ -phase morphology.

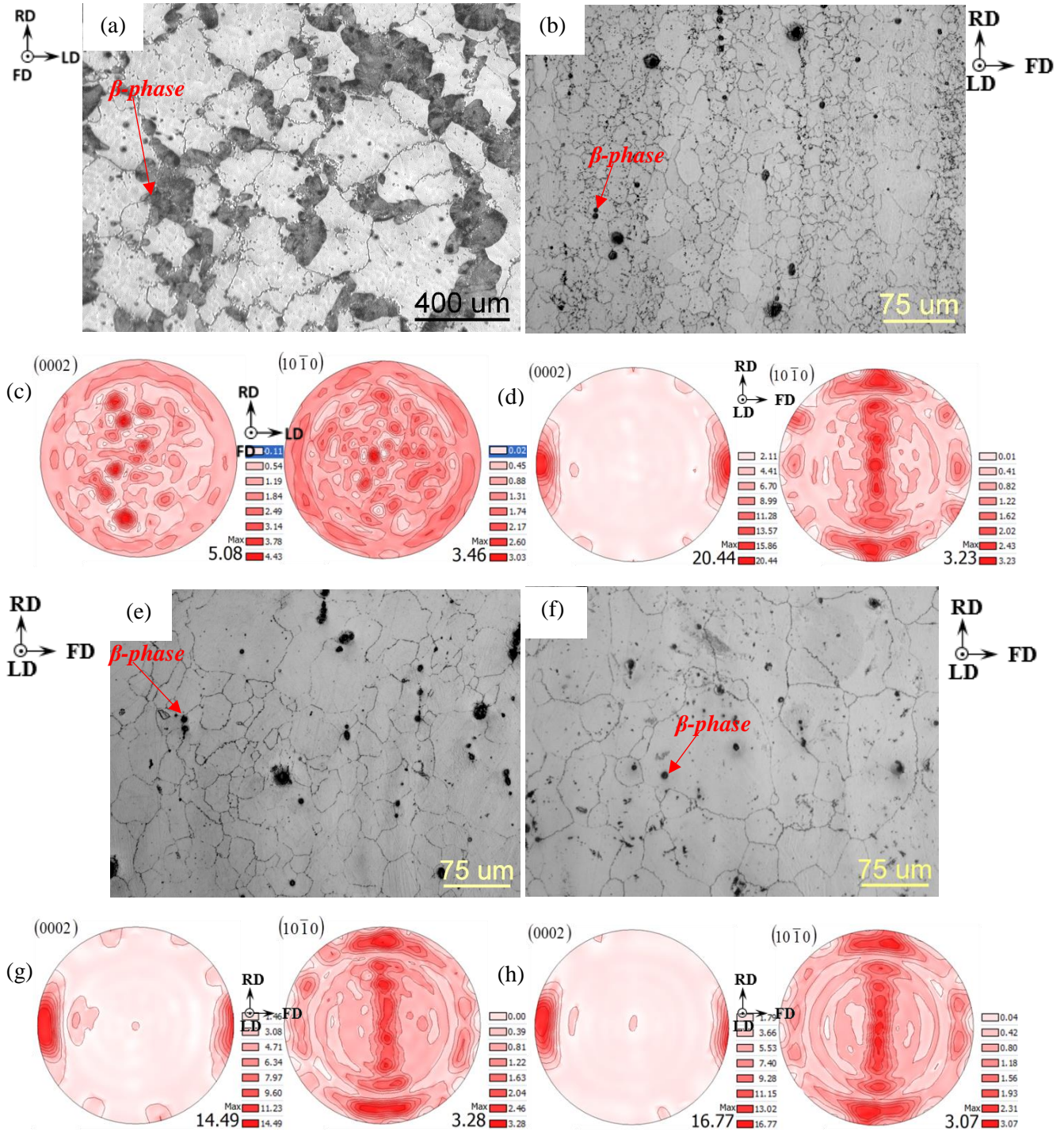


Figure 28 - Typical LOM microstructure and XRD pole figures for As-Cast ((a) and (c)), forged condition S1 ((b) and (d)), forged condition S2 ((e) and (g)), and forged condition S3 ((f) and (h))

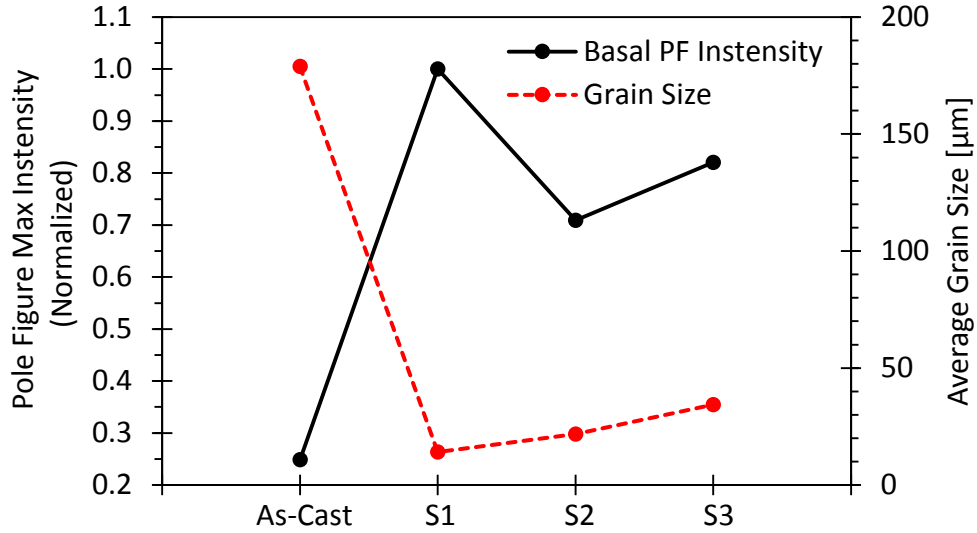


Figure 29 - Relationship between basal pole figure max intensity and average grain size for as-cast and forged conditions (S1, S2, and S3)

#### 4.3.2. Monotonic and Cyclic

Table 1 summarizes the test results of the investigated samples. Figure 30(a) and Figure 31(a) show the engineering stress-strain response in tension (Figure 4(a)) and compression (Figure 5(a)) for the as-cast and forged (S1, S2, and S3) materials in the longitudinal direction.

Table 3- The relationship between microstructural, monotonic, and cyclic properties of as-cast and forged AZ80-F Mg alloy. Tensile properties are presented first, followed by compressive properties in parenthesis.

ID	Forging rates (mm/min)	Forging Temperature (°C)	Grain size (µm)	$\sigma_{YS}$ (MPa)		$\epsilon_{Fail}$ (%)	$\sigma_{ULT}$ (MPa)
				Monotonic	Cyclic		
Cast	As-Cast	-	178.9±67	82.2 (93.8)	147.0 (153.5)	8.5 (15.3)	234.1 (318.2)
S1	39	350	14.1±0.7	173.8 (124.5)	258.3 (145.4)	14.1 (8.5)	311.9 (373.0)
S2	39	450	21.8±2.4	176.9 (111.2)		15.8 (9.6)	310.6 (366.7)
S3	390		34.4±2.7	181.7 (69.2)		14.2 (8.3)	306.1(325.9)

It can be seen that the yield, ultimate strength, and, in some cases, the fracture strain substantially increase following forging. In general, substantial increases in tensile yield stress and fracture strain were observed in the material after forging. This was coupled with a moderate increase in compressive yield strength, tensile ultimate strength, and compressive ultimate strength after forging. However, the fracture strain in compression decreased to some degree in all of the forging conditions. The increase in mechanical properties of as-forged compared to as-cast condition is attributed to the grain refinement and texture intensification that arises from the reorientation of the randomized c-axis orientation in the as-cast material in the direction of deformation once forged. All forging conditions have very similar monotonic yield/ultimate strengths and hardening behaviours under tension. At the higher temperature (450°C)

forgings (S2 and S3) a reduction in compressive yield and ultimate strength was observed, but the tensile strength remained similar to all other forged conditions. This trend partially agrees with findings presented by Kurz et al. [10] for AZ80 die forgings, who also reported a decrease in tensile strength at higher temperatures.

Figure 30(b) and Figure 31(b) show a comparison of the cyclic vs. monotonic stress-strain curves for both the as-cast and forged material in tension (Figure 4(b)) and compression (Figure 5(b)). The cyclic tension and compression stress-strain curves were constructed from the peak and valley stresses for the stabilized cycle during fatigue testing for each respective strain amplitude. Stabilized cycle is the cycle at 50% of the number of cycles to failure. In general, data from the forged conditions S1, S2, and S3 follow the same cyclic tensile stress-strain curve. For this reason the fatigue results of the three conditions will be presented collectively.

The compressive stress-strain curves shown in Figure 31(a) illustrate evidence of mixed hardening in the as-cast condition and purely sigmoidal hardening behaviour for all forged conditions. As expected from the random texture shown in Figure 28(c), the as-cast material exhibited nearly symmetric yield strength in tension and compression, with slip and diffused twinning being dominant in both directions. In contrast, the forged material exhibits a very asymmetric yielding response, with the degree of asymmetry increasing as both temperature and forging rate increase (Figure 32a). Based upon the hardening responses seen in forged conditions S1, S2, and S3, and the strong basal texture shown in Figure 28(d), (g), and (h) the deformation mechanism in tension is dominated by basal slip (as the direction of loading is parallel to the basal plane), and the deformation in compression is dominated by twinning (extension twinning activated via extension along the *c*-axis). This sigmoidal behaviour, characterized by three distinct hardening stages, has been discussed by other researchers [73][69].

Under cyclic loading, the as-cast and all 3 forged conditions show cyclic hardening, where the increase in peak and valley stresses is relative to those of the monotonic results. As seen in Figure 30 and Figure 31, the as-cast material exhibits very similar cyclic hardening in tension and compression, with the peak stresses observed in the stabilized cyclic response being 73 MPa higher than those observed in the monotonic response at and beyond strain amplitudes of 0.9%. The forged material however, shows more pronounced cyclic hardening in tension, with the highest degree of hardening occurring at a strain amplitude of 1.1%, corresponding to an increase of 80 MPa in peak (tensile) stress and 58 MPa in valley (compressive) stress relative to the monotonic response. Figure 32(b) illustrates the change in yield strengths following cyclic hardening for both the as-cast and forged material. There is an increase of 62 MPa in the yield strength of the cast material in tension and compression, and asymmetric increases of 81 MPa in tension, and 34 MPa in compression for the forged material. The asymmetric hardening responses of conditions S1,

S2, and S3 is attributed to the differences in the deformation mechanism in tension and compression reversals, induced by the texture intensification via forging.

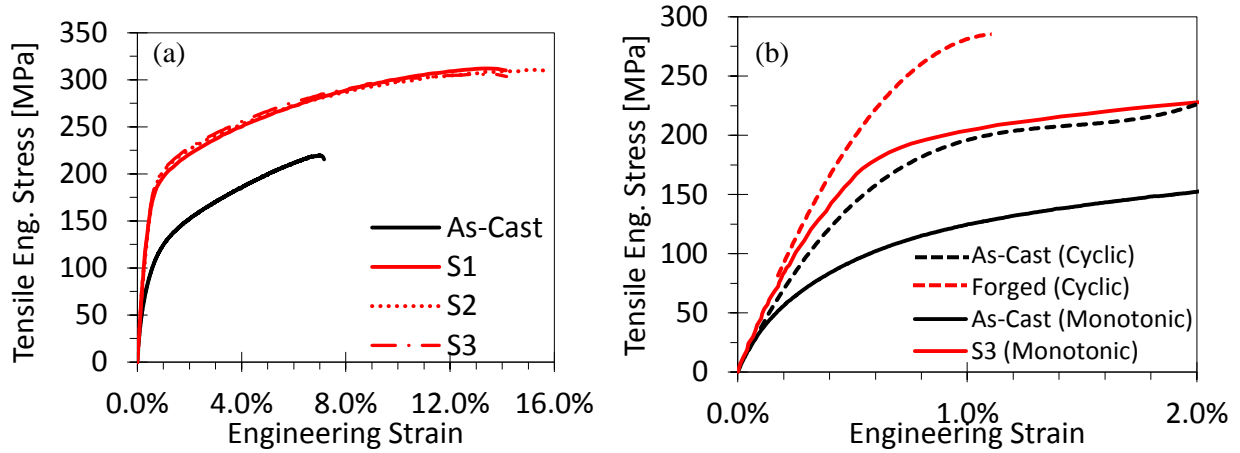


Figure 30 – Tensile (a) monotonic and (b) cyclic stress-strain curves for as-cast (black) and forged Mg (red)

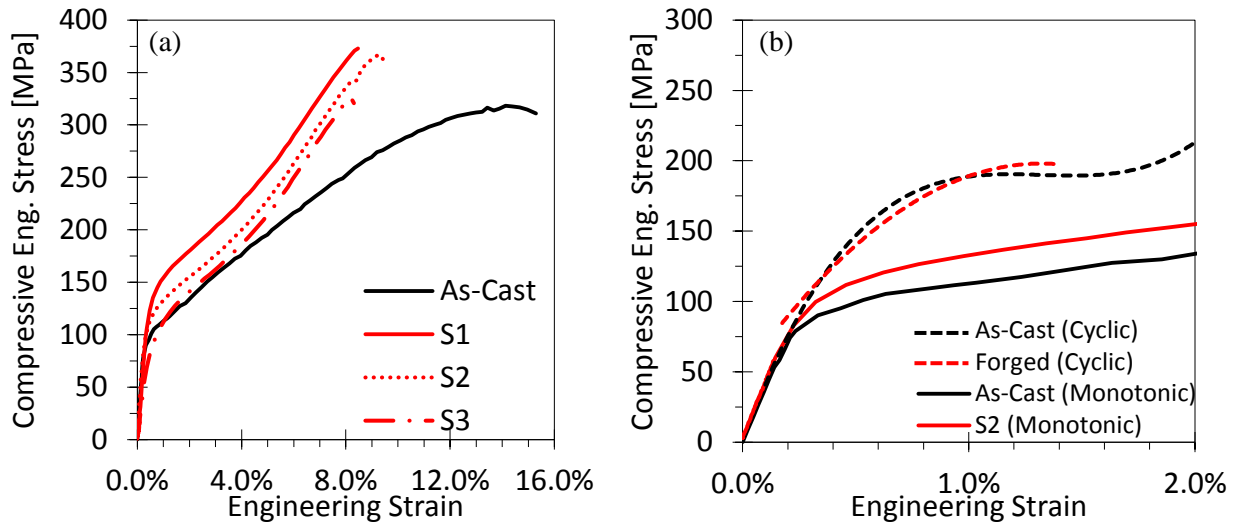


Figure 31 – Compressive (a) monotonic and (b) stabilized cyclic stress-strain curves for as-cast (black) and forged Mg (red)

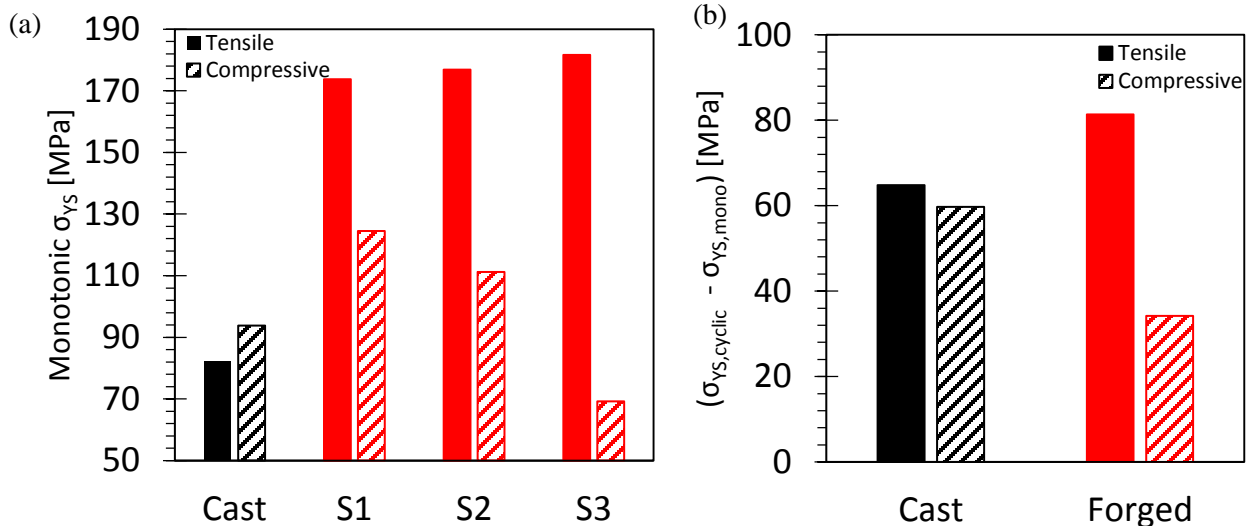


Figure 32 - Summary of (a) monotonic yield strengths and (b) change in yield strengths following cyclic testing for both the as-cast (black) and forged (red) material in tension and compression.

Figure 33 illustrates the hysteresis loops for the first cycle, and stabilized cycles for both the as-cast and forged conditions at a strain amplitude of 0.5%. It can be seen that the peak stresses at the “apex” of both the upward and downward (i.e. reverse loading) reversal are very similar in the cast material (Figure 33 a) for the first and stabilized cycles. The cyclic hardening is also evident from the significant increase in peak stresses from the first cycle to the stabilized cycle; this increase is similar in both tension and compression. The area within the stabilized hysteresis loop represents the dissipated plastic strain energy density, and is calculated to be  $0.5 \text{ MJ m}^{-3}$  in the case of the cast material at a strain amplitude of 0.5%. In contrast to this, the forged material (Figure 33(b)) exhibits an initial response (first cycle) that is asymmetric, with different curve shapes for the upward and downward reversals, indicative of the occurrence of different deformation mechanisms. The peak stress in compression evolves only marginally as the number of cycles increase, whereas the peak stress in tension increases considerably from the first to the stabilized cycle. This indicates vigorous hardening in tension, and only negligible hardening in compression. In the stabilized cycle the peak stresses in tension are about 77 MPa greater than those in compression, further reinforcing the asymmetric cyclic response of the forged material. As compared with the cast material, the cyclic plastic energy density of the forged material is  $0.31 \text{ MJ m}^{-3}$  (38% lower), indicative of a more elastic response at a strain amplitude of 0.5%.

Figure 34 illustrates the hysteresis loops for the first and stabilized cycles for the as-cast and forged materials for a high strain amplitude (1.0%). Similar to the observations at a 0.5% strain amplitude, at 1.0% the as-cast material exhibits cyclic hardening with the peak stresses increasing both symmetrically and considerably up to the stabilized cycle, with only a marginal disparity in the peak stress in tension and compression observed in the stabilized cycle. In the forged material, the asymmetric response is even more

pronounced at a strain amplitude of 1.0%, with the peak stabilized tensile stress being 114 MPa greater than that observed in the downward reversal. Cyclic hardening is now observed in both tension and compression in the forged material as the peak stresses both evolve over a cumulative number of cycles; however, the hardening is much stronger in tension than in compression. Both materials exhibit significant plasticity at the higher strain amplitude of 1.0%, as the cyclic plastic energy density of the stabilized as-cast and forged responses are  $2.0 \text{ MJ m}^{-3}$  and  $1.55 \text{ MJ m}^{-3}$ , respectively. Furthermore, the trends in the level of asymmetry observed in the monotonic response also occurred in the cyclic response of the forged material, but not in the cast material.

The asymmetric cyclic response in textured HCP Mg alloys at higher strain amplitudes have been attributed to detwinning and slip-dominated deformation in tension, and twinning-dominated deformation in compression when loading is in the direction perpendicular to the c-axis [59], [74]–[76]. The downward reversal of such materials is characterized by a lower yield strength (as illustrated in forged conditions in Figure 32(a)) followed by a hardening plateau, which is observed in all forged conditions in this study. The extension twinning deformation process observed in compression is facilitated by a reorientation of the crystal lattice by  $86.3^\circ$  towards the direction of loading [69], subsequently putting a large proportion of unit cells in an orientation that is favourable to detwinning upon reverse loading, as the loading axis is now almost aligned with many of these newly re-oriented unit cells, again activating extension twinning in the successive upward (i.e. forward loading) reversal [77][42][69]. However, this twinning-detwinning process is only slightly reversible in nature and detwinning is typically exhausted prior to the end of the reversed tensile loading. This is accompanied by a sharp increase in hardening rate, and consequently a higher tensile peak stress (relative to compressive peak stress) [59]. The shape of the upward reversal response in all forged conditions (especially in the stabilized cycles) shows strong evidence of this aforementioned behaviour, further supporting the concept of texture-induced asymmetry.

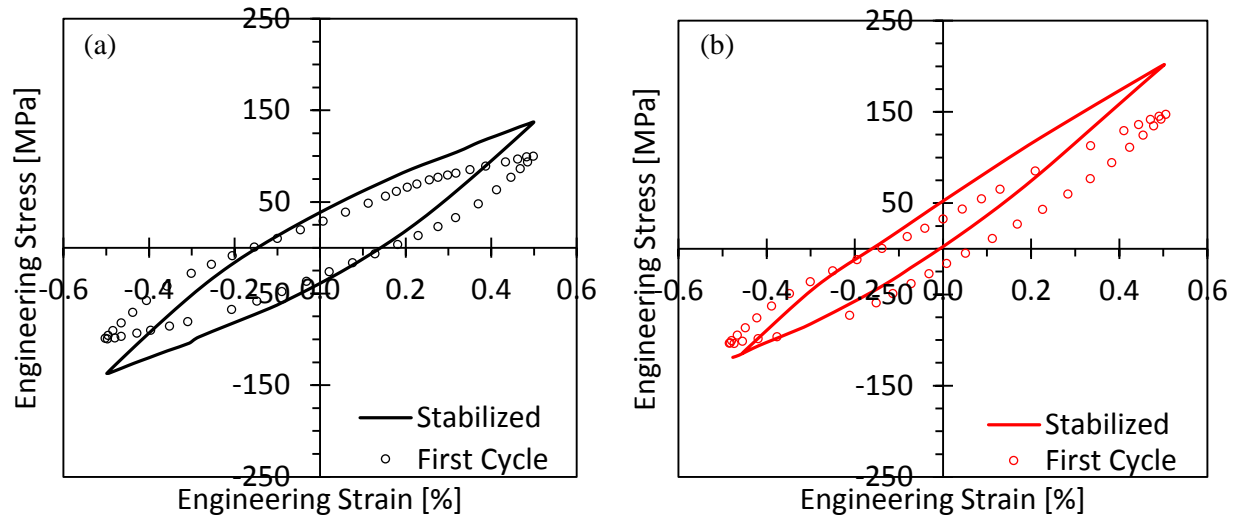


Figure 33 - Axial cyclic behaviour of AZ80 at a strain amplitude of 0.5% in (a) as-cast and (b) forged samples

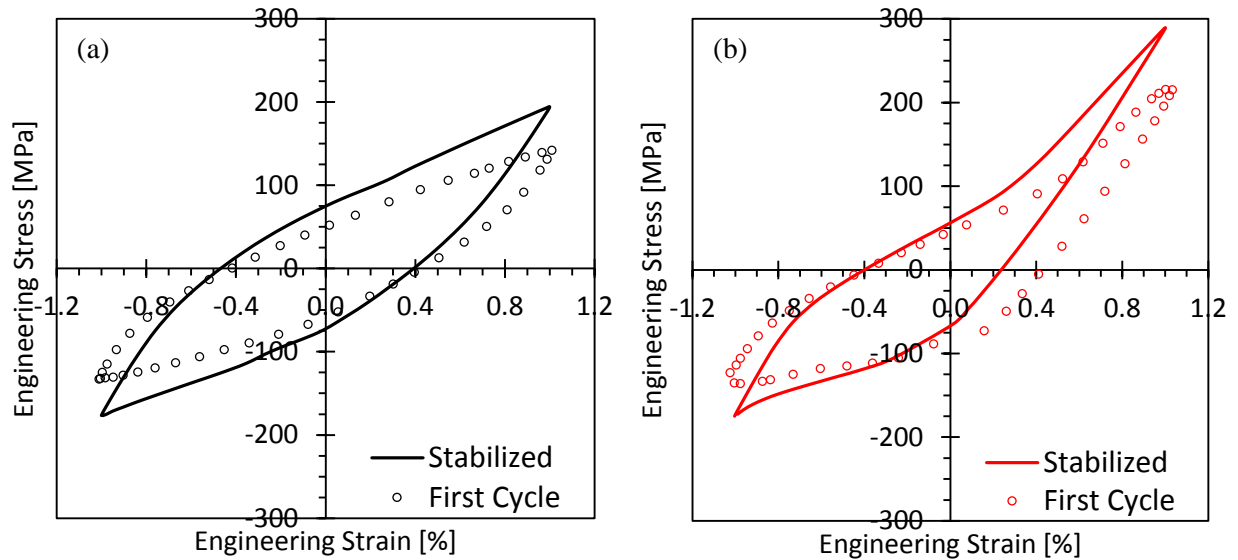


Figure 34 - Axial cyclic behaviour of AZ80 at a strain amplitude of 1.0% (a) as-cast and (b) forged samples

Figure 35 shows the plastic strain response vs. number of cycles throughout the fatigue tests for the as-cast and forged materials at strain amplitudes of 0.5% and 1.0%. As expected, higher strain amplitudes correspond to larger plastic strain components. Furthermore, there is a decrease in maximum plastic strain with number of cycles for both materials and at all strain amplitudes, supporting the cyclic hardening observation discussed earlier. It can be seen that the plastic strain observed in compression is similar between the as-cast and forged materials; the only difference being a higher number of cycles to failure in the forged material. This is due to the similarity in the cyclic yield and flow curve as depicted by Fig. 5b. However, in tension, there is a stark contrast between the plastic strain of the as-cast and forged materials (Figure 35). At a 0.5% strain amplitude, the forged material exhibits 39% less plastic strain than the as-cast

material. At a 1.0% strain amplitude, this difference decreases to 25%, but is still considerable, confirming a higher elastic response and higher cyclic yield strength in the forged material. This difference in the plastic strain observed in tension can be directly attributed to the exhaustion of detwinning in the upward reversal and the associated sudden increase in hardening rate and peak stress, as previously discussed [60].

Figure 36 shows the evolution of mean stress vs number of cycles for various strain amplitudes. For all strain amplitudes of the as-cast material, a negligible amount of mean stress develops. In contrast, in the forged material, a significant amount of mean stress (ranging from 15–55 MPa) develops, with higher mean stresses being typical of larger strain-amplitude fatigue tests. These findings are similar to those discussed earlier (e.g., [27] for AZ31B rolled sheet). The forged material responses are characterized by a fairly consistent increase in mean stress, which reaches a maxima prior to failure. The peak values of mean stress for the forged material are 30, 44, 48, and 57 MPa at strain amplitudes of 0.3%, 0.5%, 0.7%, and 1.0% respectively. The increase in mean stress occurs at a proportion of the total life of the material; this increase ranges from 20–90% depending on the strain amplitude. At low-strain amplitudes (0.3%) the peak mean stress occurs at a cycle count equivalent to 20% of the number of cycles required to cause failure. At higher strain amplitudes (1.0%, Figure 36) a higher proportion of cycles (close to 75%) of the total life is required to reach maximum mean stress

Figure 37 shows the stabilized cyclic response for the (a) as-cast and (b) forged materials at a variety of strain amplitudes. There is apparent symmetry in the as-cast material cyclic response, and hardening behaviour analogous to that observed in the monotonic response (evidence of predominantly slip in tension and weakly mixed-mode hardening (slip and diffuse twinning) in compression). In contrast, the forged material (Figure 37(b)) shows asymmetry with a sigmoidal downward reversal shape and a pronounced shift in hardening behaviour in the upward reversal. This upward reversal response is not observed in monotonic tension as the strain history plays a role in the deformation mechanism, i.e. the first cycle, which starts in tension, shows a response identical to that of the monotonic test. However, the stabilized response has a high propensity to detwin in the upward reversal due to the reorientation of the c-axis resulting from the extension twinning experienced in the previous downward reversal. This phenomenon occurred regardless of forged material condition or strain amplitude, though evidence of it was more pronounced at higher strain amplitudes. The observation that the texture intensification due to forging results in an asymmetric response in both a monotonic and cyclic manner is supported by previous work on other textures, and on material processing methods of various wrought Mg alloys [20], [25], [42], [53], [55], [59], [61], [74], [78].

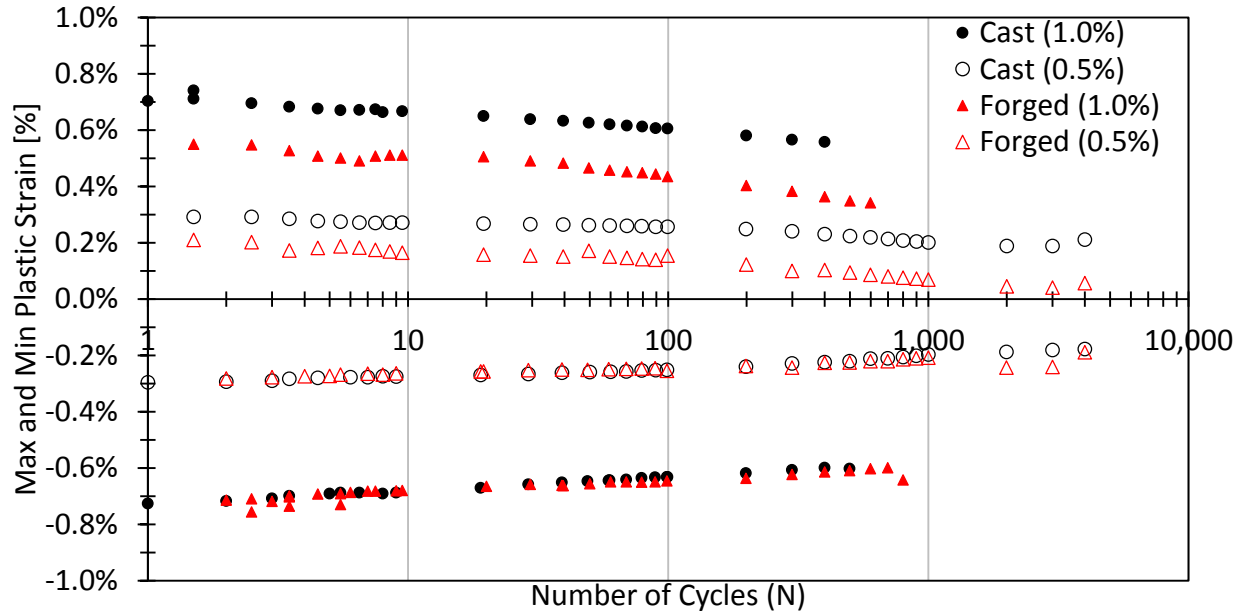


Figure 35 – Plastic strain response during strain-controlled cyclic testing showing variations in peak tensile and compressive plastic strain vs. number of cycles for both as-cast (black) and forged material (red), at 1.0% and 0.5% strain amplitudes

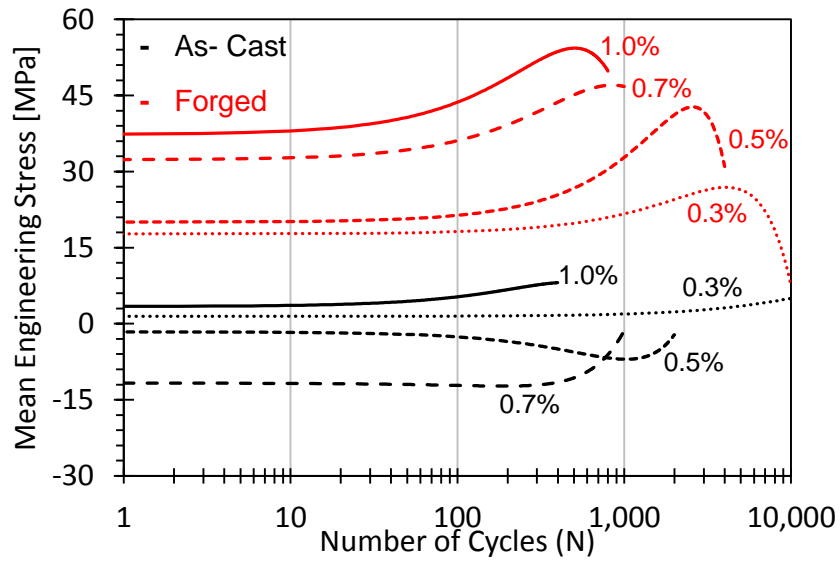


Figure 36 - Stress response during strain-controlled cyclic testing showing variations in mean stress vs. number of cycles at various strain amplitudes (results for 0.3% are only shown up to 10,000 cycles)

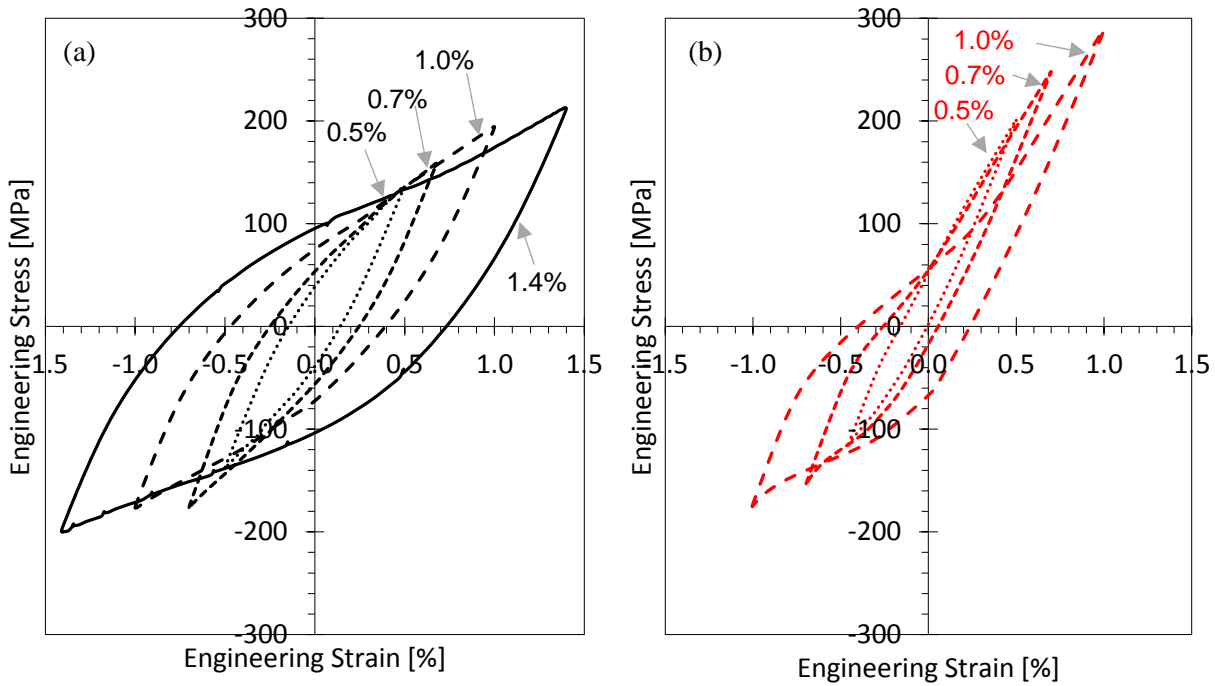


Figure 37 - Stabilized cyclic axial behaviour of (a) as-cast and (b) forged AZ80 Mg alloy

### 4.3.3. Fatigue Life

Figure 38 shows the strain-life ( $\epsilon$ -N) curve obtained from strain-controlled fatigue testing of the as-cast and forged samples. The data points represent all of the test results, which were conducted on the as-cast and forged material. The dashed lines represent the Coffin-Manson curves for both material types. The forged material has a longer life across all strain amplitudes compared to the cast material. The improvement in life as a result of forging ranges from a factor of approximately 2 times greater in the LCF regime at a 1.4% strain amplitude, to 5 times greater in the HCF regime at a 0.3% strain amplitude. The tests that did not fail after  $10^7$  cycles are considered to be “run out” and are denoted with an arrow in the figure.

Also shown are the stabilized responses for the as-cast and forged materials at strain amplitudes of 0.3%, 0.7%, and 1.4% plotted on the same axis of engineering stress and strain to facilitate a direct comparison between them. The downward reversal response is similar (in terms of peak stress) between the as-cast and forged materials; however the tensile peak stress in each hysteresis loop is much greater in the forged material. It is well known that a tensile mean stress, as exhibited by the forged materials in this study, has a detrimental effect on fatigue life [16]. This implies that the forged material would exhibit a shorter life because of the presence of positive mean stress. However, the plastic energy density or cyclic energy (area inside the hysteresis loop) is also considerably lower in the forged material for all strain

amplitudes, indicative of a lesser extent of incurred damage per cycle and a corresponding increase in fatigue life.

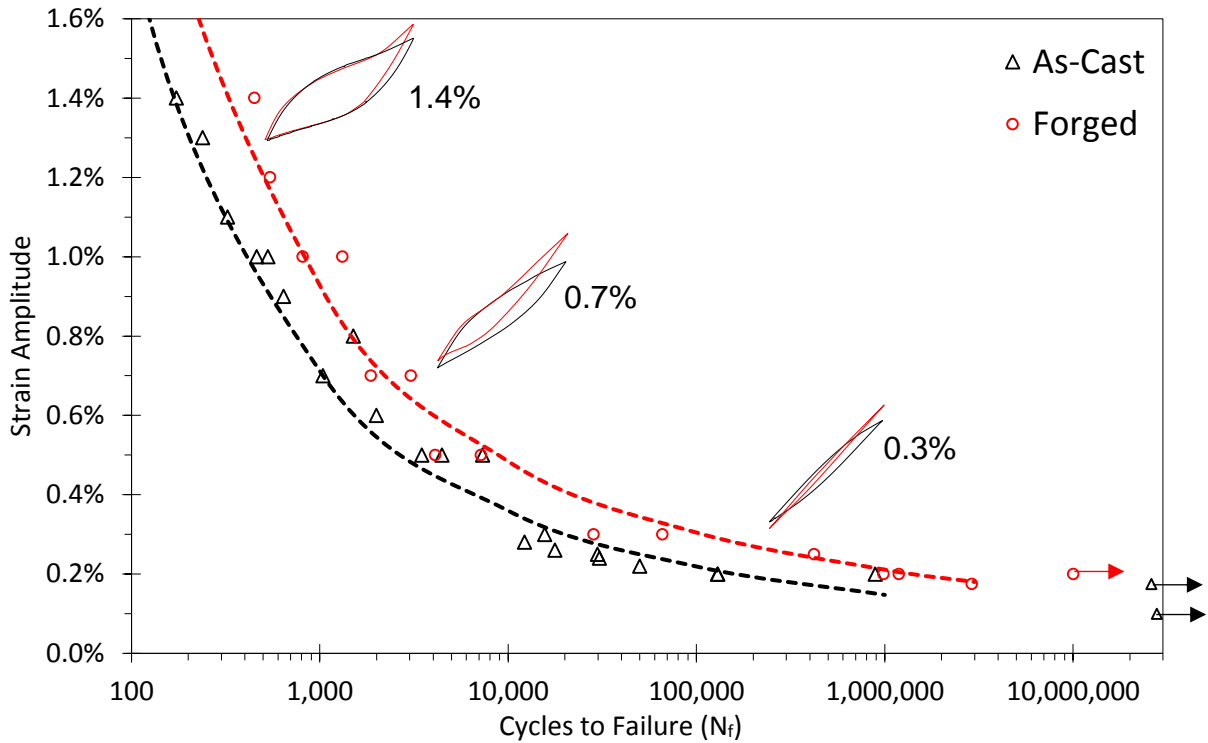


Figure 38 –  $\epsilon$ - $N$  curves for as-cast (black) and forged (red) AZ80 Mg alloy obtained at strain amplitudes between 0.1 and 1.4%

#### 4.3.4. Fracture Mechanisms

Scanning Electron Microscope images showing the macroscopic features of the fracture surface of the fatigue specimens are shown in Figure 39(a) and (c). All samples exhibited fatigue crack initiation (FCI) at the specimen surface. The as-cast material (Figure 39(a)) exhibits a fracture surface with a faceted morphology, substantial cleavage-like terraces, and widespread macroscopic striations of varying orientations. These distinct features show evidence of mixed deformation dominated by slip over a large portion of the area. The random facet orientation is indicative of varying crystal orientations associated with the randomized texture of the as-cast material. Terrace edges appear to correspond with grain boundaries, as they demark thresholds of varying macro-striation orientations. The propagation zone is also comparatively rough relative to the forged sample (Figure 39c). In contrast, the forged sample exhibited a distinct FCI with radially branching beach marks and a large propagation zone, which is much flatter and more stable than the as-cast condition. The final fracture zone is located opposite to the FCI location, indicating stable crack propagation in a direction approximately perpendicular to the initial fatigue crack propagation direction, as is typical with  $R = -1$  strain-controlled fatigue testing. Guo et al. [17] investigated the fracture behaviour of cast-homogenized AZ80 Mg alloy that was processed via multi-directional

forging. They observed that cracks initiated at the brittle  $Mg_{17}Al_{12}$  particles, and then propagated and coalesced along grain boundaries [15]. Crack initiation tends to occur at the brittle second phase particles in AZ80 Mg alloy [20][14][9]. The presence of dimpled final fracture surface morphology is the main characteristic differentiating the forged from the as-cast conditions. The depth of the dimples is an indicator of ductility, with deeper dimples occurring as a result of more plasticity. Xiong et al. [20] observed that dimple-like features were evident in the final fracture region of rolled AZ80 fatigue specimens, tested in a direction perpendicular to the c-axis (the LD orientation of fatigue samples in the forgings presented here is also orthogonal to the c-axis). This agrees well with the more ductile tensile monotonic response of the material following forging. The final fracture zone surface morphology is shown in Figure 39 (b) and (d). The as-cast material (b) shows some evidence of ductility, as well as dendrite tear-out morphology with a faceted structure. The forged sample (d) showed more evidence of ductility, including a surface morphology with pronounced dimpling, and a terrace-like structure supporting the observation of more plastic fracture behaviour.

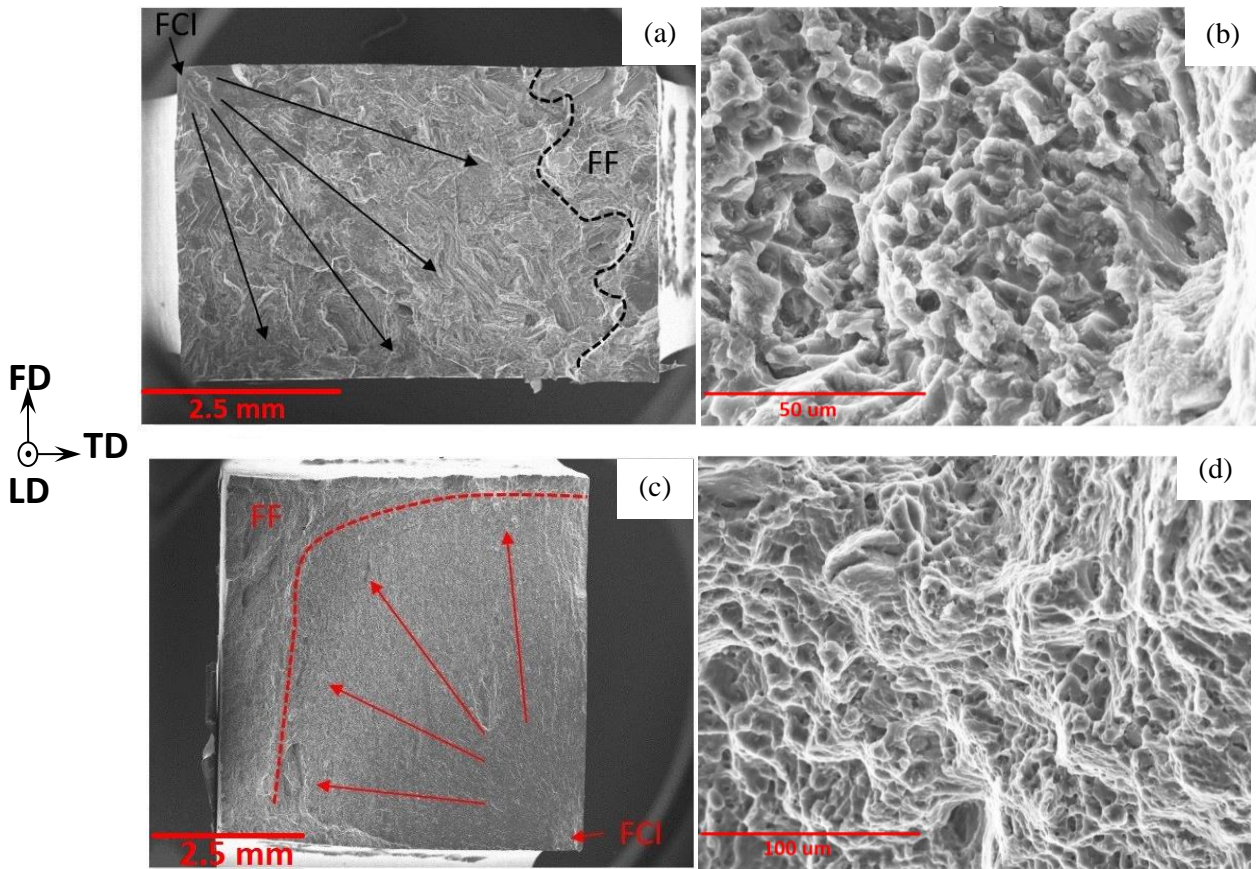


Figure 39 - Fracture surfaces of the as-cast ((a) and (b)) and forged conditions ((c) and (d)) for samples tested at a strain amplitude of  $\pm 0.3\%$ . As-cast sample fractured at 15, 644 cycles and forged sample at 66, 171 cycles. FCI denotes the fatigue crack initiation location and arrows denote the approximate propagation direction. Images (b) and (d) show a detailed view of the surface morphology in the final fracture (FF) zone.

#### 4.3.5. Fatigue Life Modelling

To quantitatively compare the damage incurred during cyclic loading in wrought Mg, numerous fatigue damage parameters, including stress, strain and energy-based parameters, have been proposed [55][53]. As exhibited in Figure 30, some forms of AZ80 may display perfectly plastic cyclic behaviour, post cyclic yield, or even cyclic softening, since within an arbitrary range of applied strain amplitudes, the stress may remain constant or may decrease. While successful attempts have been made to model fatigue life of Mg alloys using stress-based damage model (e.g., [58] for hot-rolled AZ31B), in general stress-based fatigue models are not ideal as they cannot accurately capture fatigue damage inflicted under these ranges of deformation conditions. The objective of the following is to investigate the suitability and accuracy of existing strain and energy based models at predicting the fatigue life of AZ80 as-cast and forged material. The strain-based critical plane SWT model and energy based Jahed-Varvani models are examined here.

The SWT parameter [57] was initially formulated to account for the mean stress effect during fatigue loading. Modified versions of this model have been extended for use in multiaxial life predictions of Mg alloys using a critical plane method with good success [79]. The SWT parameter is related to fatigue life in terms of four different material constants:

$$\sigma_{n,max} \frac{\Delta\varepsilon_1}{2} = \frac{\sigma'_f{}^2}{E} (2N_f)^{2n} + \sigma'_f \varepsilon'_f (2N_f)^{b+c} \quad (1)$$

The term  $\Delta\varepsilon_1$  represents the principal strain range,  $\sigma_{n,max}$  represents the maximum stress on the plane of principal strain, and E, the modulus of elasticity (in the case of Mg E=44 GPa). The Coffin-Manson constants on the right hand side of the equation were extracted from strain-controlled test results, as shown in Figure 40(a) and (b), and are summarized in Table 4. The symbols shown represent the experimental data extracted from the stabilized hysteresis loops for both the as-cast and forged material, and the dashed lines represent a fit to the elastic and plastic parts of strain. The elastic part of the strain range was calculated from  $\Delta\varepsilon^e = \Delta\sigma/E$ , and the plastic strain range was obtained from  $\Delta\varepsilon^p = \Delta\varepsilon - \Delta\varepsilon^e$ . Figure 40(c) shows the calculated SWT parameter for both the as-cast and forged material fatigue data as a function of cycles to failure. Both the as-cast and forged materials can be expressed using power-law fits, albeit with unique constants for each material. This implies that the SWT damage parameter for the forged material is higher than that of the cast material. This is expected as the maximum normal stress is higher in the tensile peak of the stabilized response in the forged material than in the cast material at an equivalent strain amplitude. Using the parameters given in Table 4, the fatigue life was predicted for both the as-cast and forged materials, and is plotted versus the experimental life in Figure 40(d). The solid diagonal line denotes a correlation match between the predicted and experimental life, and the dashed lines represent bounds that envelop deviation from this match by a factor of 2. The vast majority of life estimations fall within these

bounds of a factor of 2, with almost equal numbers of data being under and over predicted. For both the as-cast and forged materials, the LCF regime seems to be conservative in its prediction, and trends towards slightly non-conservative in the HCF regime. One of the reasons for conservative predictions in the LCF regime is that the stabilized responses are used as model inputs, and for materials that cyclically harden, the stabilized cycles are more damaging than the initial ones (as the peak stresses are higher). Since the “transient” phase of hardening is a non-negligible portion of the life for the LCF regime, a proportion of the cycles experienced by the experimental samples undergo slightly less damage than predicted, as their peak stresses are lower. This is, however, a minor discrepancy and the assumption that the stabilized response is used is widely accepted in the literature. The coefficient of determination is  $R^2 = 0.94$  for the as-cast prediction, and  $R^2 = 0.98$  for the forged material prediction.

*Table 4 - Coffin-Manson parameters for SWT model for cast and forged AZ80 Mg*

ID	$\sigma_f'$ (MPa)	b	$\epsilon_f'$	c
As-Cast	479.6	-0.141	0.2714	-0.577
Forged	598.4	-0.131	0.3395	-0.576

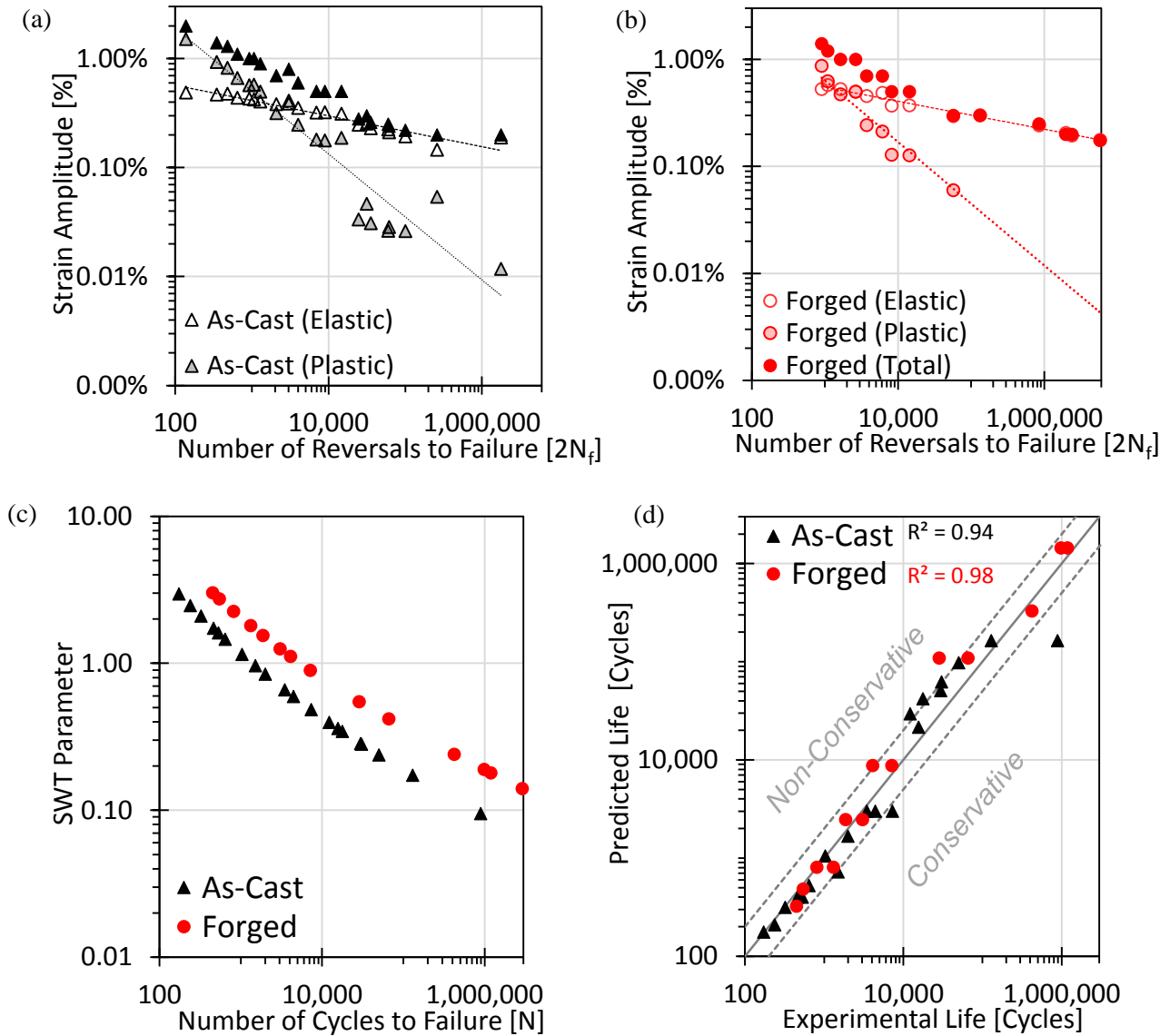


Figure 40 - Strain-life data used for extracting Coffin-Manson constants in (a) as-cast and (b) forged AZ80 Mg; (c) SWT damage parameter evolution with number of cycles to failure for both as-cast and forged AZ80 Mg; and (d) the correlation between SWT-predicted fatigue life and experimental life for both as-cast and forged AZ80 Mg

Energy-based fatigue damage models have been used by many researchers for modeling the fatigue life of Mg alloys, e.g., Park et al. [59][80] in rolled AZ31, Xiong et al. [20] for rolled AZ80, Jahed et al. [56] for many different Mg alloys and conditions, and Albinmoussa et al. [81] for AZ31 under multiaxial loading to predict the fatigue life of wrought Mg alloys. In this study, the JV model [82] is utilized. The significance of this life model is in the evaluation of the fatigue material constants from energy-life curve. In this model, the total energy density is implemented as a damage parameter and is constituted by its elastic and plastic components. The plastic component is defined as the area enveloped by the stabilized hysteresis loop and the elastic component is defined as the following equation [65]:

$$\Delta E_e^+ = \frac{\sigma_{max}^2}{2E} \quad (2)$$

where  $\sigma_{max}$  is the peak tensile stress. Adding the positive elastic strain energy density, the mean stress effect is also taken into account in this model [83] and subsequently the energy damage parameter  $\Delta E$  is related to fatigue life via an analogous equation of similar form to the Coffin-Manson equation [82][84], where  $\Delta E$  is the strain energy density:

$$\Delta E = E_e'(2N_f)^B + E_f'(2N_f)^C \quad (3)$$

Coefficient  $E_f'$  correspond to the fatigue toughness and  $E_e'$  is the fatigue strength coefficient. Exponents  $C$  and  $B$  are the fatigue toughness and fatigue strength exponents, respectively. The constants in the above equation are extracted from the strain energy density life curves presented in Figure 41 for the as-cast and forged materials, and those parameters are summarized below in Table 5. The same fatigue data extracted from the set of tests performed in this study used in the strain-based prediction results in Figure 40 are used in calculation of these energy-based model parameters. The symbols in Figure 41(a) and (b) represent this aforementioned fatigue data, and the dashed lines represent the fits to elastic and plastic portions of the energy density. Figure 41(c) shows the calculated energy damage parameter for both the as-cast and forged material fatigue data as a function of cycles to failure. Both the as-cast and forged materials can be expressed using very similar curves, as the data points almost consolidate onto one single curve. This can be attributed to the competing effect forging has on the magnitude of elastic and plastic components of the damage parameter. For a given strain amplitude, the forged material has a higher tensile peak stress causing the elastic energy to be higher, and less enveloped within the stabilized hysteresis loop area, resulting in less plastic energy. As a result, the total energy remains almost unchanged for a given life in both as-cast and forged materials.

Using the parameters in Table 5, the fatigue life was predicted for both the as-cast and forged materials, and is plotted versus the experimental life in Figure 41(d). Almost all the life estimations fall within these bounds of a factor of 2, with almost equal numbers of data being under and over predicted. The coefficient of determination is  $R^2 = 0.95$  for the as-cast prediction, and  $R^2 = 0.99$  for the forged material prediction.

Table 5 - Energy-based parameters for the Jahed-Varvani model for cast and forged AZ80 Mg

ID	$E_e'$ (MJ/m <sup>3</sup> )	$E_f'$ (MJ/m <sup>3</sup> )	$B$	$C$
Cast	3.5861	68.39	-0.309	-0.555
Forged	7.9094	758.6	-0.304	-0.836

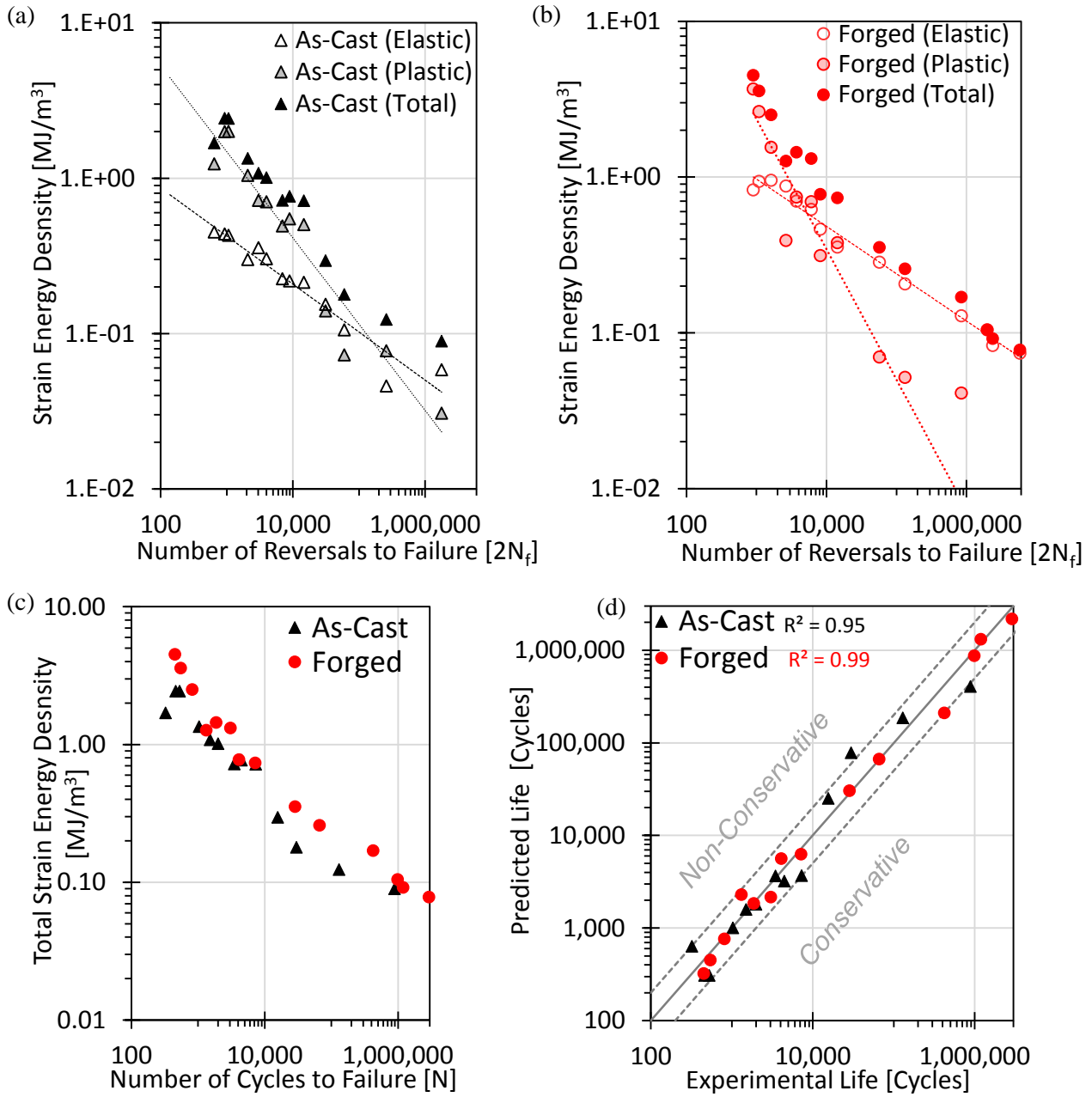


Figure 41 – Strain energy-life data used for extracting energy-based constants in (a) as-cast and (b) forged AZ80 Mg; (c) Jahed-Varvani damage parameter evolution with number of cycles to failure for both as-cast and forged AZ80 Mg; and (d) the correlation between the Jahed-Varvani predicted fatigue life and experimental life for both as-cast and forged AZ80 Mg

#### 4.4. Conclusions

Uniaxial quasi-static and fully-reversed fatigue experiments were conducted at various strain amplitudes, ranging from 0.1–1.4% of both as-cast and forged AZ80 Mg alloy. The effects of various forging parameters (temperature and deformation rate) on the quasi-static properties were investigated on a comparative basis. Based on the results the following conclusions can be drawn:

1. Microstructural analysis showed that AZ80 Mg alloy in the as-cast condition possessed a microstructure consisting of primarily  $\alpha$ -phase and aluminium-rich  $\beta$ -phase, while the forged material showed a recrystallized microstructure, with smaller, equiaxed grains. The as-cast material showed a random texture, leading to nearly symmetric properties invariant of material direction. The thermomechanical history imparted to the material via forging resulted in a texture intensification and a rotation of the crystallographic cells to align with the loading direction during forging.
2. Texture intensification due to forging results in tension-compression asymmetry in both the monotonic and cyclic responses. The forged material exhibited substantial increases in strength and ductility, especially in tension, with the benefit of compressive properties being somewhat masked by the twinning deformation mode, which requires lower stress to be activated and becomes prevalent following texture intensification. The monotonic tensile tests showed that AZ80 in the forged condition had considerably higher ultimate strength and ductility relative to the as-cast alloy. After forging of as-cast AZ80, increases in ultimate tensile strength from 234 MPa to 312 MPa in tension, and from 318 MPa to 373 MPa in compression were observed. The fracture strain increased from 8.5% to 15.8% in tension, and decreased from 15.3% to 9.6% in compression after forging.
3. The cyclic responses of AZ80 differed significantly between the as-cast and forged material. The shapes of the stabilized hysteresis loops of all the forged conditions varied from that of the as-cast material, with differences being especially marked in the tensile regime, with pronounced tensile tips and higher peak stresses, in the forged material. The unique characteristics of the cyclic response are governed by key differences in the mechanisms that control deformation. At strain amplitudes at which appreciable plasticity occurs, the as-cast material exhibits predominantly slip deformation in the upward reversal, and marginally mixed-mode in the downward reversal. In contrast, the forged material exhibits twinning in the downward reversal and detwinning, followed by slip, in the upward reversal, regardless of the forging condition. This unique characteristic of the cyclic deformation mechanism in the forged material is the primary source of the observed asymmetric response.

5. Once forged, the AZ80 Mg alloy exhibits superior fatigue properties relative to the as-cast material under strain-controlled testing over the entire strain range investigated in this study. The improvement in fatigue life as a result of forging ranges from 2 times greater in the LCF regime, to 5 times greater in the HCF regime. This improvement was observed in the forged material despite the development of significant tensile mean stress.
6. The fracture surfaces of as-cast samples were characterized by a terrace-like faceted morphology, whereas the forged conditions exhibited a more dimple-like fracture surface, indicative of greater plasticity.
7. The JV energy-based model and SWT critical plane model give reliable fatigue life predictions for as-cast and forged AZ80.

## 5. Low-cycle fatigue characterization and texture induced ratcheting behaviour of forged AZ80 Mg alloys

Following the innovative discovery level knowledge outlined in chapter 4 surrounding the characterization of forged AZ80 Mg alloy, this chapter builds upon this aforementioned foundation which has been laid. More complex facets of the material characteristics are investigated, specifically those that will illustrate themselves under a stress-controlled loading history. This spectrum of loading histories investigated were intentionally selected for this experimental campaign based on requirements from the engineering application. The service loading history was investigated and the most damaging fatigue loadcases were selected for the basis of the stress amplitude selections made here. Furthermore, as discussed in chapter 4, since pronounced asymmetry results in much higher tensile cyclic stresses in the forged alloy under a fully reversed strain controlled loading history, comparison of the  $\epsilon$ -N behaviour may not adequately contrast the differences between both base material and forging conditions. Thus stress-controlled (S-N) fatigue tests were performed to better illustrate the differences in the cyclic material characteristics between all the investigated conditions. This experimental campaign focused on comparing the cyclic behaviour of forged AZ80 Mg which was processed starting with two different base material conditions as-cast and as-extruded. Furthermore, the style of forging investigated in this chapter was intentionally made to be more complex and more multi-directional for multiple reasons. Firstly, to highlight the implications which varying the local thermomechanical history throughout the cross section of the forging has on the texture, cyclic response, and consequently the associated fatigue life. Secondly, and more pragmatically, to facilitate creation of a typical “I-beam” type cross sectional profile which is very common in structural components requiring high bending stiffness. Furthermore, since this style of forging is considered a “closed die” (i.e. implementing “flashlands” which restrict material outflow and induce internal die cavity pressure) a higher quality forging with less internal defects typically results, aligning with fulfillment of the objective of task (i) of this research work.



Figure 42 - A. Gryguć et al., “Low-cycle fatigue characterization and texture induced ratcheting behaviour of forged AZ80 Mg alloys,” *Int. J. Fatigue*, vol. 116, pp. 429–438, 2018.

Zenner et al. characterized the cyclic hysteresis in AZ80 extrusion in strain controlled fatigue testing [64]. However they demonstrated that it differed (particularly in the compressive reversal) to that of the conventional “masing” behaviour found when tested in an incremental step test (or IST where the strain amplitude is gradually increased to obtain the complete cyclic  $\sigma$ - $\epsilon$  plot from a single specimen). Practically, what masing behaviour means is that the ascending reversals of hysteresis loops obtained at different strain amplitudes are the same. I.e. the stabilized cyclic response that is found can be characterized by an inner curve (cyclic stress strain curve) and a closed outer loop (hysteresis loop). They also found that in similar Mg alloys in the AZ family, masing behaviour was only found in cast materials, not extruded (which exhibited cyclic hysteresis which varied significantly in the compressive reversal from that  $\sigma$ - $\epsilon$  curve obtained via IST). They attribute this lack of masing behaviour in the extruded Mg alloys to pronounced anisotropy in the material behaviour of the wrought alloys. However they do not explicitly mention that they expect pronounced asymmetry in the extruded alloys, and that this link between texture, asymmetry and material behaviour has not been adequately explained in their work.

This knowledge gap highlighted by Zenner et al. invites a valuable opportunity for future work and key contributions which are addressed here in the journal article outlined in Chapter 5 of this thesis. The phenomenon of ratcheting can practically be described as the shifting (or *evolution*) of the stress-strain hysteresis loop along the strain axis [85]. In the context of this thesis, the term “ratcheting” refers to “strain ratcheting” (not *creep* ratcheting), and denotes the evolution of mean strain under an imposed stress controlled loading history. Conventionally, ratcheting is most pronounced under a positive mean stress ( $R_L > -1$ ) however in the experimental campaign discussed here, significant ratcheting was observed even under fully reversed loading ( $R_L = -1$ ). The link between the ratcheting behaviour of the material and its texture is discussed. Under cyclic stress controlled loading, AZ80 Mg exhibits ratcheting behaviour to varying degrees which are dependent primarily on the texture intensity and the material's propensity to twin in either the tensile or compressive reversals. Another key contribution here is that the material behaviour of forged AZ80 Mg is a function of the loading history, such that the directionality of the initial yielding has an effect upon the subsequent material response. These two contributions are built upon the foundation of Zenners work, incorporating both loading history and material texture as fundamental links between the structure/property relationship and resulting material behaviour. These key contributions align very well to satisfy the research objectives 1 thru 4 for uniaxial stress controlled loading paths.

The following journal article published in the International Journal of Fatigue (July 2, 2018) has been presented exactly as published, with the exception of modifications made for harmonizing references, table and figure numbers to integrate into this larger thesis document. A version of this work was also

presented at the International Conference on Structural Integrity and Durability (ICSID) in Dubrovnik, Croatia in August of 2017.

### 5.1. Introduction

There has been a strong motivation to increase fuel efficiency and decrease emissions in the automotive industry over the past several decades. Implementation of lightweight materials in structural applications are at the forefront of this effort, as this strategy can improve vehicle efficiency, longevity, and performance. Magnesium (Mg) and its alloys have significant promise in this area, with widespread applicability in fatigue-critical components, such as suspension control arms, since they are the lightest commercially available structural metal and their cyclic properties are similar to those of the heavier, more conventional materials used in industry [65]. The focus of the present study is to examine the effect that closed die forging has on the monotonic, stress controlled cyclic behaviour and texture induced ratcheting of AZ80 Mg.

Although there has been some limited work done on the fatigue behaviour of the AZ family of Mg alloys [27], [59], [64], [86]–[91] virtually all of it is focused on cast, extruded or rolled varieties and not material processed by means of warm forging. Alongside this, many researchers have focused on the high temperature deformation behaviour of forged AZ80 [5], [10], [11], [17]–[19], [22], [24], [28], [29], [31], [32], [36]–[41] however little to no work had been done in the past on the characterization of forged Mg alloys. More recently, extensive work has been done thus far on the pioneering of characterizing forged Mg [69], [92]–[97] especially its fatigue behaviour. He et al. [98] explored the influence of the initial billet as well as die geometry (open-die vs. semi-closed) for a large AZ80 Mg component forged at 380°C. They found that with an open-die configuration over 32% of the final forging had an effective strain of less than 0.5 with large spatial variation in the strain indicating that a considerable part of the final component had not been sufficiently deformed to achieve the full benefit in material properties. However when utilizing a semi-closed die for the same forging only 3% of the final component had an effective strain of less than 0.5 indicating that virtually all of the forging had been evenly and sufficiently deformed. Furthermore, they stated that the semi-closed die forgings had an even and refined microstructure with virtually no material anisotropy in tensile properties between the longitudinal and transverse directions within the forging. Wang et al. [99] investigated the microstructure and mechanical properties of cast-homogenized AZ80 that was open-die forged at 8 mm/sec at temperatures ranging from 200–400°C and equivalent strains of 80–265%. They found that with increasing levels of equivalent strain the forged material exhibited higher tensile strengths and ductility, while the more ductile properties favoring higher forging temperatures. They also found that the maximum tensile strength was achieved when forged at 250°C at a maximum induced strain of 265%. Previous work by Gryguc et al. [95] investigated the monotonic and cyclic behaviour of as cast and cast-forged AZ80 Mg in a simple open die configuration at 350°C and 450°C forging temperatures and rates ranging from 0.6 – 6 mm/sec. It was found that the mechanical properties are much more sensitive to

forging temperature than forging rate and that even with an open die configuration the final component had been sufficiently deformed to have almost fully recrystallized and not exhibit any similarities to the base materials cast-dendritic microstructure. Furthermore, it was found that once forged, the material developed appreciable texture which was very different from that of the randomized as-cast materials texture, and this texture development influenced the mechanical response in both static and fatigue testing.

In this study, the effect of base material condition on the tensile/fatigue behaviour of AZ80 was examined in detail in a closed die forging with highly three-dimensional material flow. Furthermore, the spatial variation of mechanical properties throughout the forging was investigated and a texture and microstructural link to these properties were established. Furthermore, a correlation between the materials local texture and the mean strain development in the cyclic response is discussed. Results from a fully-reversed stress-controlled fatigue test in the low-cycle regime are presented. Energy-based fatigue models were used predict the fatigue life of cast, extruded, cast-forged and extruded-forged AZ80 Mg, and their accuracy was also examined.

## 5.2. Experimental

The material used in this investigation was commercially-available AZ80 Mg alloy in the forms of cast and extrusion ( $8.0 \pm 0.2\%$  aluminum content, with other elements composition as per ASTM B91-12 standard). The material was received from Magnesium Elektron North America Inc. in the form of as-cast and extruded billets in the as-fabricated condition. The dimension of the as-cast billet are 300 mm in diameter and a length of 500 mm, while the extruded billet was a diameter of 63.5 mm and a length of 1000 mm. The forging of the as-cast and extruded material was conducted at CanmetMATERIALS (Hamilton, Canada) using the billets having dimension of  $\varnothing$  63.5 mm, 65-mm long. The as-cast billets were machined from the 300-mm diameter AZ80 casting, and the as-extruded billets were simply cut to length prior to forging. All forgings were carried out on a 500-ton hydraulic press with a profiled upper and lower die with an I-beam shaped internal cavity. A typical forged part produced by these dies is shown in Figure 43. The billet and tooling were heated separately to 375°C for sufficient time to allow any thermal gradients to decay. The orientation of the billet to the press was such that the radial direction was along the direction of the press stroke (i.e. the direction of forging was parallel to the radial direction of the billet). Forging was carried out in a single step at a displacement rate of 20 mm/sec. Figure 43 illustrates a forgings conducted at 375°C and 20 mm/sec. The forging direction (FD) is normal to the web face, with the longitudinal direction (LD) being parallel to the axis of the flanges and transverse direction (TD) being perpendicular to flange axis. In the image (b) a red rectangle denotes the interface between the forged component and the flash region. Everything internal to the denoted rectangle is considered a part of the forging and everything external is considered “flash” or scrap material.

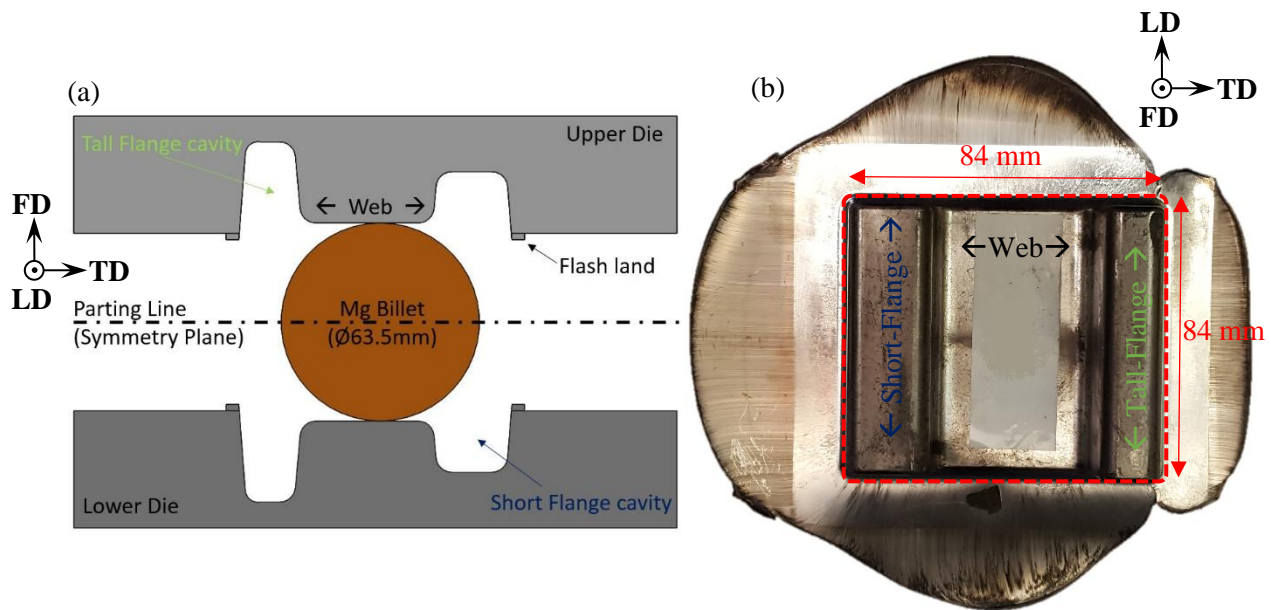


Figure 43 – (a) schematic of AZ80 Mg closed die forgings with asymmetric I-beam cross section conducted at (b) 375°C and 20 mm/sec ram speed prior to trimming off the flash extruded then forged.

The metallographic samples were prepared following the standard metallographic techniques outlined in ASTM E3-11 with acetic-picral etchant similar to that used by Roostaei et al. [61]. The microstructure was observed using a light optical microscope (LOM) and a scanning electron microscope (SEM), coupled with energy-dispersive X-ray spectroscopy (EDS). The average grain intercept method is used to quantify the grain size according to ASTM E112-12.

The texture measurements were performed on polished samples using a Bruker D8-Discover equipped with a VANTEC-500 area detector, with a radius of 135 mm and using Cu-K $\alpha$  radiation at 40kV and 40 mA. During the measurement, the incident beam and the detector were placed at a fixed  $2\theta$  angle of  $40^\circ$ . The collimator size was 1.0 mm. The sample was mounted on the motorized stage, which was oscillated at an amplitude of 1.5 and 2.5 mm, and a speed of  $3.5 \text{ mm s}^{-1}$  and  $5.5 \text{ mm s}^{-1}$  for the X and Y axis, respectively. The samples were tilted between 0 and  $75^\circ$ , with a step of  $15^\circ$  considered as the  $\Psi$ -scan, while the sample rotation, known as  $\Phi$ -scan, was between 0 and  $360^\circ$ , with a step size of  $5^\circ$ . The sample was scanned for 20 s at each orientation. The Debye–Scherrer diffraction rings were collected using the area detector in a 2-D diffraction image. Then, the incomplete pole figures for the  $\{0002\}$ ,  $\{10\bar{1}0\}$ ,  $\{10\bar{1}1\}$ , and  $\{1\bar{1}02\}$  planes were extracted from the diffraction rings. The complete pole figures were then calculated using the DIFFRAC.Suite: Texture software.

Tensile test samples with geometries according to Roostaei et al. [61] and a 4 mm thickness were extracted from the as-received billet and closed die forged samples. The as-cast samples were extracted from a location within the billet where the middle of the gauge section was at 70% of the billets radius. The extruded samples were machined along the extrusion direction and from a location where the middle of the

gauge section was at 50% of the billets radius. There were 15 test samples that were extracted from 15 different locations throughout the closed die forging (all having their axis parallel with the LD direction), as shown in Figure 44 (d). These samples were later utilized for quasi-static and cyclic testing. The quasi-static tensile tests were performed according to ASTM standard E8/E8M-15a using an MTS 810 Servo-Hydraulic test machine operating in displacement control mode with a displacement rate of 1 mm/min. Strain measurement was accomplished using a GOM ARAMIS 3D 5MP DIC system. The average strain rate within the gauge section of measurement was  $1.4E-3 \text{ sec}^{-1}$ .

The fatigue tests were performed as per ASTM E466-15 in an ambient environment using an MTS 810 Servo-Hydraulic test machine operating in stress control mode at a frequency range of 0.1 Hz to 30 Hz depending on the stress amplitude to maintain an approximately consistent loading rate between all tests. The strain was measured throughout the first 10,000 cycles using an MTS 632.26 extensometer with an 8-mm gauge and travel of  $\pm 1.2$ -mm until stabilization of the cyclic hysteresis loop was achieved. The tests were conducted at a zero mean stress (i.e.,  $R_L = -1$ , fully reversed stress cycle) and stress amplitudes of between 140 MPa and 190 MPa. The failure criteria for the tests were considered to be final rupture of the specimen gauge section. The fracture surfaces after tensile and fatigue tests were examined using SEM techniques (FEI Quanta FEG 250 ESEM with EDX).

## 5.3. Results & Discussion

### 5.3.1. Microstructure and Texture

Table 6 highlights the relationship between microstructural, monotonic and cyclic properties of as-received (as-cast and as extruded) and forged (CF: Cast Forged and EF: Extruded Forged) AZ80. The conditions for forging were the same for both CF and EF at a forging temperature of 375°C and 20 mm/sec of ram speed. The grain size is quite uniform throughout various locations of the as-received billets; however, there is notable spatial variation in the microstructure throughout the cross-section of the forgings. As such, the grain size and tensile properties are presented at two different locations within the forging, location 1 which is considered to be the top of the tall flange region of the forging and location 8 which is considered the web region which connects the two flanges. Although beyond the scope of this study, 3D forging simulation revealed that in the final step of forging, the web region was the location that incurred the most amount of equivalent plastic strain, decaying as moving up the height of the flanges [100]. This is due to the complex material flow, which is expected, in a closed die forging of this cross section as well as the fact that the web region has the most amount of height compression relative to the initial billet diameter. Gryguc et al. [95] characterized the microstructure of as-cast AZ80 to consist of primarily  $\alpha$ -phase, in which aluminium-rich  $\beta$ -phase ( $\text{Mg}_{17}\text{Al}_{12}$ ) is precipitated along the grain boundaries. This agrees with the microstructure of as-cast AZ80 observed by Nový et al. [12], the grain morphology of which was very

similar to that which is presented in this study, while the average grain size (80–140  $\mu\text{m}$ ) was slightly more refined than that observed in this study. Finally, the Rockwell hardness presented in Table 6 is an average across the entire cross-section of the forging, however, as one might expect it also spatially varies to a moderate degree as shown by the contour plots in figures Figure 44 (d) and Figure 45 (d). In these contour plots, areas in red represent the regions with the highest superficial hardness, and it can be seen that the web region (location 8-10) shows the highest indicated hardness in the cast-forged material. In the extruded-forged material, the spatial variation of hardness is much lower, and the selected scale exaggerates any non-uniformities, however it can be observed that the lowest hardness is consistently seen at the top and bottom corners of each flange. Figure 44 shows a summary of the microstructure, texture and superficial hardness variation for the cast-forged I-beam forging with Figure 44 (a) (b) and (f) show the XRD pole figures for the basal and prismatic planes for 3 different locations within the forging (the tall flange (Location 1), short flange (Location 15) and web (Location 8)). Furthermore, Figure 44 (c) and (e) illustrate the microstructure for two locations in the forging, the tall flange, and web, respectively. It can be observed that the basal pole figure shows somewhat of a randomized pattern in both of the flange locations, however in the web region evidence of a less random and more intense texture can be observed by the pattern in the basal pole figure in Figure 44 (f). This somewhat randomized texture, which remains from the parent as-cast material, can be attributed to non-fully recrystallized grain structure in certain regions of the forging as can be seen in both LOM images (c and e) where a somewhat coarse grain structure is still evident with little evidence of partial dynamic recrystallization (DRX) as noted in Figure 44 (c) and (e).

Table 6- The relationship between microstructural, superficial hardness, and monotonic properties of as-cast, as-extruded and cast-forged (CF) and extruded-forged (EF) AZ80 Mg alloy. Tensile properties are presented first, followed by compressive properties in parenthesis, where available.

Material	Rate (mm/min)	Temp (°C)	Location in Billet	Grain size ( $\mu\text{m}$ )	HR-30T	$\sigma_{\text{YS}}$ (MPa)	$\epsilon_{\text{Fail}}$ (%)	$\sigma_{\text{ULT}}$ (MPa)
As-Cast	-	-	70% of radius	178.9 $\pm$ 67	27.2	92.8 (93.8)	7.4 (15.3)	220.9 (318.2)
As-Ext	-		50% of radius	18.0 $\pm$ 0.7	35.4	195.4	11.3	341.1 (412.1)
CF	20	375	Tall flange #1	37.7 $\pm$ 5.3	19.9	110.7	7.2	239.8
			Web #8	23.2 $\pm$ 3.9	26.9	175.0	14.1	312.1
EF			Tall flange #1	17.5 $\pm$ 1.6	30.5	226.8	17.5	351.1
			Web #8	15.2 $\pm$ 1.0	32.1	219.2	20.5	341.3

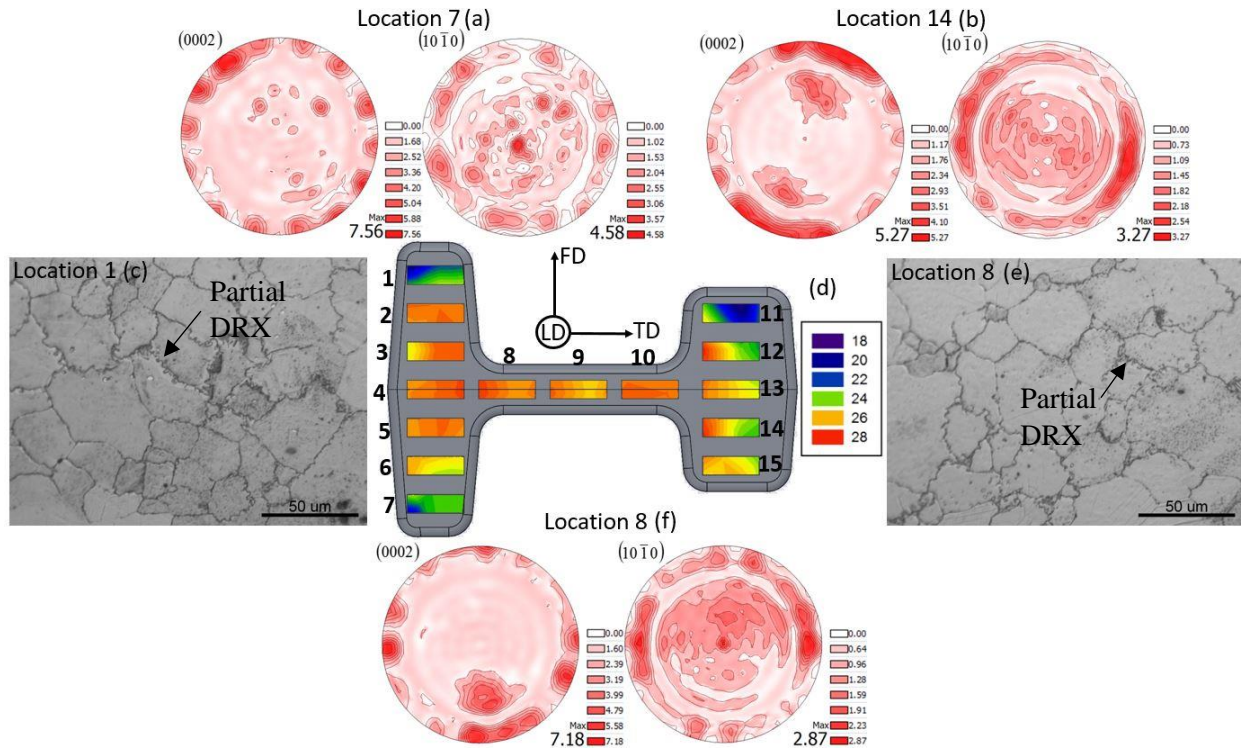


Figure 44 – Microstructural characterization of Cast AZ80 forged at 375°C and 20 mm/sec. Basal and prismatic pole figures are presented in locations 7 (a), location 15 (b), and location 8 (f) of the forging. Figure (c) and (e) show LOM images of locations 1 and 8, respectively within the forging (view in the longitudinal direction). Figure (d) denotes the spatial variation of superficial hardness (30T) in the direction normal to the cross-section of the forging. FD denotes forging direction, TD: transverse direction, and LD: longitudinal direction.

Figure 45 presents the same type of information in an identical format to that of Figure 44 however for the extruded and forged component. It is well known that AZ80 Mg has significant texture when processed by method of extrusion [94], and that forging reorients the texture in such a way that the c-axes of the HCP crystal structure are parallel with the local forging direction [55], [68], [69], [93]–[95]. Thus, it can be expected that not only will the extruded-forged component have an intense texture, but this texture will vary throughout the cross-section of the forging and be a function of the local forging direction and the complex three-dimensional material flow. This expectation is supported by the basal and prismatic pole figures presented in Figure 45 (a) (b) and (f), with relative intensities that are much higher than those of the cast-forged variety and spatially varying intensity peaks that align themselves to the local forging direction. Finally, the microstructural images in Figure 45 (c) and (e) show a much more refined microstructure relative to that of the cast-forged I-beam with the web region (location 8) having more refined structure (compared to location 1), which supports the fact that this region of the forging had the higher superficial hardness Figure 45 (d) and ductility as shown in Table 6.

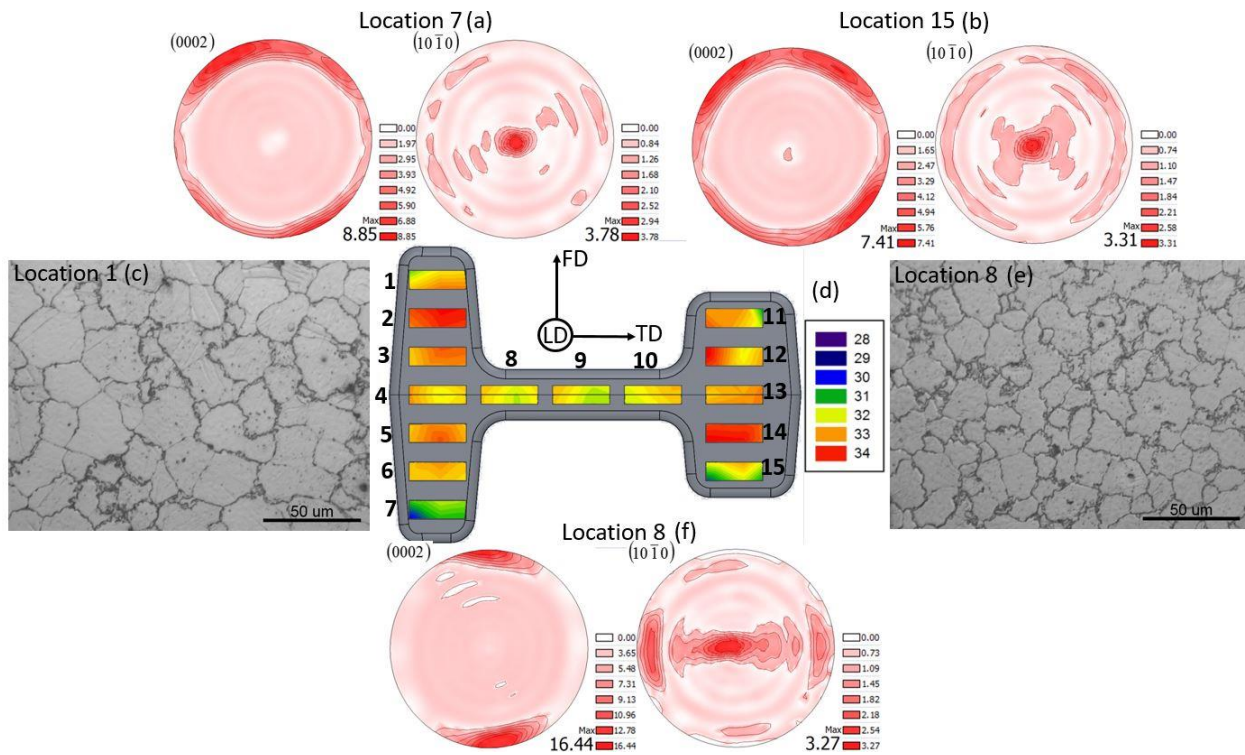


Figure 45 - Microstructural characterization of AZ80 extrusion forged at 375°C and 20 mm/sec. Basal and prismatic pole figures are presented in locations 7 (a), location 15 (b) and location 8 (f) of the forging. Figure (c) and (e) show LOM images of locations 1 and 8, respectively within the forging (view in the longitudinal direction). Figure (d) denotes the spatial variation of superficial hardness (30T) in the direction normal to the cross-section of the forging. FD denotes forging direction, TD: transverse direction, and LD: longitudinal direction.

### 5.3.2. Monotonic and Cyclic

Figure 46 shows the engineering stress vs. engineering strain tensile monotonic response for the as received and forged materials at two different locations within the forging. It can be observed that in both the CF and EF forgings, the web region has the highest ductility. Furthermore, the EF material has higher strength and ductility relative to the CF material, and a large increase in ductility once forged is apparent relative to the parent as-extruded material. The qualitative correlation can be made that in regions with higher equivalent strain imposed by forging (such as in the web region) possess a higher superficial hardness and superior strength and ductility to other regions of the forging, especially in the cast-forged material. For the extruded forged material, the yield and ultimate strength are fairly similar to the parent material, however, the ductility is much improved. Future work in this study is concentrating on lower temperature forgings, and it is expected that at temperatures ranging from 250-275°C a significant increase in strength can be achieved relative to the parent as-extruded material.

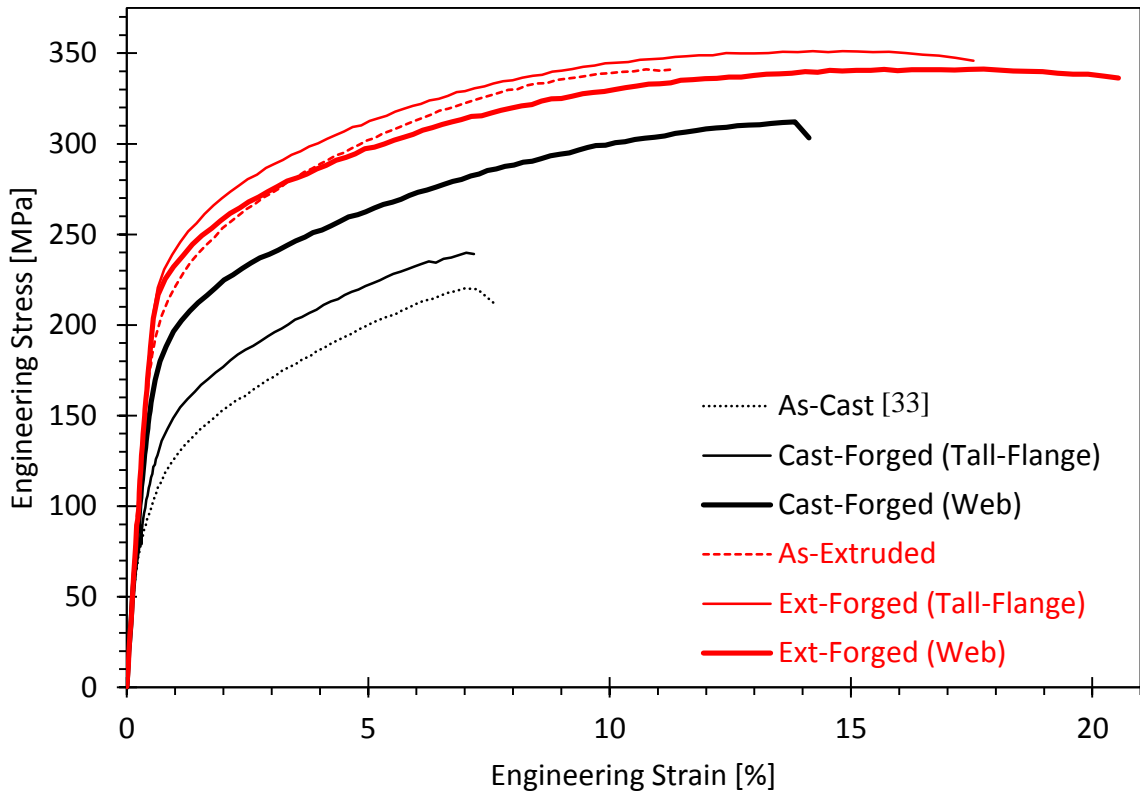


Figure 46 - Tensile monotonic engineering stress-strain curves for as-received materials as well as cast-forged and extruded forged conditions in two different locations within the forging. The tall-flange corresponds with location 1 and the web corresponds to location 8.

Figure 47 illustrates the cyclic stress-strain hysteresis response for the as-cast and cast-forged materials obtained during fully reversed ( $R_L = -1$ ) stress controlled testing at a stress amplitude of 190 MPa. The first cycle (reversals 2 and 3) is shown as symbols whereas the stabilized cycle is shown as solid lines. Figure 48 illustrates the same information for as-extruded and extruded-forged materials. For the CF and EF materials the locations within each forging where the cyclic response is presented is denoted in each caption. It can be observed that in the as-cast material the first cycle is characterized by a very large amount of plastic strain energy (or area enveloped by the hysteresis loop) and a large evolution in mean strain over the course of the first cycle (as can be seen by the disjointed tensile peaks for the first cycle hysteresis loop). This response can be attributed to the weak extension twinning in first tensile reversal which results in over 4% strain at 190 MPa. Although the as-cast material possesses a random texture, the weak twinning is caused by some proportion of grains being favorably oriented for extension twinning during the first reversal. Then, in the 2<sup>nd</sup> and 3<sup>rd</sup> reversals, the strain amplitude decreases as the material has already begun to accumulate both twin and dislocation density and cyclically harden. The twin density is not only a function of a number of cycles, it is also a function of the state of stress within each

cycle as the twinning process is not fully reversible resulting in residual twin accumulation [95], [101]. Thus, the positive mean strain begins to decrease cycle by cycle as the material hardens, this eventually leading to the stabilized response where the hysteresis loop is symmetric in compression and tension and exhibits ~0.5% of tensile mean strain. Important to note is the shape of both the ascending and descending reversals in the as-cast material is only slightly sigmoidal as the twinning and detwinning process are diffuse, and only occur to grains which possess favourable orientation within the materials randomized texture. The cast-forged material, however, exhibits a response with much fewer plastic strain energy, due to the fact that the strain required to achieve 190 MPa in tension is much lower in the cast-forged material as can be observed in Figure 46. Furthermore, as presented in previous studies [95], there is pronounced yield asymmetry in the cast-forged AZ80, more specifically the compressive yield is lower than the tensile, which manifests itself as a large strain range required to achieve 190 MPa in compression in the 2<sup>nd</sup> reversal. This results in a significant compressive mean strain in first cycle which continues as the material cyclically hardens to the stabilized response of the cast-forged material.) It can be seen in the cast-forged materials downward reversal of the first cycle that the reverse yielding is very sharp indicative of prominent compressive twinning due to the intense texture and associated large proportion of grains with a favourable orientation for extension twinning in compression. This sharp reverse yielding is characteristic of a large proportion of grains which twin to accommodate the deformation, Following this, a very sigmoidal ascending reversal occurs due to the vigorous detwinning which occurs [95]. As the cast-forged material cyclically hardens the plastic strain energy decreases as can be observed by the comparatively lower enveloped area by the stabilized hysteresis loop.

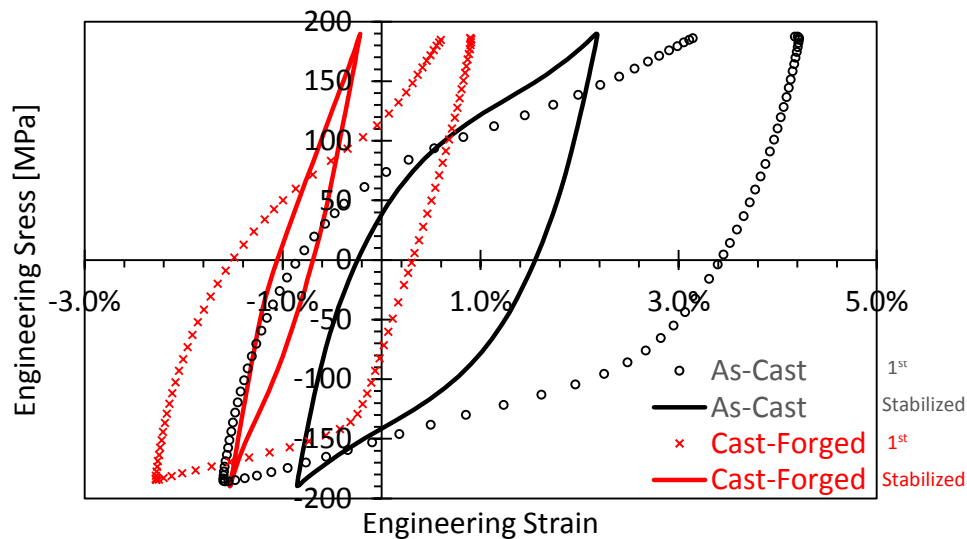


Figure 47 - The axial cyclic behaviour of as-cast and cast-forged AZ80 at a fully reversed stress amplitude of 190 MPa. Forged samples were taken from location 3 in tall-rib

Figure 48 depicts the hysteresis loops for the first cycle and the stabilized cycle for the extruded and extruded-forged material for a stress amplitude of 190 MPa. Due to the higher strengths of the extruded and EF materials (relative to the as-cast and CF varieties), in general, the plastic strain energy is always less for an equivalent stress amplitude. Both the as-extruded and EF materials display a similar first cycle response to that of the CF material, characterized by a very sharp reverse yielding due to extension twinning in compression followed by a vigorous detwinning process in the ascending reversal. Here the EF material has a much more pronounced reverse yielding in the descending reversal (relative to the extruded response). As the hysteresis loop presented here is for a sample taken from a web location, which possesses very intense texture. This intense texture is due to a dominant local forging direction with the vast majority of grains having a high propensity to exhibit extension twinning in compression due to their c-axis orientation being normal to the direction of loading. Important to note is the fact that the material with random texture (as-cast AZ80) has a positive mean strain with a very dynamic mean strain evolution whereas a material with appreciable texture (CF, as-extruded, and EF AZ80) has a negative mean strain.

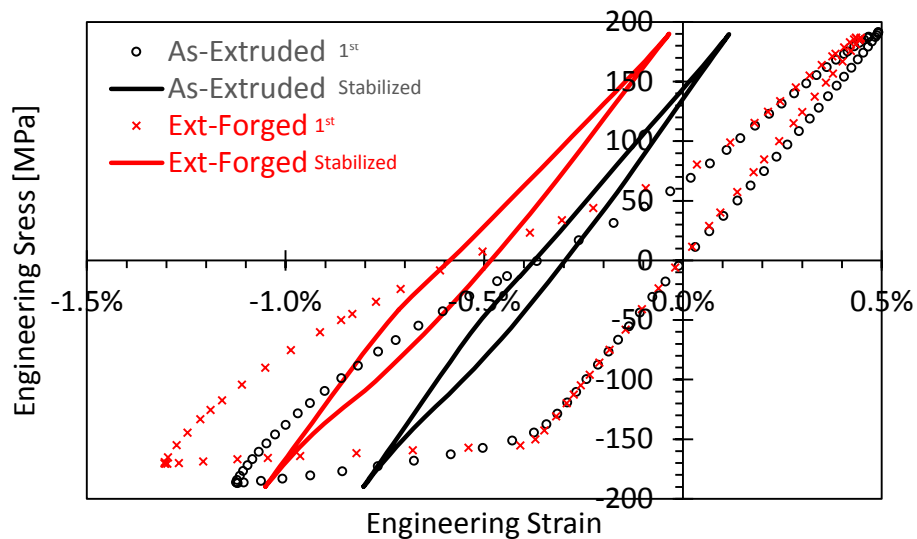


Figure 48 – The axial cyclic behaviour of as-extruded and extruded-forged AZ80 at a fully reversed stress amplitude of 180 MPa. Forged samples were taken from location 10 in the web.

Figure 49 illustrates the evolution of mean strain amplitude over the course of the cyclic testing. It can be seen that material with random texture (as-cast) will have diffuse extension twinning in the first reversal resulting in a large positive mean strain amplitude which decays as the material cyclically strain hardens. In contrast to this, all materials which possess appreciable texture (which have the c-axis oriented in a direction which is normal to the loading direction, such as the CF, extruded and EF samples), do not twin in the first reversal (as it is suppressed due to unfavourable grain orientation). That is, until the second

cycle where they twin aggressively, resulting in a negative mean strain being developed. Since this detwinning process is more reversible in the significantly textured materials [101], the evolution of the mean strain is not as dynamic as the as-cast material despite the fact that they also cyclically strain harden. Important to note that the phenomenon of ratcheting (or accumulation of mean strain with accumulated cycles) is a direct artifact of the nature of as-cast Mg (or more generally, many randomized texture Mg alloys) to exhibit kinematic hardening during stress controlled cyclic testing. This ratcheting behaviour results in a dynamic evolution of mean strain where the hysteresis loop evolves in such a way that the mean strain changes with accumulated cycles.

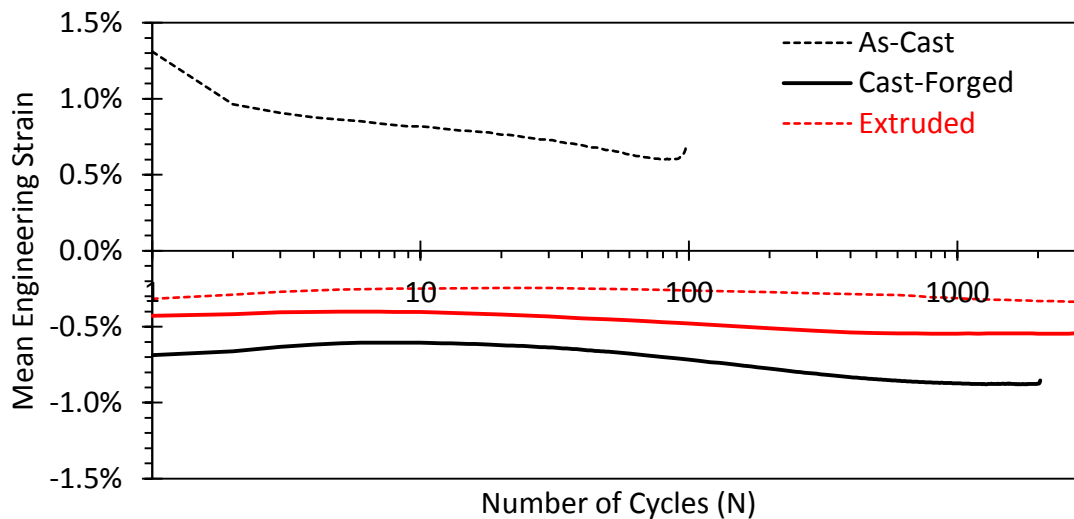


Figure 49 – Mean engineering strain response during stress-controlled cyclic testing for both as-received material as well as cast-forged and extruded-forged. Cast-forged response is shown for location 3 and extruded-forged for location number 10 within the web.

### 5.3.3. Fatigue Life

S-N data for all four material conditions have been presented in Figure 50. Axial strain was recorded only during a subset of all of these tests in order to capture the cyclic response and to gather the necessary data to check the applicability of existing energy-based life prediction models. It can be seen that there is a large improvement in the as-received materials fatigue performance once forged, with a larger improvement coming in the low-cycle regime for the CF material (as there is a large improvement in strength once the coarse cast microstructure is refined via forging). Contrasting to this, the significant improvement in fatigue performance is seen in the high-cycle regime for the EF material (as the ductility of the materials improves dramatically once forged). For LCF fatigue, the role that the elevated yield strength of the cast-forged material is the dominant factor in the improvement in fatigue performance relative to the as-cast material. However, for the mid-cycle fatigue and HCF, the response is virtually purely elastic and the effects of defect driven fatigue failures become more significant. In general, the extruded and extruded-forged materials have superior fatigue performance to the cast and cast-forged varieties which is to be expected.

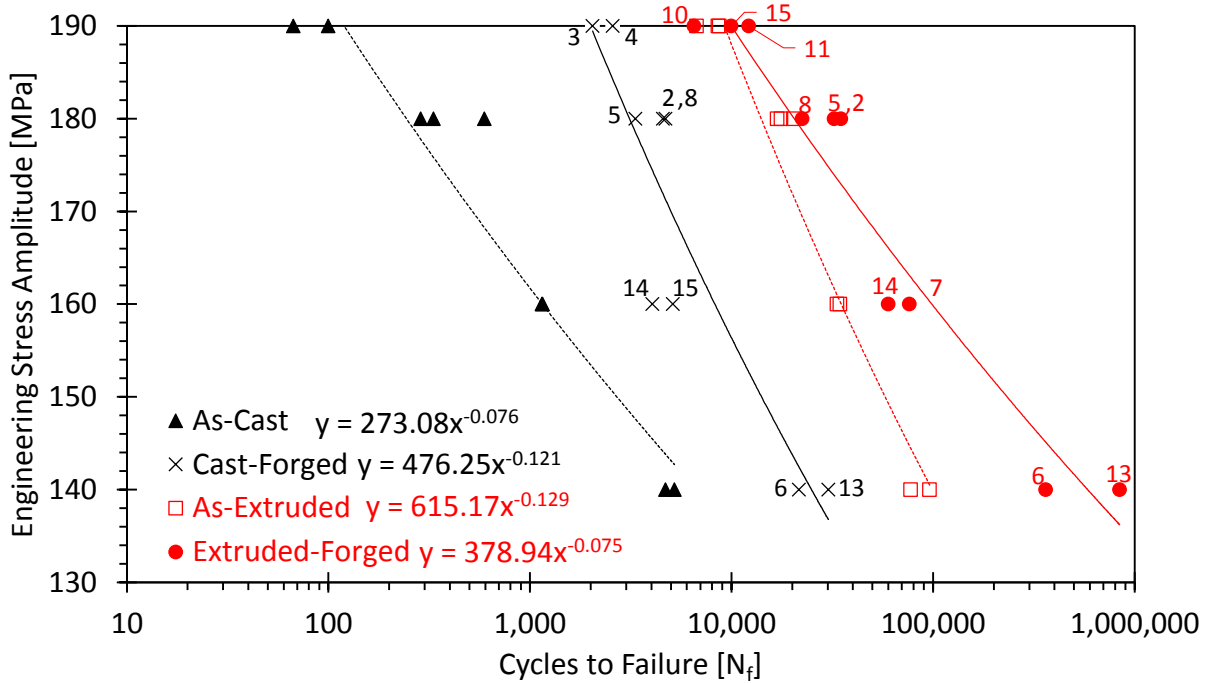


Figure 50 - S-N curves for as-cast and cast-forged (black) as well as as-extruded and extruded-forged (red) AZ80 Mg. Samples were taken from a variety of different locations throughout forging, location within forged billet denoted next to datapoint.

### 5.3.4. Fracture Mechanisms

Figure 51 illustrates the fracture surface for the cast-forged and extruded-forged material. Both surfaces are from samples at stress amplitudes of 190 MPa, which fractured at 2403 cycles and 6517 cycles respectively. The cast-forged surface is from a sample extracted from location 3 in the forged billet and the extruded forged was extracted from location 10 since both these locations have a comparable superficial hardness as indicated by previous Figure 44d and Figure 45d. The cast-forged surface, Figure 51 (a)(c)(e) exhibits multiple fatigue crack initiations (FCI's) primarily from the surface or just beneath as well as a number of large secondary cracks which progress to the interior of the sample similar to that found by Chen et al. [102]. In contrast to this, the extruded-forged fracture surface, Figure 51 (b)(d)(f), exhibits only one prominent FCI again originating virtually at the surface with no major secondary cracks. Based on EDX analysis of the FCI site, it can be determined that the cast-forged sample had several of its cracks initiate at brittle  $\beta$ -Mg<sub>17</sub>Al<sub>12</sub> intergranular precipitates which were located at the surface and could be either granular or lamellar in their morphology similar to those found in other investigations [99], [103]–[105]. The granular shape of the  $\beta$ -phase agrees well with observations made by Wang et al. [99] who found the divorced eutectic  $\beta$ -phase to be distributed along the  $\alpha$ -phase grain boundaries in the as-cast state, but following hot compression, this eutectic network was broken up into both granular and lamellar shapes. In contrast to this, the single FCI in the extruded-forged condition had a few particles of Al<sub>8</sub>Mn<sub>5</sub> compound that were located about 40  $\mu$ m subsurface. Matrix debonding from these brittle particles appears to be the

cause of crack initiation based on its proximity to the FCI and the intergranular faceted morphology of the fracture surface surrounding these granular particles emphasizing the brittle nature of that particular matrix/particle interface. Cai et al. [106] highlight the presence of this brittle compound distributed in the grain interiors and boundaries of extruded AZ80, and the microstructure of their extruded material is very similar to that which was investigated in this study.

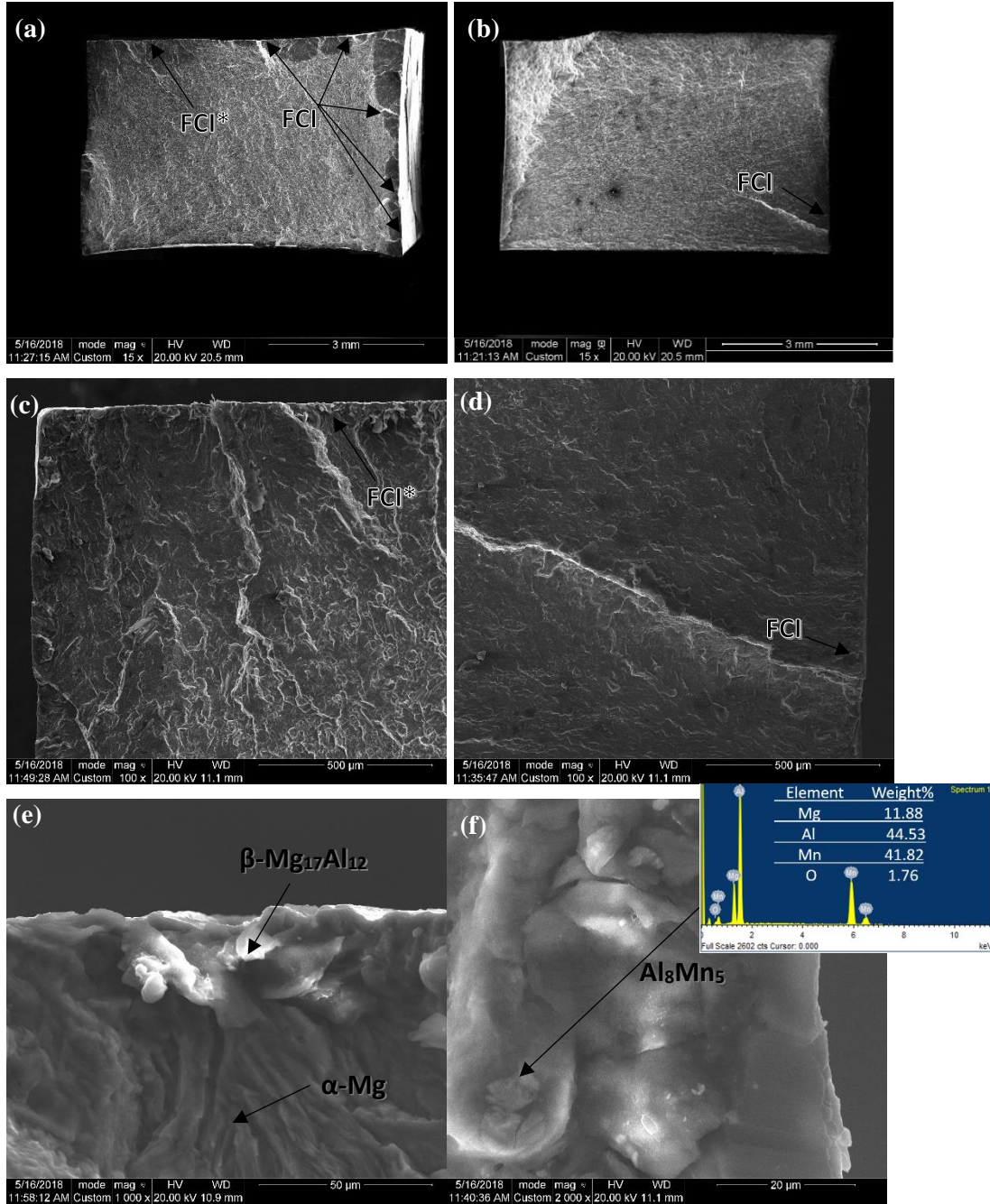


Figure 51 – Final fracture surfaces of the (a) cast-forged (b) and extruded-forged conditions for samples tested under stress control at 190 MPa. (a)(c)(e) are a cast-forged sample (b)(d)(f) are an extruded forged sample. FCI denotes fatigue crack location.

### 5.3.5. Fatigue Life Modelling

To quantitatively compare the damage incurred during cyclic loading in wrought Mg, numerous fatigue damage parameters, including stress-, strain-, and energy-based parameters have been proposed [53], [55]. Depending on the form of AZ80 being investigated the material response may vary between vigorous cyclic hardening [20], or even cyclic softening [7]. While successful attempts have been made to the model fatigue life of Mg alloys using stress-based damage model (e.g., [58] for hot-rolled AZ31B), in general, stress-based fatigue models are not ideal as they cannot accurately capture fatigue damage inflicted under these cyclic loading conditions. The objective of the following study is to investigate the suitability and accuracy of existing energy-based models at predicting the fatigue life of as-received and forged AZ80 material. The required material constants (model input parameters) were generated for each material condition according to the approach utilized in previous works [56], [107]. The energy-based two parameter model similar to Ellyin et al. [108] and Jahed-Varvani model [82] is examined here.

Energy-based fatigue damage models have been used by many researchers for modeling the fatigue life of Mg alloys, e.g., Park et al. [59], [80] in rolled AZ31, Xiong et al. [20] for rolled AZ80, for many different Mg alloys and conditions, and Albinmousa et al. [56], [81] for extruded AZ31 under multiaxial loading to predict the fatigue life of wrought Mg alloys. In this study, the JV model [82] is utilized to predict the life of the as-received material. Recent work [95] has been done utilizing this model to predict the fatigue life of as-cast and cast-forged open-die forged AZ80 Mg with good reliability. However, to predict the fatigue life of the closed-die forged material, the two-parameter energy based model was utilized, as the data presented here is from stress-controlled testing and is not adequate for generating the requisite material constants for the JV model. A comparison of the predicted fatigue life for both models is also discussed for the as-received material. The details of these models and their application to predict the fatigue life of wrought Mg alloys are described in studies by Roostaei et al. [109] and Jahed et al. [56] for the JV and two parameter model respectively.

For the JV model, the energy-based parameters for cast AZ80 Mg found by Gryguc et al. [95] in a previous study are presented in Table 7. The fatigue life of the cast material was predicted for both the strain controlled test results presented in the previous study, as well as the stress-controlled stress results presented in this current study. Similarly, the fatigue life for the extruded material was also predicted. For the closed die forged material, a simple two parameter energy based model was used to correlate fatigue damage and predicted lives according to the relation:

$$\Delta W_t = C N_f^m \quad (4)$$

Where  $\Delta W_t$ , is the total strain energy density as defined by the plastic and elastic components and C and m are fitting constants (not to be confused with the fatigue toughness exponent ‘C’, utilized in the JV model). In general uniaxial loading, the total strain energy density is defined as:

$$\Delta W_t = \oint \sigma d\varepsilon + \frac{\sigma_{max}^2}{2E} \quad (5)$$

Qualitatively Eq. (5) represents the summation of the area within the stabilized hysteresis loop (plastic component) and the elastic “unloading” energy from the tensile peak of the hysteresis loop (elastic component)[56], [62]. Previous work by Jahed et al. [56] suggested that for various forms of wrought magnesium from the AM, AZ and ZK families, one unique set of fitting constants C and m could be utilized to predict the fatigue life in both uniaxial and multiaxial loading. Their study however did not include the AZ80 alloy or forged varieties of Mg. Fitting the fatigue data presented in Figure 52a with the generalized energy-life power relation in Eq. (4), a unique set of fitting constants were found for both the cast and wrought (extruded, CF and EF) varieties of AZ80 Mg presented in this study. The distinction is made between the cast and wrought forms in the implementation of this model as their microstructural attributes, texture and mechanical properties vary dramatically, and thus their cyclic characteristics should follow. Furthermore, Jahed suggested that various forms of wrought magnesium (extrusion, rolled sheet and rolled plate) can be characterized by the same unique set of fitting constants [56], similarly in this study, the data for the as-extruded and forged (CF and EF) material was grouped together and considered all to be of the “wrought” variety.

Utilizing these energy based models, the total strain energy density vs. number of cycles is presented in Figure 52 (a). For the as-cast samples, the results presented were from a combination of all orientations (LD,RD,TD) whereas the as-extruded is only from the extrusion direction. As previously mentioned, all of the forged material sample orientations were from the longitudinal direction of the forged billet. For all materials a subset of the results presented in Figure 50 which had strain measurement throughout the test were utilized for life modelling as it is required for calculation of the energy based parameters and life prediction for both models. For the CF and EF conditions, samples were taken from different regions within the cross section of the forging, as denoted next to each datapoint (once again corresponding with the locations denoted in Figure 44d).

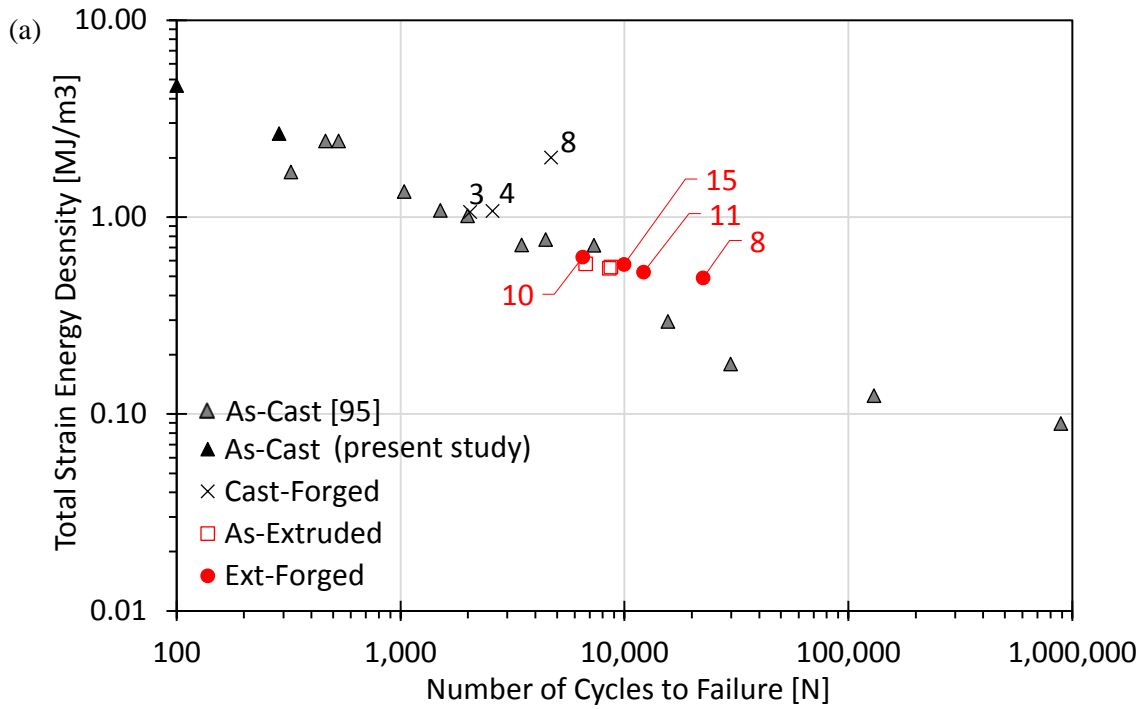
Table 7 - Energy-based parameters for the JV and two parameter models for the as-cast, as-extruded, as well as closed die cast-forged and closed die extruded forged at 375 deg C and 20 mm/sec.

Material	JV Energy Based Model				Two Parameter Energy Based Model	
	$E_e'$ (MJ/m <sup>3</sup> )	$E_f'$ (MJ/m <sup>3</sup> )	$B$	$C$	$C$ (MJ/m <sup>3</sup> )	$m$
Cast [95]	3.5861	68.39	-0.309	-0.555	35.255	-0.467
Extruded	5.4468	634.19	-0.273	-0.962	40.478	-0.456
Cast-Forged	-					
Extruded-Forged						

As can be observed in Figure 52b, with regards to the as-cast material life prediction, almost all the life estimations fall within the bounds of a factor of 2.5, with almost equal numbers of data being under and over predicted. It can be observed that the cast-forged material has a larger amount of scatter amongst the data, which can be attributed to the aforementioned spatial variation in mechanical properties throughout the forging and the fact that the samples were taken from different locations throughout the same forging. For the cast-forged material, location 8 (as denoted by in both Figure 52a and b) is considered an outlier, as it has a significantly higher total strain energy density for a given life compared with all the other material varieties. This results in an expected conservative life prediction as both the JV and two parameter models overestimate the fatigue damage for this particular location within the forging. This overestimation is a direct result of the spatial variation in both texture and monotonic properties that can be observed in Figure 44 and Figure 46 respectively. More specifically, the web region (location 8) has a comparatively different texture and dramatically different strength and ductility in comparison to other regions within the forging like the flanges. This spatial variation in properties between the web and flanges is much less pronounced in the extruded-forged material albeit still marginally evident. Since the web region of the cast-forged material has a considerably higher strength and ductility relative to the other locations in the forging for which the fitting constants are more representative of, the resulting life prediction is overly conservative at location 8 for the cast-forged material and lies well outside of the bounds of a factor of 2.5. Excluding this anomaly, the remainder of the life predictions using the two parameter model are quite reasonable and fall within the bounds of a factor of 2.5.

Figure 52c illustrates the fatigue life prediction for the as-received material (cast and extruded) for both of the models implemented here. It can be observed that for the as-cast material, both the two parameter and JV energy based models give very similar life estimates, which is to be expected since the fitting constants were generated specifically for cast material. However, it can be observed that the JV model gives a more accurate prediction for the as-extruded material as the two parameter model consistently predicts higher lives than “ideal”. This can be attributed to the two parameter model being

calibrated using data from all three forms of wrought material (extruded, CF and EF) which can be considered to be an accurate (albeit more approximate) approach.



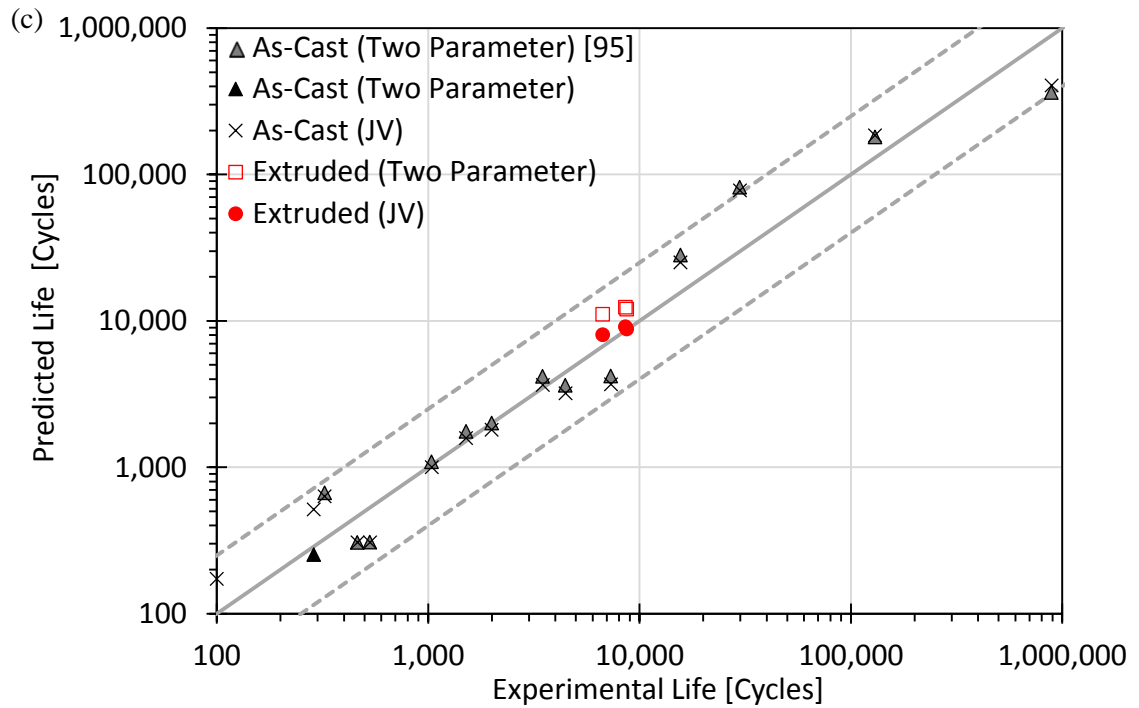
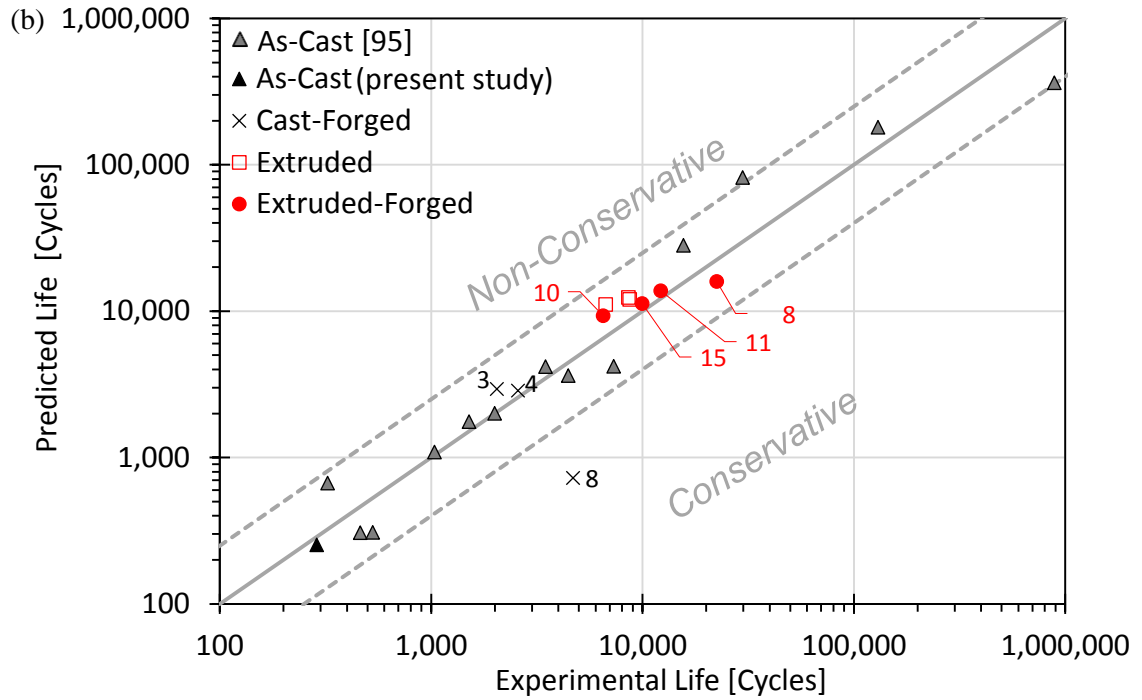


Figure 52- (a) JV damage parameter evolution with a number of cycles to failure for both as-received and forged AZ80 Mg; and (b) the correlation between two parameter predicted fatigue life and experimental life for both as-received and forged AZ80 Mg. (c) the correlation between prediction of two parameter and JV energy based model predictions for the as-received material. Locations within the billet for each forging are denoted beside each datapoint. The dashed lines in (b) and (c) denote bounds of  $\pm 2.5$

## 5.4. Conclusions

Uniaxial quasi-static and fully-reversed fatigue experiments were conducted at various stress amplitudes, ranging from 140 – 190 MPa of as-cast, as extruded, cast-forged and extruded-forged AZ80 Mg alloy. The effects of various starting microstructure/texture and thermomechanical history on the quasi-static properties were investigated on a comparative basis. Based on the results the following conclusions can be drawn:

1. Following forging, both the cast-forged and extruded-forged material exhibited an increase in fatigue life in some instances of up to 15 times for a given stress amplitude. The degree of fatigue life improvement depending on the processing conditions and the type of base material.
2. All materials exhibited tension/compression asymmetry to varying degrees, depending on the thermomechanical processing conditions. It was discovered that the style of closed-die forging being investigated had spatially varying properties with texture orientations which varied based on the local forging directions and intensities which were dependent on the starting texture as well as the thermomechanical history.
3. The as-cast material possessed a random texture and exhibited diffuse extension twinning in the first reversal of cyclic testing at high-stress amplitudes. All of the textured materials cast-forged, extruded and extruded forged possessed sharp texture which resulted in extension twinning in compression during the second reversal at higher stress amplitudes.
4. Under fatigue testing, the materials all developed some form of mean strain, with the nature and magnitude of this mean strain being dependent on primarily its texture intensity and propensity to twin in either tension or compression reversals. The type of mean strain (tensile or compressive) depends upon both the orientation and intensity of the starting texture of the material.
5. The texture induced ratcheting and resulting mean strain evolution was most pronounced in the as-cast material and had a significant impact on the fatigue life.
6. Strain energy density was demonstrated to be a good parameter for predicting the fatigue damage for both cast and wrought forms of AZ80 Mg. Both a simple two parameter and more complex four parameter Jahed-Varvani energy based models were able to provide reliable life prediction for cast, extruded and closed-die forged AZ80 Mg at a variety of different stress amplitudes.

## 6. Multiaxial cyclic behaviour of extruded and forged AZ80 Mg alloy

This penultimate chapter builds upon the discovery level knowledge, and structure-properties relationship that was developed in previous chapters 4 and 5. A link between the microstructure and texture and its influence on the cyclic behaviour and fatigue life has been developed for forging geometries that range from simple uni-directional forging to complex multi-directional forging with spatially varying properties. The complex nuances of the material behaviour in tension and compression have been understood and characterized and links between the activity of various deformation modes, hardening behaviours and the cyclic damage mechanisms have been established. Furthermore, the nature of the cyclic response of forged AZ80 Mg has been observed to be a function of the loading history. More specifically, the orientation, and sequence of the loading are factors which have a profound effect in both a strain and stress controlled loading environment. These contributions are immense, however they only encompass the material behaviour from a uniaxial sense (that is to say, only in the tensile and compressive “axial” directions). Building upon this foundational knowledge to extend towards combined loading such as bi-axial (shear/tension) is a domain of research which has been largely unexplored for AZ80 Mg.

Due to the limited number of slip systems (comparatively to other FCC or BCC metals) which the HCP crystal structure of Mg possesses, the plastic deformation is largely facilitated by twinning [110]. When loaded uniaxially, the principal strain axis (or axis of maximum strain) remains constant regardless of the magnitude of the load (or its direction). Quite simply, if the critical resolved shear stress (CRSS) of a certain mode of deformation is less than the actual stress along the principal axis induced by the external loading, the material will plastically deform. Under combined loading which has contributions of axial and shear stresses which are applied in proportional quantities (subsequently referred to as “proportional loading”) this principal axis (although different from the uniaxial case) remains constant throughout the loading history. It has been established that the twinning-detwinning mechanism occurs predominantly for grains

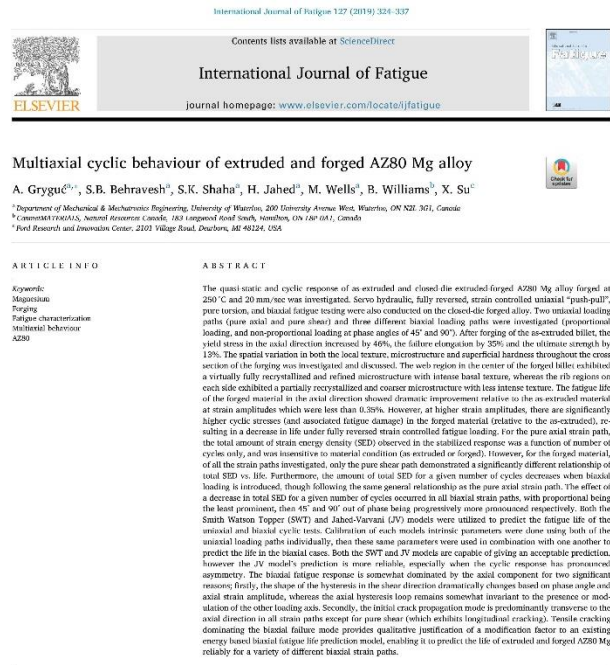


Figure 53 - A. Gryguć et al., “Multiaxial cyclic behaviour of extruded and forged AZ80 Mg alloy,” *Int. J. Fatigue*, vol. 127, pp. 324–337, 2019.

which have preferential orientation to activate such a deformation mode [91][111]. Thus, in uniaxial and proportional bi-axial loading the constant principal axis will permit twinning/detwinning only on the proportion of grains which have favourable orientation for the mechanism to occur. However, under combined loading which is bi-axial and *non*-proportional (i.e. some non-zero phase angle between the axial and shear loading), the principal axis will rotate with respect to time, and this potentially allows the twinning-detwinning mechanism to access a larger proportion of grains and further damage the material. Xiong et al. made a similar observation to this in multi-axial fatigue characterization of AZ31B extrusion. [111]. Some materials will exhibit additional non-proportional hardening caused by dislocation-dislocation interaction [56][112][108], however this is dependent on the nature of the twinning-detwinning mechanism to cause cyclic hardening or softening which is governed by various factors such as the crystal structure and initial texture. More generally, ductile materials will exhibit a degradation in fatigue characteristics under non-proportional loading, an observation that was also found by other researchers on various Mg alloys in the AZ family [111][91][113][114]. The influence of this knowledge framework on the research objectives of tasks (i) and (v) is fairly complex. Since the service loading of the physical component is a combination of a spectrum of various forces and moments, the stress state at the critical locations can be considered to be highly multi-axial in nature. Thus, characterization of the bi-axial fatigue behaviour of forged AZ80 Mg is of utmost importance, and more specifically understanding the non-proportionality effect is paramount in fulfilling task objective (v) within this research work.

The relative contributions of the axial and shear components of loading to the cyclic damage mechanism is a topic which is under recent development in the realm of wrought Mg alloys. Several researchers have attempted to link the early cracking behaviour (or macroscopic crack directions) in Mg alloys to the damage and failure mechanisms in multiaxial loading [111][91][115]. This approach to predicting fatigue life has its basis in relating fatigue damage to the local stress and strain associated with a material plane where fatigue crack initiation (FCI) and early growth take place. What defines this critical plane is a topic which is highly dependent on the criterion which one adopts to assess the fatigue damage, it could be the plane upon where maximum shear occurs (Fatemi-Socie) [116], maximum normal strain (SWT) [57][79] as well as others [117]. A key scientific contribution highlighted in this chapter is the development of a link between the macroscopic crack path, the loading path and the damage mechanism for forged AZ80 Mg alloy. This knowledge is instrumental in accurately assessing the fatigue life under multiaxial loading where axial loading proves to dominate the bi-axial response of the material. These two contributions form the foundation towards comprehensive understanding and characterization of the fatigue of forged AZ80 Mg alloy and act to completely achieve the task objectives of this thesis work. More specifically, these key contributions align very well to satisfy the research objectives 1 thru 4 for both uniaxial and multiaxial strain controlled loading paths

The following journal article published in the International Journal of Fatigue (June 19, 2019) has been presented exactly as published, with the exception of modifications made for harmonizing references, table and figure numbers to integrate into this larger thesis document. A version of this work was also presented in the Fatigue and Damage of Structural Materials Conference (FDSM XII) in Hyannis, USA in September 2018 as well as the International Conference on Multiaxial Fatigue and Fracture (ICMFF 12) in Bordeaux, France in June 2019.

## 6.1. Introduction

Vehicle lightweighting is one of the most effective methods of improving fuel efficiency and decreasing greenhouse gas emissions. Magnesium is a great candidate for decreasing the weight of many vehicle components due to its high specific strength and the fact that it is the lightest commercially available structural metal [65]. Traditionally, magnesium has been utilized for many years as a die-casting alloy since it has favourable kinematic viscosity and good castability [118]. However, die-cast magnesium alloys are typically characterized by both poor strength and ductility limiting them mostly to non-structural applications. Wrought magnesium alloys however exhibit a superior class of performance with strength and ductility which are suitable for structural automotive applications. Recently there has been a strong impetus towards forging of magnesium to create near net shape vehicle components that possess superior mechanical properties that offer substantial weight savings to more conventional structural materials. Recent work has been done on characterizing the behaviour of several forged Mg alloys [29], [98], [99], [103], [119]–[121] and [62], [69], [92]–[97], [122], [123], among these, the AZ80 alloy is a Mg alloy with good forgability, high aluminum content and superior strength and fatigue performance. The vast majority of fatigue characterization which has been done on Mg is uniaxial tension-compression loading [12], [20], [61], [87], [95], [110], [122], [124]–[128], very limited work has been done on the multiaxial fatigue of Mg alloys. Thus, there still remains a large and significant knowledge gap as structural components are often subjected to highly multiaxial stress states when in service.

Early work on multiaxial fatigue of various steels by Socie et al. indicated that the majority of the fatigue life is spent growing cracks on planes of maximum shear strain amplitude [79]. More recently, crack nucleation was found to occur at the planes of persistent slip bands (PSB), and this forms the basis for critical plane approach for predicting fatigue failure [55], [112]. The phase angle between [129] the loading axis acts to manipulate the orientation of this critical plane within the material and in combination with modulation of the relative SED's corresponding to each axis, governs the fatigue life and preferred crack orientation. A few pioneering studies have been done on multi-axial fatigue of Mg alloys. Bentachfine et al. [130] concluded that in-phase loading (i.e. proportional axial and shear) results in the highest fatigue life, non-proportional loading acts to generate a more complex defect structure with higher dislocation density, resulting in lower life. This observation also observed by Xiong et al. in extruded

AZ31B Mg alloy [111]. Yu et. al investigated the multiaxial fatigue of extruded AZ61 Mg and concluded that unlike cast varieties of Mg (where fatigue cracks initiate at casting defects), wrought Mg alloys preferentially have fatigue cracks initiate at these PSB's inclusions or deformation twins [91]. Furthermore, Yu indicated that the manufacturing process, microstructure, environmental effects, and loading ratio all influence the fatigue behaviour of Mg alloys. Roostaei et. al investigated the multiaxial cyclic behaviour of extruded AM30 Mg and observed that the axial cyclic response is insensitive to the presence of the shear strain, its magnitude, or the phase angle [109]. However, they observed that the cyclic shear response was strongly sensitive to the presence, magnitude and phase angle of the axial strain. Several of these studies [55], [56], [91], [109], [111], [131] employ critical plane approaches to model the fatigue life of Mg alloys, namely the Fatemi-Socie and Modified Smith-Watson-Topper approaches, as well as energy based models such as the Jahed-Varvani, which has shown to provide reliable results. Despite this, no work has been done thus far on modelling the multiaxial fatigue behaviour forged Mg alloys, which is the focus of this current work.

## 6.2. Experimental

The material used in this investigation was commercially-available AZ80 Mg extruded billet (8.0 ±0.2% aluminum content, with other elements composition as per ASTM B91-12 standard). The material was received from Magnesium Elektron North America Inc. in the as-fabricated condition. The dimension of the extruded billet was a diameter of 63.5 mm and a length of 1000 mm. The forging was conducted at CanmetMATERIALS (Hamilton, Canada) using the billets having dimension of  $\varnothing$  63.5 mm, 65-mm long. All forgings were carried out on a 500-ton hydraulic press with a profiled upper and lower die with an I-beam shaped internal cavity. A schematic representation of the billet and die geometry is shown in Figure 54 (a). The billet and tooling were heated separately to 250°C for sufficient time to allow any thermal gradients to decay. The orientation of the billet to the press was such that the radial direction was along the direction of the press stroke (i.e. the direction of forging was parallel to the radial direction of the billet). Forging was carried out in a single step at a displacement rate of 20 mm/sec.

Axial tensile test samples shown in Figure 55(a) with geometries according to Roostaei et al. [61] and a 4 mm thickness were extracted from the as-received billet and closed die forged samples. The extruded samples were machined along the extrusion direction and from a location where the middle of the gauge section was at 50% of the billets radius. There were 15 test samples that were extracted from 15 different locations throughout the closed die forging (all having their axis parallel with the LD direction), as shown in Figure 57 (d). The axial test samples had a nominal surface finish of  $R_a \leq 0.2 \mu\text{m}$ , however in practice the actual roughness was substantially less, around  $0.05 \mu\text{m}$ . These samples were later utilized for quasi-static and cyclic testing. Torsional (hollow tubular) test samples shown in Figure 55 (b) were extracted

with geometries according to Roostei et. al [109] from each of the ribs on either side of the forging's cross section as shown in Figure 54 (b). These tubular samples that were used for shear testing had a surface finish of  $R_a \approx 0.2\mu\text{m}$ . The quasi-static tensile tests were performed according to ASTM standard E8/E8M-15a using an MTS 810 Servo-Hydraulic test machine operating in displacement control mode with a displacement rate of 1 mm/min. The quasi-static shear tests were performed under rotation control mode at a rate of 12 deg/min. Strain measurement was accomplished using a GOM ARAMIS 3D 5MP DIC system which passively functioned to measure the shear strain. The average strain rate within the gauge section of measurement was  $1.4\text{E}-3 \text{ sec}^{-1}$  for the axial tests and  $6.7\text{E}-4 \text{ sec}^{-1}$  for the shear tests.

The axial fatigue tests were performed as per ASTM E606 in an ambient environment using an MTS 810 Servo-Hydraulic test machine and shear/biaxial using an Instron 8874 test machine operating in strain control mode at a frequency ranges of 0.05 Hz to 2 Hz, and 1 to 30 Hz in force control mode depending on the strain amplitude to maintain an approximately consistent loading rate between all tests. During strain control, the max strain rate averaged over the gauge section of measurement was  $\sim 1.5\text{E}-2 \text{ sec}^{-1}$  for the pure axial and torsional tests, and  $\sim 3.2 \text{E}-3 \text{ sec}^{-1}$  for the biaxial tests. For the purely axial tests, the strain was measured throughout the first 10,000 cycles using an MTS 632.26 extensometer with an 8-mm gauge and travel of  $\pm 1.2\text{-mm}$  until stabilization of the cyclic hysteresis loop was achieved. Similarly, for the pure shear and biaxial tests, the strain was measured for using an Epsilon biaxial extensometer (model 3550) with axial and shear ranges of  $\pm 5\%$  and  $\pm 3^\circ$  mounted on the specimen's gauge length. The tests were conducted at a zero mean strain (i.e.,  $R_L = -1$ , fully reversed strain cycle) and strain amplitudes ranging from 0.32% to 2.0%. The failure criteria for the fatigue tests was considered to be a 50% reduction in the peak tensile axial stress or a 50% reduction in peak or valley shear stress. The fracture surfaces after tensile and fatigue tests were examined using SEM techniques (FEI Quanta FEG 250 ESEM with EDX).

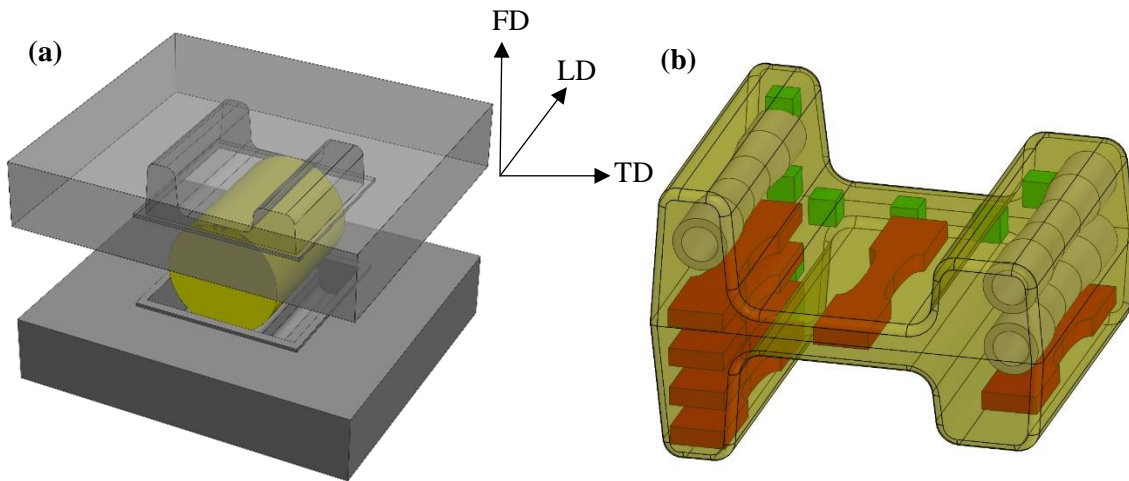


Figure 54 - a) Closed die forging schematic with top/bottom dies shown (grey) and extruded billet (yellow) prior to forging. (b) Axial (Red), shear (white) and microstructural/texture (green) sample orientation within forged billet. FD denotes forging direction, LD: Longitudinal Direction and TD: Transverse Direction.

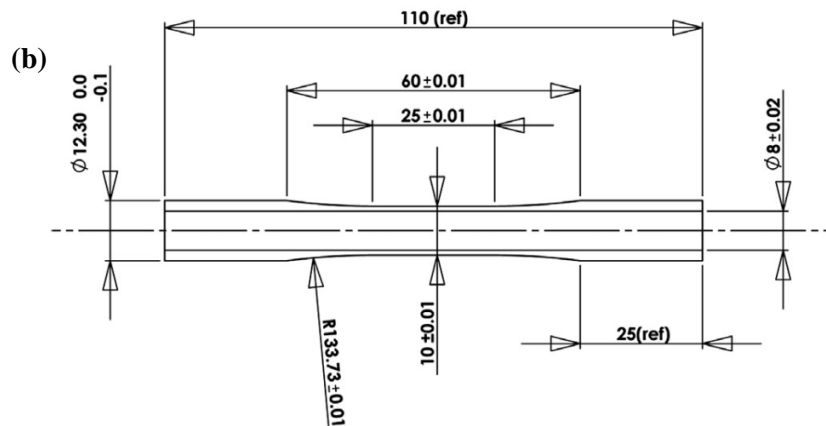
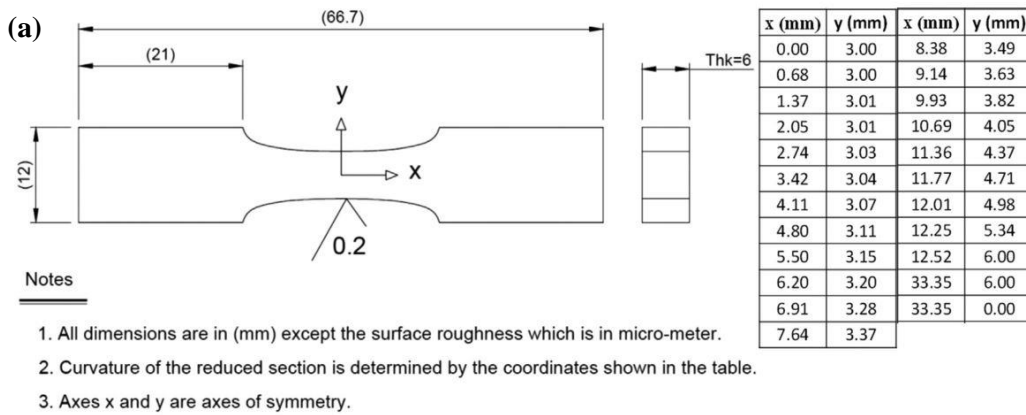


Figure 55 - Specimens' geometries and sizes: (a) flat specimen for axial tests, (c) tubular specimen for torsion tests. All dimensions in mm.

### 6.3. Results & Discussion

A summary of the quasi-static behaviour of the as-extruded and forged material is presented in Table

1. As expected there is a large difference in the both strength and ductility between the extrusion direction

(ED) and radial direction (RD) in the as-extruded material. This disparity in properties has been explored by numerous researchers [61], [69], [93]–[95], [122] and results from magnesium’s HCP crystal structure, and resulting anisotropic plastic response. The forged material however exhibits a yield strength which is 162% higher vs. the RD and 46% higher vs the ED than that of the as-extruded material. Furthermore, a significant increase in failure elongation of 35% was observed relative to the extrusion direction. The forged material exhibited a more modest 33% increase vs. the RD and 13% increase in the ED in the ultimate strength. From a monotonic loading perspective, the forged material has properties which have superior strength and ductility relative to the parent as-extruded material. The shear properties are also summarized for the forged material in Table 1 however the shear behaviour of the as-extruded material has not been investigated in this study. The forged material investigated here shows significant improvement in properties relative to another alloy in the AZ family of Mg, AZ31B extrusion investigated by Albinmoussa et al. [60] Evidence of the spatial variation of quasi-static properties in the closed-die forged material is indicated by the magnitude of the tolerance on each quantity as it represents one standard deviation above and below the average value which is considered to be representative for the forgings cross section as a whole.

Table 8 - The relationship between monotonic axial and shear properties of as-extruded and extruded-forged at 250°C and 20 mm/sec AZ80 Mg. Note: Values in parenthesis show delta to cyclic yield strength (i.e. increase in yield strength due to cyclic hardening)

Material	Axial					Shear					
	E	$\sigma_{ys}$	n	$\epsilon_{Fail}$	$\sigma_{UTS}$	G	$\sigma_{ys}$	H	$\epsilon_{Fail}$	$\sigma_{UTS}$	
	[GPa]	[MPa]		[%]	[MPa]	[GPa]	[MPa]	[MPa]	[%]	[MPa]	
		Tension	Comp								
As Ext (ED)	46.8	197.3 (+54%)	-155.5 (+37%)	0.218	11.3	341.1					
As Ext (RD)	42.2	113.6 (+41%)	-116.4 (+46%)	0.283	15.3	290.2					
Forged	44.7±2.5	286.0±8.1 (+7%)	-161.8 (+65%)	0.146	15.3±7.8	384.9±5.8	16.0±1.0	83.2 ±1.8 (+12%)	317.1±14.7	18.1±1.8	196.7±2.7

For the fatigue investigation, five different strain paths were investigated, two uniaxial and three biaxial. Each of the two uniaxial loading paths were tested at a variety of strain amplitudes, and the biaxial paths at various combinations of axial and shear strain amplitudes, as denoted in Table 9. For the proportional in-phase biaxial (path C) experiments, strain amplitudes were intentionally selected to give various combinations of low, medium and high amplitudes, whereas for the non-proportional paths (D and E) the shear amplitude was held constant at 0.5% since it was determined that the axial strain amplitude and phase angle were the dominant factors governing the fatigue response.

Table 9 - Description of the investigated strain amplitudes for fatigue experiments for each loading path.

Loading Path	Strain Amplitude		Equivalent Strain Amplitude
	$\Delta\epsilon/2$ [%]	$\Delta\gamma/2$ [%]	$\Delta\epsilon_{eq}$ [%]
<b>A</b> (Pure-Axial)	0.2 – 2.0	-	$= \Delta\epsilon/2$
<b>B</b> (Pure-Shear)	-	0.4 – 2.0	$= \Delta\gamma/2$
<b>C</b> (Proportional) In-Phase	0.4	0.5	0.493
	0.7	0.5	0.757
	0.4	0.75	0.589
	0.7	0.75	0.823
	0.5	1.0	0.764
<b>D</b> (Non-Proportional) 45° out of Phase	0.9	1.0	1.069
	0.4	0.5	0.399
			0.569
<b>E</b> (Non-Proportional) 90° out of Phase	0.7	0.5	0.696
			0.297
			0.503
	0.9	0.5	0.643

Figure 56 graphically illustrates the five strain paths which were investigated under fully reversed loading plotted in the  $\epsilon$  vs  $\gamma$  strain space. Path A (Figure 56 a) is pure axial, (b) path B - pure torsional, (c) path C - biaxial proportional, (d) path D – biaxial 45° out of phase which is an oval shaped strain path, and finally (e) path E - 90° out of phase which is a circular shaped strain path. Similar to the representation done by Yu et al. [91] in the  $\epsilon$  vs  $\gamma/\sqrt{3}$  strain space, the equivalent strain amplitude is calculated as the radius of the minimum circle inscribing the loading path. The magnitude of  $\Delta\epsilon_{eq} / 2$  is given in Table 9 for each of the investigated strain paths. It should be noted that the equivalent strain defined here does not possess any physical significance and it is only used to facilitate the presentation of fatigue results under different strain paths.

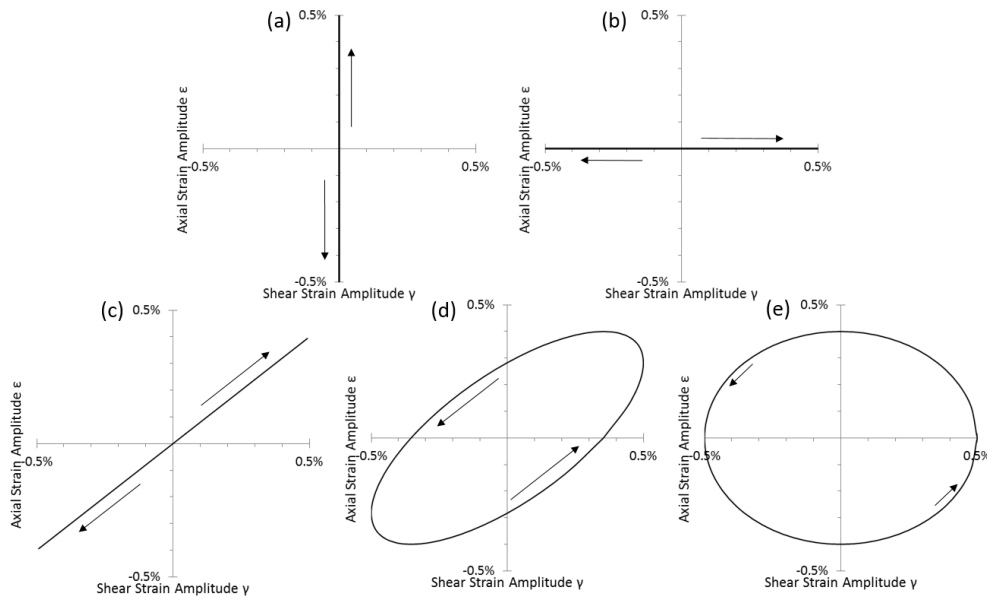


Figure 56 - Loading paths used for the fatigue experiments (a) pure-axial, (b) pure shear, (c) proportional (d) 45° out of phase and (e) 90° out of phase.

The microstructure, texture and superficial hardness for various locations throughout the cross section of the forging are shown in Figure 57. The spatial variation is obvious, especially between the center “web” region (locations 8, 9 and 10) and the outer rib regions. Figure 57 (d) illustrates a contour plot of the variation of superficial hardness throughout the forging cross section, areas in red represent the regions with the highest superficial hardness and areas of blue, the lowest. The axial material properties provided in Table 8 are an average throughout the entire cross section, whereas the shear properties are an average throughout the tall (1 – 7) and short (11-15) ribs of the forging since that is the location where the tubular samples were extracted from. It can be seen that compared to previous studies [122] where forgings were done at higher temperatures (375°C), the spatial variation in microstructure, texture and hardness are more pronounced in these lower temperature forgings investigated here despite similar strain histories and forging rates. Furthermore, at 250°C the level of recrystallization seems to spatially vary throughout the cross section with the middle “web” region having a more refined microstructure, and smaller more randomly distributed eutectic morphology. Ogushi et al. [104] characterized the as-extruded form of AZ80 as having clustered “stringers” of precipitates aligned along the extrusion direction composed of Mg<sub>17</sub>Al<sub>12</sub> and Mg-rich solid solution phases. The forged microstructure in location 1 (Figure 57d) shows no evidence of a preferred alignment direction of the darker second phases following the thermomechanical forging process. These second phases appear to be smaller in size and more pancake like in their morphology in the center “web” region (Figure 57e). Li et al. investigated the hot deformation of extruded AZ80 in a simple upset type process, and observed similar eutectic morphologies at 250°C to those presented here, as well as dissolution of the eutectic phase back into the matrix at temperatures between 350-400°C. This transition temperature of eutectic dissolution into the matrix agrees well with the microstructure observed in previous investigations by Gryguc et al. [122] in forgings done at 375°C whose microstructures were void of a large eutectic fraction and only possessed evidence of small β-phase precipitates at the grain boundaries. It is believed that the presence of precipitants at 250°C and their dissolution back into the matrix at >350°C resulted in a meaningful contribution to the higher strength values observed at lower temperature forgings.

Figure 57f illustrates the basal and prismatic pole figure for location 8 (web region) within the forging. It can be observed that a preferential alignment of the poles indicates a stronger texture compared to the more randomly distributed poles in the other locations (Figure 57 a and b) where the local forging directions are less uni-directional. Similar to previous investigations of this style of forging, [122], [123] the direction of the c-axis (as indicated by the basal pole figures in Figure 57 align themselves to be oriented along the local forging direction. The effect which this spatial variation in microstructure and texture has on the mechanical and fatigue response is significant, thus for the purposes of this investigation, the web region (location 8-10) is not focused upon due to its inherent dissimilarities. The focus of this study is to investigate the sensitivity of the fatigue response to the strain path for the “representative” forged material,

which can be considered to be the regions outside of the “web” of the forging which exhibited a significantly different thermomechanical history during the forging process.

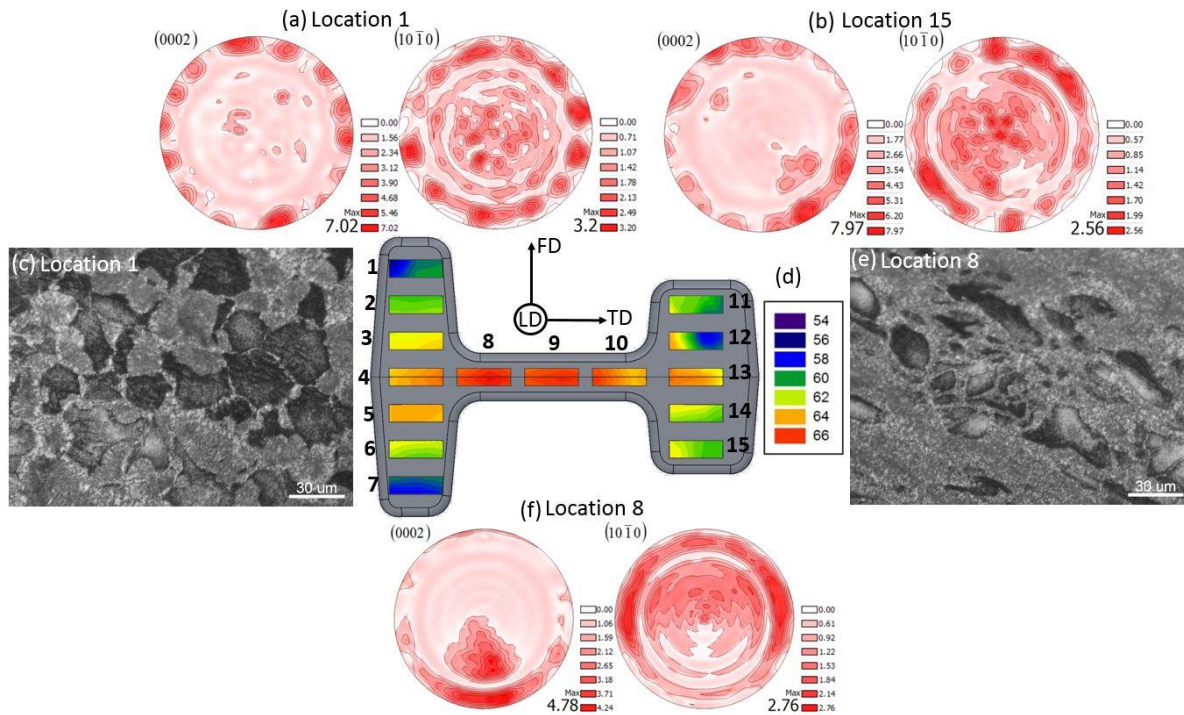


Figure 57 - Microstructural characterization of AZ80 extrusion forged at 250°C and 20 mm/sec. Basal and prismatic pole figures are presented in locations 1 (a), location 15 (b) and location 8 (f) of the forging. Figure (c) and (e) show LOM images of locations 1 and 8, respectively within the forging (view in the longitudinal direction). Figure (d) denotes the spatial variation of superficial hardness (30T) in the direction normal to the cross-section of the forging. FD denotes forging direction, TD: transverse direction, and LD: longitudinal direction.

### 6.3.1. Monotonic and Cyclic

Figure 58 illustrates the engineering stress vs. engineering strain response for monotonic tension/compression and path A (pure axial) fatigue tests for the as-received and forged material. The cyclic response is given by the dotted symbols which were extracted from the tensile and compressive peaks of the stabilized half-life hysteresis loop for each of the investigated strain amplitudes. It can be observed that the cyclic hardening is very significant in the as-extruded material in both the investigated directions. The forged material however, has a much higher tensile yield stress compared with the as-extruded material and the cyclic hardening is only marginal in tension. In monotonic compression, there is a premature yield and a high level of asymmetry in both the ED and forged materials due to a large number of grains having their c-axis aligned in a preferential direction to activate twinning in compression but not in tension. Extruded samples extracted from the RD direction are able to activate twinning in both the tensile and compressive directions and thus exhibit a more symmetric response. The 65% increase in compressive yield stress after cyclic hardening is a well-documented characteristic of wrought magnesium alloys and results primarily from the irreversible nature of the twinning-detwinning

process and the associated increase in both twin and dislocation density during the transient phase of the cyclic response. Finally, it can be observed that following forging, the material exhibits superior monotonic and cyclic properties relative to the parent as-extruded material due to its refined grain size and eutectic microstructures which are more random in distribution and more pancake like in their morphology.

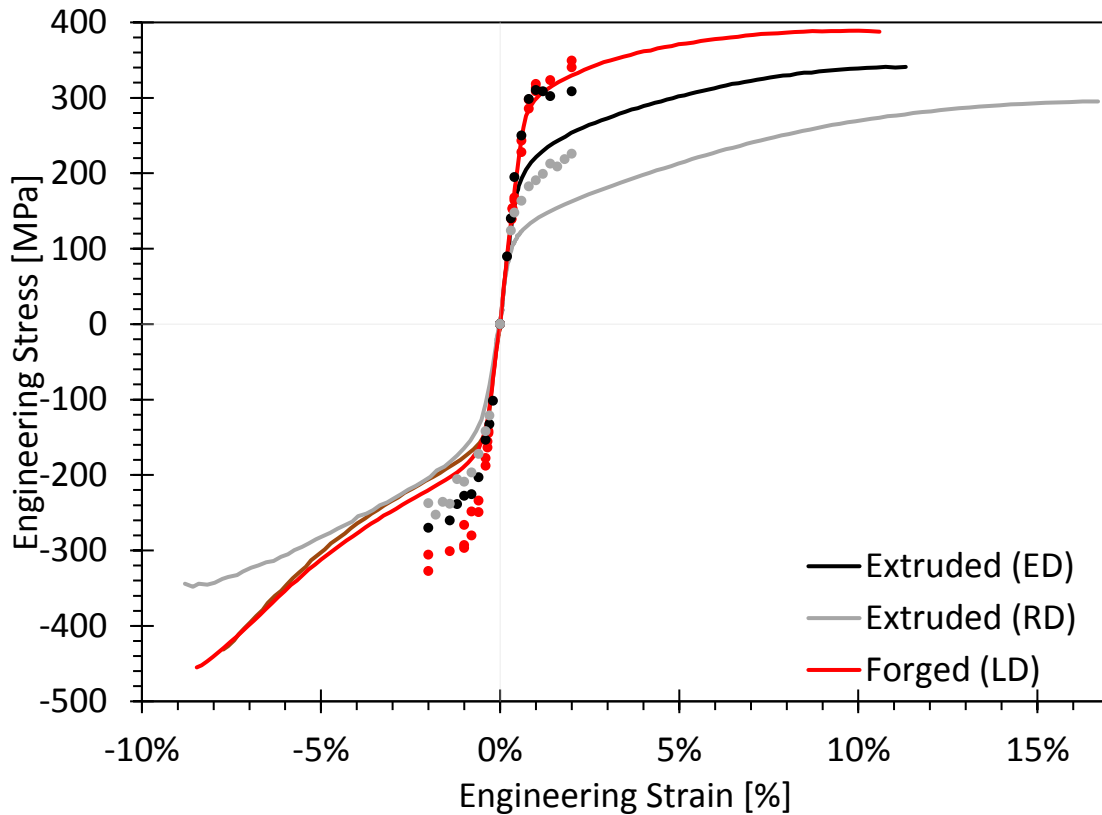


Figure 58 - Axial stress strain response for as-extruded and extruded forged AZ80 Mg. Solid lines indicate monotonic response and dotted symbols indicate the stabilized cyclic response.

Figure 59 illustrates the torsional monotonic and pure shear cyclic response (path B) for the forged material. It can be observed, that the material has only a mild propensity for cyclic hardening in shear, similar to that which was observed in tension. Furthermore, since the pure torsional strain path is characterized by the slip deformation mechanism which accommodates the deformation (since twinning is not favourable), the response which is observed is a linear hardening behaviour (not sigmoidal in nature as was observed in axial compression). Furthermore, the response under cyclic torsion was observed to be virtually symmetric due to the lack of activation of the twinning-detwinning mechanism that is favourable in axial deformation. This symmetry manifests itself as maximum and minimum stresses in the stabilized hysteresis loop being almost identical for a given strain amplitude of pure shear deformation and the associated absence of mean stress which results from this.

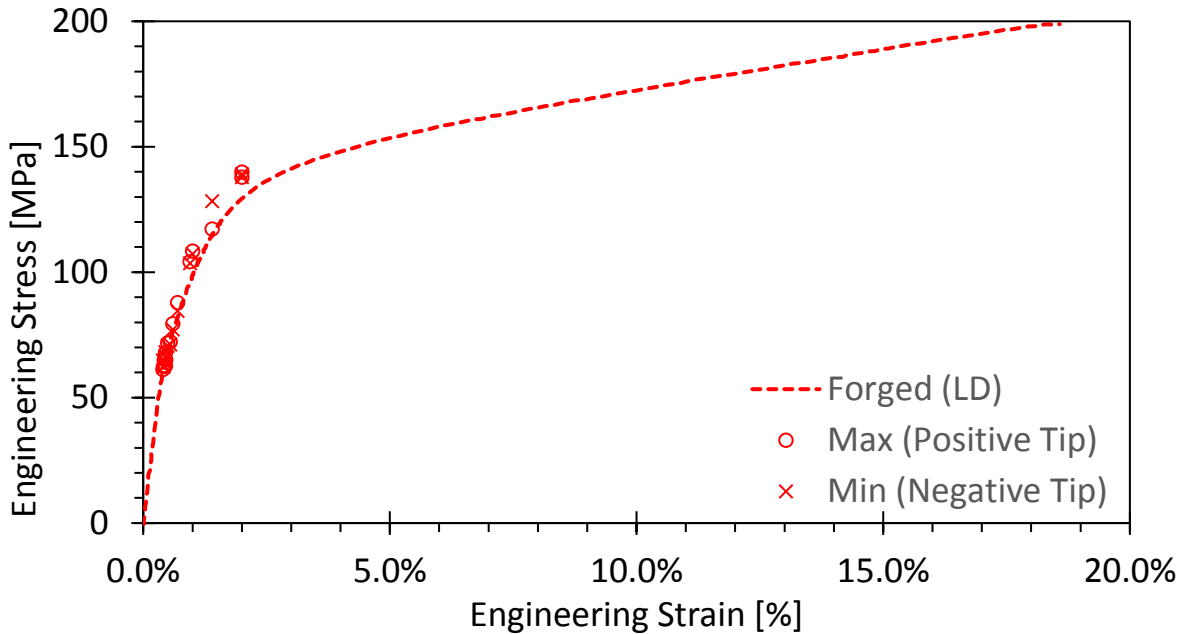


Figure 59 - Shear stress strain response for extruded forged AZ80 Mg. Solid lines indicate monotonic response and symbols indicate the stabilized cyclic response.

The evolution of peak (tensile) and mean axial stress magnitude vs number of cycles for the forged material is shown in Figure 60 a and b respectively for a variety of different strain amplitudes. It can be seen that only a marginal amount of cyclic hardening occurs for all strain amplitudes with the exception being the 0.8% axial strain amplitude case which exhibits a modest 9% increase in peak stress (due to the delayed onset of yielding following cyclic hardening. At strain amplitudes which are sufficient to induce plasticity, in general, yielding occurs much easier (that is, at a lower stress level) in compression than it does in tension due to the aforementioned twinning-detwinning mechanism. At strain amplitudes high enough to activate twinning in compression ( $\Delta\epsilon/2 > 0.8\%$ ) a non-zero mean stress develops within the first cycle (since the first compressive reversal causes the material to twin vigorously). As can be observed in Figure 60b this mean stress is most significant at the strain amplitude of 0.8% (where it reaches a peak of 25 MPa) since there is no significant plasticity induced in the tensile reversal. At even higher strain amplitudes this twinning-detwinning mechanism is still predominant, however twinning now reaches exhaustion and more generalized plasticity is now activated in the tensile reversal causing a drop in mean stress. This decrease in mean stress at higher strain amplitudes is a phenomenon also observed by Xiong et al. in extruded AZ31B Mg [132]. For strain amplitudes which are not-sufficient to induce appreciable plasticity, the mean stress that develops can be considered to be negligible and the deformation is mainly accommodated by dislocation slips [20], [91]. This transitional strain amplitude where mean stress becomes highly dependent on strain level has been discussed by other researchers before for other wrought forms of AZ Mg and can be observed as a “kink” in the strain-life curve as will

be subsequently discussed. This kink represents a shift in degree of involvement of mechanical twinning in the cyclic deformation, and the strain amplitude at which it occurs depends heavily on both the strength and the texture of the material. Yu et al. [91] found this kink to occur at 0.5% at approximately 4500 cycles for pure axial (path A).

Similarly the evolution of shear stress amplitude and mean shear stress vs number of cycles for the forged material is shown in Figure 61a and b respectively for a variety of different strain amplitudes. There is only very marginal hardening regardless of the strain amplitude, and the mean stress is less than 4 MPa in magnitude and can be considered to be negligible. These observations are as to be expected since under pure torsion (path B) the hysteresis loops are virtually symmetric even at higher strain amplitudes up to 2.0%.

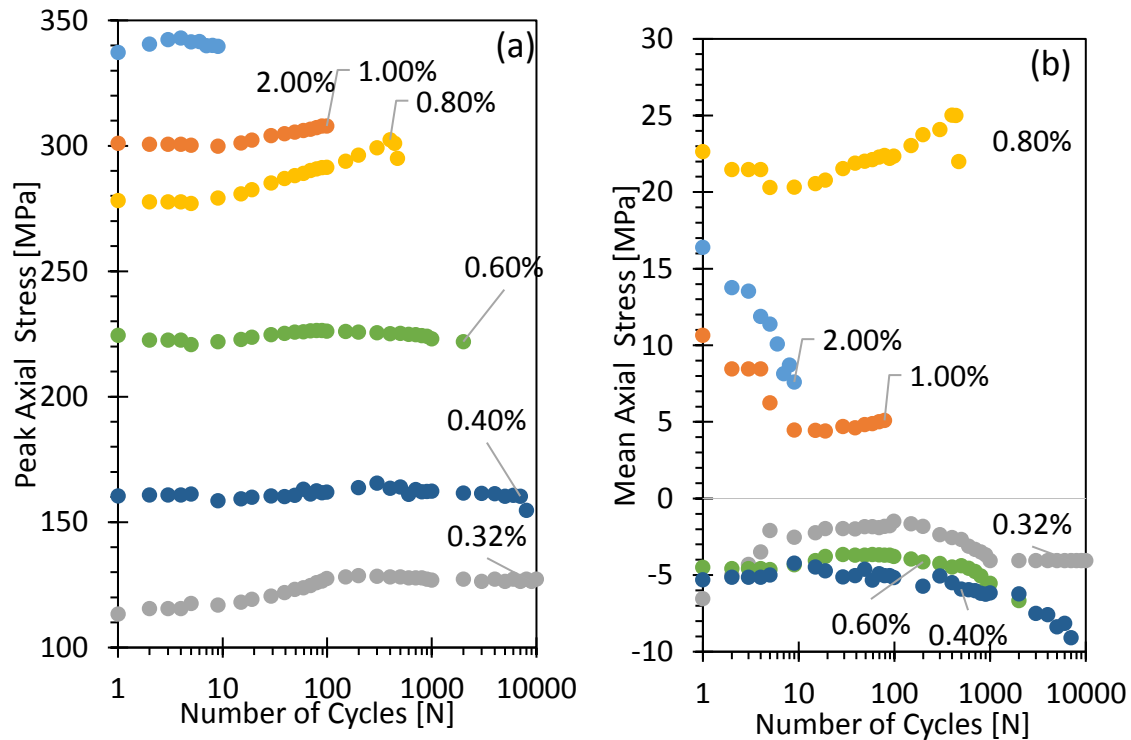


Figure 60- Evolution of (a) peak axial stress and (b) mean axial stress with number of cycles for various Path A (pure axial) strain amplitudes.

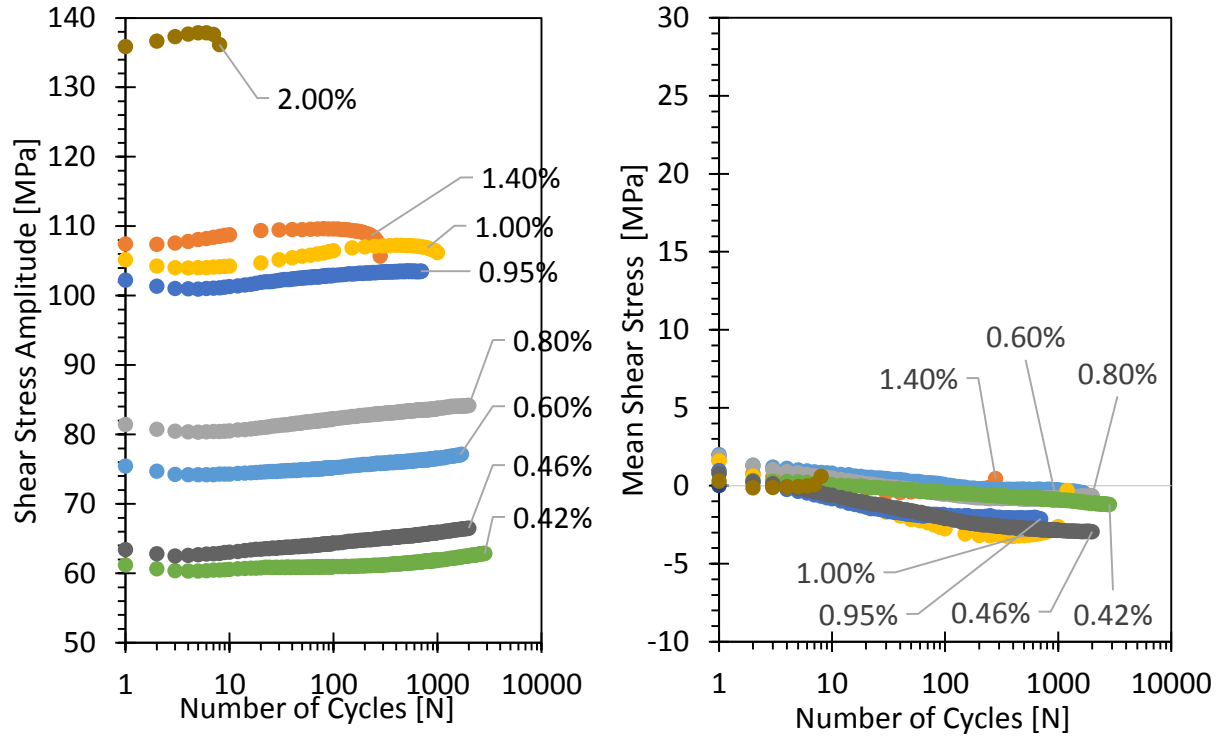


Figure 61 - Evolution of shear (a) stress amplitude and (b) mean shear stress with number of cycles for various Path B (pure shear) strain amplitudes.

### 6.3.2. Uniaxial Fatigue Life (Paths A and B)

$\epsilon$ -N data has been presented for the pure axial strain path A (Figure 62) for a variety of different material conditions as well as for all strain paths (A-E) illustrated in Figure 65. The Smith-Watson-Topper (SWT) parameter [57] was initially formulated to account for the mean stress effect during fatigue loading. Modified versions of this model have been extended for use in multiaxial life predictions of Mg alloys using a critical plane method with good success [79], [109]. The SWT parameter is related to fatigue life in terms of four different material constants:

$$\sigma_{n,max} \frac{\Delta \epsilon_1}{2} = \frac{\sigma'_f{}^2}{E} (2N_f)^{2b} + \sigma'_f \epsilon'_f (2N_f)^{b+c} \quad (Axial) \quad (6)$$

$$\tau_{max} \frac{\Delta \gamma}{2} = \frac{\tau'_f{}^2}{G} (2N_f)^{2b_s} + \tau'_f \gamma'_f (2N_f)^{b_s+c_s} \quad (Shear) \quad (7)$$

The term  $\Delta \epsilon_1$  represents the principal strain range,  $\sigma_{n,max}$  represents the maximum stress on the plane of principal strain, and E, the modulus of elasticity (see Table 8). Analogous to this, in the shear direction,  $\Delta \gamma$  represents the shear strain range,  $\tau_{max}$  the maximum shear stress magnitude, and G is the shear modulus (see Table 8). The Coffin-Manson constants on the right hand side of the equation were extracted from strain-controlled test results (Figure 62 & Figure 65) independently for each uniaxial

direction and are summarized in Table 10 for pure axial and Table 11 for pure shear. For the axial direction the elastic part of the strain range was calculated from  $\Delta\varepsilon^e = \Delta\sigma/E$ , and the plastic strain range was obtained from  $\Delta\varepsilon^p = \Delta\varepsilon - \Delta\varepsilon^e$  with a lower threshold of  $\Delta\varepsilon^p = 0.01\%$ . Similarly for the shear direction, the elastic part of the strain range was calculated from  $\Delta\gamma^e = \Delta\tau/G$  and the plastic strain range was obtained from  $\Delta\gamma^p = \Delta\gamma - \Delta\gamma^e$ . The calculated SWT parameter for both the as-extruded and forged material fatigue data as a function of cycles to failure is shown for strain path A (pure axial - Figure 63a). Previous work from Gryguc et al. [95] has also been presented for comparative purposes, since that data was collected from axial strain controlled fatigue tests on cast AZ80 Mg which was open-die forged at higher temperatures. This highlights the effect of the starting condition, style of forging and thermomechanical history has on the properties of the forged material for the same alloy of Mg. Both the as-extruded and forged materials can be expressed using power-law fits, albeit with unique constants for each material. This implies that for a given amount of cycles to failure, the SWT damage parameter for the forged material is higher than that the extruded material in the RD direction but lower than that of the ED direction. Using the parameters given in Table 10, the fatigue life was predicted for both the as-extruded and forged materials, and is plotted versus the experimental life in Figure 64. The solid diagonal line denotes a correlation match between the predicted and experimental life, and the dashed lines represent bounds that envelop deviation from this match by a factor of 2. The vast majority of life estimations fall within these bounds of a factor of 2, furthermore, for the as-extruded material the predictions are very reliable with almost equal numbers of data being under and over predicted. However, for the forged material the LCF regime seems to be conservative in its prediction, and trends towards slightly non-conservative in the HCF regime. One of the reasons for conservative predictions in the LCF regime is that the stabilized responses are used as model inputs, and for materials that cyclically harden, the stabilized cycles are more damaging than the initial ones (as the peak stresses are higher). Since the “transient” phase of hardening is a non-negligible portion of the life for the LCF regime, a proportion of the cycles experienced by the experimental samples undergo slightly less damage than predicted, as their peak stresses are lower. This is, however, a minor discrepancy and the assumption that the stabilized response is used is widely accepted in the literature.

Energy-based fatigue damage models have been used by many researchers for modeling the fatigue life of Mg alloys, e.g., Park et al. [59], [80] in rolled AZ31, Xiong et al. [20] for rolled AZ80, Jahed et al. [56], [95] for many different Mg alloys and conditions, and Albinmousa et al. [81] for AZ31 under multiaxial loading to predict the fatigue life of wrought Mg alloys. In this study, the JV model [82] is utilized. The novelty of this life model is in the evaluation of the fatigue material constants from energy-life curve. In

this model, the total energy density is implemented as a damage parameter and is constituted by its elastic and plastic components. The plastic component is defined as the area enveloped by the stabilized hysteresis loop and the elastic component is defined as the following equation [65]:

$$\Delta E_e^+ = \frac{\sigma_{max}^2}{2E} \quad (Axial) \quad (8) \quad \Delta E_e = \frac{\tau_{max}^2 + \tau_{min}^2}{2G} \quad (Shear) \quad (9)$$

where  $\sigma_{max}$  is the peak tensile stress (path A) and  $\tau_{max}$  &  $\tau_{min}$  are the peak and valley shear stresses (path B) for the stabilized half-life response. Through including the positive elastic strain energy density, the mean stress effect which is prominent in the pure axial strain path A is also taken into account in this model [83] and subsequently the energy damage parameter  $\Delta E$  is related to fatigue life via an analogues equation of similar form to the Coffin-Manson equation. [82][84], where  $\Delta E$  is the strain energy density:

$$\Delta E_A = E_e'(2N_f)^B + E_f'(2N_f)^C \quad (Axial) \quad (10) \quad \Delta E_S = W_e'(2N_f)^{B_s} + W_f'(2N_f)^{C_s} \quad (Shear) \quad (11)$$

In the pure axial strain path A, coefficient  $E_f'$  correspond to the fatigue toughness and  $E_e'$  is the fatigue strength coefficient. Exponents  $C$  and  $B$  are the fatigue toughness and fatigue strength exponents, respectively. Analogous parameters  $W_e', W_f', B_s, C_s$  are derived from the pure shear strain path B fatigue data. The constants in the above equation(s) are extracted from the strain energy density life curves and are summarized below in Table 10 (axial) and Table 11 (shear). Figure 63 (b) shows the calculated energy damage parameter for both the as-extruded and forged material fatigue data as a function of cycles to failure. Both the as-extruded and forged materials can be expressed using very similar curves, as the data points almost consolidate onto one single curve. Similar to that which was done for the SWT model using the energy based parameters in Table 10, the fatigue life was predicted for strain path A, for both the as-extruded and forged materials, and is plotted versus the experimental life in Figure 64. Virtually all the life estimations fall within these bounds of a factor of 2, with almost equal numbers of data being under and over predicted.

Table 10 - Coffin-Manson parameters for SWT model and Energy based parameters for Jahed-Varvani model for as-extruded and forged AZ80 Mg for Path A (pure axial)

Material	Axial (Path A)							
	Coffin-Manson (SWT)				Energy (Jahed-Varvani)			
	$\sigma_i'$	b	$\epsilon_i'$	c	$E_e'$	$E_f'$	B	C
	[MPa]				[MJ m <sup>-3</sup> ]	[MJ m <sup>-3</sup> ]		
As Ext (ED)	566.3	-0.111	0.975	-0.808	8.5934	410.91	-0.306	-0.796
As Ext (RD)	485.3	-0.125	0.505	-0.646	1.8670	318.91	-0.209	-0.715
Forged	527.5	-0.103	0.13	-0.626	3.6831	113.87	-0.225	-0.709

Table 11 - Coffin-Manson parameters for SWT model and Energy based parameters for Jahed-Varvani model forged AZ80 Mg for Path B (pure shear)

Material	Shear (Path B)							
	Coffin-Manson (SWT)				Energy (Jahed-Varvani)			
	$\tau_f'$	$b_s$	$\nu_f'$	$c_s$	$W_e'$	$W_f'$	$B_s$	$C_s$
[MPa]				[MJ m <sup>-3</sup> ]	[MJ m <sup>-3</sup> ]			
Forged	169.6	-0.069	0.0234	-0.241	1.6986	6.8011	-0.130	-0.302

Figure 62 illustrates the strain-life ( $\epsilon$ -N) curve for the pure axial (path A) fully reversed strain controlled fatigue testing for a variety of different strain amplitudes and material conditions. Typical stabilized cyclic responses are shown beside the strain life curves for the as-extruded and forged materials for two different strain amplitudes. It can be seen that for a given strain amplitude, the maximum and minimum stresses are consistently higher for the forged material, furthermore, the as-extruded material in the radial direction exhibits virtually symmetric behaviour, whereas both the extrusion direction and forged material display similar levels of cyclic asymmetry in their stabilized hysteresis loops. It can be observed that at strain amplitudes below 0.4% the forged material exhibits superior fatigue life compared to the as-extruded material since the cyclic response is predominantly linear, and the peak and valley stresses are similar amongst all of the conditions. At higher strain amplitudes however, the higher peak tensile stresses induce more damage per cycle and result in a lower eventual life as compared to the as-extruded material. For the forged material, the variation in life at a given strain amplitude is quite low, indicating somewhat consistent fatigue properties at the various locations throughout the cross section of the forging which were investigated here. In general, the amount of total strain energy density for a given number of reversals to failure is somewhat insensitive to the material condition as can be observed in Figure 63b. This supports the observation in the  $\epsilon$ -N data that for the forged material at higher strain amplitudes, (where comparatively higher max and min stresses cause an increase in total strain energy density) a lower life is observed.

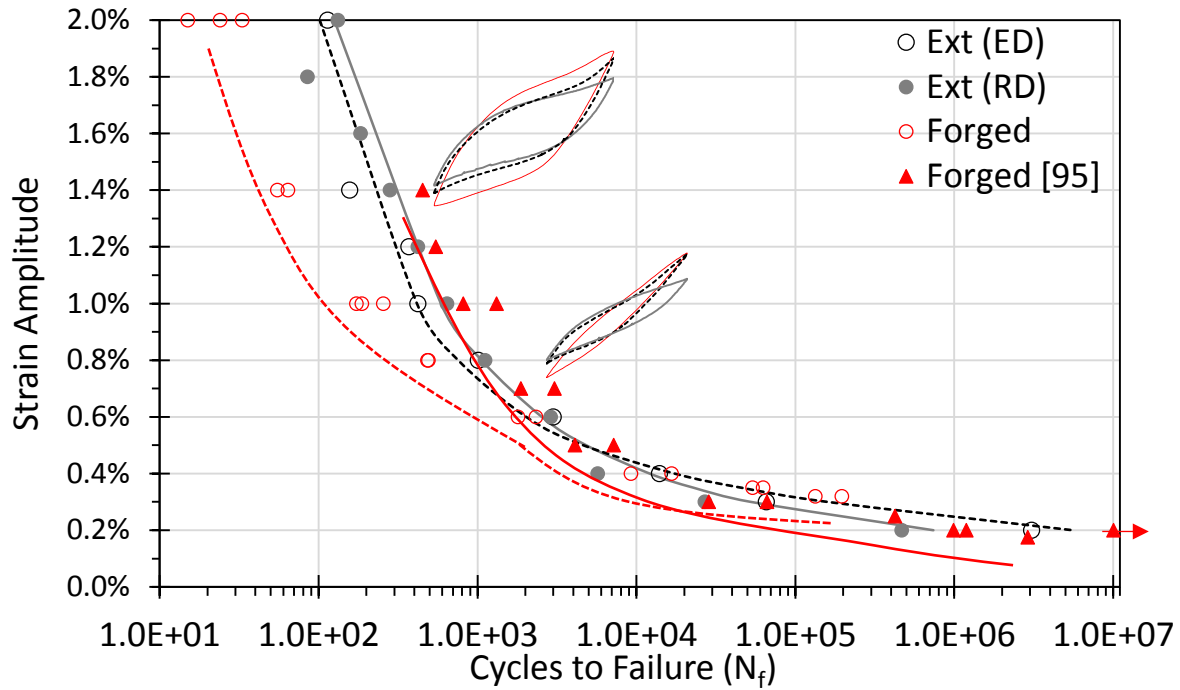


Figure 62 -  $\epsilon$ - $N$  curves for loading path A (pure axial) for as-extruded (black) and forged (red) AZ80 Mg alloy obtained at strain amplitudes between 0.2 and 2.0%. For reference, triangular symbols are included showing a previous study done on cast and forged AZ80 Mg by Gryguc et al. [95]. (For interpretation of the references to colour in this figure legend, the reader is referred to the web version of this article.)

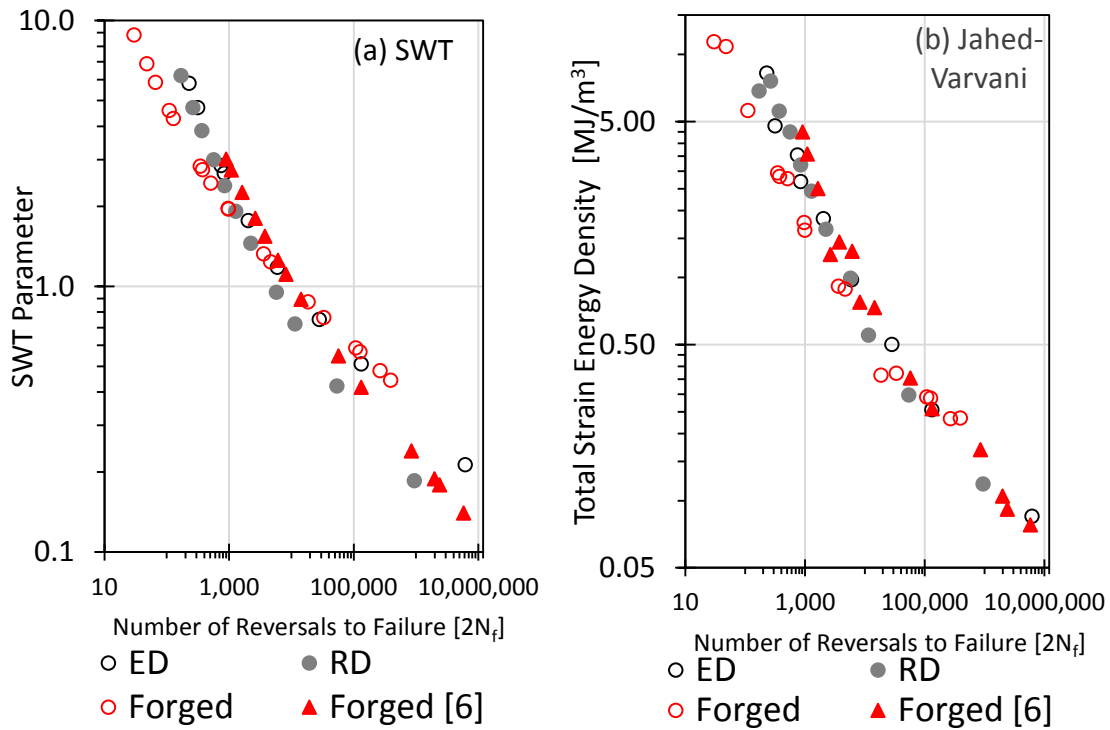


Figure 63 - Relationship between SWT damage parameter (a) and Total Energy (Jahed-Varvani) (b) vs. number of reversals to failure for loading path A (pure axial) for all three material conditions (ED, RD, forged).

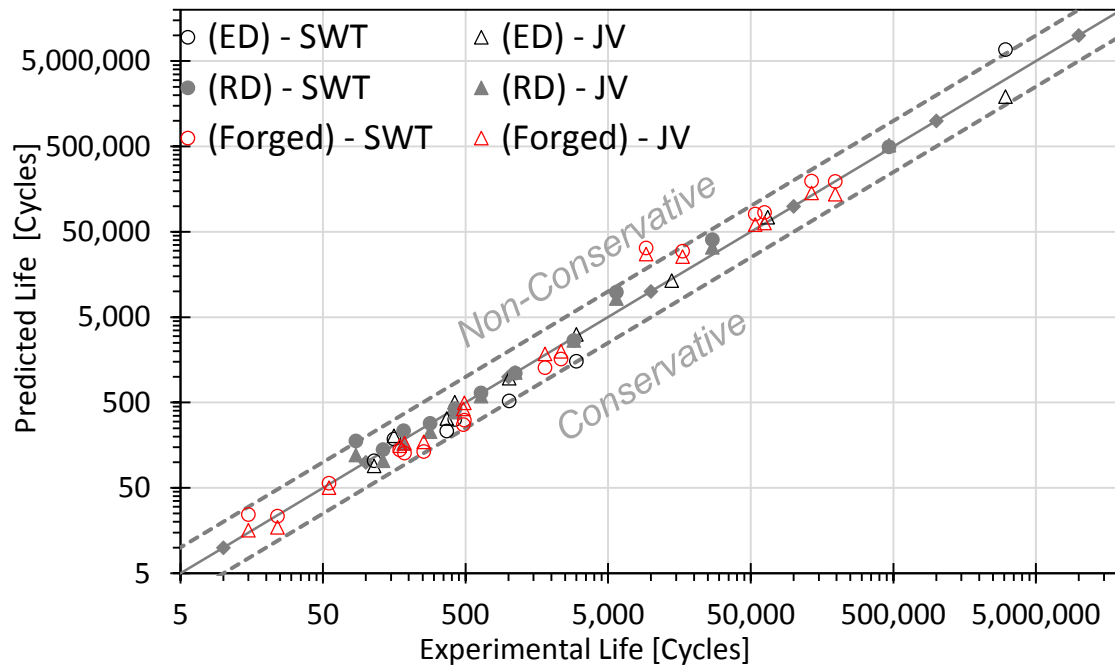


Figure 64 - Correlation between experimental life and predicted life for loading path A (pure axial) for all three material conditions (ED, RD, forged). Circular symbols denote life predictions using SWT model, and the triangular symbols denote life predictions using the Jahed-Varvani Model. The dashed lines denote bounds of  $\pm 2.0$ .

### 6.3.3. Biaxial Fatigue Life (Paths C, D and E)

Multi-axial cyclic tests were conducted by imposing fully-reversed axial and shear strains simultaneously at various strain amplitudes and/or phase angles. The axial strain amplitudes in particular were selected so as to induce adequate cyclic plasticity to observe any effects associated with the activation of profuse extension twinning. The results of these multiaxial experiments can be broadly deconstructed into two general classifications: (i) the effect of the proportionality constant between the axial and shear loading and the resultant influence on each other's cyclic behaviour, and (ii) the effect which phase angle has on the cyclic hardening, stabilized cyclic response and fatigue life.

Figure 65 illustrates the strain life ( $\epsilon$ -N) curves for closed die forged AZ80 extrusion for all of the five strain paths which were investigated. For comparison purposes equivalent strain amplitude is plotted vs number of cycles until failure. The equivalent strain amplitude for Paths A and B (pure axial and pure shear) is equal to each individual axes strain amplitude however, for the biaxial paths C, D and E, the equivalent strain amplitude is defined as the radius of the minimum circle inscribing the loading path in the  $\epsilon$  vs  $\gamma/\sqrt{3}$  strain space similar to that done by both Noban et al. [133] and Yu et al. [91]. It can be observed that for a given equivalent strain amplitude, the number of cycles until failure are highly dependent on the strain path, furthermore, the two non-proportional strain paths (D, E) exhibit

significantly shorter lives vs the other strain paths investigated. Both uniaxial strain paths exhibit similar  $\epsilon$ -N behaviour in the mid-cycle and high cycle regime (HCF), however in the low cycle regime (LCF) pure shear strain path B exhibits the shortest life for a given equivalent strain amplitude, this is congruent with what Xiong et al. [111] observed in the multiaxial behaviour of AZ31B Mg extrusion. Several researchers [20], [91], [109], [111], [132], [134] observe a “kink” in the strain life curve in wrought Mg alloys in the regime of life between  $10^3$ - $10^4$  cycles which varies depending on both the strain path and alloy/processing conditions. Castro et al. [134] observed a distinct kink in the  $\epsilon$ -N curve in pure axial fully reversed loading (path A) in extruded AZ31B Mg at a strain amplitude of  $\Delta\epsilon/2 = 0.45\%$  and describe it as being associated with a change of the salient deformation mechanism between twinning-detwinning activity dominating the plastic deformation above the kink point and dislocation slip below the kink point. Xiong et al. observed a similar phenomenon also in AZ31 extrusion, and they also linked the mean stress development with the plastic deformation mechanism. More specifically, they classified the axial mean stress development into 3 domains of plastic deformation mechanism; dislocation slip at low strain amplitudes (below the kink), partial twinning/complete detwinning above the kink and twinning exhaustion at in the LCF regime at strain amplitudes above 1%. They observe the kink to occur at a strain amplitude of  $\Delta\epsilon/2 = 0.35\%$  with mean stress progressively developing with increasing strain amplitude above the “kink” level reaching a maximum at 0.8%. At higher strain amplitudes this mean stress begins to decrease due to twinning exhaustion. Finally Yu et al. [91] observed this kink to occur at 0.5% in extruded AZ61 Mg alloy in a fully reversed pure axial strain path. Although not the focus of this particular work, evidence of similar “kinks” in the  $\epsilon$ -N curves have been observed here at strain amplitudes comparable to those cited by the aforementioned researchers, however the exact amplitudes are generally higher in this study since the strength of closed die forged AZ80 Mg is comparatively much higher than the other alloys previously investigated in literature. To truly characterize this transition amplitude between dislocation slip and partial twinning/complete detwinning plastic deformation mechanism, additional tests would need to be conducted at the strain amplitudes surrounding this “kink” region in the  $\epsilon$ -N curve, especially with the biaxial strain paths which only had few amplitudes investigated in this study. Furthermore, the lack of kink in the  $\epsilon$ -N curve of the as-extruded material in the radial direction, supports the symmetric behaviour of the material which was observed and lack of twinning-detwinning cyclic hardening mechanism, this agrees well with findings by Xiong et al in rolled AZ80 Mg sheet [20]. Finally, it can be observed that the proportional strain path C exhibited a fatigue life which was similar to the uniaxial paths, with the pure axial and pure shear paths representing an approximate upper and lower bound respectively. The two non-proportional strain paths exhibited comparatively shorter lives to the un-axial and proportional strain paths for a given equivalent strain amplitude with shorter lives occurring as loading became increasingly out of phase (Path E).

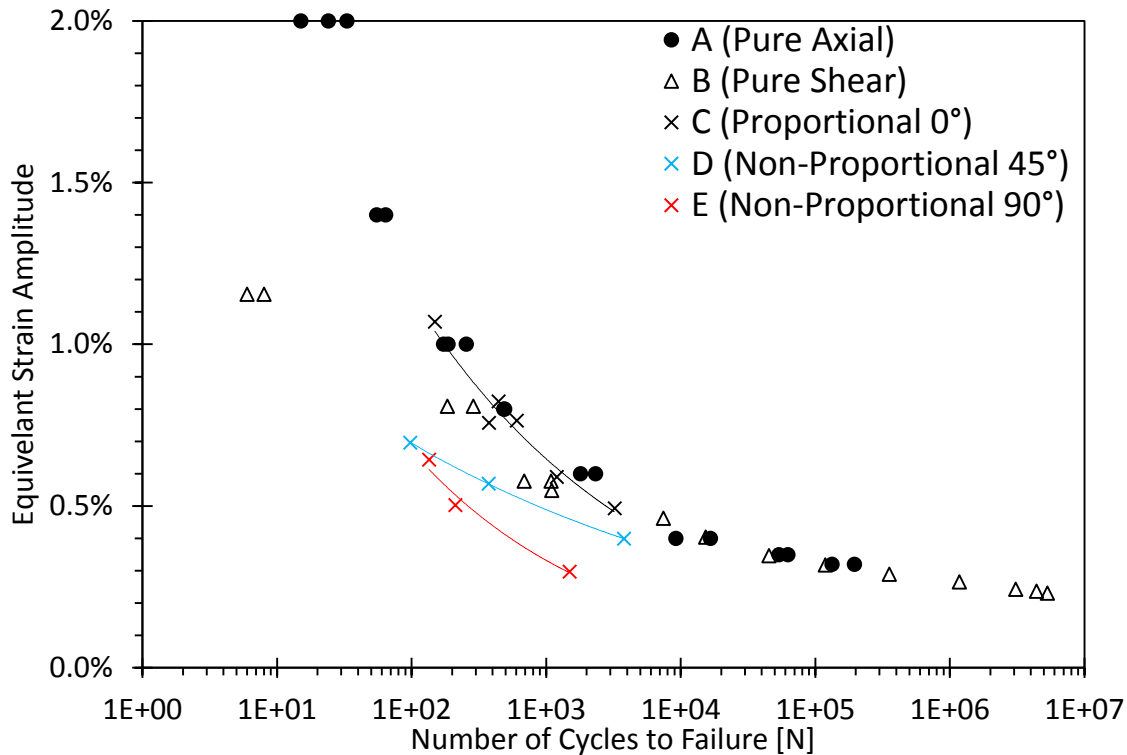


Figure 65 -  $\epsilon$ -N curves for loading paths A,B,C,D and E for the forged material

Figure 66 illustrates the stabilized half-life cyclic response for forged AZ80 Mg for a variety of different strain paths. Figure 66 (a) illustrates the axial and (b) shear hysteresis loops for a variety of different equivalent strain amplitudes for which the twinning-detwinning plastic deformation mechanism is significantly active. It can be observed that in (a) for the pure axial strain path A, moderate asymmetry and plastic strain energy density (SED) characterize the cyclic response with sharp peaks and valleys denoting boundary between ascending and descending reversals. The non-proportional strain path C is largely similar, with the exception that the controlled axial amplitude was slightly smaller, and the peak/valley stresses were marginally lower. The non-proportional strain paths (D and E) were virtually identical to one another, with peak stresses only marginally higher than the proportional case indicating a low level of sensitivity of the axial response to the phase angle in the biaxial loading. Figure 66b illustrates that for the stabilized shear response, the effect of non-proportionality and phase angle are pronounced. Firstly, the addition of 0.9% of axial strain to the pure shear strain path has the effect of dramatically decreasing the peak and valley stresses whilst retaining the symmetric nature of the response as illustrated by the rotated hysteresis loop in strain path C. Once the loading became non-proportional, the stabilized response's shape dramatically changed, with pronounced peak and valley tip blunting and comparatively linear ascending and descending responses. Furthermore, for strain path D (45° phase angle), the peak and valley stresses occurred out of phase from the peak and valley strains, more

specifically they occurred  $\sim 36^\circ$  prior to the peak and valley strains, a feature of the shear cyclic response which is unique to strain path D ( $45^\circ$  out of phase). This advancement of the peak and valley stress was not observed in the axial direction once again supporting the observation of a low level of sensitivity of the axial response to phase angle, a phenomenon which agrees well with the findings of Roostaei et al. [109] for extruded AM30 Mg alloy and Albinmoussa et al. [55] in extruded AZ31B. Strain path E ( $90^\circ$  out of phase) results in an increase in peak and valley shear stresses and a return of these peak stresses to be approximately synchronized with the peak strains. From a cyclic strain energy density (SED) perspective, the effect of non-proportionality and phase angle on the axial component is virtually non-existent. However, that is not the case for the shear response which is characterized by a large decrease in elastic SED and a large increase in plastic SED in proportional loading, and a moderate change in the elastic and plastic SED's with changing phase angle. In general, the cyclic energy in the axial direction is virtually insensitive to the presence of the second axis of loading, its proportionality constant or its phase angle, whereas in the shear direction, the proportionality constant (or axial strain amplitude) and phase angle playing a significant role in the magnitude of the cyclic energy.

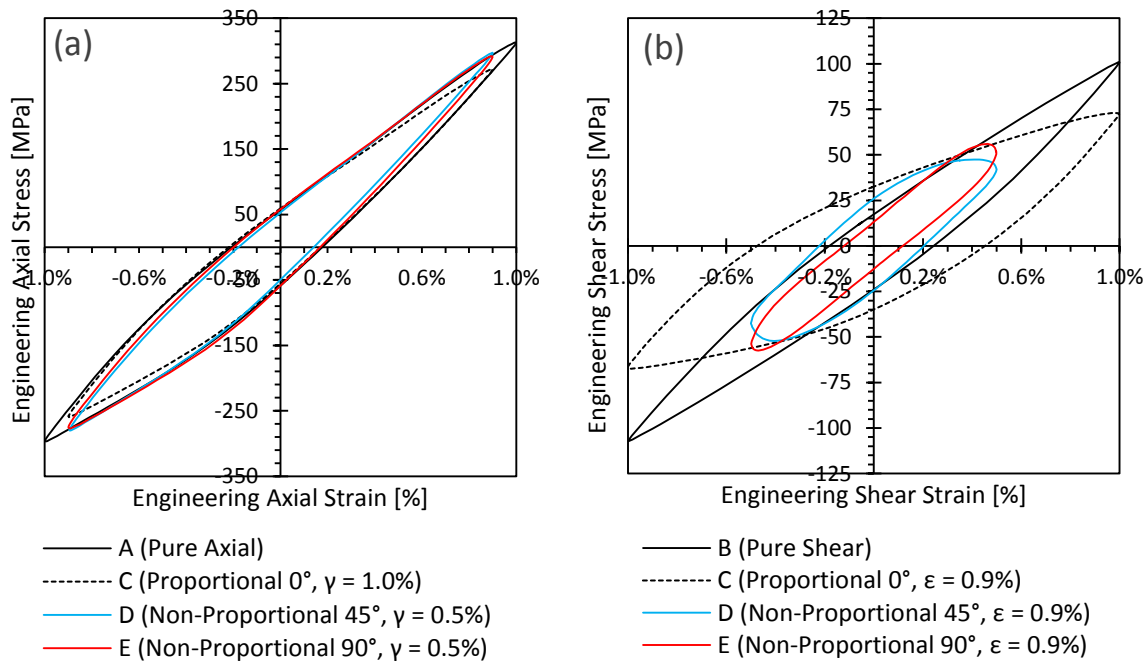


Figure 66 - Stabilized cyclic hysteresis loops for (a) axial and (b) shear for various strain paths. For biaxial paths (C, D and E) the corresponding strain of the other axis is shown following the phase angle.

Energy-based fatigue damage models have been used by many researchers for modeling the uniaxial fatigue life of Mg alloys, e.g., Park et al. [59], [80] in rolled AZ31, Xiong et al. [20] for rolled AZ80. Furthermore, limited work by Albinmoussa et al. [56], [81] for extruded AZ31 and Roostaei et al. [109] for extruded AM30 has been done to model wrought Mg under multiaxial strain paths. In this study, the

JV energy based model [82] is utilized to predict the biaxial fatigue life. Multi-axial fatigue life predictions were obtained by considering independent uniaxial fatigue life predictions for both the axial ( $N_a$ ) and shear ( $N_s$ ) models assuming the total multi-axial energy dissipation ( $E_{Total}$ ) to be equal to the summation of the axial and shear SED's ( $E_a$  and  $W_s$  respectively). These independent axial/shear life predictions were obtained using the uniaxial damage models which were independently calibrated using the material constants for pure axial and pure shear (Table 10 and Table 11 respectively) and then were weighted by considering the ratio of axial/shear energy to total multi-axial energy according to:

$$N_f = \left( \frac{E_a}{E_{Total}} N_a + 0.3 * \frac{W_s}{E_{Total}} N_s \right) \quad \text{where } E_{Total} = E_a + W_s \quad (12)$$

A coefficient of 0.3 was utilized to scale the shear component of the life prediction model similar to what Roostaei et al. [109] utilized for extruded AM30. The physical significance of this correction factor is to bias the overall life prediction to match qualitatively with the type of crack orientation that is observed in the biaxial failures. More specifically, if shear cracks (similar to those longitudinal cracks observed in pure torsion) are the mode of failure in biaxial loading, the biaxial shear coefficient should increase in magnitude (to bias the overall life prediction to be closer to that of the pure shear response). For tensile cracking (which was observed here), the biaxial shear coefficient should decrease to account for the relative importance of the axial damage mechanisms in the crack orientation during early crack growth. A biaxial shear coefficient of 0.3 yields the best predicted life for the biaxial data presented in this study. Roostaei et al. [109] utilized a value of 0.5 stating that the shear cracking mode is dominant for the AM30 alloy. Figure 67 illustrates the relationship between total SED and number of reversals to failure for the forged material for a variety of different strain paths. It can be observed that the strain path has a large effect upon amount of total SED for a given life. Path B (pure shear) exhibits a dramatically different response as compared with the pure-axial and multi-axial cases. This can be attributed to the different cracking mode observed in Path B loading, and provides further justification for the implementation of biaxial shear coefficient of 0.3. Furthermore, the amount of total SED for a given number of cycles decreases when biaxial loading is introduced, though following the same general relationship as the pure axial strain path. Using the parameters given in Table 10 and Table 11, the fatigue life was predicted for the forged material and is plotted versus the experimental life in Figure 68. The solid diagonal line denotes a correlation match between the predicted and experimental life, and the dashed lines represent bounds that envelop deviation from this match by a factor of 2. The vast majority of life estimations fall within these bounds of a factor of 2, furthermore, the uniaxial and proportional strain path predictions are very reliable with almost equal numbers of data being under and over predicted. The non-proportional

biaxial predictions however tend towards being non-conservative, especially strain path E (90° out of phase) which has a few predictions that fall marginally outside the bounds of 2.

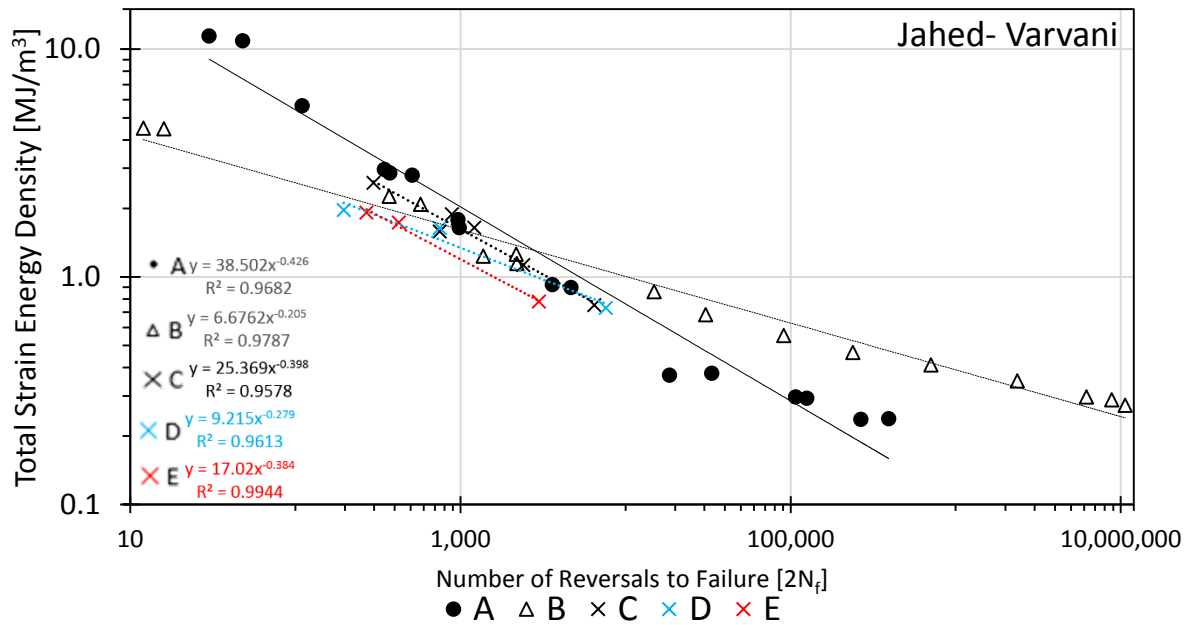


Figure 67 – Relationship between Total Energy (Jahed-Varvani) vs. number of reversals to failure for the forged material for loading paths A,B,C,D and E.

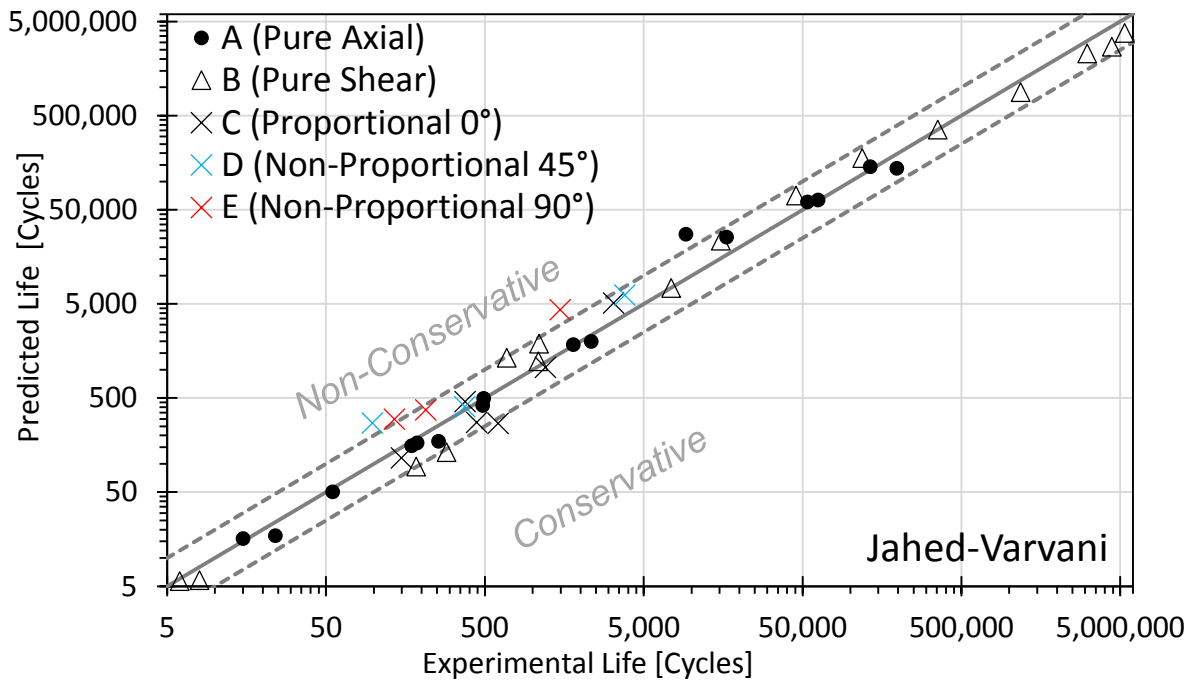


Figure 68 - Correlation between experimental life and predicted life for the loading paths A,B,C,D, and E for the forged material. The dashed lines denote bounds of ±2.0.

#### 6.3.4. Fracture Mechanisms

An examination of the early crack growth behaviour of forged material under two different uniaxial strain paths (monotonic and cyclic) and 3 different biaxial strain paths is shown below in Figure 69. It can be observed that for pure shear strain paths Figure 69 (b and d), the early crack growth is in the longitudinal direction (along the axis of the sample), whereas all other strain paths exhibit evidence of transverse early crack growth. This indicates that the axial loading is dominating both the cyclic response and early crack growth, as a transverse crack is congruent with the critical plane for failure in axial loading. Figure 70 highlights the morphology of the fracture surface for a sample subjected to pure axial strain (path A) and a non-proportional biaxial strain path with a phase angle of  $90^\circ$ . It can be observed that for two different strain paths and two different specimen geometries, failure initiated at the surface of the specimen, and the crack propagated such that the plane of the short crack was consistently in a direction perpendicular to the axis of the specimen. These observations agree very well with those found by other researchers [132], [134] for various other forms of wrought Mg. Important to note is that it is well known that for a strain path, several material planes might exhibit identical or similar fatigue damage, however inhomogeneity in the material may favour crack initiation on a plane which does not coincide with the same plane of maximum fatigue damage. Thus the fractography results presented here are a cursory observation intended to highlight the dependence on the macroscopic crack growth plane on the strain path and to provide a qualitative justification towards axial strain energy density being a comparatively more significant damage quantity relative to shear SED in multiaxial loading for forged AZ80 Mg.

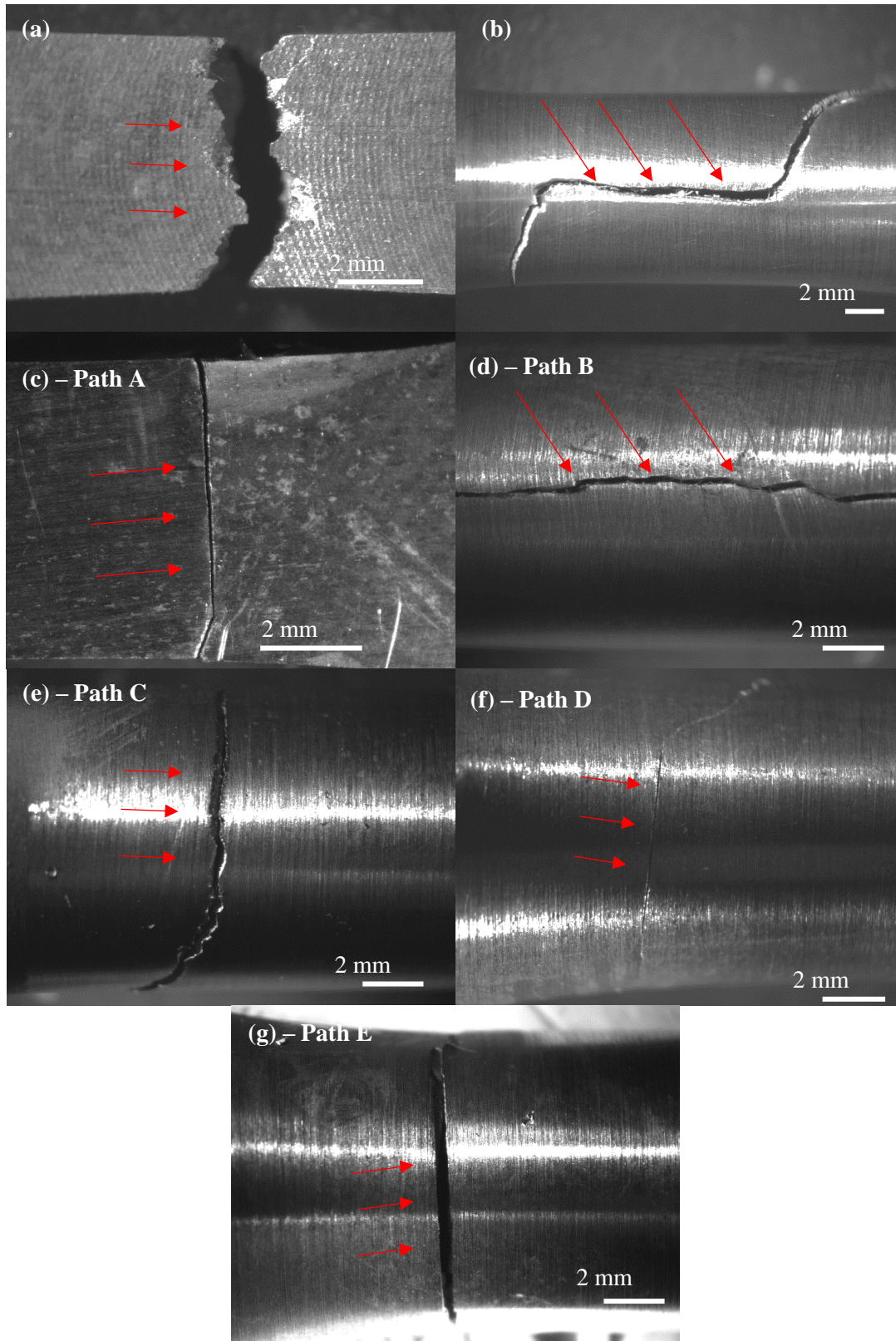


Figure 69 – Macroscopic crack path of forged specimens: (a) monotonic axial (b) monotonic shear, (c) path A  $\Delta\epsilon/2 = 0.4\%$  and  $N_f = 9220$  cycles, (d) path B  $\Delta\epsilon/2 = 0.7\%$  and  $N_f = 15\,296$  cycles, (e) Path C,  $N_f = 1201$  cycles, (f) Path D,  $N_f = 3798$  cycles, (g) Path E,  $N_f = 1492$  cycles. Scale bars shown for reference.

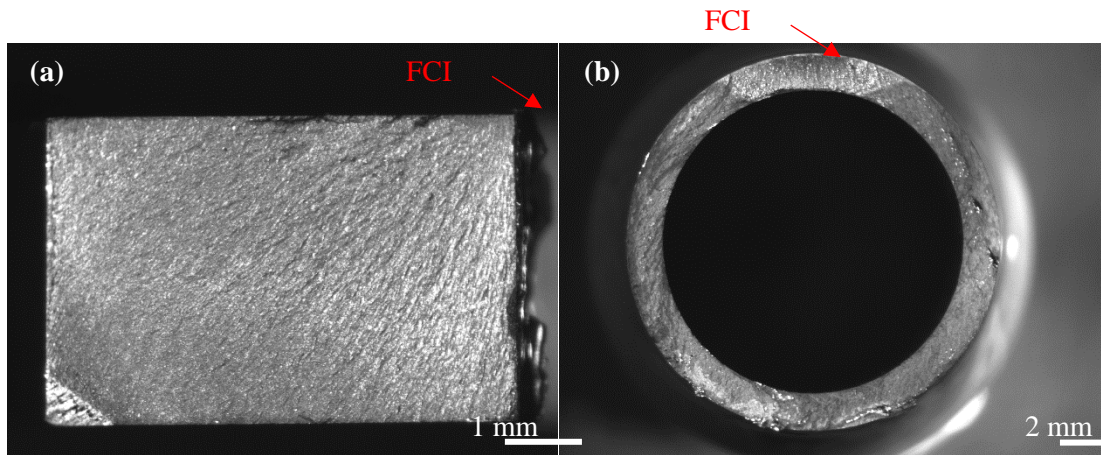


Figure 70 – Fracture surface of (a) path A  $\Delta\varepsilon/2 = 0.4\%$  and  $N_f = 9220$  cycles and (b) Path E,  $\Delta\varepsilon/2 = 0.4\%$ ,  $\Delta\gamma/2 = 0.5\%$ ,  $N_f = 1492$  cycles. Fatigue crack initiation site is denoted by 'FCI'. Scale bars shown for reference.

#### 6.4. Conclusions

The quasi-static and cyclic response of as-extruded and closed-die extruded-forged AZ80 Mg alloy forged at 250°C and 20mm/sec was investigated. Servo hydraulic, fully reversed, strain controlled uniaxial "push-pull", pure torsion, and biaxial fatigue testing were also conducted on the closed-die forged alloy. Two uniaxial loading paths (pure axial and pure shear) and three different biaxial loading paths were investigated (proportional loading, and non-proportional loading at phase angles of 45° and 90°). Based on the results, the following conclusions can be drawn.

1. After forging of the as-extruded billet, the yield stress in the axial direction increased by 46%, the failure elongation by 35% and the ultimate strength by 13%.
2. The web region in the center of the forged billet exhibited a virtually fully recrystallized and refined microstructure with intense texture, whereas the rib regions on each side exhibited a partially recrystallized and coarser microstructure with less intense local texture.
3. The fatigue life of the forged material in the axial direction showed dramatic improvement relative to the as-extruded material at strain amplitudes which were less than 0.35%.
4. For the pure axial strain path, the total amount of strain energy density (SED) observed in the stabilized response was a function of number of cycles only, and was insensitive to material condition (as-extruded or forged).
5. For the forged material, of all the strain paths investigated, only the pure shear path demonstrated a significantly different relationship of total SED vs. life.
6. The effect of a decrease in total SED for a given number of cycles occurred in all biaxial strain paths, with proportional being the least prominent, then 45° and 90° out of phase being progressively more pronounced respectively.

7. The biaxial fatigue response is somewhat dominated by the axial component for two significant reasons; firstly, the shape of the hysteresis in the shear direction dramatically changes based on phase angle and axial strain amplitude, whereas in the axial hysteresis loop remains somewhat invariant to the presence of the other loading axis.
8. The initial crack propagation mode is predominantly transverse to the axial direction in all strain paths except for pure shear (which exhibits longitudinal cracking).

## 7. Discussion

The following chapter discusses the impact of the discovery level knowledge in the preceding three chapters towards real-life engineering applications. The focus of the chapter is advanced vehicle lightweighting using forged Mg alloys. The motivation of this chapter is to provide further discussion in the context of the research objectives that was not addressed in the journal articles, as well as pragmatically summarize the scientific contributions by comparing and contrasting the behaviours of all of the material conditions investigated. A discussion of the forging process optimization procedure will outline optimization function that was developed to select the optimum forging condition for advanced vehicle lightweighting applications. These key contributions align very well to satisfy research objectives 5 enabling effective utilization of forged AZ80 Mg as a lightweight material in structural applications which are fatigue critical.

### 7.1. Advanced Vehicle Lightweighting using Forged AZ80 Mg Alloy

Reducing vehicle weight is an important approach for increasing fuel economy, addressing regulatory requirements, and meeting consumer needs. Magnesium alloys are among the lightest structural metals and offer tremendous weight saving potential; however, many technical and commercial barriers limit their use in today's automotive industry. A critical barrier that needs to be overcome to adopt such a material is the difficulty in processing magnesium via a forging method to create near-net shape components. The culmination of this thesis work aims to develop the technology to enable automotive manufacturers to successfully produce high quality forgings, as well as the knowledge required for mechanical characterization, fatigue life prediction. AZ80 is already a widely commercially available alloy with good strength and ductility in wrought form, however the ability to forge it, and the resulting properties are obstacles which currently inhibit its widespread adoption. In addition to this knowledge developed in the thermomechanical process characterization, optimization of the forging conditions for automotive front lower control arm applications. However, this discussion is applicable towards lightweighting of automotive structural components in general using forged AZ80 Mg alloy.

### 7.2. Forging Process Optimization

The forging process is quite complex as it has a number of parameters which influence the thermomechanical history of the material. The temperature profile, strain rate, total strain, material flow path and induced stress state are all factors which influence the quality of the final forged product. A high quality forging in the context of this work has a number of different attributes, where the relative importance of each attribute is dictated by the requirements of the specific engineering application. Firstly, a high quality forging can be considered to be one with good dimensional accuracy (relative to the

desired geometry) free of underfills, cold shuts or warping. Secondly, it possess a smooth surface finish free of defects which have the potential to initiate cracks under cyclic loading. Finally, and arguably most important is that the forged product possesses the properties (from both a mechanical and fatigue sense) which enable it to have high performance with respect to these aforementioned application requirements. In addition to these optimum properties, careful attention must also be paid to ensure the spatial variation in these parameters is low, as to ensure a consistent quality throughout the forging and prevent local areas within the forging volume which possess inferior properties to limit overall optimal performance from being achieved. These aforementioned parameters are highly coupled to one another in a way that a holistic approach was adopted in the method of optimizing the process to produce the highest quality forging. Equation 13 illustrates the form of an objective function which is used in generating a non-dimensional parameter which represents how “optimal” a given forging condition is. The objective parameter  $\Phi$  is formulated in such a way that higher values represent a more optimal solution (i.e. the objective function will achieve a maximum for an optimal solution). The individual terms in the function  $\varphi_1, \varphi_2$  and  $\varphi_3$  are components which are (*from a physical nature*) connected to the aforementioned attributes which characterize a high quality forging.  $\varphi_1$  is a parameter which takes into account the quasi-static behaviour of the material,  $\varphi_2$  the fatigue behaviour and  $\varphi_3$  the spatial variation in the properties. The coefficients for each term were selected based upon meeting the set of requirements for the specific engineering application investigated here (a front lower control arm in an automobile). This function was effectively calibrated using these coefficients in connection with the relative importance of application requirement, and thus can be recalibrated to suit a variety of different engineering applications.

$$\Phi = 0.5\varphi_1 + 0.4\varphi_2 + 0.1\varphi_3 \quad (13)$$

Equation 14 allows one to look at each component of the objective function in more detail,  $\varphi_1$  can be considered to have the highest importance as it governs the domain of properties which are important for strength and ductility driven loadcases. The parameter  $S_y^T$  represents the yield strength of the forged material for a given forging condition (forging temperature and rate), where  $S_{y,max}^T$  represents the maximum yield strength observed in all the investigated forging conditions. Similarly,  $E^T$  represents the strain energy density which the material exhibits under monotonic loading to a maximum plastic strain of  $\epsilon_p = 4.5\%$ . Equal weighting is given to both the strength and ductility parameters as a combination of both is important to satisfy the quasi-static requirements of the engineering application investigated in this work. Figure 71 graphically illustrates the definition of each component of the static behaviour term in the objective function.

$$\varphi_1 = 0.5 \frac{S_y^T}{S_{y,max}^T} + 0.5 \frac{E^T}{E_{max}^T} \quad (14)$$

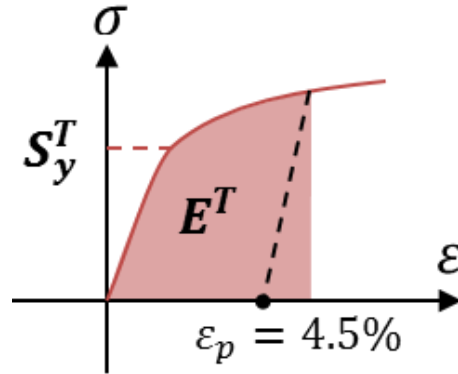


Figure 71 - Definition of components of static behaviour contribution to the objective function.

Equation 15 illustrates the contribution of the fatigue behaviour towards the objective function.  $\sigma'_f$  is the fatigue strength coefficient as extracted from the traditional basquin parameters of average S-N fatigue properties for a given forging condition. Similar to  $\varphi_1$ ,  $\sigma'_{f,max}$  represents the maximum value of the fatigue strength coefficient over all of the forging conditions investigated. The  $b$  parameter represents the fatigue strength exponent, and  $b_{min}$  and  $b_{max}$  represent the maximum and minimum strength exponents observed over all of the forging conditions investigated. More weighting is given towards the strength coefficient as this favours optimum performance in the low to mid cycle fatigue cases which represent the most damaging cases for the engineering application which is of the focus of this work.

$$\varphi_2 = 0.65 \frac{\sigma'_f}{\sigma'_{f,max}} + 0.35 \frac{b_{max} - b}{b_{max} - b_{min}} \quad (15)$$

A graphical representation of the two fatigue behaviour parameters can be seen in Figure 72, important to note is the fact that if spatial variation in the fatigue properties throughout the forging is pronounced, engineering judgement must be used to ensure reliable and conservative approaches are used in calculating the requisite parameters.

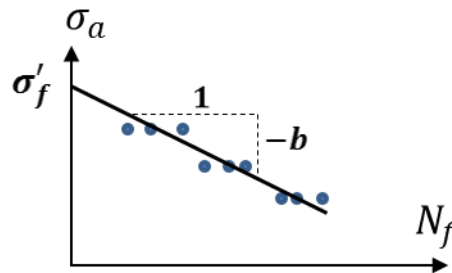


Figure 72 - Definition of components of fatigue behaviour contribution to the objective function

Equation 16 illustrates the contribution which spatial variation in superficial hardness has on the objective function.  $H$  represents the standard deviation in the superficial hardness over the entire cross section.  $\varphi_3$ , effectively represents where in the range of standard deviations the specific forging condition lies (i.e. is it the highest level of spatial variation in superficial hardness, or the lowest). Somewhat pragmatically, superficial hardness was used as a parameter to infer spatial variation of properties since many measurements throughout the cross section could be obtained in a relatively short period of time without sacrificing much of the bulk volume of the forging. There is substantial literature to support the correlation between Rockwell hardness and tensile strength, thus as a “screening” technique to assess the spatial variation in hardness (and infer that it correlates to spatial variation in properties) can be considered to be rigorous for this application.

$$\varphi_3 = \frac{H_{max} - H}{H_{max} - H_{min}} \quad (16)$$

Figure 73 illustrates contour plots of superficial hardness throughout the cross section of forgings done at 300°C. It can be observed that since both hardness maps are plotted to the same scale, more colour uniformity will equate to lower standard deviation in the hardness and thus lower spatial variation in the properties (as can be seen in the (b) the extruded-forged condition).

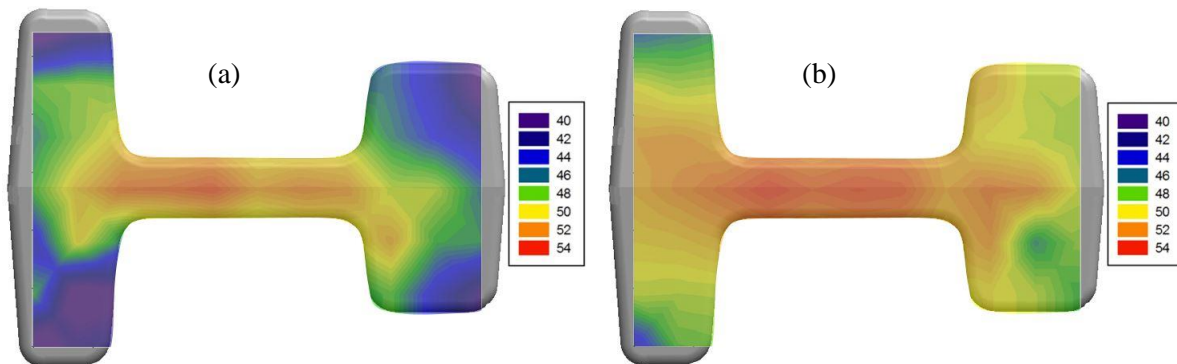


Figure 73 - Superficial hardness maps from forgings done at 300°C. (a) Cast-Forged AZ80, (b) Extruded-Forged AZ80, (30T scale).

Now the three components of the objective function are utilized to generate an optimization parameter for each of the investigated forging conditions (a variety of forging temperatures and rates). Once again, this optimization parameter is non-dimensional in nature and is formulated in such a way that higher values equate to a more optimal solution (i.e. higher quality forging). It can be observed in Figure 74 that the forging of as-cast material results in a less optimal solution (i.e. a lower quality/performance forging) compared with forging as-extruded material for all of the conditions which were investigated. It can be seen that the topology of the optimization surface for both base materials favours lower temperatures and higher strain rates as producing an optimal result. It can be observed that the objective function is more

sensitive to temperature than to strain rate (that is to say that temperature has more of an influence on the quality of the forging than the strain rate).

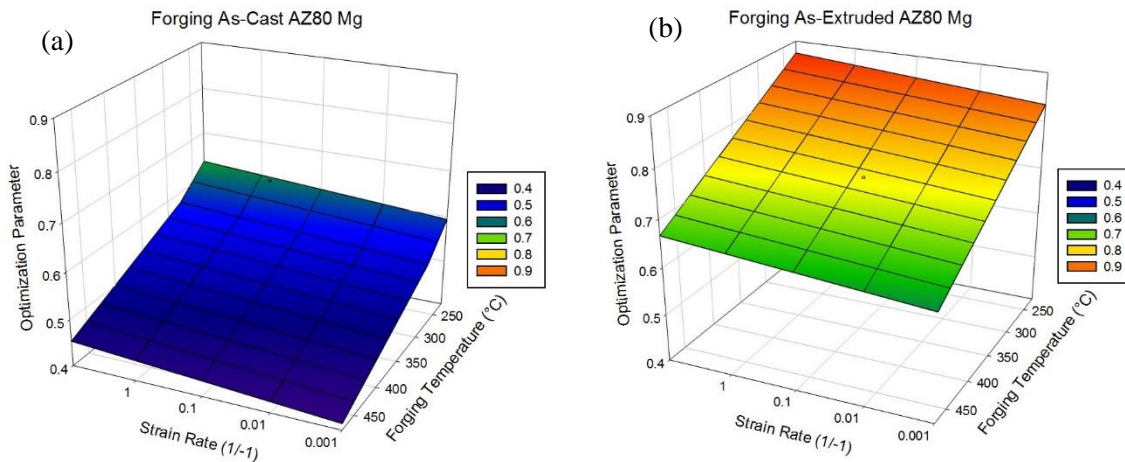


Figure 74 - Optimization surfaces for (a) as-cast then forged and (b) as-extruded then forged material for AZ80 Mg. Areas in red indicate the processing temperature and strain rate which results in the optimum performance of the forged material.

Based on these surfaces illustrated in Figure 74, one can easily conclude that free of practical processing constraints the most optimal forging condition for AZ80 Mg is to begin with as-extruded material and forge at 250°C and 10 s<sup>-1</sup> as it has the highest resulting objective function value. However, there are some additional constraints which limit this processing window. From a temperature perspective, incipient melting occurs of the Mg<sub>17</sub>Al<sub>12</sub> phase at 427°C [10], which acts as a upper bound on the process window to ensure no shrinkage or cold shut defects occur or segregation within the microstructure. The lower bound is less exact and depends upon which defects manifest themselves and their severity, typically both macroscopic and microscopic cracking (especially at the extremities of the forging where edge stretch is pronounced) will occur. These types of defects typically occur below 250°C and are undesirable as they produce a forging which has incipient cracks that have dramatically fatigue performance. These thresholds both depend upon on the strain rate, as higher strain rates instigate higher flow stresses (thus causing poor material flow in the colder temperatures), and can induce more heat of deformation (thus exacerbating the likelihood of incipient melting close to the upper threshold of temperature). Coupled with this is the separate constraint that the flow behaviour of AZ80 Mg alloy is highly dependent on strain rate as well, more specifically the peak and steady state flow stresses increase with increasing stain rate [37]. This has the resultant effect of increasing the press tonnage required to fully forge the material at a given temperature. Often this poses a hard physical constraint as operating within a certain domain of the processing window will not be feasible as the required force to forge the material is too high for the equipment being utilized. Figure 75 illustrates the peak flow stress for forging of both as-cast and as-extruded material. Comparison of peak flow stress for various forging conditions can act as a conservative indicator as to what the required forging load will be for a given processing

condition. It can be observed that decreasing temperature and increasing the strain rate has the effect of increasing the flow stress. Furthermore, the peak flow stress of the as-extruded material higher than that of the as-cast material, as one might expect due to the wrought form of AZ80 Mg having higher strength at room temperature. Important to note is that these flow stresses are reported in a simple upset open die forging of cylindrical billets (similar to those investigated in chapter 4), and although general trends may apply towards closed die forging of more complex and multi-dimensional material flow paths, the information should be used as reference only for those types of cases. The nature of these response surfaces results from the limited number of slip systems magnesium has available at room temperature. However, the individual CRSS's for several slip systems begins to dramatically decrease with increasing temperature (as was discussed in section 2.1.4 and Figure 7 of this thesis), thus collectively lowering the overall flow stress from the bulk deformation of the material. These pragmatic constraints of physically being able to forge the material free of undesirable defects in combination with optimizing the developed objective function comprised the methodology for selection of the optimum forging condition for this advanced vehicle lightweighting application of extruded then forged at 250°C and 20 mm/sec

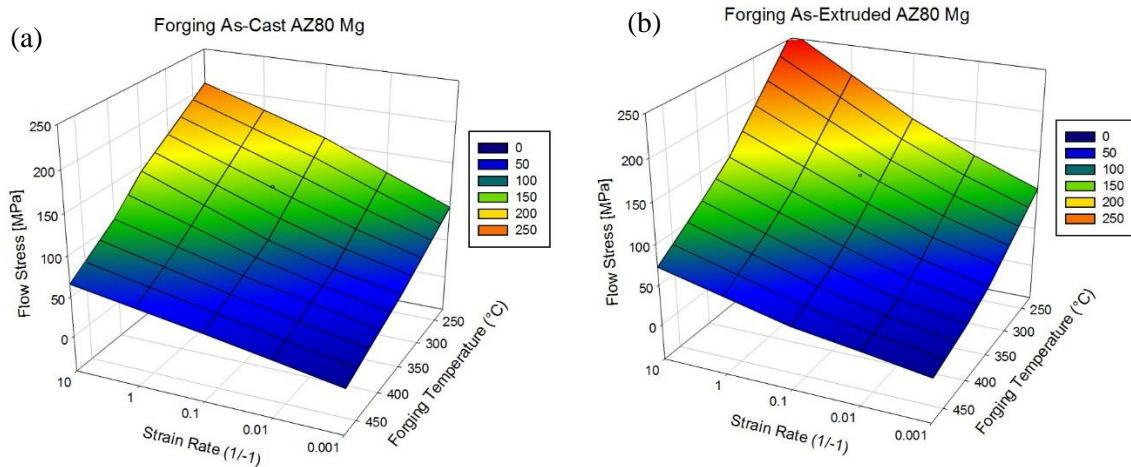


Figure 75 - Peak flow stress for (a) as-cast then forged and (b) as-extruded then forged material AZ80 Mg alloy. Areas in red indicate the processing temperature and strain rate which results in the highest flow stress during isothermal open die simple upset forging of cylindrical billets. Data shown for extruded material was taken as the maximum from either the radial or transverse directions.

Each journal article which comprises this thesis focuses on characterizing different forged material conditions somewhat in isolation, however comparing and contrasting the strain life ( $\epsilon$ -N) and energy life curves amongst all of the investigated material conditions can provide valuable insight into how a given material condition will behave in fatigue critical applications. Table 12 summarizes all of the relevant strain life (Coffin-Manson) and energy life (Jahed-Varvani) parameters in the axial direction for the base materials, and two varieties of forged material.

Table 12 - Summary of the axial loading path strain life ( $\epsilon$ - $N$ ) and energy life parameters for all the investigated material conditions.

Material		Axial (Path A)							
		Coffin-Manson (SWT)				Energy (Jahed-Varvani)			
		Chapter	$\sigma_i'$ [MPa]	b	$\epsilon_i'$	c	$E_e'$ [MJ m <sup>-3</sup> ]	$E_f'$ [MJ m <sup>-3</sup> ]	B
As Cast (Average)	4	479.6	-0.141	0.271	-0.577	3.5861	68.39	-0.309	-0.555
As Ext (ED)	6	566.3	-0.111	0.975	-0.808	8.5934	410.91	-0.306	-0.796
As Ext (RD)	6	485.3	-0.125	0.505	-0.646	1.8670	318.91	-0.209	-0.715
Cast-Forged (Open-Die Forged @ 350-450°C)	4	598.4	-0.131	0.340	-0.576	7.9094	758.6	-0.304	-0.836
Extruded-Forged (Closed-Die Forged @ 250°C)	6	527.5	-0.103	0.13	-0.626	3.6831	113.87	-0.225	-0.709

Using the appropriate modelling parameters shown in Table 12, Figure 76 graphically illustrates the strain life curves between axial strain amplitudes of 0.2-1.0% for all of the investigated material conditions. It can be seen that the low cycle regime generally favours material conditions which have a high ductility (as the life for a given amount of strain is the highest), whereas the high cycle fatigue regime generally favours those materials with highest strength. It can be observed that the effect of forging on the cast base material is an improvement in both the low and high cycle regimes since both the strength and ductility were dramatically improved through the thermomechanical processing. However, for the extruded and forged material and improvement relative to the base material is only realized in the high cycle regime since in general the strength was marginally increased at the compromise of ductility and texture intensification.

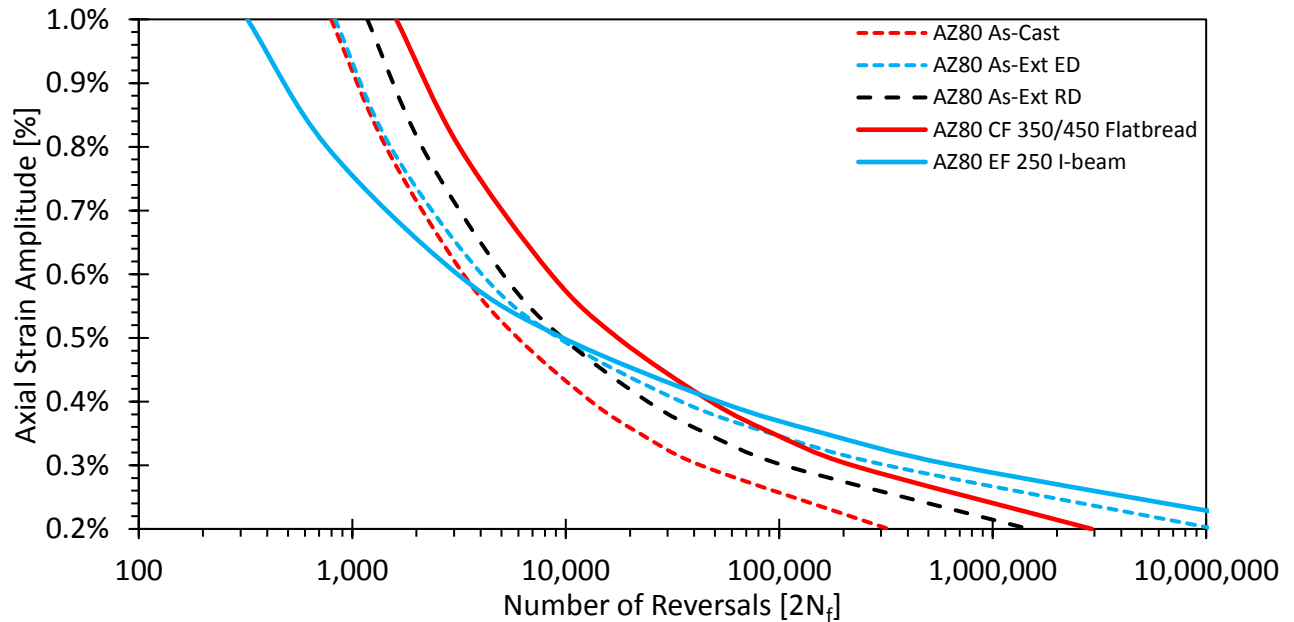


Figure 76 –  $\epsilon$ - $N$  curves for all of the investigated AZ80 Mg material conditions

Using the appropriate modelling parameters shown in Table 12, Figure 77 graphically illustrates the energy life curves between strain energy densities of 0.1-10 MJ/m<sup>3</sup> for all of the investigated material

conditions. Similar conclusions can be drawn to those from the strain life model, however this representation of the data signifies the materials ability to tolerate fatigue damage. For a given lifetime (number of reversals), if a material has a higher total strain energy density in its stabilized cyclic response it can be said that it tolerates a larger amount of fatigue “work” (that is to say strain energy per unit volume) before failure. Important to note is the convenience of this representation being a scalar quantity and thus invariant of material direction, however, the modelling parameters intrinsically have material parameters embedded in the fatigue data utilized in the modelling methodology.

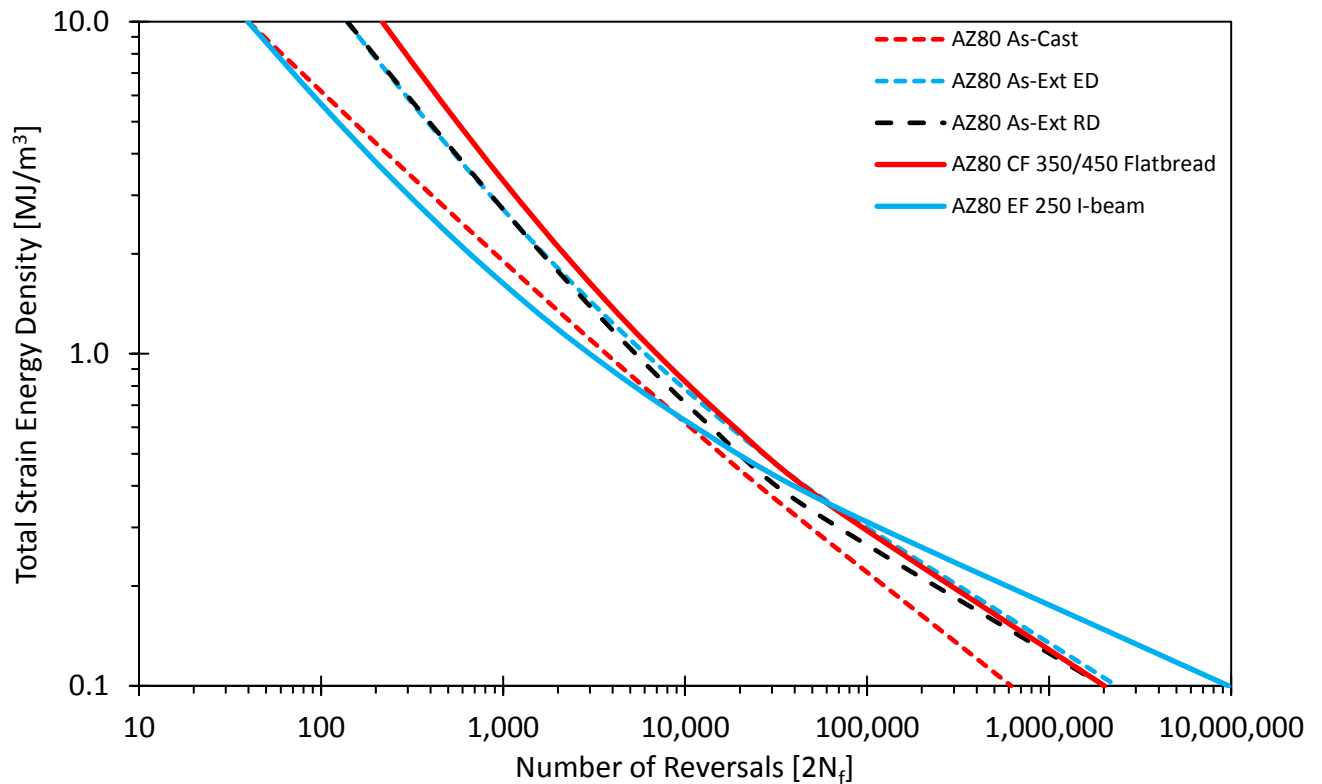


Figure 77 - Energy Life curves for all of the investigated AZ80 Mg material conditions

### 7.3. Conclusions

To summarize, a number of different methodologies have been adopted to characterize the mechanical and fatigue behaviour and model the fatigue life of several forms of AZ80 Mg and assess their suitability for advanced vehicle lightweighting applications. An optimization function was developed that has its foundation in the physical nature of the structural requirements imposed by the engineering application, this allowed rigorous selection of an optimal forging condition for the front lower suspension control arm which is the target engineering application in this work. It was concluded that the optimal forging condition is the coldest temperature and fastest strain rate which are pragmatically possible which produce a forging free of defects and of high quality. This corresponded to extruded AZ80 Mg forged at a

temperature of 250°C and 20 mm/sec being the optimal conditions for the style of closed die forging investigated here. The weighting of each individual component of the optimization function was determined based upon the engineering requirements of the investigated application, but can be calibrated for other advanced vehicle lightweighting initiatives. An overview of the modelling parameters used to predict the fatigue life was discussed and each material condition was compared and contrasted to enable both those within the research community and those within industry to utilize AZ80 Mg to make prolific contributions towards advanced vehicle lightweighting initiatives.

## 8. Summary, Conclusions and Future Work

### 8.1. Summary

In summary, the research objectives of this work have been fulfilled through the comprehensive experimental and modelling campaigns highlighted within this thesis. A comprehensive introduction which frames the context and motivation for this research work was discussed. More importantly, the research objectives were founded upon addressing the knowledge gap in the current state-of-the-art within the field and constructed as to make this a novel and useful research undertaking. Secondly, an exhaustive literature review highlighting the key works surrounding the fatigue of AZ80 Mg was conducted and summarized. Next a detailed overview of the research methodology was presented to enable future researchers to not only replicate the experimental and modelling data presented here, but build upon it to achieve even greater scientific contributions moving forward. Over the course of this work, 6 articles have been published in international journals, 3 of which have been presented here. This work has also been disseminated at over 6 international conferences with a variety of poster and oral presentations which have been well received. Furthermore, countless exhibitions of this research have been conducted in the form of update meetings, oral presentations, seminars, amongst both other academics and industry partners to facilitate knowledge transfer and foster the strong connection between this discovery level research and the widespread engineering application.

### 8.2. Conclusions

Summarizing the conclusions of the research work presented here is a vast undertaking. The research objectives form the basis for which the conclusions were drawn, and are reiterated below:

1. To characterize the effect of forging on the mechanical properties of both cast and extruded AZ80 Mg.
2. To develop an understanding of the influence of texture on the cyclic deformation mechanism and fatigue life.
3. To characterize the cyclic response and fatigue behaviour of forged AZ80 Mg in a variety of different loading paths.
4. To predict the fatigue life of forged AZ80 Mg in a variety of different loading paths.
5. To enable the effective utilization of forged AZ80 Mg as a lightweight material in structural applications which are fatigue critical for a variety of engineering applications.

Firstly, uniaxial strain controlled fatigue experiments were conducted at various strain amplitudes, ranging from 0.1–1.4% of both as-cast and open-die forged AZ80 Mg alloy. The effects of various forging parameters (temperature and strain rate) were investigated on a comparative basis. Based on the results the following conclusions can be drawn which act to address research objectives (1, 2, 3 and 4):

- The thermomechanical history imparted to the material via forging resulted in a texture intensification and a rotation of the crystallographic cells to align with the loading direction during forging.
- Texture intensification due to forging results in tension-compression asymmetry in both the monotonic and cyclic responses.
- At strain amplitudes at which appreciable plasticity occurs, the as-cast material exhibits predominantly slip deformation in the upward reversal, and marginally mixed-mode in the downward reversal. In contrast, the forged material exhibits twinning in the downward reversal and detwinning, followed by slip, in the upward reversal, regardless of the forging condition.
- Once forged, the AZ80 Mg alloy exhibits superior fatigue properties relative to the as-cast material under strain-controlled testing over the entire strain range investigated in this study. The improvement in fatigue life as a result of forging ranges from 2 times greater in the LCF regime, to 5 times greater in the HCF regime.
- The fracture surfaces of as-cast samples were characterized by a terrace-like faceted morphology, whereas the forged conditions exhibited a more dimple-like fracture surface, indicative of greater plasticity.
- The JV energy-based model and SWT critical plane model give reliable fatigue life predictions for as-cast and forged AZ80.

Secondly, uniaxial stress controlled fatigue experiments were conducted at various stress amplitudes, ranging from 140 – 190 MPa on both as-received and closed die forged AZ80 Mg alloy. The effects of various starting microstructure/texture and thermomechanical were investigated on a comparative basis. Based on the results the following conclusions can be drawn which act to directly address research objectives (2) and enhance the fulfillment of research objectives (1,3 and 4):

- Following forging, both the cast-forged and extruded-forged material exhibited an increase in fatigue life in some instances of up to 15 times for a given stress amplitude. The degree of fatigue life improvement depending on the processing conditions and the type of base material.
- It was discovered that the style of closed-die forging being investigated had spatially varying properties with texture orientations which varied based on the local forging directions and intensities which were dependent on the starting texture as well as the thermomechanical history.

- Under fatigue testing, the materials all developed some form of mean strain, with the nature and magnitude of this mean strain being dependent on primarily its texture intensity and propensity to twin in either tension or compression reversals. The type of mean strain (tensile or compressive) depends upon both the orientation and intensity of the starting texture of the material.
- The texture induced ratcheting and resulting mean strain evolution was most pronounced in the as-cast material and had a significant impact on the fatigue life.
- Strain energy density was demonstrated to be a good parameter for predicting the fatigue damage for both for cast, extruded and closed-die forged AZ80 Mg at a variety of different stress amplitudes.

The multiaxial fatigue behaviour of as-extruded and closed-die forged AZ80 Mg alloy forged at the optimum forging condition of 250°C and 20mm/sec was investigated. Two uniaxial loading paths (pure axial and pure shear) and three different biaxial loading paths were investigated (proportional loading, and non-proportional loading at phase angles of 45° and 90°). Based on the results, the following conclusions can be drawn which directly address research objectives (3 and 4) and act to enhance the fulfillment of research objectives (1 and 2).

- The biaxial fatigue response is somewhat dominated by the axial component for two significant reasons; firstly, the shape of the hysteresis in the shear direction dramatically changes based on phase angle and axial strain amplitude, whereas in the axial hysteresis loop remains somewhat invariant to the presence of the other loading axis.
- For the pure axial strain path, the total amount of strain energy density (SED) observed in the stabilized response was a function of number of cycles only, and was insensitive to material condition (as-extruded or forged).
- For the forged material, of all the strain paths investigated, only the pure shear path demonstrated a significantly different relationship of total SED vs. life.
- The effect of a decrease in total SED for a given number of cycles occurred in all biaxial strain paths, with proportional being the least prominent, then 45° and 90° out of phase being progressively more pronounced respectively. In short, the non-proportional effect is detrimental to the fatigue life.
- The initial crack propagation mode is predominantly transverse to the axial direction in all strain paths except for pure shear (which exhibits longitudinal cracking).

Finally, these discovery level contributions towards the current knowledge were utilized in an advanced vehicle lightweighting engineering application.

- An optimization function was developed that has its foundation in the physical nature of the structural requirements imposed by the engineering application, this allowed rigorous selection of an optimal forging condition for the front lower suspension control arm.
- It was concluded that the optimal forging condition is the coldest temperature and fastest strain rate which are pragmatically possible which produce a forging free of defects and of high quality. This optimal condition corresponded to extruded AZ80 Mg forged at a temperature of 250°C and 20 mm/sec.

### 8.3. Recommendations and Future Work

Despite the prolific scientific contributions of this research work and the fact that these contributions are both novel and useful in nature, there still remains a vast region to explore to fully comprehend the complex nature of AZ80 Mg. Some recommendations for future work would be to utilize this discovery level knowledge described here to develop elasto-plastic material models which specifically capture the mechanics and physics of the problem. Much of this research relies on experimental measurement of the strains, and stresses which a material undergoes, which is a difficult and resource intensive task. Capturing the anisotropy and asymmetry of the deformation is critical in predicting the cyclic behaviour of AZ80 Mg, and without accurate modelling techniques, one relies on experimental data to do so.

Secondly, an overwhelming theme to this work is that the more complexity that is introduced into the forging geometry the more difficult it is to understand and characterize the resulting materials behaviour, mainly because of the spatial variation in texture. A recommendation towards the direction of “texture engineering” to tailor material properties of wrought varieties of AZ80 Mg to suit the application level requirements is an emerging idea which has many merits. Often intensified texture and anisotropic behaviour is viewed in a negative way as it makes predicting the material response more difficult, however now given this better understanding enabled by this research work, we can utilize these perceived drawbacks to our advantage to engineer more intelligent lightweight materials.

Finally, this research work is pioneering the way for understanding the multiaxial effects of fatigue on AZ80 Mg, a topic which until now has not been explored. Future work should focus on understanding and characterizing the behaviour of this material in more complex strain paths and tri-axial stress states. This will enable confidence in reliably predicting the cyclic response fatigue life under random loading spectrums relevant to many other engineering applications.

## Letter of Copyright Permission

The necessary copyright permissions have been obtained to re-use published materials. This section provides the licenses and permissions for Chapters 3, 4 and 5 from the publishers (Elsevier). It is Elsevier's current policy that, "as the author of the Elsevier article, you retain the right to include it in a thesis or dissertation, provided it is not published commercially. Permission is not required, but please ensure that you reference the journal as the original source." Proper referencing within this thesis has been done to give credit to the respective journal articles in chapters 3, 4 and 5. At the time of this writing chapter 6 has not been submitted for publication so no permissions are given. Below contains the obtained permissions for chapters 3, 4 and 5.

Orders Billing History Payable Invoices

**SEARCH**

Order Number:

Date Range: From  To

**View:**  All  Response Required  Pending  Completed  Canceled  Denied  Credited

**Results:** 1-3 of 3

Order Date	Article Title	Publication	Type Of Use	Order Status	Order Number
4-Jul-2019	Multiaxial cyclic behaviour of extruded and forged AZ80 Mg alloy	International Journal of Fatigue	reuse in a thesis/dissertation	Completed <input checked="" type="checkbox"/>	<a href="#">4622080467078</a>
4-Jul-2019	Low-cycle fatigue characterization and texture induced ratcheting behaviour of forged AZ80 Mg alloys	International Journal of Fatigue	reuse in a thesis/dissertation	Completed <input checked="" type="checkbox"/>	<a href="#">4622080425613</a>
4-Jul-2019	Monotonic and cyclic behaviour of cast and cast-forged AZ80 Mg	International Journal of Fatigue	reuse in a thesis/dissertation	Completed <input checked="" type="checkbox"/>	<a href="#">4622080271556</a>



Rights and Permissions (ELS) <Permissions@elsevier.com>

Today, 3:10 PM  
Andrew Gryguc

Reply all

Thank you for your email. If you are requesting permission to reuse content from any publication found on <http://www.ScienceDirect.com>, Elsevier requires that you follow the directions below to obtain permission.

Please understand that Elsevier will **not** reply to your permission request if the publication you wish to use content from is available on ScienceDirect.

**IF THE CONTENT YOU WISH TO USE IS AVAILABLE ON SCIEDIRECT, PLEASE FOLLOW THESE INSTRUCTIONS:**

- Locate the publication containing your desired content on <http://www.sciencedirect.com/science/jrnlallbooks>
- Click on the article/chapter name to access the abstract
- Below the author details, click "Get Rights and Content"
- The Rightslink request page will then be launched (please disable your pop-up blocker)
- Select the way you would like to reuse the content
- Create a Rightslink account if you haven't done so already
- Accept the terms and conditions and you're done

Please note that certain requests may require review before a license to reuse is available; should this occur, you will be emailed to accept or decline the fee and/or terms of the license as set by Elsevier's Global Rights Department upon review.

For questions about using the Rightslink service, please contact Rightslink Customer Support via phone - US 877/622-5543 (toll free) or 978/777-9929, 8:00 am – 6:00 pm Eastern Time, or email [customer@copyright.com](mailto:customer@copyright.com).



**Title:** Monotonic and cyclic behaviour of cast and cast-forged AZ80 Mg alloy  
**Author:** A. Gryguc, S.K. Shaha, S.B. Behravesh, H. Jahed, M. Wells, B. Williams, X. Su  
**Publication:** International Journal of Fatigue  
**Publisher:** Elsevier  
**Date:** November 2017  
 Crown Copyright © 2017 Published by Elsevier Ltd. All rights reserved.

**LOGIN**  
 If you're a copyright.com user, you can login to RightsLink using your copyright.com credentials. Already a RightsLink user or want to learn more?

Please note that, as the author of this Elsevier article, you retain the right to include it in a thesis or dissertation, provided it is not published commercially. Permission is not required, but please ensure that you reference the journal as the original source. For more information on this and on your other retained rights, please visit: <https://www.elsevier.com/about/our-business/policies/copyright#Author-rights>

BACK CLOSE WINDOW

Copyright © 2019 Copyright Clearance Center, Inc. All Rights Reserved. [Privacy Statement](#) [Terms and Conditions](#). Comments? We would like to hear from you. E-mail us at [customerservice@copyright.com](mailto:customerservice@copyright.com)



**Title:** Low-cycle fatigue characterization and texture induced ratcheting behaviour of forged AZ80 Mg alloys  
**Author:** A. Gryguc, S.B. Behravesh, S.K. Shaha, H. Jahed, M. Wells, B. Williams, X. Su  
**Publication:** International Journal of Fatigue  
**Publisher:** Elsevier  
**Date:** November 2018  
 Crown Copyright © 2018 Published by Elsevier Ltd. All rights reserved.

**LOGIN**  
 If you're a copyright.com user, you can login to RightsLink using your copyright.com credentials. Already a RightsLink user or want to learn more?

Please note that, as the author of this Elsevier article, you retain the right to include it in a thesis or dissertation, provided it is not published commercially. Permission is not required, but please ensure that you reference the journal as the original source. For more information on this and on your other retained rights, please visit: <https://www.elsevier.com/about/our-business/policies/copyright#Author-rights>

BACK CLOSE WINDOW

Copyright © 2019 Copyright Clearance Center, Inc. All Rights Reserved. [Privacy Statement](#) [Terms and Conditions](#). Comments? We would like to hear from you. E-mail us at [customerservice@copyright.com](mailto:customerservice@copyright.com)



**Title:** Multiaxial cyclic behaviour of extruded and forged AZ80 Mg alloy  
**Author:** A. Gryguc, S.B. Behravesh, S.K. Shaha, H. Jahed, M. Wells, B. Williams, X. Su  
**Publication:** International Journal of Fatigue  
**Publisher:** Elsevier  
**Date:** October 2019  
 © 2019 Elsevier Ltd. All rights reserved.

**LOGIN**  
 If you're a copyright.com user, you can login to RightsLink using your copyright.com credentials. Already a RightsLink user or want to learn more?

Please note that, as the author of this Elsevier article, you retain the right to include it in a thesis or dissertation, provided it is not published commercially. Permission is not required, but please ensure that you reference the journal as the original source. For more information on this and on your other retained rights, please visit: <https://www.elsevier.com/about/our-business/policies/copyright#Author-rights>

BACK CLOSE WINDOW

Copyright © 2019 Copyright Clearance Center, Inc. All Rights Reserved. [Privacy Statement](#) [Terms and Conditions](#). Comments? We would like to hear from you. E-mail us at [customerservice@copyright.com](mailto:customerservice@copyright.com)



**Title:** Monotonic and cyclic behaviour of cast and cast-forged AZ80 Mg alloy  
**Author:** A. Gryguc, S.K. Shaha, S.B. Behravesh, H. Jahed, M. Wells, B. Williams, X. Su  
**Publication:** International Journal of Fatigue  
**Publisher:** Elsevier  
**Date:** November 2017  
 Crown Copyright © 2017 Published by Elsevier Ltd. All rights reserved.

Logged in as: Andrew Gryguc  
[Logout](#)

**Order Completed**

Thank you for your order.

This Agreement between Andrew Gryguc ("You") and Elsevier ("Elsevier") consists of your license details and the terms and conditions provided by Elsevier and Copyright Clearance Center.

Your confirmation email will contain your order number for future reference.

[Printable details](#)

License Number: 462208045153  
 License date: Jul 04, 2019  
 Licensed Content: Elsevier  
 Licensed Content Publisher: Elsevier  
 Licensed Content Publication: International Journal of Fatigue  
 Licensed Content Title: Monotonic and cyclic behaviour of cast and cast-forged AZ80 Mg alloy  
 Licensed Content Author: A. Gryguc, S.K. Shaha, S.B. Behravesh, H. Jahed, M. Wells, B. Williams, X. Su  
 Licensed Content Date: Nov 1, 2017  
 Licensed Content Volume: 104  
 Licensed Content Issue: N/A  
 Licensed Content Pages: 14  
 Type of Use: reuse in a thesis/dissertation  
 Portion: full article  
 Circulation: 1  
 Format: both print and electronic  
 Are you the author of this Elsevier article? No  
 Will you be translating? No  
 Order reference number: TheaLjgryguc  
 Title of your thesis/dissertation: Fatigue of Forged AZ80 Magnesium Alloy  
 Expected completion date: Sep 2019  
 Estimated size (number of pages): 150  
 Requestor Location: Andrew Gryguc, 200 University Avenue West, Waterloo, ON N2L 3G1, Canada, Attn: Andrew Gryguc, GB 494 6272 12, 0.00 CAD

ORDER MORE CLOSE WINDOW

Copyright © 2019 Copyright Clearance Center, Inc. All Rights Reserved. [Privacy Statement](#) [Terms and Conditions](#). Comments? We would like to hear from you. E-mail us at [customerservice@copyright.com](mailto:customerservice@copyright.com)



**Title:** Low-cycle fatigue characterization and texture induced ratcheting behaviour of forged AZ80 Mg alloys  
**Author:** A. Gryguc, S.B. Behravesh, S.K. Shaha, H. Jahed, M. Wells, B. Williams, X. Su  
**Publication:** International Journal of Fatigue  
**Publisher:** Elsevier  
**Date:** November 2018  
 Crown Copyright © 2018 Published by Elsevier Ltd. All rights reserved.

Logged in as: Andrew Gryguc  
[Logout](#)

**Order Completed**

Thank you for your order.

This Agreement between Andrew Gryguc ("You") and Elsevier ("Elsevier") consists of your license details and the terms and conditions provided by Elsevier and Copyright Clearance Center.

Your confirmation email will contain your order number for future reference.

[Printable details](#)

License Number: 462208045153  
 License date: Jul 04, 2019  
 Licensed Content: Elsevier  
 Licensed Content Publisher: Elsevier  
 Licensed Content Publication: International Journal of Fatigue  
 Licensed Content Title: Low-cycle fatigue characterization and texture induced ratcheting behaviour of forged AZ80 Mg alloys  
 Licensed Content Author: A. Gryguc, S.B. Behravesh, S.K. Shaha, H. Jahed, M. Wells, B. Williams, X. Su  
 Licensed Content Date: Nov 1, 2018  
 Licensed Content Volume: 116  
 Licensed Content Issue: N/A  
 Licensed Content Pages: 10  
 Type of Use: reuse in a thesis/dissertation  
 Portion: full article  
 Circulation: 1  
 Format: both print and electronic  
 Are you the author of this Elsevier article? No  
 Will you be translating? No  
 Order reference number: TheaLjgryguc  
 Title of your thesis/dissertation: Fatigue of Forged AZ80 Magnesium Alloy  
 Expected completion date: Sep 2019  
 Estimated size (number of pages): 150  
 Requestor Location: Andrew Gryguc, 200 University Avenue West, Waterloo, ON N2L 3G1, Canada, Attn: Andrew Gryguc, GB 494 6272 12, 0.00 CHF

ORDER MORE CLOSE WINDOW

Copyright © 2019 Copyright Clearance Center, Inc. All Rights Reserved. [Privacy Statement](#) [Terms and Conditions](#). Comments? We would like to hear from you. E-mail us at [customerservice@copyright.com](mailto:customerservice@copyright.com)



**Title:** Multiaxial cyclic behaviour of extruded and forged AZ80 Mg alloy  
**Author:** A. Gryguc, S.B. Behravesh, S.K. Shaha, H. Jahed, M. Wells, B. Williams, X. Su  
**Publication:** International Journal of Fatigue  
**Publisher:** Elsevier  
**Date:** October 2019  
 © 2019 Elsevier Ltd. All rights reserved.

Logged in as: Andrew Gryguc  
[Logout](#)

**Order Completed**

Thank you for your order.

This Agreement between Andrew Gryguc ("You") and Elsevier ("Elsevier") consists of your license details and the terms and conditions provided by Elsevier and Copyright Clearance Center.

Your confirmation email will contain your order number for future reference.

[Printable details](#)

License Number: 4622080467078  
 License date: Jul 04, 2019  
 Licensed Content: Elsevier  
 Licensed Content Publisher: Elsevier  
 Licensed Content Publication: International Journal of Fatigue  
 Licensed Content Title: Multiaxial cyclic behaviour of extruded and forged AZ80 Mg alloy  
 Licensed Content Author: A. Gryguc, S.B. Behravesh, S.K. Shaha, H. Jahed, M. Wells, B. Williams, X. Su  
 Licensed Content Date: Oct 1, 2019  
 Licensed Content Volume: 127  
 Licensed Content Issue: N/A  
 Licensed Content Pages: 14  
 Type of Use: reuse in a thesis/dissertation  
 Portion: full article  
 Circulation: 1  
 Format: both print and electronic  
 Are you the author of this Elsevier article? No  
 Will you be translating? No  
 Order reference number: TheaLjgryguc  
 Title of your thesis/dissertation: Fatigue of Forged AZ80 Magnesium Alloy  
 Expected completion date: Sep 2019  
 Estimated size (number of pages): 150  
 Requestor Location: Andrew Gryguc, 200 University Avenue West, Waterloo, ON N2L 3G1, Canada, Attn: Andrew Gryguc, GB 494 6272 12, 0.00 CAD

ORDER MORE CLOSE WINDOW

Copyright © 2019 Copyright Clearance Center, Inc. All Rights Reserved. [Privacy Statement](#) [Terms and Conditions](#). Comments? We would like to hear from you. E-mail us at [customerservice@copyright.com](mailto:customerservice@copyright.com)

The necessary copyright permissions have been obtained to re-use published materials. This section provides the licenses and permissions for reproduction of figures found in various articles from various publishers found in the literature review chapter of this work (Chapter 2).

Permission for Figure 4:

Permission for Figure 6:

# Permission for Figure 6 (cont...)

Copyright Clearance Center RightsLink® Home Account Help

**SAGE Publishing**

Title: Warm forging of magnesium AZ30 alloy for the crankshaft in an automobile  
 Author: Jonathan Youn, Sang-ik Lee  
 Publication: Proceedings of the Institution of Mechanical Engineers, Part D: Journal of Automobile Engineering  
 Publisher: SAGE Publications  
 Date: 13/01/2015  
 Copyright © 2015, © SAGE Publications

Logged in as: Andrew Grigg Account # 300449381

**Gratis Reuse**

Permission is granted at no cost for use of content in a Master's Thesis and/or Doctoral Dissertation. If you intend to distribute or sell your Master's Thesis/Doctoral Dissertation to the general public through print or web-on-publication, please refer to the previous page and select 'Republish in a Book/Journal' or 'Post on internet/password-protected website to complete your request.'

[BACK](#) [CLOSE WINDOW](#)

Copyright © 2015 Copyright Clearance Center, Inc. All Rights Reserved. Privacy Statement Terms and Conditions. Comments? We would like to hear from you. E-mail us at [info@copyright.com](mailto:info@copyright.com)

Copyright Clearance Center RightsLink® Home Account Help

**SPRINGER NATURE**

Title: Process design of Warm-Forging with extruded Mg-DMG-Zn alloy for automotive crank in automobile transmission  
 Author: Jonathan Youn, Sang-ik Lee  
 Publication: International Journal of Precision Engineering and Manufacturing  
 Publisher: Springer Nature  
 Date: Jan 1, 2015  
 Copyright © 2015, Springer Nature for Precision Engineering and Manufacturing Series Holdings

Logged in as: Andrew Grigg Account # 300449381

**Order Completed**

Thank you for your order.

This Agreement between Andrew Grigg ("You") and Springer Nature ("Springer Nature") consists of this license details and the terms and conditions provided by Springer Nature and Copyright Clearance Center.

Your confirmation email will contain your order number for future reference.

**Order Details**

Order Number: 4643743002229  
 Invoice date: Aug 24, 2015  
 Issued Content: Article  
 Journal Content: International Journal of Precision Engineering and Manufacturing  
 Journal Content: Precision design of Warm-Forging with extruded Mg-DMG-Zn alloy for automotive crank in automobile transmission  
 Journal Content Author: Jonathan Youn, Sang-ik Lee  
 Journal Content Date: Jan 1, 2015  
 Journal Content Volume: 18  
 Journal Content Issue: 4  
 Type of file: Text/Document  
 Republish type: Academic/University or research institute  
 Format: pdf and electronic  
 Rights: Copyright/Reproduction  
 No. new. of reproduction/permissions: 1  
 Will you be translating? no  
 Distribution restriction: no  
 Report of this content: no  
 Title: Process design of Warm-Forging with extruded Mg-DMG-Zn alloy for automotive crank in automobile transmission  
 Distribution name: no  
 Special identifier: No 2310  
 Authors: Figure 6  
 Republish location: Andrew Grigg, 200 University Avenue West, Ypsilanti, MI 48198, USA  
 Total: 6.00 USD

[ORDER HISTORY](#) [CLOSE WINDOW](#)

Copyright © 2015 Copyright Clearance Center, Inc. All Rights Reserved. Privacy Statement Terms and Conditions. Comments? We would like to hear from you. E-mail us at [info@copyright.com](mailto:info@copyright.com)

## References

- [1] M. P. Brady, W. J. Joost, and C. David Warren, “Insights from a Recent Meeting: Current Status and Future Directions in Magnesium Corrosion Research,” *Corrosion*, vol. 73, no. 5, pp. 452–462, 2017.
- [2] W. J. Joost and P. E. Krajewski, “Towards magnesium alloys for high-volume automotive applications,” *Scr. Mater.*, vol. 128, pp. 107–112, 2017.
- [3] T. W. Skszek, M. Zaluzec, J. Conklin, and D. Wagner, “MMLV : Project Overview,” *SAE Int.*, no. 10.4271/2015-01-0407, 2016.
- [4] Q. Guo, H. G. Yan, Z. H. Chen, and H. Zhang, “Grain refinement in as-cast AZ80 Mg alloy under large strain deformation,” *Mater. Charact.*, vol. 58, no. 2, pp. 162–167, 2007.
- [5] P. Moldovan, G. Popescu, D. Bojin, D. Constantinescu, and M. Pana, “Improving the fatigue resistance of magnesium alloys for forged parts in automotive industry,” *Metal. Int.*, vol. 14, no. SPEC. ISS. 2, pp. 23–26, 2009.
- [6] P. Zhang and J. Lindemann, “Influence of shot peening on high cycle fatigue properties of the high-strength wrought magnesium alloy AZ80,” *Scr. Mater.*, vol. 52, no. 6, pp. 485–490, 2005.
- [7] R. Zhu, W. Ji, Y. Wu, X. Cai, and Y. Yu, “Effect of aging treatment on low-cycle fatigue behavior of extruded Mg-8Al-0.5Zn alloys,” *Mater. Des.*, vol. 41, pp. 203–207, 2012.
- [8] R. Liu, D. L. Yin, and J. T. Wang, “Elimination of yielding asymmetry in extruded AZ80 alloy by ageing,” *Trans. Nonferrous Met. Soc. China (English Ed.)*, vol. 24, no. 4, pp. 915–921, 2014.
- [9] Y. Uematsu, K. Tokaji, and M. Matsumoto, “Effect of aging treatment on fatigue behaviour in extruded AZ61 and AZ80 magnesium alloys,” *Mater. Sci. Eng. A*, vol. 517, no. 1–2, pp. 138–145, 2009.
- [10] G. Kurz, B. Clauw, W. H. Sillekens, D. Letzig, and P. Manufacturing, “Die Forging of the Alloys Az80 and Zk60,” *Mater. Soc. Annu. Meet.*, pp. 197–202, 2009.
- [11] P. Moldovan and D. M. Constantinescu, “Magnesium Alloys for Automotive Applications,” *Metal. Int.*, vol. 14, no. 7, pp. 19–23, 2009.
- [12] F. Nový, M. Janeček, V. Škorik, J. Muller, and L. Wagner, “Very high cycle fatigue behaviour of as-extruded AZ31, AZ80, and ZK60 magnesium alloys,” *Int. J. Mater. Res.*, vol. 100, no. 3, pp. 288–291, 2009.
- [13] K. Shiozawa, T. Kashiwagi, T. Murai, and T. Takahashi, “Fatigue behaviour and fractography of extruded AZ80 magnesium alloys in very high cycle regime,” *Procedia Eng.*, vol. 2, no. 1, pp. 183–191, 2010.
- [14] M. S. Bhuiyan, Y. Mutoh, T. Murai, and S. Iwakami, “Corrosion fatigue behavior of extruded magnesium alloy AZ80-T5 in a 5% NaCl environment,” *Eng. Fract. Mech.*, vol. 77, no. 10, pp. 1567–1576, 2010.
- [15] P. Zhang, J. Lindemann, and C. Leyens, “Shot peening on the high-strength wrought magnesium alloy AZ80-Effect of peening media,” *J. Mater. Process. Technol.*, vol. 210, no. 3, pp. 445–450, 2010.
- [16] K. Shiozawa, J. Kitajima, T. Kaminashi, T. Murai, and T. Takahashi, “Low-cycle fatigue deformation behavior and evaluation of fatigue life on extruded magnesium alloys,” *Procedia Eng.*, vol. 10, pp. 1244–1249, 2011.

- [17] Q. Guo, H. G. Yan, Z. H. Chen, and H. Zhang, "Fracture behaviors of AZ80 magnesium alloy during multiple forging processes," *Trans. Nonferrous Met. Soc. China (English Ed.)*, vol. 16, no. 4, pp. 922–926, 2006.
- [18] H. T. Zhou, Q. B. Li, Z. K. Zhao, Z. C. Liu, S. F. Wen, and Q. D. Wang, "Hot workability characteristics of magnesium alloy AZ80-A study using processing map," *Mater. Sci. Eng. A*, vol. 527, no. 7–8, pp. 2022–2026, 2010.
- [19] G. Z. Quan, T. Song, Y. J. Zhou, F. B. Wang, and J. Zhou, "Relationship between mechanical properties and grain size of AZ80 at 350 °c under different strain rates," *Trans. Nonferrous Met. Soc. China (English Ed.)*, vol. 20, no. SUPPL. 2, pp. 0–4, 2010.
- [20] Y. Xiong and Y. Jiang, "Cyclic deformation and fatigue of rolled AZ80 magnesium alloy along different material orientations," *Mater. Sci. Eng. A*, vol. 667, pp. 58–67, 2016.
- [21] H. Okada, Y. Uematsu, and K. Tokaji, "Fatigue behaviour in AZ80A magnesium alloy with DLC/thermally splayed WC-12Co hybrid coating," *Procedia Eng.*, vol. 2, no. 1, pp. 283–290, 2010.
- [22] G. Rivers, "Cyclic Fatigue Behaviour of Wrought AZ80 Magnesium Alloy from Forged Automotive Wheel," McMaster University, 2011.
- [23] P. Zhang and J. Lindemann, "Effect of roller burnishing on the high cycle fatigue performance of the high-strength wrought magnesium alloy AZ80," *Scr. Mater.*, vol. 52, no. 10, pp. 1011–1015, 2005.
- [24] G. Rivers, "Cyclic Fatigue Testing of Wrought Magnesium AZ80 Alloy for Automotive Wheels," 2009.
- [25] C. Wang, T. Luo, and Y. Yang, "Low cycle fatigue behavior of the extruded AZ80 magnesium alloy under different strain amplitudes and strain rates," *J. Magnes. Alloy.*, vol. 4, no. 3, pp. 181–187, 2016.
- [26] R. C. Zeng, Y. B. Xu, W. Ke, and E. H. Han, "Fatigue crack propagation behavior of an as-extruded magnesium alloy AZ80," *Mater. Sci. Eng. A*, vol. 509, no. 1–2, pp. 1–7, 2009.
- [27] R. Zeng, E. Han, and W. Ke, "A critical discussion on influence of loading frequency on fatigue crack propagation behavior for extruded Mg-Al-Zn alloys," *Int. J. Fatigue*, vol. 36, no. 1, pp. 40–46, 2012.
- [28] V. Kevorkijan, "AZ80 and ZC71/SiC/12p closed die forgings for automotive applications: technical and economic assessment of possible mass production," *Materials science and technology*, vol. 19, no. 10, pp. 1386–1390, 2003.
- [29] Q. Wang, Z. M. Zhang, X. Zhang, and J. M. Yu, "Precision forging technologies for magnesium alloy bracket and wheel," *Trans. Nonferrous Met. Soc. China (English Ed.)*, vol. 18, no. SPEC. ISSUE 1, pp. s205–s208, 2008.
- [30] F. Guo, "Understanding the microstructure and fatigue behavior of magnesium alloys A thesis submitted for the Degree of Master of Philosophy in the University of Leicester," 2009.
- [31] J. Yoon and S. Lee, "Warm forging of magnesium AZ80 alloy for the control arm in an automobile," *Proc. Inst. Mech. Eng. Part D J. Automob. Eng.*, vol. 229, no. 13, pp. 1732–1738, 2015.
- [32] J. Yoon and J. Lee, "Process design of Warm-Forging with extruded Mg-8Al-0.5Zn alloy for

- differential case in automobile transmission,” *Int. J. Precis. Eng. Manuf.*, vol. 16, no. 4, pp. 841–846, 2015.
- [33] S. Sepahi-Boroujeni and A. Sepahi-Boroujeni, “Improvements in microstructure and mechanical properties of AZ80 magnesium alloy by means of an efficient, novel severe plastic deformation process,” *J. Manuf. Process.*, vol. 24, pp. 71–77, 2016.
- [34] C. Wang, R. Xin, D. Li, B. Song, M. Wu, and Q. Liu, “Enhancing the age-hardening response of rolled AZ80 alloy by pre-twinning deformation,” *Mater. Sci. Eng. A*, vol. 680, no. October 2016, pp. 152–156, 2017.
- [35] F. W. Bach, A. Roßberg, M. Schäperkötter, M. Schaper, L. Walden, and J. Weber, “Today’s sheet metal materials and their forming properties,” *Materwiss. Werksttech.*, vol. 35, no. 7, pp. 423–430, 2004.
- [36] D. Kobold, T. Pepelnjak, G. Gantar, and K. Kuzman, “Analysis of deformation characteristics of magnesium AZ80 wrought alloy under hot conditions,” *Stroj. Vestnik/Journal Mech. Eng.*, vol. 56, no. 12, pp. 823–832, 2010.
- [37] H. Z. Li, X. Y. Wei, J. Ouyang, J. Jiang, and Y. Li, “Hot deformation behavior of extruded AZ80 magnesium alloy,” *Trans. Nonferrous Met. Soc. China (English Ed.)*, vol. 23, no. 11, pp. 3180–3185, 2013.
- [38] Z. Su, L. Wan, C. Sun, Y. Cai, and D. Yang, “Hot deformation behavior of AZ80 magnesium alloy towards optimization of its hot workability,” *Mater. Charact.*, vol. 122, pp. 90–97, 2016.
- [39] L. Wang *et al.*, “Effects of texture and grain size on mechanical properties of AZ80 magnesium alloys at lower temperatures,” *Mater. Des.*, vol. 89, pp. 1–8, 2016.
- [40] M. Madaj, M. Greger, and V. Karas, “Magnesium-alloy die forgings for automotive applications,” *Mater. Tehnol.*, vol. 49, no. 2, pp. 267–273, 2015.
- [41] A. Gontarz and A. Dziubińska, “Forming of flat parts with ribs from magnesium alloy,” *Aircr. Eng. Aerosp. Technol.*, vol. 86, no. 4, pp. 356–360, 2014.
- [42] X. Y. Lou, M. Li, R. K. Boger, S. R. Agnew, and R. H. Wagoner, “Hardening evolution of AZ31B Mg sheet,” *Int. J. Plast.*, vol. 23, no. 1, pp. 44–86, 2007.
- [43] M. O. Andar, T. Kuwabara, and D. Steglich, “Material modeling of AZ31 Mg sheet considering variation of r-values and asymmetry of the yield locus,” *Mater. Sci. Eng. A*, vol. 549, pp. 82–92, 2012.
- [44] O. Cazacu and F. Barlat, “A criterion for description of anisotropy and yield differential effects in pressure-insensitive metals,” *Int. J. Plast.*, vol. 20, no. 11 SPEC. ISS., pp. 2027–2045, 2004.
- [45] O. Cazacu, B. Plunkett, and F. Barlat, “Orthotropic yield criterion for hexagonal closed packed metals,” *Int. J. Plast.*, vol. 22, no. 7, pp. 1171–1194, 2006.
- [46] B. Plunkett, O. Cazacu, and F. Barlat, “Orthotropic yield criteria for description of the anisotropy in tension and compression of sheet metals,” *Int. J. Plast.*, vol. 24, no. 5, pp. 847–866, 2008.
- [47] J. Yoon, O. Cazacu, and R. K. Mishra, “Constitutive modeling of AZ31 sheet alloy with application to axial crushing,” *Mater. Sci. Eng. A*, vol. 565, pp. 203–212, 2013.
- [48] M. A. Khayamian, B. Behraves, and H. Jahed, “Incorporation of asymmetric yield and hardening behaviour in axisymmetric elastoplastic problems,” *Mater. Des.*, vol. 99, pp. 490–499, 2016.

- [49] H. Jahed and J. Bidabadi, "An axisymmetric method of creep analysis for primary and secondary creep," *Int. J. Press. Vessel. Pip.*, vol. 80, no. 9, pp. 597–606, 2003.
- [50] A. A. Roostaei and H. Jahed, "A cyclic small-strain plasticity model for wrought Mg alloys under multiaxial loading: Numerical implementation and validation," *Int. J. Mech. Sci.*, vol. 145, no. July, pp. 318–329, 2018.
- [51] L. F. V. Qian, A. A. Roostaei, U. Dighrasker, G. Glinka, and H. Jahed, "Notch Plasticity and Fatigue Modelling of AZ31B-H24 Magnesium Alloy Sheet," *SAE Tech. Pap. Ser.*, vol. 1, pp. 1–11, 2019.
- [52] S. B. Behraves, H. Jahed, S. B. Lambert, and M. Chengji, "Constitutive Modeling for Cyclic Behavior of AZ31B Magnesium Alloy and its Application," *Adv. Mater. Res.*, vol. 891–892, pp. 809–814, 2014.
- [53] E. Kalatehmollaei, H. Mahmoudi-Asl, and H. Jahed, "An asymmetric elastic-plastic analysis of the load-controlled rotating bending test and its application in the fatigue life estimation of wrought magnesium AZ31B," *Int. J. Fatigue*, vol. 64, pp. 33–41, 2014.
- [54] M. Noban, J. Albinmousa, H. Jahed, and S. Lambert, "A continuum-based cyclic plasticity model for AZ31B magnesium alloy under proportional loading," *Procedia Eng.*, vol. 10, no. October 2015, pp. 1366–1371, 2011.
- [55] J. Albinmousa and H. Jahed, "Multiaxial effects on LCF behaviour and fatigue failure of AZ31B magnesium extrusion," *Int. J. Fatigue*, vol. 67, pp. 103–116, 2014.
- [56] H. Jahed and J. Albinmousa, "Multiaxial behaviour of wrought magnesium alloys - A review and suitability of energy-based fatigue life model," *Theor. Appl. Fract. Mech.*, vol. 73, pp. 97–108, 2014.
- [57] R. N. Smith, P. Watson, and T. H. Topper, "A Stress-Strain Function for the Fatigue of Metals," *J. Mater.*, vol. 5, no. 4, pp. 767–788, 1970.
- [58] Y. C. Lin, Z. H. Liu, X. M. Chen, and J. Chen, "Stress-based fatigue life prediction models for AZ31B magnesium alloy under single-step and multi-step asymmetric stress-controlled cyclic loadings," *Comput. Mater. Sci.*, vol. 73, pp. 128–138, 2013.
- [59] S. Hyuk Park, S. G. Hong, B. Ho Lee, W. Bang, and C. Soo Lee, "Low-cycle fatigue characteristics of rolled Mg-3Al-1Zn alloy," *Int. J. Fatigue*, vol. 32, no. 11, pp. 1835–1842, 2010.
- [60] J. Albinmousa, H. Jahed, and S. Lambert, "Cyclic axial and cyclic torsional behaviour of extruded AZ31B magnesium alloy," *Int. J. Fatigue*, vol. 33, no. 11, pp. 1403–1416, 2011.
- [61] A. A. Roostaei and H. Jahed, "Role of loading direction on cyclic behaviour characteristics of AM30 extrusion and its fatigue damage modelling," *Mater. Sci. Eng. A*, vol. 670, pp. 26–40, 2016.
- [62] S. M. H. Karparvarfard, S. K. Shaha, S. B. Behraves, H. Jahed, and B. W. Williams, "Fatigue characteristics and modeling of cast and cast-forged ZK60 magnesium alloy," *Int. J. Fatigue*, vol. 118, no. November 2017, pp. 282–297, 2019.
- [63] S. Sepahi-Boroujeni and A. Sepahi-Boroujeni, "Improvements in microstructure and mechanical properties of AZ80 magnesium alloy by means of an efficient, novel severe plastic deformation process," *J. Manuf. Process.*, vol. 24, pp. 71–77, 2016.
- [64] H. Zenner and F. Renner, "Cyclic material behaviour of magnesium die castings and extrusions," *Int. J. Fatigue*, vol. 24, no. 12, pp. 1255–1260, 2002.

- [65] J. Pan, "Sound Package Design for Lightweight Vehicles," *SAE Int.*, no. 10.4271/2015-01-2343, 2015.
- [66] Y. Lou, L. Li, J. Zhou, and L. Na, "Deformation behavior of Mg-8Al magnesium alloy compressed at medium and high temperatures," *Mater. Charact.*, vol. 62, no. 3, pp. 346-353, 2011.
- [67] W. J. Lai, Y. Y. Li, Y. F. Hsu, S. Trong, and W. H. Wang, "Aging behaviour and precipitate morphologies in Mg-7.7Al-0.5Zn-0.3Mn (wt.%) alloy," *J. Alloys Compd.*, vol. 476, no. 1-2, pp. 118-124, 2009.
- [68] D. Sarker and D. L. Chen, "Texture transformation in an extruded magnesium alloy under pressure," *Mater. Sci. Eng. A*, vol. 582, pp. 63-67, 2013.
- [69] A. Gryguc, S. K. Shaha, H. Jahed, M. Wells, B. Williams, and J. McKinley, "Tensile and fatigue behaviour of as-forged AZ31B extrusion," *Frat. ed Integrita Strutt.*, vol. 10, no. 38, pp. 251-258, 2016.
- [70] B. Wang, R. Xin, G. Huang, and Q. Liu, "Effect of crystal orientation on the mechanical properties and strain hardening behavior of magnesium alloy AZ31 during uniaxial compression," *Mater. Sci. Eng. A*, vol. 534, pp. 588-593, 2012.
- [71] J. Li, J. Liu, and Z. Cui, "Microstructures and mechanical properties of AZ61 magnesium alloy after isothermal multidirectional forging with increasing strain rate," *Mater. Sci. Eng. A*, vol. 643, pp. 32-36, 2015.
- [72] L. Liu and H. Ding, "Study of the plastic flow behaviors of AZ91 magnesium alloy during thermomechanical processes," *J. Alloys Compd.*, vol. 484, no. 1-2, pp. 949-956, 2009.
- [73] D. Sarker and D. L. Chen, "Detwinning and strain hardening of an extruded magnesium alloy during compression," *Scr. Mater.*, vol. 67, no. 2, pp. 165-168, 2012.
- [74] J. Albinmoussa, H. Jahed, and S. Lambert, "Cyclic behaviour of wrought magnesium alloy under multiaxial load," *Int. J. Fatigue*, vol. 33, no. 8, pp. 1127-1139, 2011.
- [75] A. Staroselsky and L. Anand, "A constitutive model for hcp materials deforming by slip and twinning: Application to magnesium alloy AZ31B," *Int. J. Plast.*, vol. 19, no. 10, pp. 1843-1864, 2003.
- [76] L. Wu *et al.*, "Twinning-detwinning behavior during the strain-controlled low-cycle fatigue testing of a wrought magnesium alloy, ZK60A," *Acta Mater.*, vol. 56, no. 4, pp. 688-695, 2008.
- [77] S. Kleiner and P. J. Uggowitzer, "Mechanical anisotropy of extruded Mg-6% Al-1% Zn alloy," *Mater. Sci. Eng. A*, vol. 379, no. 1-2, pp. 258-263, 2004.
- [78] Y. Chino, K. Kimura, M. Hakamada, and M. Mabuchi, "Mechanical anisotropy due to twinning in an extruded AZ31 Mg alloy," *Mater. Sci. Eng. A*, vol. 485, no. 1-2, pp. 311-317, 2008.
- [79] D. Scoie, "Multiaxial Fatigue Damage Models," *J. Eng. Mater. Technol.*, vol. 109, no. OCTOBER, pp. 293-298, 1987.
- [80] S. H. Park, S. G. Hong, W. Bang, and C. S. Lee, "Effect of anisotropy on the low-cycle fatigue behavior of rolled AZ31 magnesium alloy," *Mater. Sci. Eng. A*, vol. 527, no. 3, pp. 417-423, 2010.
- [81] J. Albinmoussa, H. Jahed, and S. Lambert, "An Energy-Based Fatigue Model for Wrought Magnesium Alloy under Multiaxial Load," *Ninth Int. Conf. Multiaxial Fatigue Fract.*, pp. 471-

- 478, 2010.
- [82] H. Jahed and A. Varvani-Farahani, "Upper and lower fatigue life limits model using energy-based fatigue properties," *Int. J. Fatigue*, vol. 28, no. 5–6, pp. 467–473, 2006.
- [83] K. Golos and F. Ellyin, "A Total Strain Energy Density Theory for Cumulative Fatigue Damage," *J. Press. Vessel Technol.*, vol. 110, pp. 36–41, 1988.
- [84] H. Jahed, A. Varvani-Farahani, M. Noban, and I. Khalaji, "An energy-based fatigue life assessment model for various metallic materials under proportional and non-proportional loading conditions," *Int. J. Fatigue*, vol. 29, no. 4, pp. 647–655, 2007.
- [85] J. Roesler, H. Harders, and M. Baeker, *Mechanical Behaviour of Engineering Materials*. Springer-Verlag Berlin Heidelberg, 2007.
- [86] S. Begum, D. L. Chen, S. Xu, and A. A. Luo, "Low cycle fatigue properties of an extruded AZ31 magnesium alloy," *Int. J. Fatigue*, vol. 31, no. 4, pp. 726–735, 2009.
- [87] S. Hasegawa, Y. Tsuchida, H. Yano, and M. Matsui, "Evaluation of low cycle fatigue life in AZ31 magnesium alloy," *Int. J. Fatigue*, vol. 29, no. 9–11, pp. 1839–1845, 2007.
- [88] M. Lugo *et al.*, "Role of different material processing methods on the fatigue behavior of an AZ31 magnesium alloy," *Int. J. Fatigue*, vol. 52, pp. 131–143, 2013.
- [89] F. Lv *et al.*, "Fatigue properties of rolled magnesium alloy (AZ31) sheet: Influence of specimen orientation," *Int. J. Fatigue*, vol. 33, no. 5, pp. 672–682, 2011.
- [90] S. Ishihara, S. Taneguchi, H. Shibata, T. Goshima, and A. Saiki, "Anisotropy of the fatigue behavior of extruded and rolled magnesium alloys," *Int. J. Fatigue*, vol. 50, pp. 94–100, 2013.
- [91] Q. Yu, J. Zhang, Y. Jiang, and Q. Li, "Multiaxial fatigue of extruded AZ61A magnesium alloy," *Int. J. Fatigue*, vol. 33, no. 3, pp. 437–447, 2011.
- [92] D. Toscano, S. K. Shaha, B. Behraves, H. Jahed, and B. Williams, "Effect of forging on the low cycle fatigue behavior of cast AZ31B alloy," *Mater. Sci. Eng. A*, vol. 706, no. August, pp. 342–356, 2017.
- [93] A. Gryguc, H. Jahed, B. Williams, and J. McKinley, "Magforge – Mechanical behaviour of forged AZ31B extruded magnesium in monotonic compression," *Mater. Sci. Forum*, vol. 828–829, pp. 291–297, 2015.
- [94] A. Gryguc, S. K. Shaha, S. B. Behraves, H. Jahed, M. Wells, and B. Williams, "Compression Behaviour of Semi-Closed Die Forged AZ80 Extrusion," *Charact. Miner. Met. Mater. 2017*, pp. 361–369, 2017.
- [95] A. Gryguc *et al.*, "Monotonic and cyclic behaviour of cast and cast-forged AZ80 Mg," *Int. J. Fatigue*, vol. 104, pp. 136–149, 2017.
- [96] S. M. H. Karparvarfard, S. K. Shaha, S. B. Behraves, H. Jahed, and B. W. Williams, "Microstructure, texture and mechanical behavior characterization of hot forged cast ZK60 magnesium alloy," *J. Mater. Sci. Technol.*, vol. 33, no. 9, pp. 907–918, 2017.
- [97] D. Toscano, S. K. Shaha, B. Behraves, H. Jahed, and B. Williams, "Effect of Forging on Microstructure, Texture, and Uniaxial Properties of Cast AZ31B Alloy," *J. Mater. Eng. Perform.*, vol. 26, no. 7, pp. 3090–3103, 2017.
- [98] H. He, S. Huang, Y. Yi, and W. Guo, "Simulation and experimental research on isothermal

- forging with semi-closed die and multi-stage-change speed of large AZ80 magnesium alloy support beam,” *J. Mater. Process. Technol.*, vol. 246, pp. 198–204, 2017.
- [99] Z. Wang, Y. Yang, B. Li, Y. Zhang, and Z. Zhang, “Effect of hot-deformation on microstructure and mechanical properties of AZ80 magnesium alloy,” *Mater. Sci. Eng. A*, vol. 582, pp. 36–40, 2013.
- [100] G. Yu, “Forging Specimen Design for Magnesium Alloys,” 2016.
- [101] S. Dong *et al.*, “Characteristic cyclic plastic deformation in ZK60 magnesium alloy,” *Int. J. Plast.*, vol. 91, pp. 25–47, 2017.
- [102] X. M. Chen, Y. C. Lin, and J. Chen, “Low-cycle fatigue behaviors of hot-rolled AZ91 magnesium alloy under asymmetrical stress-controlled cyclic loadings,” *J. Alloys Compd.*, vol. 579, pp. 540–548, 2013.
- [103] C. A. Sager *et al.*, “Physical metallurgy of Mg AZ80 alloys for forging applications,” *Mater. Soc. Annu. Meet.*, vol. 12, no. April, pp. 405–410, 2009.
- [104] Y. Ogushi, E. Mostaed, D. Dellasega, M. Vedani, H. Miyamoto, and H. Fujiwara, “Aging behavior of ECAP processed AZ80 Mg alloy,” *IOP Conf. Ser. Mater. Sci. Eng.*, vol. 63, no. 1, 2014.
- [105] H. Yu, S. Hyuk, and B. S. You, “Development of extraordinary high-strength Mg – 8Al – 0.5Zn alloy via a low temperature and slow speed extrusion,” *Mater. Sci. Eng. A*, vol. 610, pp. 445–449, 2014.
- [106] Y. Cai *et al.*, “Hot deformation characteristics of AZ80 magnesium alloy: Work hardening effect and processing parameter sensitivities,” *Mater. Sci. Eng. A*, vol. 687, no. December 2016, pp. 113–122, 2017.
- [107] A. Gryguc, S.B. Behravesh, S.K. Shaha, H. Jahed, M. Wells, B. Williams, X. Su, “Effect of warm forging on monotonic and cyclic behaviour of AZ80 casting,” *Int. J. Fatigue*, no. SI: Proceedings of FDSM XI, 2017.
- [108] F. Ellyin, K. Golos, and Z. Xia, “In-Phase and Out-of-Phase Multiaxial Fatigue,” *J. Eng. Mater. Technol.*, vol. 113, no. 1, p. 112, 1991.
- [109] A. A. Roostaei and H. Jahed, “Multiaxial cyclic behaviour and fatigue modelling of AM30 Mg alloy extrusion,” *Int. J. Fatigue*, vol. 97, pp. 150–161, 2017.
- [110] H. Li, G. Kang, C. Yu, and Y. Liu, “Experimental investigation on temperature-dependent uniaxial ratchetting of AZ31B magnesium alloy,” *Int. J. Fatigue*, vol. 120, no. September 2018, pp. 33–45, 2019.
- [111] Y. Xiong, Q. Yu, and Y. Jiang, “Multiaxial fatigue of extruded AZ31B magnesium alloy,” *Mater. Sci. Eng. A*, vol. 546, pp. 119–128, 2012.
- [112] A. Fatemi and N. Shamsaei, “Multiaxial fatigue: An overview and some approximation models for life estimation,” *Int. J. Fatigue*, vol. 33, no. 8, pp. 948–958, 2011.
- [113] D. Toscano, S. K. Shaha, B. Behravesh, H. Jahed, and B. Williams, “Multiaxial Cyclic Response of Low Temperature Closed-Die Forged AZ31B Mg Alloy,” *Miner. Met. Mater. Ser.*, pp. 289–296, 2019.
- [114] J. Albinmousa, H. Jahed, and S. Lambert, “Estimation of Fatigue Crack Orientation using Critical Plane Parameters : An Experimental Investigation,” *10th Int. Conf. Multiaxial Fatigue Fract.*, no.

- 1, pp. 1–8, 2013.
- [115] J. Albinmousa, “Multiaxial fatigue crack path prediction using critical plane concept,” *Frat. ed Integrita Strutt.*, vol. 10, no. 35, pp. 182–186, 2016.
- [116] A. Fatemi and D. F. Socie, “a Critical Plane Approach To Multiaxial Fatigue Damage Including Out-of-Phase Loading,” *Fatigue Fract. Eng. Mater. Struct.*, vol. 11, no. 3, pp. 149–165, 1988.
- [117] Y. Jiang, “Fatigue criterion for general multiaxial loading,” *Fatigue Fract. Eng. Mater. Struct.*, vol. 23, no. 1, pp. 19–32, 2000.
- [118] T. Al-Samman, “Magnesium: The Role of Crystallographic Texture, Deformation Conditions and Alloying Elements on Formability,” p. 233, 2008.
- [119] G. Kurz, J. Swiostek, P. A. Beaven, and D. Letzig, “Die Forging of Magnesium Materials,” vol. 2008, no. 724, 2018.
- [120] P. Skubisz, J. Sińczak, and S. Bednarek, “Forgeability of Mg-Al-Zn magnesium alloys in hot and warm closed die forging,” *J. Mater. Process. Technol.*, vol. 177, no. 1–3, pp. 210–213, 2006.
- [121] A. Salandari-Rabori, A. Zarei-Hanzaki, H. R. Abedi, J. S. Lecomte, and H. Khatami-Hamedani, “Micro and macro texture evolution during multiaxial forging of a WE43 magnesium alloy,” *J. Alloys Compd.*, vol. 739, pp. 249–259, 2018.
- [122] A. Gryguc *et al.*, “Low-cycle fatigue characterization and texture induced ratcheting behaviour of forged AZ80 Mg alloys,” *Int. J. Fatigue*, vol. 116, pp. 429–438, 2018.
- [123] S. M. H. Karparvarfard, S. K. Shaha, S. B. Behraves, H. Jahed, and B. Williams, “Fatigue life improvement of cast ZK60 Mg alloy through low temperature closed-die forging for automotive applications,” vol. 06009, pp. 1–6, 2018.
- [124] Y. Xiong and Y. Jiang, “Fatigue of ZK60 magnesium alloy under uniaxial loading,” *Int. J. Fatigue*, vol. 64, pp. 74–83, 2014.
- [125] J. Dallmeier, O. Huber, H. Saage, and K. Eigenfeld, “Uniaxial cyclic deformation and fatigue behavior of AM50 magnesium alloy sheet metals under symmetric and asymmetric loadings,” *Mater. Des.*, vol. 70, pp. 10–30, 2015.
- [126] A. N. Chamos, S. G. Pantelakis, G. N. Haidemenopoulos, and E. Kamoutsi, “Tensile and fatigue behaviour of wrought magnesium alloys AZ31 and AZ61,” *Fatigue Fract. Eng. Mater. Struct.*, vol. 31, no. 9, pp. 812–821, 2008.
- [127] Q. Yu, J. Zhang, Y. Jiang, and Q. Li, “An experimental study on cyclic deformation and fatigue of extruded ZK60 magnesium alloy,” *Int. J. Fatigue*, vol. 36, no. 1, pp. 47–58, 2012.
- [128] Y. Xiong, Q. Yu, and Y. Jiang, “An experimental study of cyclic plastic deformation of extruded ZK60 magnesium alloy under uniaxial loading at room temperature,” *Int. J. Plast.*, vol. 53, pp. 107–124, 2014.
- [129] A. Pahlevanpour, S. Karparvarfard, S. K. Shaha, S. B. Behraves, S. Adibnazari, and H. Jahed, “Anisotropy in the Quasi-static and Cyclic Behavior of ZK60 Extrusion: Characterization and Fatigue Modeling,” *Mater. Des.*, vol. 160, pp. 936–948, 2018.
- [130] S. Bentachfine, G. Pluvinage, L. S. Toth, and Z. Azari, “Biaxial low cycle fatigue under non-proportional loading of a magnesium-lithium alloy,” *Eng. Fract. Mech.*, vol. 54, no. 4, pp. 513–522, 1996.

- [131] M. J. Mahtabi and N. Shamsaei, "Multiaxial fatigue modeling for Nitinol shape memory alloys under in-phase loading," *J. Mech. Behav. Biomed. Mater.*, vol. 55, no. March, pp. 236–249, 2015.
- [132] Y. Xiong, Q. Yu, and Y. Jiang, "Cyclic deformation and fatigue of extruded AZ31B magnesium alloy under different strain ratios," *Mater. Sci. Eng. A*, vol. 649, pp. 93–103, 2016.
- [133] M. Noban, H. Jahed, E. Ibrahim, and A. Ince, "Load path sensitivity and fatigue life estimation of 30CrNiMo8HH," *Int. J. Fatigue*, vol. 37, pp. 123–133, 2012.
- [134] F. Castro and Y. Jiang, "Fatigue life and early cracking predictions of extruded AZ31B magnesium alloy using critical plane approaches," *Int. J. Fatigue*, vol. 88, pp. 236–246, 2016.

## 9. Appendix A – Experimental Data

The following appendix summarizes the experimental data collected throughout the stress and strain controlled fatigue tests which were conducted as a part of this research work. For the purposes of making the data presented in the table more concise and easier to read, the following abbreviations are used for each of the material conditions. Please note that  $N_f$  is the fatigue life at a 50% drop in the load/torque.

Table 13 – List of abbreviations for all AZ80 Mg material conditions presented in appendix experimental data.

As-Received Conditions	Forged Conditions:
Cast – As-Cast	A - Cast-Forged Open-Die (350°C @0.65 mm/min)
RD – Radial Direction	B - Cast-Forged Open-Die (450°C @0.65 mm/min)
TD – Transverse Direction	C - Cast-Forged Open-Die (450°C @6.50 mm/min)
LD – Longitudinal Direction	D - Cast-Forged Closed-Die (275°C @20.0 mm/min)
Ext – As-Extruded	E - Ext-Forged Closed-Die (250°C @20.0 mm/min)
RD – Radial Direction	F - Cast-Forged Closed-Die (250°C @20.0 mm/min)
TD – Transverse Direction	G - Ext-Forged Closed-Die (375°C @20.0 mm/min)
ED – Extrusion Direction	H - Ext-Forged Closed-Die (375°C @20.0 mm/min)

Table 14 - Cyclic Axial Test Summary (Path A - Uni-Axial)

Test ID	Cond.	Direction	$\epsilon_a$ [%]	$\sigma_{max}$ [MPa]	$\sigma_{min}$ [MPa]	$E_{el}$ [MJ/m <sup>3</sup> ]	$E_{pl}$ [MJ/m <sup>3</sup> ]	$E_{tot}$ [MJ/m <sup>3</sup> ]	$N_f$
TD1	Cast	TD	0.50	141.1	-139.9	0.23	0.49	0.7195	3,482
TD2	Cast	TD	0.50	138.7	-144.9	0.22	0.55	0.7673	4,461
TD3	Cast	TD	0.30	116.7	-106.3	0.15	0.14	0.2951	15,644
TD4	Cast	TD	0.20	61.5	-109.7	-	-	-	129,487
TD5	Cast	TD	0.70	162.6	-174.7	0.30	1.05	1.3470	1,039
TD6	Cast	TD	0.25	96.5	-100.4	0.11	0.07	0.1791	29,847
RD1	Cast	RD	0.10	44.1	-42.0	-	-	-	27,906,160
RD2	Cast	RD	1.20	198.3	-215.6	-	-	-	50
RD3	Cast	RD	1.00	196.4	-182.7	0.44	2.00	2.4350	463
RD4	Cast	RD	0.20	71.9	-93.8	0.06	0.03	0.0895	889,689
LD1	Cast	LD	0.50	137.1	-137.5	0.21	0.50	0.7173	7,320
LD2	Cast	LD	1.00	194.4	-176.7	0.43	2.00	2.4310	530
LD3	Cast	LD	0.20	63.6	-64.9	0.05	0.08	0.1238	130,133
LD4	Cast	LD	0.18	59.5	-76.5	-	-	-	26,112,067
A1	A	LD	1.20	287.7	-219.1	0.94	2.64	3.5768	546
A2	A	LD	0.70	233.4	-195.8	0.62	0.69	1.3137	3,052
A3	A	LD	0.20	86.5	-86.8	-	-	-	10,021,002
A4	A	LD	0.30	134.8	-129.9	0.21	0.05	0.2584	66,171
B1	B	LD	0.20	96.0	-84.6	0.10	0.00	0.1048	987,411
B2	B	LD	0.50	176.7	-151.6	0.35	0.38	0.7341	7,188
B3	B	LD	1.40	269.8	-196.6	0.83	3.67	4.4990	451
B4	B	LD	1.00	277.8	-162.7	0.88	0.39	1.2685	1,320
B5	B	LD	0.18	80.7	-75.5	0.07	0.00	0.0780	2,902,713
C1	C	LD	0.50	201.8	-125.1	0.46	0.31	0.7756	4,106
C2	C	LD	1.00	289.5	-175.2	0.95	1.55	2.5037	814
C3	C	LD	0.70	248.1	-153.2	0.70	0.75	1.4447	1,871

C4	C	LD	0.30	158.2	-101.4	0.28	0.07	0.3544	28,532
C5	C	LD	0.20	85.4	-86.0	0.08	0.01	0.0918	1,191,031
C6	C	LD	0.25	106.4	-106.1	0.13	0.04	0.1697	422,811
LD7	Cast	LD	0.60	163.7	-147.3	0.30	0.71	1.0120	1,998
LD8	Cast	LD	0.80	177.4	-164.1	0.36	0.72	1.0779	1,511
LD9	Cast	LD	0.90	186.9	-168.1	-	-	-	644
LD10	Cast	LD	1.10	199.4	-185.7	0.45	1.24	1.6917	324
LD11	Cast	LD	1.30	215.1	-203.4	-	-	-	239
LD12	Cast	LD	1.40	212.2	-199.0	-	-	-	173
ED3	Ext	ED	1.40	301.8	-260.7	0.97	3.82	4.7935	157
ED4	Ext	ED	1.20	308.2	-238.8	1.01	2.53	3.5491	370
ED5	Ext	ED	1.00	310.0	-228.0	1.03	1.67	2.6928	421
ED6	Ext	ED	0.80	298.2	-225.6	0.95	0.89	1.8400	1,012
ED7	Ext	ED	0.60	249.8	-203.4	0.67	0.31	0.9775	2,995
RD2	Ext	RD	1.40	212.4	-238.6	0.53	3.97	4.5046	282
RD3	Ext	RD	1.20	198.9	-205.7	0.47	2.74	3.2044	422
RD4	Ext	RD	1.00	190.3	-209.4	0.43	2.02	2.4444	641
RD5	Ext	RD	0.80	182.3	-196.8	0.39	1.25	1.6487	1,116
RD6	Ext	RD	0.60	163.1	-172.2	0.32	0.68	0.9963	2,878
ED8	Ext	ED	2.00	308.1	-270.1	1.01	7.25	8.2668	114
RD7	Ext	RD	2.00	225.8	-237.5	0.60	6.99	7.5964	132
LD13	Cast	LD	2.00	224.3	-206.8	-	-	-	69
ED10	Ext	ED	0.40	194.8	-153.6	0.41	0.10	0.5019	13,968
ED11	Ext	ED	0.30	139.9	-132.9	0.21	0.05	0.2561	65,652
ED12	Ext	ED	0.20	89.3	-101.8	0.09	0.00	0.0853	3,063,612
RD9	Ext	RD	0.40	147.5	-142.1	0.26	0.29	0.5523	5,702
RD10	Ext	RD	0.30	123.7	-121.2	0.18	0.12	0.2979	26,900
RD11	Ext	RD	0.20	91.3	-98.0	0.10	0.02	0.1191	467,496
TD8	Cast	TD	0.28	108.5	-108.5	-	-	-	12,257
TD9	Cast	TD	0.26	100.8	-100.8	-	-	-	17,753
TD10	Cast	TD	0.24	93.0	-93.0	-	-	-	30,623
TD11	Cast	TD	0.22	85.3	-85.3	-	-	-	50,127
ED_1	Ext	ED	$\sigma$ -N	180.0	-180.0	-	-	-	16,829
LD_1	Cast	LD	$\sigma$ -N	180.0	-180.0	-	-	-	332
41_1	E	LD	$\sigma$ -N	180.0	-180.0	-	-	-	24,480
44_1	F	LD	$\sigma$ -N	180.0	-180.0	-	-	-	2,780
38_1	D	LD	$\sigma$ -N	180.0	-180.0	-	-	-	5,107
59_1	G	LD	$\sigma$ -N	180.0	-180.0	-	-	-	32,349
62_1	H	LD	$\sigma$ -N	180.0	-180.0	-	-	-	3,339
ED_2	Ext	ED	$\sigma$ -N	160.0	-160.0	-	-	-	33,337
LD_2	Cast	LD	$\sigma$ -N	160.0	-160.0	-	-	-	1,154
44_2	F	LD	$\sigma$ -N	160.0	-160.0	-	-	-	4,130
59_2	G	LD	$\sigma$ -N	160.0	-160.0	-	-	-	76,284
ED_3	Ext	ED	$\sigma$ -N	140.0	-140.0	-	-	-	96,187
LD_3	Cast	LD	$\sigma$ -N	140.0	-140.0	-	-	-	5,209
44_3	F	LD	$\sigma$ -N	140.0	-140.0	-	-	-	23,314
38_3	D	LD	$\sigma$ -N	140.0	-140.0	-	-	-	14,107
62_3	H	LD	$\sigma$ -N	140.0	-140.0	-	-	-	21,637
ED_4	Ext	ED	$\sigma$ -N	180.0	-180.0	-	-	-	20,329
LD_4	Cast	LD	$\sigma$ -N	180.0	-180.0	-	-	-	594

41_4	E	LD	$\sigma$ -N	180.0	-180.0	-	-	-	28,821
44_4	F	LD	$\sigma$ -N	180.0	-180.0	-	-	-	2,962
59_4	G	LD	$\sigma$ -N	180.0	-180.0	-	-	-	34,876
62_4	H	LD	$\sigma$ -N	180.0	-180.0	-	-	-	4,569
ED_5	Ext	ED	$\sigma$ -N	160.0	-160.0	-	-	-	34,535
LD_5	Cast	LD	$\sigma$ -N	160.0	-160.0	-	-	-	1,146
44_5	F	LD	$\sigma$ -N	160.0	-160.0	-	-	-	7,031
38_5	D	LD	$\sigma$ -N	160.0	-160.0	-	-	-	2,851
59_5	G	LD	$\sigma$ -N	160.0	-160.0	-	-	-	60,001
62_5	H	LD	$\sigma$ -N	160.0	-160.0	-	-	-	4,054
ED_6	Ext	ED	$\sigma$ -N	140.0	-140.0	-	-	-	77,430
LD_6	Cast	LD	$\sigma$ -N	140.0	-140.0	-	-	-	4,701
44_6	F	LD	$\sigma$ -N	140.0	-140.0	-	-	-	34,771
38_6	D	LD	$\sigma$ -N	140.0	-140.0	-	-	-	14,522
62_6	H	LD	$\sigma$ -N	140.0	-140.0	-	-	-	30,210
44_7	F	LD	$\sigma$ -N	160.0	-160.0	-	-	-	6,034
38_7	D	LD	$\sigma$ -N	160.0	-160.0	-	-	-	2,920
62_7	H	LD	$\sigma$ -N	160.0	-160.0	-	-	-	5,116
38_8	D	LD	$\sigma$ -N	160.0	-160.0	-	-	-	3,335
RD_1	Ext	RD	$\sigma$ -N	180.0	-180.0	-	-	-	1,190
RD_2	Ext	RD	$\sigma$ -N	180.0	-180.0	-	-	-	1,403
RD_3	Ext	RD	$\sigma$ -N	160.0	-160.0	-	-	-	4,799
RD_4	Ext	RD	$\sigma$ -N	160.0	-160.0	-	-	-	4,895
RD_5	Ext	RD	$\sigma$ -N	140.0	-140.0	-	-	-	14,145
RD_6	Ext	RD	$\sigma$ -N	140.0	-140.0	-	-	-	9,141
ED13	Ext	ED	$\sigma$ -N	274.7	-245.9	0.86	4.02	4.8824	7
ED14	Ext	ED	$\sigma$ -N	271.7	-284.4	0.84	3.24	4.0823	6
RD12	Ext	RD	$\sigma$ -N	208.6	-236.1	0.52	5.06	5.5791	184
RD13	Ext	RD	$\sigma$ -N	218.2	-252.8	0.56	6.31	6.8700	85
ED15	Ext	ED	$\sigma$ -N	275.0	-246.8	0.86	3.29	4.1459	7
ED16	Ext	ED	$\sigma$ -N	341.3	-286.2	1.32	3.17	4.4965	17
41_7	E	LD	$\sigma$ -N	180.0	-180.0	0.37	0.18	0.5456	32,497
44_8	F	LD	$\sigma$ -N	180.0	-180.0	0.37	0.26	0.6329	10,496
38_9	D	LD	$\sigma$ -N	180.0	-180.0	0.37	0.39	0.7596	8,484
59_7	G	LD	$\sigma$ -N	180.0	-180.0	0.37	0.12	0.4912	22,456
62_8	H	LD	$\sigma$ -N	180.0	-180.0	0.37	1.64	2.0094	4,699
ED_7	Ext	ED	$\sigma$ -N	180.0	-180.0	0.37	0.51	0.8737	17,593
RD_7	Ext	RD	$\sigma$ -N	180.0	-180.0	0.37	1.91	2.2782	767
LD_7	Cast	LD	$\sigma$ -N	180.0	-180.0	0.37	2.29	2.6603	287
LD_9	Cast	LD	$\sigma$ -N	200.0	-200.0	0.45	-	0.4545	2
LD_10	Cast	LD	$\sigma$ -N	190.0	-190.0	0.41	-	0.4102	7
62_10	H	LD	$\sigma$ -N	190.0	-190.0	0.41	-	0.4102	0
62_11	H	LD	$\sigma$ -N	190.0	-190.0	0.41	-	0.4102	68
LD_11	Cast	LD	$\sigma$ -N	190.0	-190.0	0.41	-	0.4102	67
TD_12	Cast	TD	$\sigma$ -N	190.0	-190.0	0.41	4.24	4.6516	100
62_12	H	LD	$\sigma$ -N	190.0	-190.0	0.41	0.65	1.0621	2,043
62_13	H	LD	$\sigma$ -N	190.0	-190.0	0.41	0.66	1.0736	2,574
ED_8	Ext	ED	$\sigma$ -N	190.0	-190.0	0.41	0.15	0.5574	8,697
ED_9	Ext	ED	$\sigma$ -N	190.0	-190.0	0.41	0.14	0.5500	8,557
59_8	G	LD	$\sigma$ -N	190.0	-190.0	0.41	0.11	0.5248	12,170

59_9	G	LD	$\sigma$ -N	190.0	-190.0	0.41	0.16	0.5748	9,961
59_10	G	LD	$\sigma$ -N	190.0	-190.0	0.41	0.22	0.6273	6,517
ED_10	Ext	ED	$\sigma$ -N	190.0	-190.0	0.41	0.17	0.5784	6,699
TR1	E	LD	1.00	-	0.0	-	-	-	1
TR2	E	LD	1.00	318.1	-266.5	1.13	1.71	2.8443	187
TR3	E	LD	1.00	308.2	-293.1	1.06	1.89	2.9479	173
TR4	E	LD	1.40	323.1	-301.4	1.17	4.45	5.6207	55
TR5	E	LD	2.00	340.3	-327.7	1.30	10.11	11.4050	15
TR7	E	LD	1.00	312.9	-297.0	1.10	1.69	2.7815	255
TR9	E	LD	0.80	285.3	-280.6	0.91	0.72	1.6308	491
TR10	E	LD	0.40	164.1	-177.8	0.30	0.06	0.3654	9,220
TR11	E	LD	0.60	243.0	-249.3	0.66	0.25	0.9146	1,801
TR12	E	LD	0.80	297.5	-248.8	0.99	0.78	1.7687	484
TR13	E	LD	0.60	227.6	-234.1	0.58	0.31	0.8882	2,333
SR1	E	LD	2.00	349.0	-306.0	1.36	9.51	10.8773	24
SR2	E	LD	0.40	167.3	-187.8	0.31	0.06	0.3725	16,630
URA_1	E	LD	0.35	152.1	-163.7	0.26	0.03	0.2887	62,611
URA_2	E	LD	0.35	153.5	-155.8	0.26	0.03	0.2925	53,686
URA_3	E	LD	0.32	139.0	-142.0	0.22	0.02	0.2353	195,903
URA_4	E	LD	0.32	138.5	-144.7	0.21	0.02	0.2332	133,275

Table 15 - Cyclic Shear Test Summary (Path B Uni-Axial). \*Note all samples are from the Longitudinal Direction (LD) of forged condition E (Ext-Forged Closed-Die (250°C @20.0 mm/min).

Test ID	Cond.	Direction	$\gamma_a$ [%]	$\tau_{max}$ [MPa]	$\tau_{mean}$ [MPa]	$W_{el}^+$ [MJ/m <sup>3</sup> ]	$W_{pl}$ [MJ/m <sup>3</sup> ]	$W_{tot}$ [MJ/m <sup>3</sup> ]	$N_f$
TR1	E	LD	1	106.9	5.1	0.654	0.580	1.234	1,000
TR2	E	LD	1	108.3	0.5	0.677	0.580	1.257	1,202
TR3	E	LD	1.4	128.3	-5.5	0.923	1.337	2.260	291
TR4	E	LD	1.4	110.7	0.5	0.744	1.337	2.081	276
TR5	E	LD	2	137.8	0.0	1.183	3.288	4.471	8
TR6	E	LD	2	139.9	0.5	1.212	3.288	4.501	6
TR7	E	LD	0.6	78.5	-1.9	0.367	0.185	0.552	45,404
TR8	E	LD	0.8	85.4	-1.9	0.436	0.425	0.861	7,454
TR9	E	LD	0.7	82.3	-1.3	0.411	0.272	0.683	15,296
TR11	E	LD	0.5	70.6	-2.3	0.292	0.118	0.411	354,400
TR12	E	LD	0.4	64.7	-5.2	0.223	0.050	0.273	5,314,646
SR2	E	LD	0.55	71.2	-2.5	0.294	0.171	0.466	118,989
TR15	E	LD	0.41	61.6	-1.1	0.229	0.060	0.289	4,413,549
TR16	E	LD	0.42	62.9	-1.2	0.238	0.059	0.297	3,094,416
TR18	E	LD	0.95	106.0	-4.7	0.643	0.504	1.146	1,098
SR5	E	LD	0.46	66.5	-2.9	0.253	0.096	0.349	1,180,689

Table 16 – Cyclic Bi-Axial Test Summary (Path C,D,E). \*Note all samples are from the Longitudinal Direction (LD) of forged condition E (Ext-Forged Closed-Die (250°C @20.0 mm/min).

Test ID	$\epsilon_a$ [%]	$\gamma_a$ [%]	$\Theta$ [°]	$\sigma_{max}$ [MPa]	$\sigma_{min}$ [MPa]	$\tau_{max}$ [MPa]	$\tau_{mean}$ [MPa]	$E_{el}$ [MJ/m <sup>3</sup> ]	$E_{pl}$ [MJ/m <sup>3</sup> ]	$W_{el}^+$ [MJ/m <sup>3</sup> ]	$W_{pl}$ [MJ/m <sup>3</sup> ]	$N_f$
SR6	0.70	0.50	0	259.1	-253.2	52.2	0.9	0.750	0.484	0.149	0.202	375
SR7	0.40	0.50	0	161.9	-162.5	60.8	-3.5	0.300	0.084	0.218	0.149	3,230
SR8	0.70	0.75	0	228.7	-229.6	60.0	1.5	0.608	0.614	0.216	0.445	444
SR9	0.40	0.75	0	165.8	-166.8	86.4	0.4	0.274	0.093	0.408	0.351	1,201
SR10	0.70	0.50	90	265.6	-261.1	69.6	-0.9	0.782	0.568	0.210	0.170	212
SR11	0.70	0.50	45	261.4	-264.3	61.5	-1.0	0.750	0.416	0.179	0.293	374
SR12	0.40	0.50	90	169.7	-169.3	68.6	-1.4	0.317	0.091	0.230	0.141	1,492
SR13	0.40	0.50	45	164.4	-221.0	64.3	-0.8	0.265	0.041	0.226	0.199	3,798
SR14	0.90	1.00	0	272.5	-260.0	73.4	2.8	0.829	0.510	0.309	0.938	149
SR15	0.50	1.00	0	186.9	-192.0	88.8	2.6	0.387	0.079	0.463	0.717	606
SR16	0.90	0.50	90	294.5	-279.7	69.1	-0.7	0.954	0.523	0.201	0.237	135
SR17	0.90	0.50	45	299.2	-283.9	57.0	-2.4	0.989	0.452	0.156	0.366	98